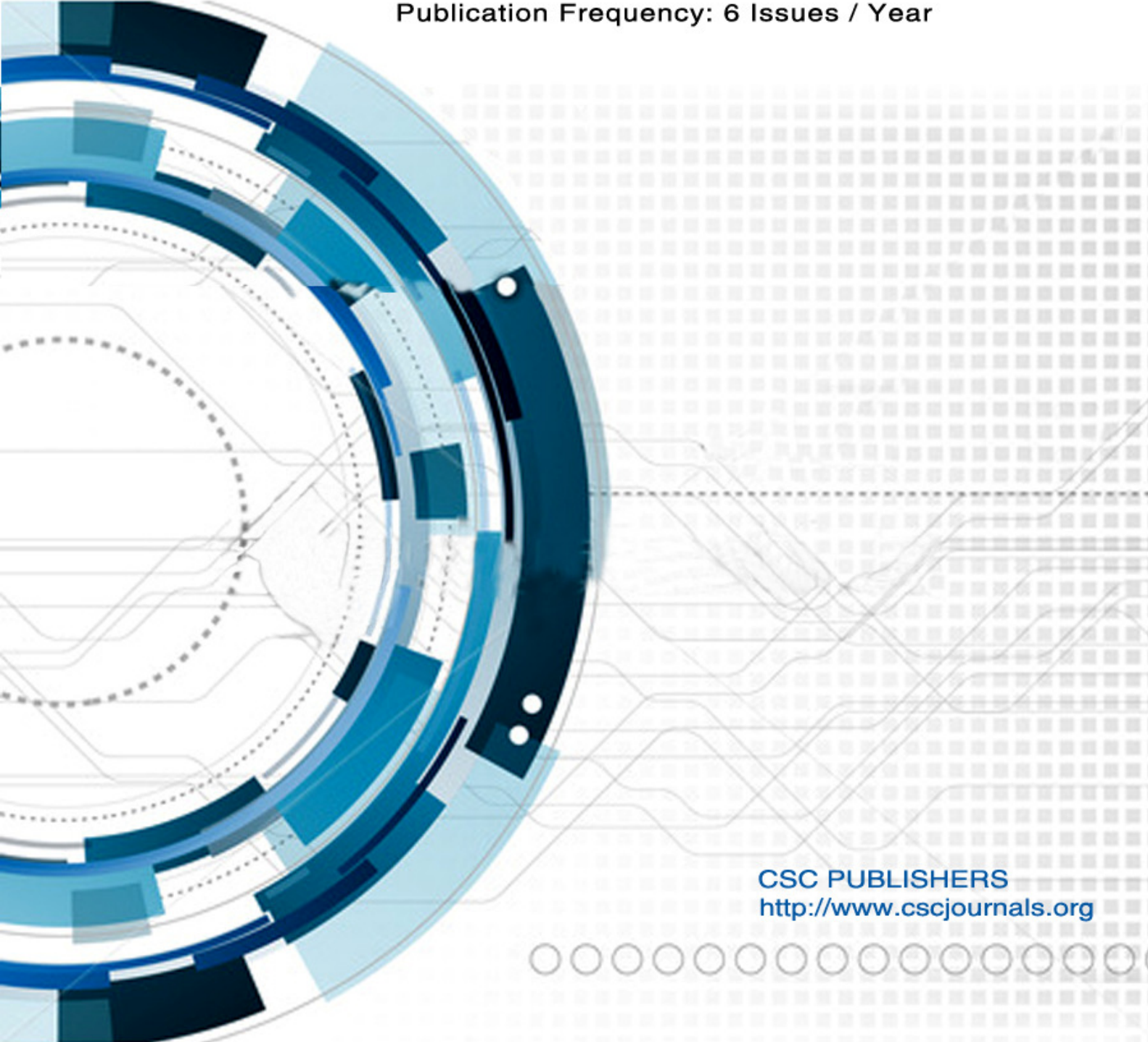


Editor-in-Chief
Dr. Kouroush Jenab

INTERNATIONAL JOURNAL OF
ENGINEERING (IJE)

ISSN : 1985-2312

Volume 5 ▪ Issue 1 ▪ March 2011
Publication Frequency: 6 Issues / Year



CSC PUBLISHERS
<http://www.cscjournals.org>



INTERNATIONAL JOURNAL OF ENGINEERING (IJE)

VOLUME 5, ISSUE 1, 2011

**EDITED BY
DR. NABEEL TAHIR**

ISSN (Online): 1985-2312

International Journal of Engineering is published both in traditional paper form and in Internet. This journal is published at the website <http://www.cscjournals.org>, maintained by Computer Science Journals (CSC Journals), Malaysia.

IJE Journal is a part of CSC Publishers

Computer Science Journals

<http://www.cscjournals.org>

INTERNATIONAL JOURNAL OF ENGINEERING (IJE)

Book: Volume 5, Issue 1, March 2011

Publishing Date: 04-04-2011

ISSN (Online): 1985-2312

This work is subjected to copyright. All rights are reserved whether the whole or part of the material is concerned, specifically the rights of translation, reprinting, re-use of illustrations, recitation, broadcasting, reproduction on microfilms or in any other way, and storage in data banks. Duplication of this publication of parts thereof is permitted only under the provision of the copyright law 1965, in its current version, and permission of use must always be obtained from CSC Publishers.

IJE Journal is a part of CSC Publishers

<http://www.cscjournals.org>

© IJE Journal

Published in Malaysia

Typesetting: Camera-ready by author, data conversion by CSC Publishing Services – CSC Journals, Malaysia

CSC Publishers, 2011

EDITORIAL PREFACE

This is the first issue of volume five of International Journal of Engineering (IJE). The Journal is published bi-monthly, with papers being peer reviewed to high international standards. The International Journal of Engineering is not limited to a specific aspect of engineering but it is devoted to the publication of high quality papers on all division of engineering in general. IJE intends to disseminate knowledge in the various disciplines of the engineering field from theoretical, practical and analytical research to physical implications and theoretical or quantitative discussion intended for academic and industrial progress. In order to position IJE as one of the good journal on engineering sciences, a group of highly valuable scholars are serving on the editorial board. The International Editorial Board ensures that significant developments in engineering from around the world are reflected in the Journal. Some important topics covers by journal are nuclear engineering, mechanical engineering, computer engineering, electrical engineering, civil & structural engineering etc.

The initial efforts helped to shape the editorial policy and to sharpen the focus of the journal. Starting with volume 5, 2011, IJE appears in more focused issues. Besides normal publications, IJE intend to organized special issues on more focused topics. Each special issue will have a designated editor (editors) – either member of the editorial board or another recognized specialist in the respective field.

The coverage of the journal includes all new theoretical and experimental findings in the fields of engineering which enhance the knowledge of scientist, industrials, researchers and all those persons who are coupled with engineering field. IJE objective is to publish articles that are not only technically proficient but also contains information and ideas of fresh interest for International readership. IJE aims to handle submissions courteously and promptly. IJE objectives are to promote and extend the use of all methods in the principal disciplines of Engineering.

IJE editors understand that how much it is important for authors and researchers to have their work published with a minimum delay after submission of their papers. They also strongly believe that the direct communication between the editors and authors are important for the welfare, quality and wellbeing of the Journal and its readers. Therefore, all activities from paper submission to paper publication are controlled through electronic systems that include electronic submission, editorial panel and review system that ensures rapid decision with least delays in the publication processes.

To build its international reputation, we are disseminating the publication information through Google Books, Google Scholar, Directory of Open Access Journals (DOAJ), Open J Gate, ScientificCommons, Docstoc and many more. Our International Editors are working on establishing ISI listing and a good impact factor for IJE. We would like to remind you that the success of our journal depends directly on the number of quality articles submitted for review. Accordingly, we would like to request your participation by submitting quality manuscripts for review and encouraging your colleagues to submit quality manuscripts for review. One of the great benefits we can provide to our prospective authors is the mentoring nature of our review process. IJE provides authors with high quality, helpful reviews that are shaped to assist authors in improving their manuscripts.

Editorial Board Members

International Journal of Engineering (IJE)

EDITORIAL BOARD

Editor-in-Chief (EiC)

Dr. Kouroush Jenab
Ryerson University (Canada)

ASSOCIATE EDITORS (AEiCs)

Professor. Ernest Baafi
University of Wollongong
Australia

Dr. Tarek M. Sobh
University of Bridgeport
United States of America

Professor. Ziad Saghir
Ryerson University
Canada

Professor. Ridha Gharbi
Kuwait University
Kuwait

Professor. Mojtaba Azhari
Isfahan University of Technology
Iran

Dr. Cheng-Xian (Charlie) Lin
University of Tennessee
United States of America

EDITORIAL BOARD MEMBERS (EBMs)

Dr. Dhanapal Durai Dominic P
Universiti Teknologi Petronas
Malaysia

Professor. Jing Zhang
University of Alaska Fairbanks
United States of America

Dr. Tao Chen
Nanyang Technological University
Singapore

Dr. Oscar Hui

University of Hong Kong
Hong Kong

Professor. Sasikumaran Sreedharan

King Khalid University
Saudi Arabia

Assistant Professor. Javad Nematian

University of Tabriz Iran

Dr. Bonny Banerjee

Senior Scientist at Audigence
United States of America

AssociateProfessor. Khalifa Saif Al-Jabri

Sultan Qaboos University
Oman

Dr. Alireza Bahadori

Curtin University
Australia

TABLE OF CONTENTS

Volume 5, Issue 1, April 2011

Pages

- 1 - 9 The New Role of Renewable Energy Systems In Developing GCC Electricity Market
Amir J. Majid
- 10 - 14 Modeling MEMS With Matlab's Simulink
Amir J. Majid
- 15 - 22 A LabVIEW Model For the Operation and Control Strategy of a Hybrid System
Amir J. Majid
- 23 - 40 Numerical Simulation and Prediction for Steep Water Gravity Waves of Arbitrary Uniform
Depth using Artificial Neural Network
Mostafa Abdeen, Samir Abohadima
- 41 – 61 Conceptual Designing and Numerical Modeling of Micro Pulse Jet for Controlling Flow
Separation
Zakir Mahfooz, Mohsin Khalil Ahmed, Huang Guoping
- 62-72 HW/SW Partitioning Approach on Reconfigurable Multimedia System on Chip
Kais Loukil, Nader Ben Amor, Mohamed Abid
- 73-101 A New Paradigm in User Equilibrium-Application in Managed Lane Pricing
Asapol Sinprasertkool, Siamak Ardekani, Stephen P. Mattingly
- 102-113 Design and Simulation of a Modified Architecture of Carry Save Adder
Chakib Alaoui
- 114-121 Peltier Thermoelectric Modules Modeling and Evaluation
Chakib Alaoui

- 122-133 Margin Parameter Variation for an Adaptive Observer to a Class of Systems
Elleuch Dorsaf, Damak Tarak
- 134-158 Cluster Based Web Search Using Support Vector Machine
Rita. S. Shelke, Devendra Singh Thakore
- 159-175 Impact of Ground Effect on Circulation Controlled Cylindrical Surfaces
Gerald M Angle II, Byron Patterson, Emily Pertl, James Smith

The New Role of Renewable Energy Systems In Developing GCC Electricity Market

Amir J. Majid

*College of Engineering
Ajman University of S&T
POB 2202, Fujairah, UAE*

abac.majid.a@ajman.ac.ae

Abstract

Due to the present high oil prices, prices fluctuations and their future upward trend, some investments can be now directed to the utilization of solar and other renewable energy systems, such as hydrogen cells and cyclic hydro systems. It is believed that the infrastructure of these systems is particularly feasible through the already large constructions and investments in real estate industry throughout GCC countries. It is also feasible in rural areas such as farms and small villages due to the relatively low power demand and load characteristics. This can also lead to the disintegration, liberalization and privatization of energy systems. The electric energy and power disintegration of such small corporations would save resources, reduce interactions and increase reliability. This paper focuses on suggested new regulations needed to control the utilization of renewable energy systems in rural areas in order to make benefit of high oil prices. It also focuses on the category and types of renewable energy systems that can be implemented in this project.

Keywords: Oil price, Solar system, Investment, PV-Utility, Housing Complexes, Infrastructure, Ring Distribution

1. INTRODUCTION

It is apparent over the last 10 years that oil prices is taking a steady upward leap bringing the prices over a historical value of 60-70 \$/barrel and more. This price can also move higher with increased demands worldwide and limited resources and raw oil reservoirs. This hick in oil prices also fluctuates chronologically with political and economical events. During this period, PV system installation costs for example, have been dropping to currently around 5 \$/W_p. In the same time the efficiency of these solar systems is increasing during same period to around 10 ¢/kWh. The GCC countries are favorite zones for solar systems and can highly benefit from these advantages by substituting part of their conventional energy systems with solar systems.

Due to this increase in oil prices, much of the return funds have been reinvested in properties and real estate industries. Legislations have been passed to allow expatriates to own their properties in this region. There is a portfolio of housing complexes stretching throughout the gulf area. This rapid increase in real estate industries, and yet to increase even more, would initialize a rush in electric power demands. It is assumed that currently electric feeders are tied off from main busses to supply such expanded demands due to the fact that power generation stations normally require long time to be built. This makes electrical power distribution radial in nature and not circular, which reduces supply reliability and distribution control. However this can be rectified by supplying part of the power through solar systems with no time-consuming installation periods. It is assumed that this would be in favor to the customer paying the electricity bill. Normal home electrification can be achieved by PV cells, hot water by natural thermal circulation and cooling & refrigeration by hydrogen cells. Roofs of thousands newly constructed houses can be used as the infrastructure of this solar system. PV development, predicts that with a reasonable set of incentives the solar photovoltaic market in the US for

example could grow more than 30% per year over the next 20 years; from 340 MW of installed capacity to 9600 MW.

Therefore, new regulations are needed to control the integration of solar energy system with the electric grid in terms of housing, connecting and interfacing, pricing, and developing these systems. It is to be noted here that such regulations are applicable not only on newly constructed real estates but any remotely built site such as villages, communication sites and farms. The policy is that they must have solar electric supply beside utility grid feeders. These regulations may also address beneficial environmental aspects of such implementation of renewable energy systems. A comparison between fossil oil, PV and diesel units for different load types and irradiation is shown in the FIGURE 1. It is apparent that for \$3/W_p PV system is competitive with either diesel or grid feeder cable extension of a few kilometers distance and for typical average daily loads of up to 100 kWh/day. This constitutes of more than 30% of the needed load for a small community area; say a residential street.

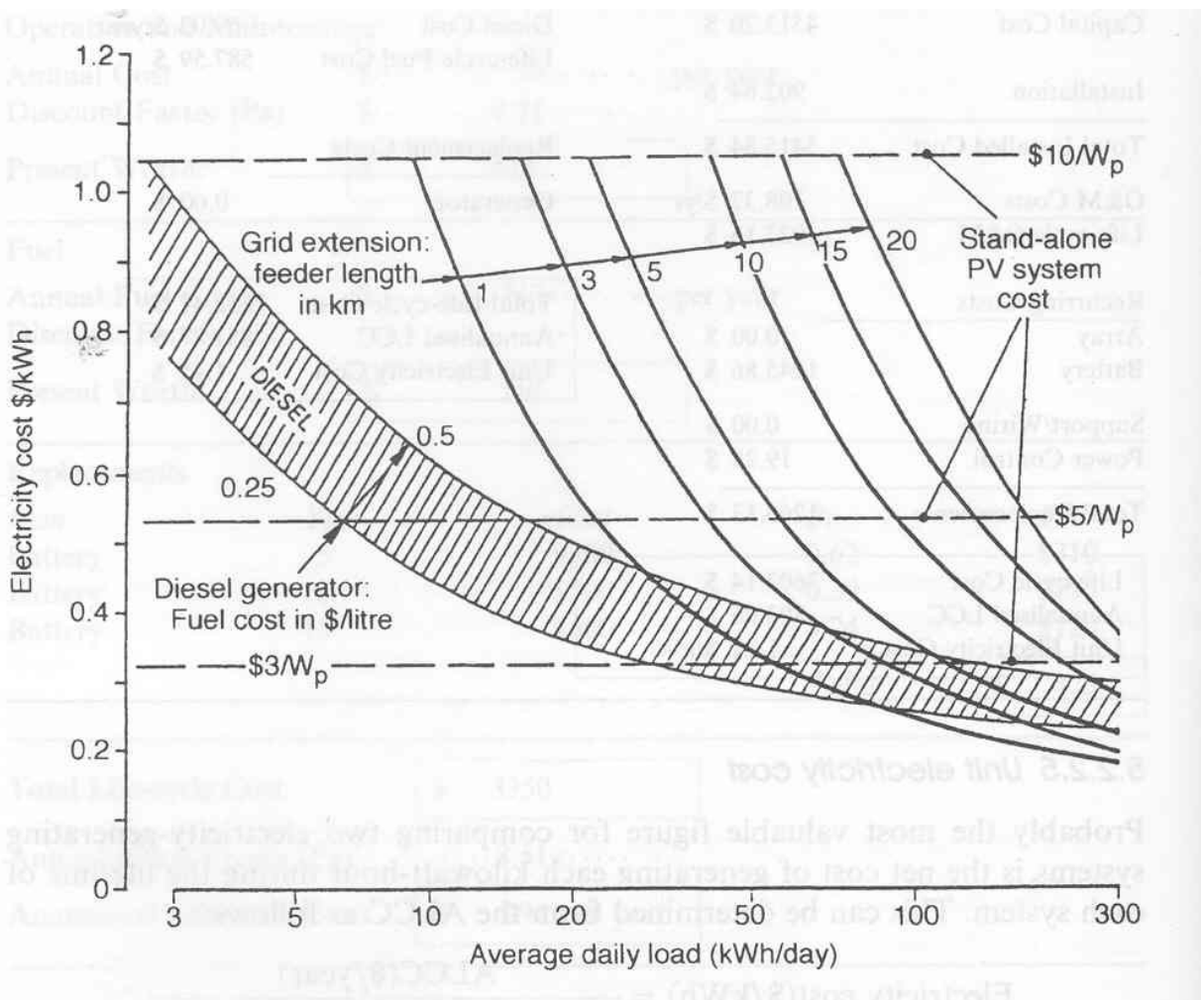


FIGURE 1: Unit electricity cost against load Comparison between PV, Diesel and Grid

OIL PRICES TREND

Oil prices have been more than tripled over the last a few decades and the trend is still up due to increasing demands and limited resources worldwide. Contrary to other raw materials, these prices experienced many fluctuations in the same period due to political and economic events. Some of these fluctuations tend to be sharp, which greatly affects energy and power planning.

FIGURE 2 depicts nominal world oil prices over the last three decades and their fluctuation events. The landmarks of these events are also shown.

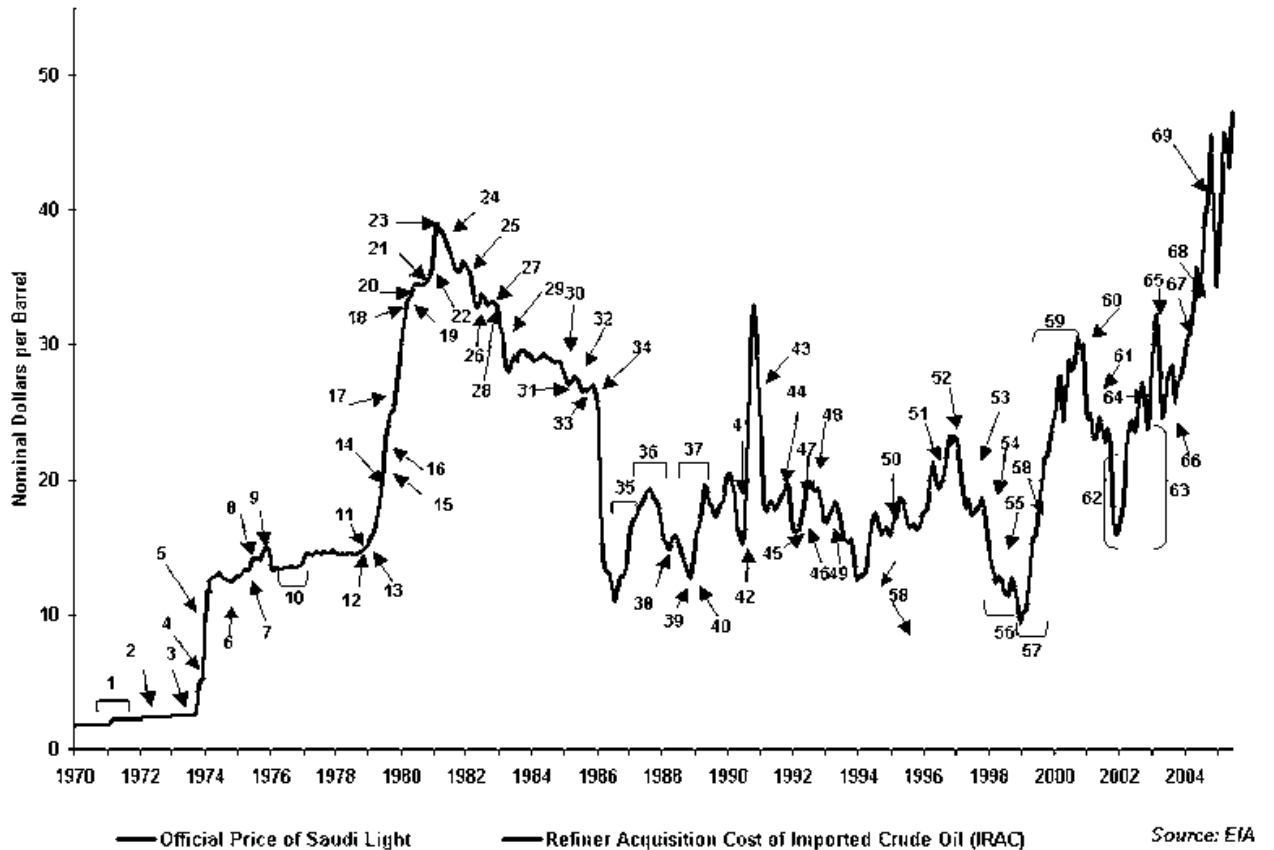


FIGURE 2: World Nominal Oil Price Chronology: 1970-2005

Currently oil price stands at 80 \$/barrel and expected to rise. A lot of GCC revenues come from oil which constitutes a high value in return if pumped more to the export market and less to the local one by integrating part of the consumed energy with solar energy.

2. SOLAR ENERGY

Solar energy constitutes a primary and potential renewable energy source to all GCC countries due to high irradiation in the region. FIGURE 3 depicts this geographical fact. Solar power systems covering the area indicated by the red stars would provide the world's current total primary energy demand (assuming an available efficiency of 8%). That is, all energy currently consumed is produced as electricity with solar cells, including heat, electricity, fuels, etc. The colors in the map show the regional solar irradiance obtained from satellite data.

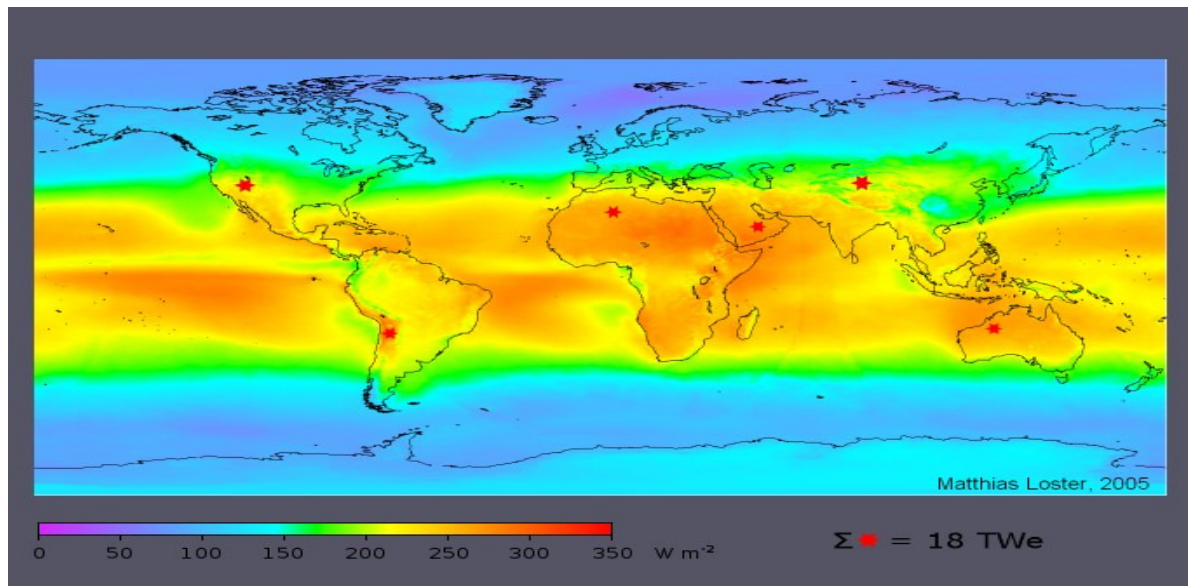


FIGURE 3: Global Solar Irradiation Map With Potential Landmarks

One study showed Photovoltaic systems installed in the areas indicated by the stars on the above map would produce an average electric output of 18 TWe, i.e. 3 TWe each when assuming a conversion efficiency from incident sunlight to electricity of 8 %. This corresponds to an energy output of 13,567 Mtoe per year (world total primary energy supply (TPES) in 2003: 10,579 Mtoe [4]). The following table lists the locations in the map to give an idea of land area requirements and availability, although the particular scenario shown is suboptimal for many political and technical reasons.

Location / Desert	Desert Size / km² [5]	Irradiation / W m⁻²	Area required / km²
Africa, Sahara	9,064,960	260	144,231
Australia, Great Sandy	388,500	265	141,509
China, Takla Makan	271,950	210	178,571
Middle-East, Arabian	2,589,910	270	138,889
South	139,860	275	136,364

America, Atacama			
U.S.A., Great Basin	492,100	220	170,455

TABLE 1: World Energy Production From six Assumed Areas

3. RECITES FROM PV ROADMAP

In 2001, we, the U.S. photovoltaic industry, stated a vision in solar electric power as **“providing consumers with competitive electricity generation products and services from thriving, self-sustaining domestic solar power industry.”** Targeted goals for 2030 are solar power system costs of \$2.33 per watt, solar electricity prices of 3.8 cents per kilowatt-hour (kWh) delivered to the customer, installed solar power generation of 200 Giga-watts (GW), and direct employment of 260,000 people. Recommended actions for market expansion are:

- Enact a residential and commercial tax credit that augments current state and federal support. The first 10 kW installed would receive a 50% tax credit capped at \$3 per watt. Any amount above 10 kW would be eligible for a 30% tax credit capped at \$2 per watt. Decreasing the caps by 5% per year will encourage a steady decline in prices and ease the transition to a market without tax credits.
- Modify the wind tax credit for solar so that it can be used in concert with the existing 10% investment tax credit.
- Establish uniform net metering and interconnection standards to give solar power owners simple equitable access to the grid and fair compensation.
- Boost federal government procurement of solar power to \$100 million per year to build public sector markets for solar power.
- Support state public benefit charge programs and other state initiatives to advance solar power and build strategic alliances with public and private organizations to expand solar markets.

It can be deduced that due to recent and future developments in solar energy systems would make them very competitive with conventional ones. The following table summarizes such developments

	Unit	2005	2010	2015
Construction cost	\$/W_p	6	5	4
Energy cost	¢/kWh	15	10	8
Efficiency	%	10	15	20
Generated power	Annual MW	100	250	500

TABLE 2: PV Systems Potential Developments

4. SOLAR ENERGY ROLE

Beside the use of cheap energy source, some of the other global benefits from a rapid and progressive transition to solar energy are:

1. It provides worldwide secure access to inexhaustible energy resources, some already at low and all at further decreasing costs: energy security. Cooperation will lead to understanding and peace rather than to armed conflicts.
2. It will reduce the dependence on a few oil and gas exporting countries and thus enhance *geopolitical stability*.
- 3.
4. It allows elimination of nuclear power and the continuing dangers of nuclear weapon proliferation: *strategic security*.
5. It requires the use of a variety of resources and many technologies: increased diversity for greater *supply security*.
6. Economy and reliability of supply can be improved by inter-regional exchange: Enhanced
7. It provides a timely pathway towards global greenhouse gas emissions reduction. According to the assessments of the IPCC, global emissions must begin to decrease at around 2030 to achieve global *climate security*.

In order to practically implement this, solar energy systems would be installed at thousands of newly built real estate complexes throughout the region, either as villa roof mounted, building facades or newly established community land. PV, dynamic and passive solar as well as hydrogen cell technologies can be utilized to supply part of the electricity, heating and cooling demand of such dwellings.

5. SOLAR ENERGY POLICIES

It can be deduced from above that utility grid-connected PV cells would have to be installed at each dwelling, forming a second feeder of electric supply which runs parallel to existing tie-off feeders and establishing a circular supply circuit. Appropriate metering, control and monitoring circuits are to be installed against nominal tenant fees, allowing both grid-connected and isolated stand-alone electrification switching operation. This is depicted in the following figures:

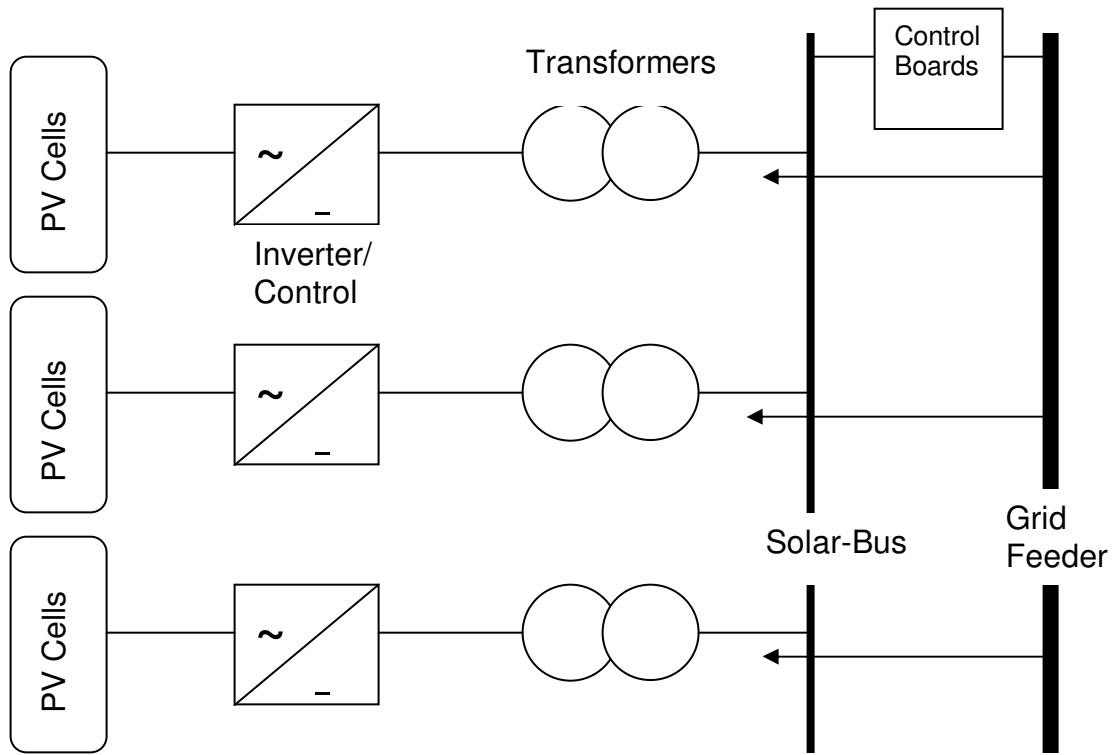


FIGURE 4: Grid-Solar Bus Connection

Besides PV cells installed per dwelling, other solar energy systems can be installed such as dynamic and passive thermal system for water heating and shedding, as well as hydrogen cells for some of the cooling power needed as depicted in the following figure. Community collective cooling system can also be integrated with these home dwellings so that one has an option to select own heating & cooling energy or relies on the electric grid.

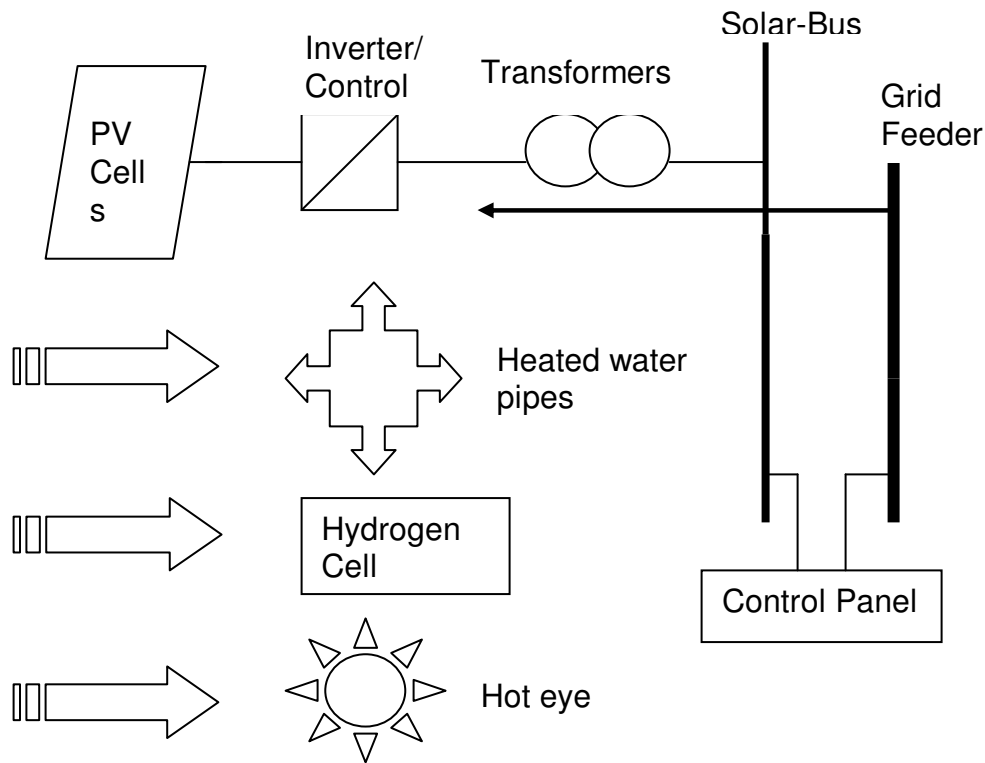


FIGURE 7: Home Dwelling Grid-Solar Electricity Connection

Since these installations are national grid properties, they are subjected to regular maintenance and monitored supervision. The occupants will receive collective energy price reduction according to community energy surplus. This would enhance the potential of solar and in general renewable energy systems in the community as a whole and improves environmental aspects in the region. Implementing a program of this size will create a substantial, new demand for the components and sub-components that go into solar systems installation.

6. CONCLUSION

It has been stressed in this paper that solar energy systems must be implemented in GCC region due to all-high and increasing and fluctuating oil prices, and decreasing solar systems with improving efficiencies on the other hand, as well as to improve environmental aspects in arid areas of heavy city concentrations with little plantations.

Due to recent huge investments in housing complexes, it is proposed in this study to employ policies for implementing solar systems in terms of using housing roofs, installing PV cells, inverters and transformers, control panels and metering and monitoring devices by the electric grid, as well as certain policies governing the installing of dynamic and passive heating and cooling systems by community collective companies, with national electric grid integration.

7. REFERENCES

1. J. Williams; “*Oil Price History and Analysis*”, [<http://www.wtrg.com/prices.htm>]
2. Energy Information Administration; “*Annual Oil Market Chronology*”, [<http://www.eia.doe.gov/emeu/cabs/AOMC/Overview.html>]

3. Sandia National Laboratories, “*PV roadmap*”;
[http://www.sandia.gov/pv/docs/PVRMExecutive_Summary.htm]
4. Arab News; “*The real estate boom*”;
[<http://www.arabnews.com/?page=15§ion=0&article=74288&d=17&m=12&y=2005>]
5. T. Markvart; *Solar Electricity*, 2nd Edition , John Wiley 2000, *PP 154*
6. M. Cohen; “*Country analysis briefs*”, [<http://www.eia.doe.gov/emeu/cabs/index.html>]
7. Energetics & NCPV; “*PV technology roadmap workshop*”, [<http://www.nrel.gov/ncpv/>]
and [<http://www.nrel.gov/ncpv/pdfs/27450.pdf#search='PV%20roadmap'>]
8. TREC; [<http://www.trecers.net/>] and [<http://www.cogeneration.net/>]
9. G. Boyle, “*Energy Systems and Sustainability*”, Oxford university press, *PP(227-291)*, 2003

Modeling MEMS With Matlab's Simulink

Amir J. Majid

*College of Engineering
Ajman University of S&T
POB 2202, Fujairah, UAE*

abac.majid.a@ajman.ac.ae

Abstract

Matlab's Simulink has been used to simulate a dynamic feedback MEMS comprising a generator with field winding, mechanical shaft system and encoder as well as a feedback to a referenced signal. The model of this system has been suggested used in Simulink for simulation.

Keywords: Simulink, MEMS, Modeling, Feedback, Field Winding, Simulation

1. INTRODUCTION

With Matlab's Simulink, it's possible to simulate dynamical models of linear and time invariant systems (LTI) implemented in MEMS applications [1], whereby a prime-mover such as a DC motor being the electromechanical system [2] driving an inertial load in a closed loop feedback configuration with supplementary blocks such as compensating blocks, filters, integrators and geometrically coordinated converters such as those used for robotic systems.

More complicated types of models can be studied and simulated, ranging from single-input, single-output (SISO) and multi-input, multi-output (MIMO) to non-linear and discrete models [3].

The operands of the interconnected linear models can be of many types such as state-space, transfer function, pole/zero plots, etc. Other procedures such as system inversion, transposition and per-transposition can be performed. More complicated feedback structure operations to derive closed loop models and to convert continuous to discrete, discrete to continuous and re-sampling [discrete to discrete] can be manipulated too.

Various discretization /interpolation methods such as a zero or first hold, Tustin approximations with or without pre-warping and matched zero-pole can also be conducted.

Simulink LTI viewer is an open and extensible graphical user interface GUI environment used to linearize models or parts of models, analyze linearized models and compare linear with nonlinear models. It's used to obtain:

- Step/impulse response
- Bode/Nyquist plots
- Nichols plots
- Singular values of frequency response
- Pole/zero plots
- Response to general input signals
- Unforced response starting from given initial states

Most importantly one can identify locations of inputs and outputs of the portions of a model and specify the operating conditions about which the model is linearized for further analysis. Other important feature of Simulink is a Linear-Quadratic-Gaussian LQG control technique which is used to design optimal dynamic regulators, Kalman estimators and filters.

2. MEMS MODEL

The electromechanical prime mover in MEMS is basically a DC motor with series field to avoid having another supply for the field. DC series motor is used extensively in traction applications

where steady state speed is determined by the friction and gradient forces. The dynamical model of the load is expressed as an inertial system with friction and assuming different line-of-shaft orientation both for the input and output.

For precise speed control of servo system, a closed loop control system is advised to get advantages of improved accuracy, fast dynamic responses and reduced effects of load disturbances and system nonlinearities.

Finally a phase locked loop PLL configuration can be implemented for speed sensing and comparing means. In PLL control system the motor speed is converted to a digital pulse train by using a speed encoder. The output of the encoder acts as speed feedback signal of frequency F_o . The phase detector compares the reference pulse train F_i with the feedback frequency F_o and provide a pulse width modulated output voltage V_c which is proportional to the difference in phases and frequencies of the reference and feedback pulse trains. The phase detector can be available in IC form. A LP filter then converts V_c to a continuous DC level which varies the output motor speed.

This can be depicted in the following figure:

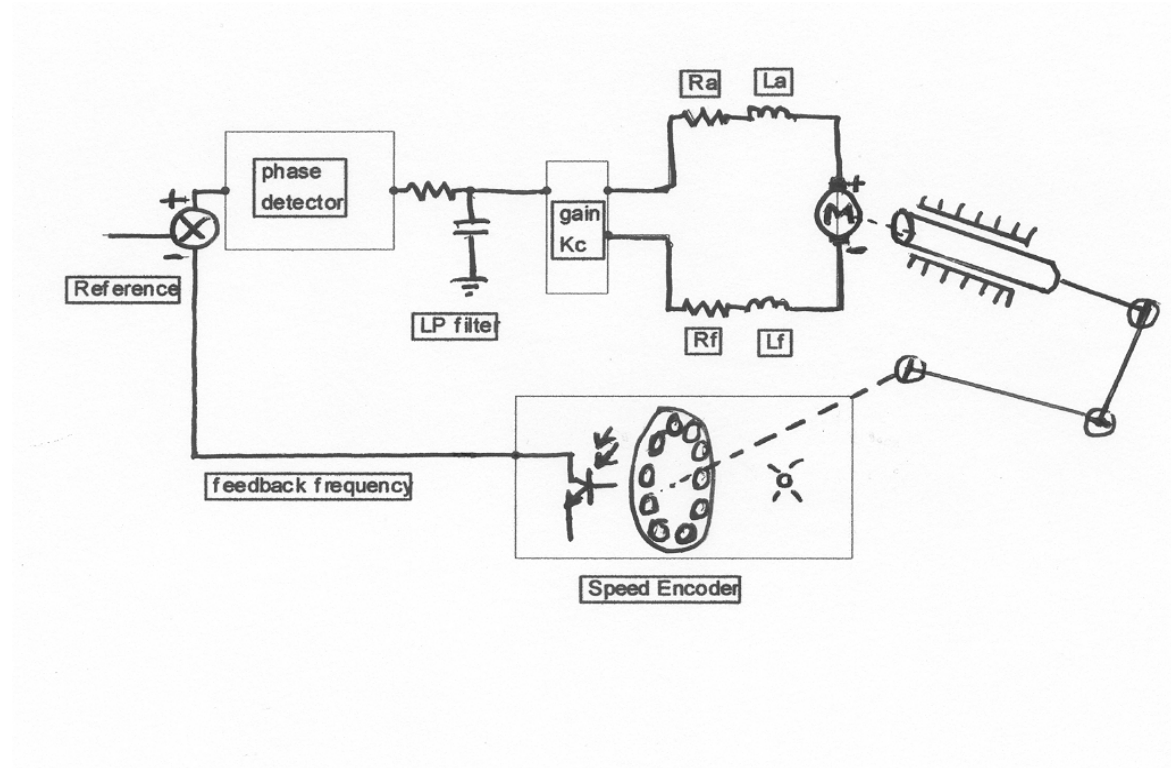


FIGURE 1: Typical MEMS Dynamical Model

The armature voltage is related to the control or reference voltage by a linear gain K_c , with the assumption that the back emf constant K_v remains constant. Then:

$$v_a = K_c v_c$$

$$e_g = K_v i_a \omega$$

also $v_a = R_m i_a + e_g + L_m di_a/dt$

$$t_d = K_t i_a = K_t i_a^2$$

also $t_d = J d\omega/dt + B\omega + t_l$

Due to nonlinear terms, these equations can be made linear by considering a small perturbation at the operating point, noting that: $\Delta i_a \Delta w$ and $(\Delta i_a)^2$ are too small; hence

$$\begin{aligned} \Delta v_a &= K_c \Delta v_c \\ \Delta e_g &= K_v (I_{a0} \Delta w + w_0 \Delta i_a) \\ \text{And } \Delta v_a &= R_m \Delta i_a + L_m d(\Delta i_a)/dt + \Delta e_g \\ \Delta t_d &= 2 K_v I_{a0} \Delta i_a \\ \text{And } \Delta t_d &= J d(\Delta w)/dt + B \Delta w + \Delta t_l \end{aligned}$$

I_{a0} and w_0 are the steady state values. Transferring these equations in Laplace's domain yields:

$$\begin{aligned} \Delta V_a(S) &= K_c \Delta V_s(S) \\ \Delta E_g(S) &= K_v [I_{a0} \Delta W(S) + w_0 \Delta I_a(S)] \\ \text{And } \Delta V_a(S) &= R_m \Delta I_a(S) + S L_m \Delta I_a(S) + \Delta E_g(S) \\ \Delta T_d(S) &= 2 K_v I_{a0} \Delta I_a(S) \\ \text{And } \Delta T_d(S) &= S J \Delta W(S) + B \Delta W(S) + \Delta T_l(S) \end{aligned}$$

The block diagram for these open-loop series drive equations is depicted as:

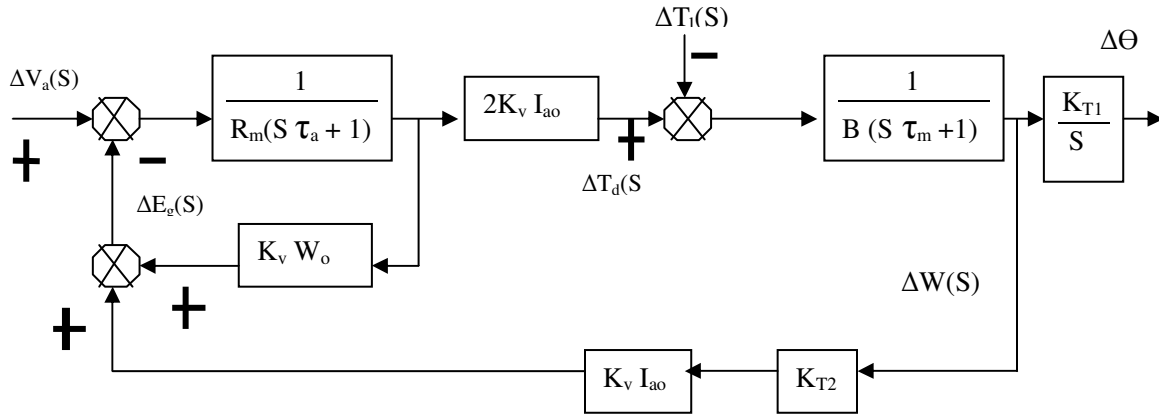


FIGURE 2: Transfer Function Feedback Model of MEMS

where τ_a and τ_m are electrical and mechanical time constants $\tau_a = L_m/R_m$ and $\tau_m = J/B$. It can be noted that any change in either control voltage or load torque will result in a change of speed. Obviously, there may be succession of joints and links which can be either linear (prismatic) or rotational (revolute), and which can be in any order or sequence and in any plane too.

These links can also be of any length, including zero, can be twisted or bent; thus the transformation matrices to any reference coordination can be calculated using different methods such as Denavit-Hartenberg representation. This is shown in the block diagram as K_{T1} and K_{T2} .

Now, by adding the PLL closed loop feedback the final block diagram becomes as shown:

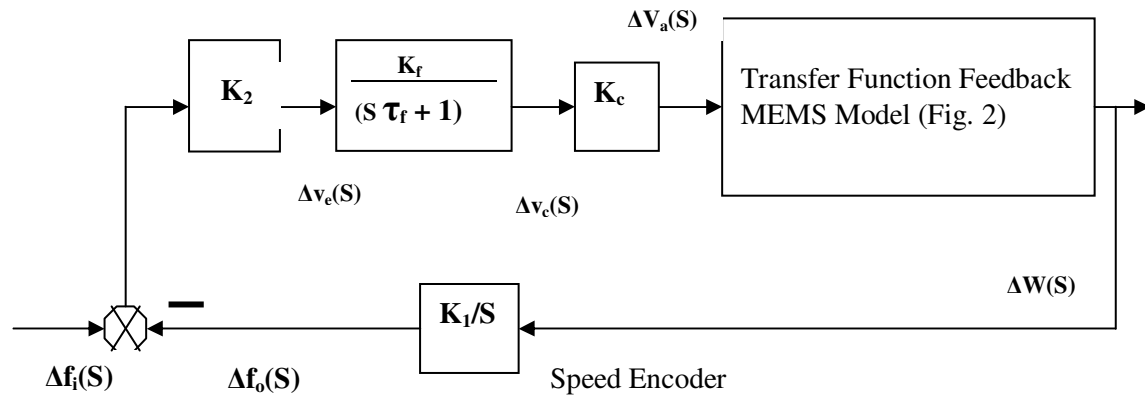


FIGURE 3: Complete MEMS Model with PLL

3. SIMULINK

The derived dynamical electromechanical linear model represented in S-domain, can be now simulated in Matlab's Simulink represented as S-domain block diagram. Input and output outlets can be specified at different locations in order to get; among others:

- Response due to a step change in the control/reference voltage keeping constant load torque
- Response due to a change in load torque disturbances keeping constant control voltage
- Response due to a change in links location and orientation keeping both constant voltage and load
- Multiple view screens at different locations simultaneously
- Platform for solver parameters to be varied for further simulations
- Platform for embedded libraries related to the blocks implemented
- Platform to integrate Matlab files and C codes
- Platform to visualize and input different signals such as noise and vibrations
- Platform to add hierarchical features of blocksets and general parameters

It can be noticed from the above features that precise and accurate simulation of MEMS models can be obtained.

4. CONCLUSION

It has been demonstrated that MEMS models can be derived and later simulated with Matlab's Simulink, which shows to be an esteemed and powerful platform for multi domain simulation and a model based design environment for dynamic systems. It provides an interactive graphical environment and a customizable set of block libraries that let help to accurately design, simulate, and test control, signal processing, communications, and other time-varying systems.

5. REFERENCES

1. W.C. Wilson, "Geometrical Matrix Toolbox for Modeling of a MOEMS System"; Manuscript # TE-2003-000045.R1, IEEE/Transactions on Education, 2004.
2. M. Rashid, "Power Electronics", Book, second edition, ISBN 0-13-334483-5, Prentice Hall, 1993.

3. The Mathworks, "*Control System Toolbox*", Matlab manual
4. J.B. Dabney, "*Mastering SIMULINK*", Pearson Prentice Hall, PP(2-7, 78-88, 197-227), 2004
5. D.Hanselman, "*Mastering MATLAB 6*", Prentice Hall, PP(336-453), 2001
6. S. Chapman, "*Matlab Programming for Engineers*", Brooks/Cole Thomson Learning, PP(392-447), 2202

A LabVIEW Model For the Operation and Control Strategy of a Hybrid System

Amir J. Majid

*College of Engineering
Ajman University of S&T
POB 2202, Fujairah, UAE*

abac.majid.a@ajman.ac.ae

Abstract

Due to the varying nature of the load demand and the fluctuating power supplies by a renewable energy system, a decision-making strategy to operate and control a hybrid system is considered. The proposed hybrid system is comprised of PV/wind and diesel units with battery backup. The aim is to ensure high operational battery bank, running diesel units in their most efficient operational ranges and maximizing the utilization of the renewable energy sources. A *LabVIEW* model is designed whereby the hybrid system components are simulated as virtual instruments [VI] interacted with functional blocks. The PV/wind VI measure continuously the available power generated from the designed system capacity, and the functional VI compare this with the actual load demand over short periods. Consequently, a decision-making scheme is considered in which optimum operation of diesel units and battery banks is reached, and also whereby scenarios can be drawn for further prediction of system power flows and State-of Charge [SOC] of the battery bank.

Keywords: LabVIEW, Hybrid, Renewable Energy, Control, Virtual Instrument

1. INTRODUCTION

Today, the most common application of standalone hybrid system is that of diesel generator augmentation (FIGURE 1), where the renewable energy source such as PV or wind and the battery bank are sized to reduce the run-time and therefore fuel consumption of the diesel generators. These systems provide sufficient storage to allow the load to be shifted, therefore ensuring that the generator is always substantially loaded. Recall that engine-driven generators are inherently inefficient when operated at light loads; for example less than 40% which can shorten their life and increase maintenance costs. Further, the hybrid system formed by the combining of renewable and conventional energy sources with a battery bank of storage, avoids the need for a spinning reserve which is the extra rotating capacity on line to overcome sudden load surges, and thus decreasing their fuel efficiency. In the same time, it provides an economic and reliable supply of electricity with reduced Loss of Load Probability LLP, especially when the daily load demand is highly variable with a ratio of peak load to minimum load of 3 or more.

On the other hand, the sizing of this hybrid system, which is based on solar radiation data for the site, load profile and back-up supplements, doesn't guarantee supply continuity or optimum operation. In addition, operational economics, which are used as constraints on the design may not necessary hold. This is due to the fact that radiation data and global irradiation are given in form of monthly averaged daily data for selected angles of panel inclinations are used. Annual load data is based, on the other hand, on number and hours of operation of appliances in the form of energy supplied in Wh/day and charge capacity in Ah/month, it's obvious that the annual load profile is different from the actual daily load profile.

Any mismatch between generation and load is usually taken out by battery storage mean. Thus, battery storage plays vital role in maintaining reliable and economical power supply. Yet, the daily/hourly cycling characteristics of battery have a pronounced effect on its lifetime as depicted in FIGURE 2

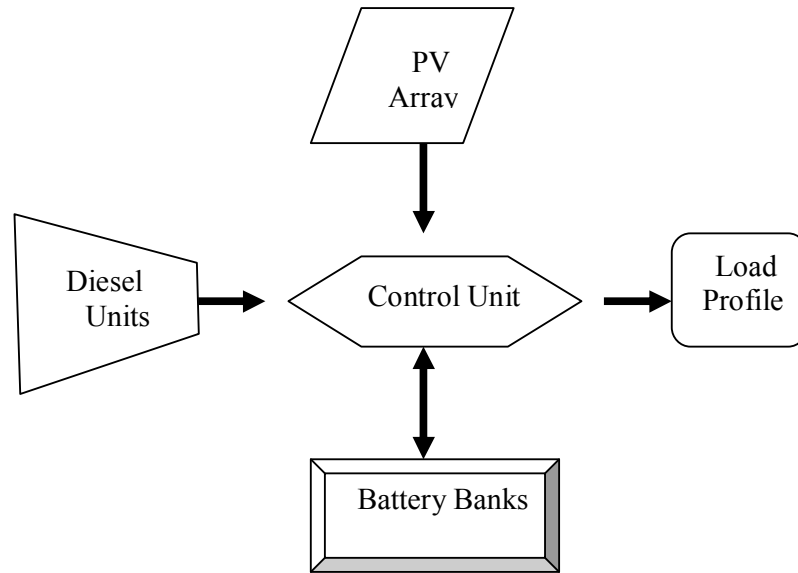


FIGURE 1: PV-diesel-battery Hybrid System

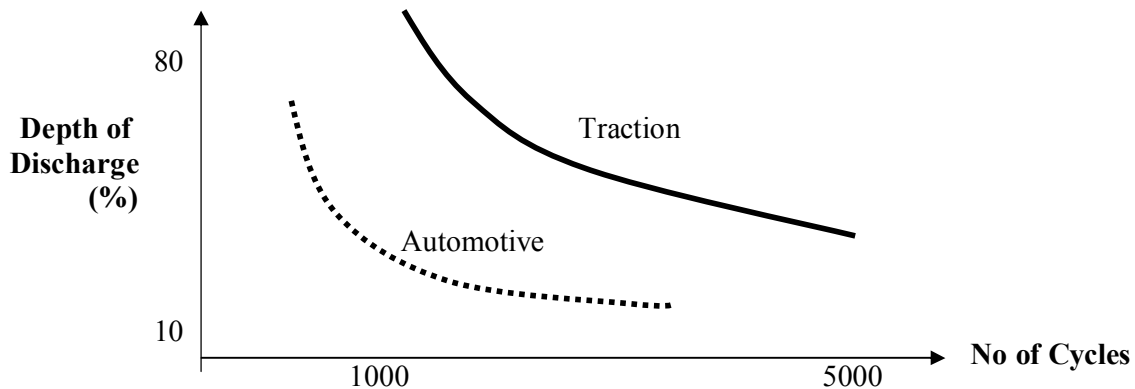


FIGURE 2: Battery lifetime in Terms of DOD and Number of Cycles

In order to ensure a continuous and optimum operation of this hybrid system, operational simulation is an essential tool to control the system in order to achieve optimum performance. Thus the goal is to prevent inefficient operation of diesel and “damping” of excess energy, reduce number of cycles and improves Depth-of-Discharge [DoD] for battery banks, maximize the utilization of PV and ensures high reliability LLP. It is to be here noted that due to varying nature of load demand, the fluctuating power supplied by PV and the resulting variation of battery State-of-Charge [SoC], the hybrid system has to respond continuously to these changing conditions.

A *LabVIEW* model is proposed to control the hybrid system by reading the hourly generation and load, either online or assumed and decide when switching diesel units on or off in order to alleviate battery cycling and improves DoD. The model continuously monitors hourly generation and load and displays status of battery bank and cycling as well as generation from different sources. It also displays warnings for malfunction. This model can be updated for modified site and load data.

2. MODES OF OPERATION

In order to propose a strategy of control for the standalone PV-diesel with battery bank system, one should analyze the different operating modes of such system over 24 hours of a typical day as shown in FIGURE 3. Typical load and generation profiles are assumed. Arbitrary units of rated capacities are used.

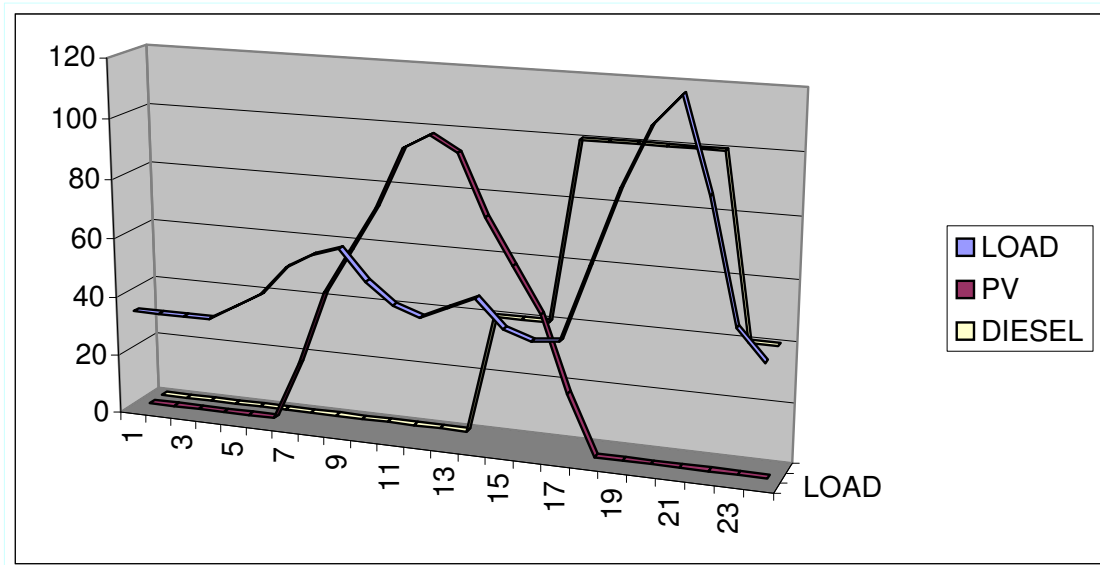


FIGURE 3: Operating modes for a PV-diesel-battery hybrid system

Mode I:

The base load, which is typically experienced at night-time and during the early morning hours, is supplied by energy storage in the battery. PV power is not available and the diesel generator is not normally started, but might be started to reduce battery DoD.

Mode II:

PV power is supplemented by stored energy to meet the medium load demand.

Mode III:

The medium load demand is supplied from PV. Excess energy available from PV is stored in battery.

Mode IV:

The diesel generator is started and operated at its best efficiency power to meet the high evening load. Excess energy available from the diesel units is used to recharge the batteries.

Mode V:

The diesel generator power is increased to its maximum or nominal power to meet the high evening load. Again, excess energy available from the diesel units is used to recharge the batteries.

Mode VI:

Diesel generator power is now sufficient to meet the peak load demand. Additional power is supplied from the battery.

Mode VII:

The diesel units power exceed the load demand, but it may be kept operational until the batteries are recharged to a high SoC.

In principle, most efficient operation is achieved if the generated power is supplied directly to load from source, which reduce cycling of battery banks. However, since diesel at light loads is inherently inefficient, it is common to operate diesel at its most efficient or maximum/nominal capacity and recharge battery from excess energy. Thus, with optimized cycling procedure of battery, long-term performance of the system is achieved. The selection for best strategy depends on fuel, maintenance, environmental aspects, etc.

3. SYSTEM ANALYSIS

In order to apply a control strategy, the following procedures are considered on individual system components:

1. Diesel Unit:
 - (a) Once started, it should operate continuously for a minimum of 30 minutes to reduce engine wear and thus maintenance costs and stoppages
 - (b) Not to allow to operate below a minimum of 40% to prevent low fuel efficiency and “glazing” on cylinder walls.

This is depicted in FIGURE 4

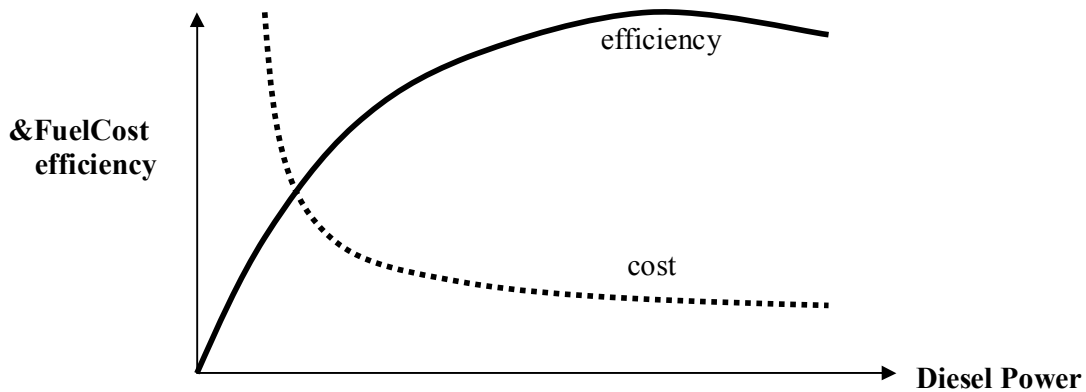


FIGURE 4: Fuel efficiency and cost of a diesel generator

2. Battery bank :

In order to increase their lifetime, the following steps are considered:

 - (a) A 70-80% SoC should be maintained.
 - (b) A minimum DoD is maintained by controlling the number of cycling as shown in Fig()
3. PV Array:

Here, the only consideration to apply is increasing supply reliability through Loss-of-Load-Probability LLP . Extra PV array or storage banks are added or removed according to the following figure:

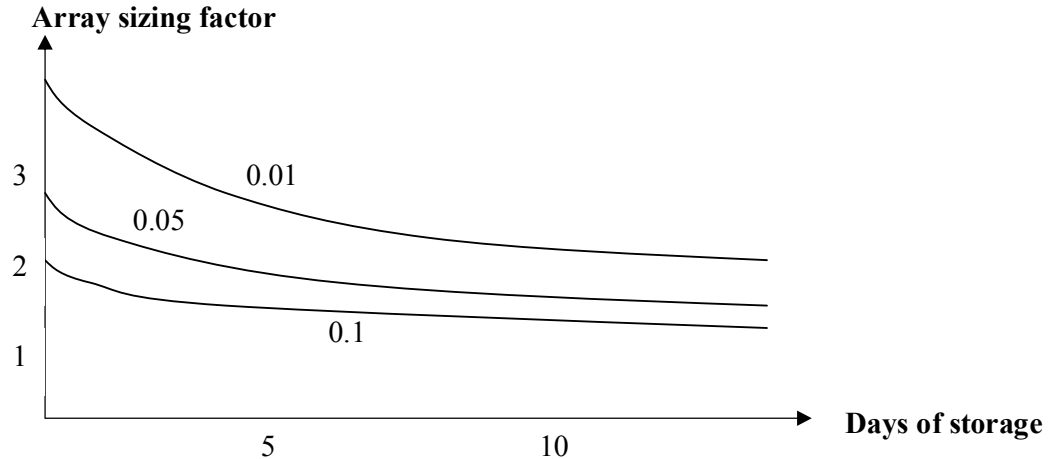


FIGURE 5: Sizing based on Loss-of-Load probability LLP

4. **Load:**
 For a typical load profile (Fig. 6) generation is supplied by PV, diesel, battery or any of their combinations and switched off only when there is not enough generation according to the overall strategy used in this study. Percentage or rated capacity is assumed.

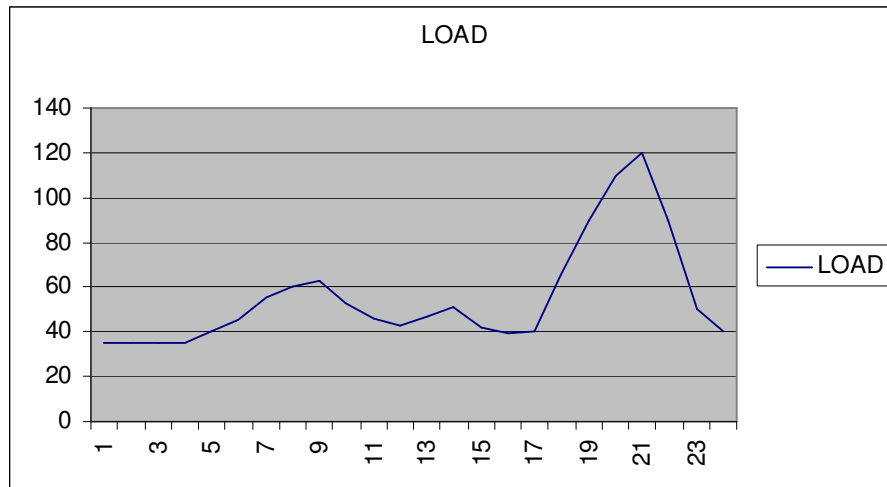
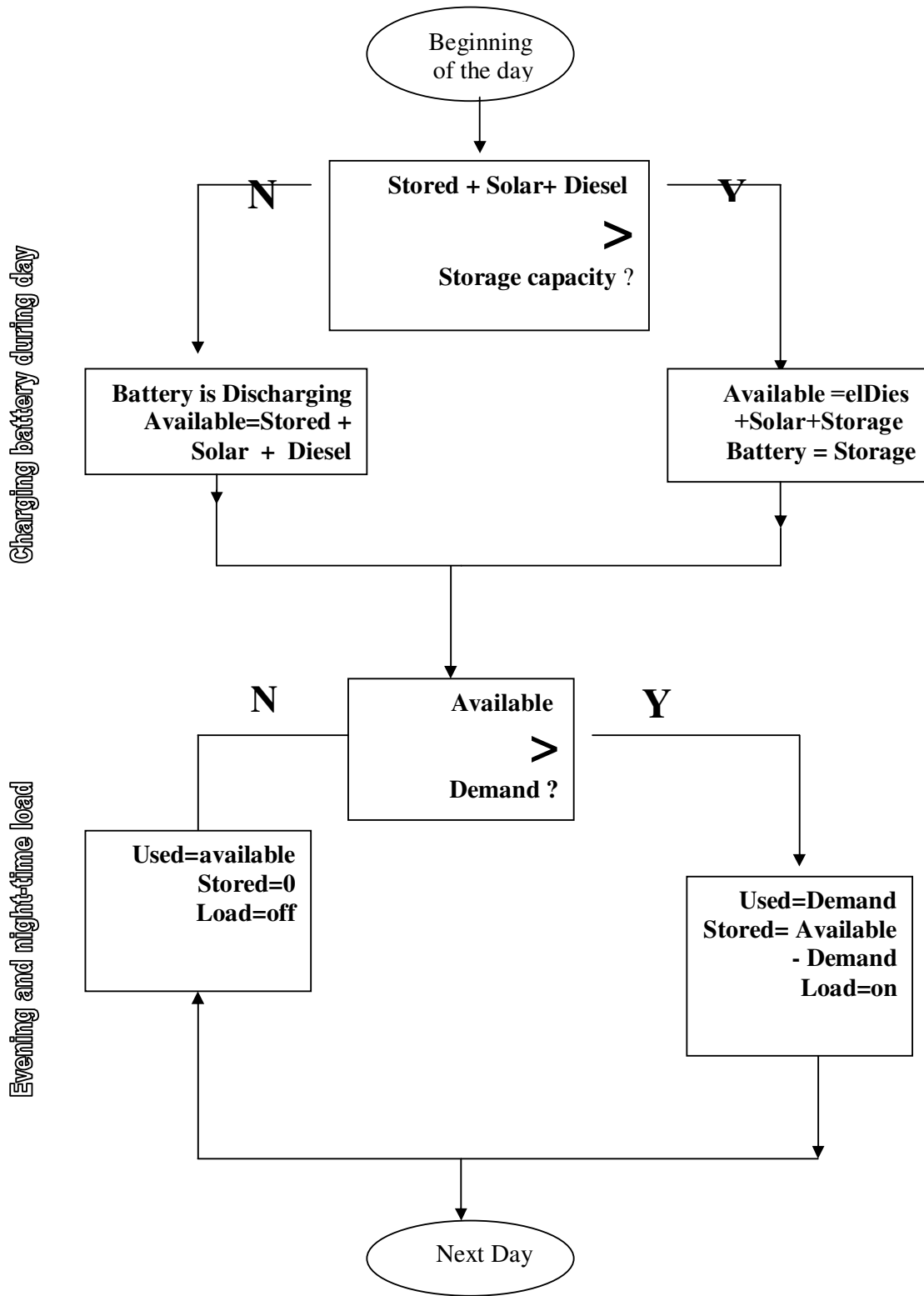


FIGURE 6: Typical load demand profile

5. **Control & Monitoring Unit:**
 Once the storage capacity, PV panels and diesel units have been selected and sized, one must simulate numerically the operation of the system using hourly solar energy data and load demand in order to improve the reliability. The following flow chart outlines the procedure for controlling the system:



Hourly Energy Balance Flow Chart

4. LabVIEW MODEL

The model provide the following controls:

1. Automatic start/stop of diesel
2. Optimum loading of diesel
3. Charge limiting of PV when batteries are at high SoC and PV > load to prevent “gazing”.
4. Possible disconnect load at low battery voltage and insufficient diesel to prevent excess battery discharge.
5. Continuous control of power flow
6. Load sharing
7. Monitoring of all the above. (See Control & Monitoring Unit)

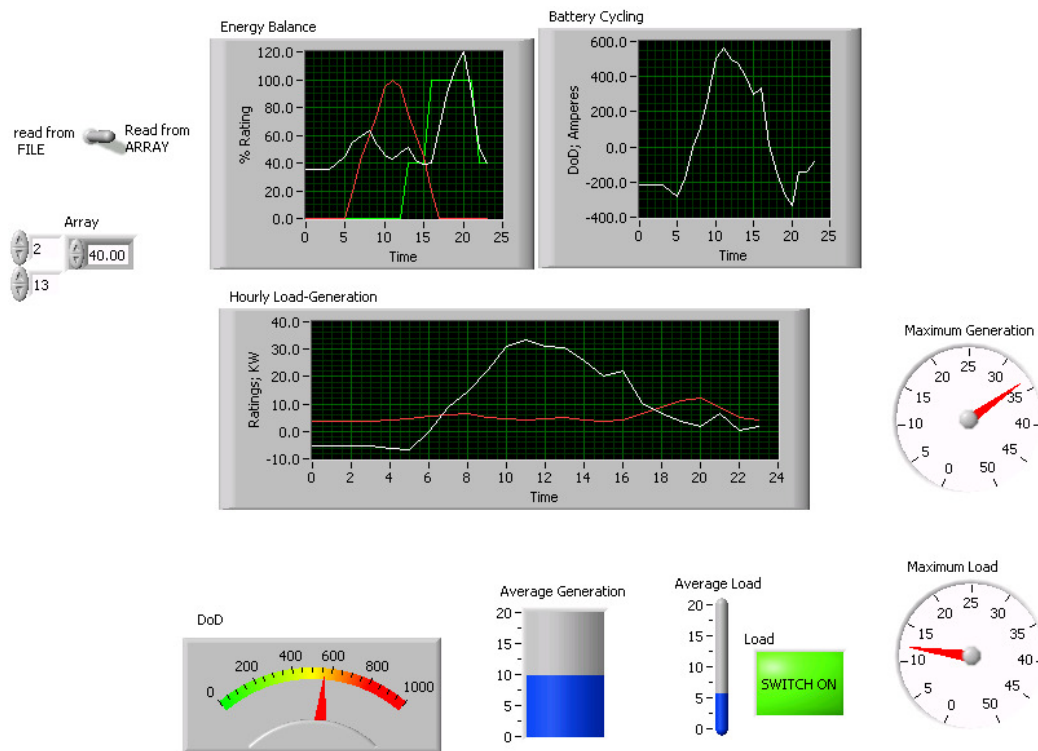


FIGURE 7: shows the Front Panel of *LabVIEW* model with different controls and monitors

It is assumed in this study that a 10KW PV array panel, 20 KVA diesel generator and 1000 Ah battery banks are used. An expected load of maximum 15 KW and typical profile are assumed. These data are calculated based on an adequate sizing. The source Block Diagram, which is used in the model can be made available on request by contacting the author. Different generations/loads profiles are implemented in the form of 24 hours array data. Hourly display of different generating sources including battery charge/discharge, SoC battery cycling and DoD status are displayed. Load shedding can also be determined and displayed.

5. CONCLUSION

A control panel using *LabVIEW* is proposed and implemented on an already sized PV-diesel-battery hybrid system to operate diesel units, control battery DoD, monitor battery SoC and display hourly sharing of different generating sources. Thus, a more reliable and economical

operation is achieved. The inputted data can be either direct measurement or in the form of pre assumed hourly array.

The model provides extra valuable means of controlling and monitoring a hybrid system with ease of updating for future developments. Other types of renewable energy systems such as wind or any combinations can be used in this system modeling.

6. REFERENCES

1. Egido, M.A. and Lorenzo, E., "*The Sizing of Standalone PV System*", Solar Energy Materials and Solar Cells 26, PP. 51-69, (1992)
2. Kalhaurmer, F.R., "*Energy-Storage Systems*", Scientific American 241 (6), PP.42-51, (1979)
3. Lorenzo, E., et al., "*Electricidad Solar Fotovoltanica*", E.T.S.I. Telecommunication, (1984)
4. Macomber, H.L., et al., "*Energizing Design Handbook for Standalone PV Systems*", NASA, PP. DEN 3-195, (1981)
5. <http://www.ecs.umass.edu/mie/labs/>

Numerical Simulation and Prediction for Steep Water Gravity Waves of Arbitrary Uniform Depth using Artificial Neural Network

Mostafa A. M. Abdeen

*Faculty of Engineering/Dept. of Engineering
Mathematics and Physics
Cairo University Giza, 12211, Egypt*

mostafa_a_m_abdeen@hotmail.com

Samir Abohadima

*Faculty of Engineering/Dept. of Engineering
Mathematics and Physics
Cairo University Giza, 12211, Egypt*

s@abohadima.com

Abstract

Nonlinear permanent progressive wave is one of the most important applications in water waves. In this study, analytic formulation of the steep water gravity waves is presented. Abohadima and Isobe [1] showed that Cokelet solution [2] is the most accurate among many other solutions. Due to the nonlinearity of analytic equations, the need to numeric simulation is raised up. In the current paper, consequence numerical models, using one of the artificial intelligence techniques, are designed to simulate and then predict the non linear properties of permanent steep water waves. Artificial Neural Network (ANN), one of the artificial intelligence techniques, is introduced in the current paper to simulate and predict the wave celerity, momentum, energy and other wave integral properties for any permanent waves in water of arbitrary uniform depth. The ANN results presented in the current study showed that ANN technique, with less effort, is very efficiently capable of simulating and predicting the non linear properties of permanent steep water waves.

Keywords: Steep water gravity waves; Nonlinear permanent progressive wave; Numerical simulation; Artificial Neural Network.

1. INTRODUCTION

The Nonlinear permanent progressive wave is one of the most important applications in water waves. Although, the problem boundary conditions are simple, however wave nonlinearity is main source of complexity especially near limiting waves. For calculating the integrated properties of nonlinear waves, various nonlinear wave theories are used. Dean [3, 4], Chaplin [5], and Rienecker and Fenton [6] used the stream function wave theory while Longuet-Higgins and Fenton [7], Schwartz [8], Longuet-Higgins [9], and Cokelet [2] used higher order perturbation techniques with different expansion parameters. Yamada and Shiotani [10] used complete integral functions. Abohadima and Isobe [1] showed that Cokelet solution [2] is the most accurate among many other solutions, however the solution was very complicated.

Due to complexity of Cokelet solution, The ANN was examined in this article to get solution at any wave conditions and to keep the same level of Cokelet accuracy. Artificial intelligence has proven its capability in simulating and predicting the behavior of the different physical phenomena in most of the engineering fields. ANN is one of the artificial intelligence techniques that have been incorporated in various scientific disciplines. Minns [11] investigated the general application of ANN in modeling rainfall runoff process. Kheireldin ([12] presented a study to model the hydraulic characteristics of severe contractions in open channels using ANN technique. The successful results of his study showed the applicability of using the ANN approach in determining

relationship between different parameters with multiple input/output problems. Abdeen [13] developed neural network model for predicting flow characteristics in irregular open channels. The developed model proved that ANN technique was capable with small computational effort and high accuracy of predicting flow depths and average flow velocities along the channel reach when the geometrical properties of the channel cross sections were measured or vice versa. Allam [14] used the artificial intelligence technique to predict the effect of tunnel construction on nearby buildings, which is the main factor in choosing the tunnel route. Abdeen ([15] presented a study for the development of ANN models to simulate flow behavior in open channel infested by submerged aquatic weeds. Mohamed [16] proposed an artificial neural network for the selection of optimal lateral load-resisting system for multi-story steel frames. Abdeen [17] utilized ANN technique for the development of various models to simulate the impacts of different submerged weeds' densities, different flow discharges, and different distributaries operation scheduling on the water surface profile in an experimental main open channel that supplies water to different distributaries. Abdeen et al. [18] introduced the ANN technique to investigate the effect of light local weight aggregate on the performance of the produced lightweight concrete. The results of their study showed that the ANN method with less effort was very efficiently capable of simulating the effect of different aggregate materials on the performance of lightweight concrete. Hodhod et al. [19] introduced the ANN technique to simulate the strength behavior using the available experimental data and predict the strength value at any age in the range of the experiments or in the future. The results of the numerical study showed that the ANN method was very efficiently capable of simulating the effect of specimen shape and type of sand on the strength behavior of tested mortar with different cement types.

2. AIM OF THE WORK

The analytic formulation for the steep water gravity waves is presented in details. The Cokerly analytic solution is described in the present work and is considered the most accurate among many other solutions. Consequence numerical models are developed in the current work, using ANN technique, to understand, simulate and predict, the wave celerity, momentum, energy and other wave integral properties for any permanent waves in water of arbitrary uniform depth.

3. ANALYTICAL FORMULATION

Consider two dimensional, periodic, surface waves of wavelength λ and wave number $k=2\pi/\lambda$ propagating under the influence of gravity, g , in the fluid of constant density, ρ . Take units of mass, length and time such that $k = \rho = g = 1$ and hence $\lambda = 2\pi$. Assume that the fluid is inviscid and incompressible and the flow is irrotational. The waves are assumed to flow from left to right over a horizontal bottom without change in form. By a choice of reference frame, the fluid velocity at any fixed depth always within the fluid averaged over one wave cycle may be taken as zero. The frame of reference is unique as is the propagation speed, c , of the waves with respect to that frame.

Choose rectangular coordinates (x, y) such that the x -axis is horizontal and the y -axis is directed vertically upwards. Locate the free surface at $y= \eta$ and the bottom at $y=-d$ where d is referred to the undisturbed fluid depth and represents the depth of a uniform stream flowing with speed c whose mass flux, $Q= c d$ equals that of the wave. The mean elevation of the free surface is $\bar{\eta}$ where an over bar denotes an average over one wave cycle. Therefore the mean depth is $D=d+\bar{\eta}$ and does not in general equal-to-equal d . Since the fluid is irrotational and incompressible, a velocity potential, ϕ , and stream function, ψ , can be defined such that the velocity, (u, v) , may be written as follows:

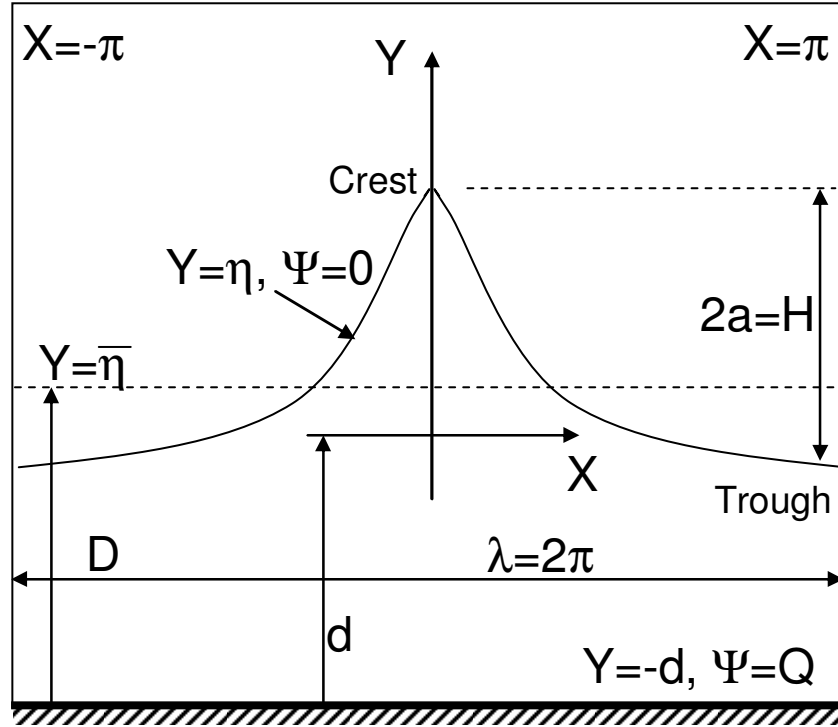


FIGURE 1: Wave Profile in Z-Plane

$$\left. \begin{aligned} u &= \frac{\partial \phi}{\partial x} = \frac{\partial \psi}{\partial y} \\ v &= \frac{\partial \phi}{\partial y} = -\frac{\partial \psi}{\partial x} \end{aligned} \right\} \quad (1)$$

And both ϕ and ψ satisfy Laplace's equation, $\nabla^2 \phi = \nabla^2 \psi = 0$

Now considering a second rectangular coordinate system (X, Y) moving in the positive x -direction with the waves at speed c , In this reference frame the motion is independent of time, t . The velocity potential, Φ , stream function, Ψ , and velocity (U, V) , in this frame are related to similar quantities in the (x, y) frame by:

$$\left. \begin{aligned} X &= x - ct, \quad Y = y, \quad \Phi = \phi - cx, \quad \Psi = \psi - cy \\ U &= u - c = \frac{\partial \Phi}{\partial X} = \frac{\partial \Psi}{\partial Y} \\ V &= v = \frac{\partial \Phi}{\partial Y} = -\frac{\partial \Psi}{\partial X} \end{aligned} \right\} \quad (2)$$

It is convenient to define the complex variables $Z = X + iY$ and $W = \Phi + i\Psi$ which are analytic functions of one another. The Z -plane is shown in Figure (1)

The boundary conditions to be imposed on the flow are that the free surface and bottom are streamlines, that is

$$\left. \begin{aligned} \Psi = 0 \quad \text{on} \quad Y = \eta \\ \Psi = Q \quad \text{on} \quad Y = -d \end{aligned} \right\} \quad (3)$$

In addition, the pressure along the free surface is assumed to be equal to the constant atmospheric pressure ($p=0$) with the effects of surface tension neglected. So the Bernoulli equation at the free surface becomes:

$$U^2 + V^2 + 2\eta = K \quad \text{on} \quad \Psi=0, \quad (4)$$

Where K is the Bernoulli constant in the moving coordinates system.

Following Coker, by taking Z as a Fourier series in W of the form

$$Z(W) = A_0 \frac{W}{c} + B_0 + \sum_{j=1}^{\infty} (A_j e^{ijW/c} + B_j e^{-ijW/c}) \quad (5)$$

Applying the bottom boundary condition (3) and the fact that wave profile must be symmetric, Equation (5) will simplified to

$$X = -\frac{\Phi}{c} - \sum_{j=1}^{\infty} \frac{a_j}{j} (e^{-j\Psi/c} + e^{-2jd} e^{j\Psi/c}) \text{Sin} \left(j \frac{\Phi}{c} \right) \quad (6)$$

$$Y = -\frac{\Psi}{c} + \sum_{j=1}^{\infty} \frac{a_j}{j} (e^{-j\Psi/c} - e^{-2jd} e^{j\Psi/c}) \text{Cos} \left(j \frac{\Phi}{c} \right) \quad (7)$$

The real constant a_j in equations (6) and (7) are determined by satisfying the Bernoulli equation (4) on the free surface. The complex velocity, q , is given by

$$q = U - iV = \frac{dW}{dZ} = \left(\frac{dZ}{dW} \right)^{-1} = \frac{-c}{1 + \sum_{j=1}^{\infty} a_j (e^{-ijW/c} + e^{-2jd} e^{-ijW/c})} \quad (8)$$

Substitution of (6), (7) and (8) into (4) gives

$$c^2 + \left\{ 2 \sum_{j=1}^{\infty} \frac{a_j}{j} \delta_j \text{Cos} \left(j \frac{\Phi}{c} \right) - K \right\} \left\{ \begin{aligned} & \left[1 + \sum_{j=1}^{\infty} a_j \sigma_j \text{Cos} \left(j \frac{\Phi}{c} \right) \right]^2 \\ & + \left[\sum_{j=1}^{\infty} a_j \delta_j \text{Sin} \left(j \frac{\Phi}{c} \right) \right]^2 \end{aligned} \right\} = 0 \quad (9)$$

Where two parameters depending only on d and defined by

$$\sigma_j = 1 + e^{-2jd}, \quad \delta_j = 1 - e^{-2jd} \quad (10)$$

Expanding equation (9) as a cosine series and equating the harmonic coefficients to zero, we get:

$$\left. \begin{aligned} c^2 + 2 \sum_{n=1}^{\infty} \frac{a_n}{n} \delta_n f_1 &= K f_0, \\ \sum_{n=1}^{\infty} \frac{a_n}{n} \delta_n (f_{|n-j|} + f_{n+j}) &= K f_j \quad (j = 1, 2, \dots) \end{aligned} \right\} \quad (11)$$

Where f_j have been introduced for convenience and are defined in terms of the a_j by

$$\left. \begin{aligned} f_o &= 1 + \sum_{n=1}^{\infty} a_n^2 \sigma_{2n}, \\ f_j &= a_j \sigma_j + \sum_{n=1}^{\infty} a_n a_{n+j} \sigma_{2n+j} + \frac{1}{2} \sum_{n=1}^{j-1} a_n a_{j-n} (\sigma_n - \delta_{j-n}) \quad (j = 1, 2, \dots) \end{aligned} \right\} \quad (12)$$

In all summations, each term is taken to be identical zero if the lower limit exceeds the upper.

Equations (11) and (12) are a set of nonlinear algebraic equations that determine the Fourier coefficients a_j completely. These can be solved in a consistent manner by perturbation expansion technique. Let ϵ denote a global perturbation parameter, which is zero for infinitesimal waves and is positive for higher waves.

$$\left. \begin{aligned} a_j &= \sum_{k=0}^{\infty} \alpha_{jk} \epsilon^{j+2k}, \quad (j = 1, 2, \dots) \\ f_j &= \sum_{k=0}^{\infty} \beta_{jk} \epsilon^{j+2k}, \quad (j = 1, 2, \dots) \\ c^2 &= \sum_{n=0}^{\infty} \gamma_n \epsilon^{2n} \\ K &= \sum_{n=0}^{\infty} \Delta_n \epsilon^{2n} \end{aligned} \right\} \quad (13)$$

Substituting of (13) into (11) and (12), then equating coefficients of equal powers of ϵ yields the following recurrence relations:

$$\gamma_n + 2 \sum_{j=0}^{n-1} \frac{\delta_{n-j}}{n-j} \sum_{m=0}^j \alpha_{n-j, j-m} \beta_{n-j, m} = \sum_{k=0}^n \Delta_{n-k} \beta_{0k}, \quad (n = 0, 1, 2, \dots) \quad (14)$$

$$\sum_{n=0}^p \Delta_n \beta_{j, p-n} = \sum_{n=1}^j \frac{\delta_n}{n} \sum_{k=0}^p \alpha_{n, p-k} \beta_{j-n, k} + \sum_{n=1}^p \frac{\delta_{n+j}}{n+j} \sum_{k=0}^{p-n} \alpha_{n+j, p-n-k} \beta_{nk} \quad (15)$$

$$+ \sum_{n=0}^{p-1} \frac{\delta_{p-n}}{p-n} \sum_{k=0}^n \alpha_{p-n, n-k} \beta_{j+p-n, k}, \quad (j = 1, 2, \dots; p = 0, 1, \dots)$$

$$\beta_{00} = 1 \quad (16)$$

$$\beta_{0k} = \sum_{n=0}^k \sigma_{2n} \sum_{p=0}^{k-n} \alpha_{np} \alpha_{n, k-n-p}, \quad (k = 0, 1, 2, \dots) \quad (17)$$

$$\beta_{jk} = \alpha_{jk} \sigma_j + \frac{1}{2} \sum_{n=1}^{j-1} (\sigma_j - \delta_{j-n}) \sum_{p=0}^k \alpha_{np} \alpha_{j-n, k-p} \quad (18)$$

$$+ \sum_{n=1}^k \sigma_{2n+j} \sum_{p=0}^{k-n} \alpha_{np} \alpha_{n+j, k-n-p}, \quad (j = 1, 2, \dots; k = 0, 1, \dots)$$

Cokelet selected the expansion parameter ϵ as follow:

$$\epsilon^2 = 1 - \frac{q_{crest}^2 q_{trough}^2}{c^4} \quad (19)$$

The fluid speeds at the wave crest and trough are obtained from (8) with $\Psi=0$ and $\Phi/c=0$ and π respectively. Expanding the right hand side of (19) in powers of ϵ leads to:

$$\varepsilon^2 = 1 - \frac{1}{\left(1 + \sum_{j=1}^{\infty} \sum_{k=0}^{\infty} \sigma_j \alpha_{jk} \varepsilon^{j+2k}\right)^2 + \left(1 + \sum_{j=1}^{\infty} \sum_{k=0}^{\infty} (-1)^j \sigma_j \alpha_{jk} \varepsilon^{j+2k}\right)^2} \quad (20)$$

Rearrange and expanding (20) and equating powers of ε gives

$$\begin{aligned} \frac{(-1)^j \left(-\frac{1}{2}\right)!}{j! \left(-j - \frac{1}{2}\right)!} &= 2 \sum_{k=0}^{j-1} \alpha_{2(j-k),k} \sigma_{2(j-k)} \\ &+ \sum_{n=1}^{j-1} \sum_{k=0}^{j-n-1} \sum_{m=0}^{j-n-k-1} \sigma_{2(j-n-k-m)} \sigma_{2n} \alpha_{2(j-n-k-m),k} \alpha_{2n,m} \\ &- \sum_{n=0}^{j-1} \sum_{k=0}^{j-n-1} \sum_{m=0}^{j-n-k-1} \sigma_{2(j-n-k-m)-1} \sigma_{2n+1} \alpha_{2(j-n-k-m)-1,k} \alpha_{2n+1,m} \end{aligned} \quad (21)$$

The calculation procedure is as follows:

- 1- Specify the maximum order, N, of the perturbation expansion,
- 2- Specify the undisturbed fluid depth, d, and calculate $\delta_j \sigma_j$ using (10)
- 3- Calculate the coefficient at order ε^p in terms of the previously determined coefficients with $p=0, 1, \dots, 2M, 2M+1, \dots, N$
 - (a) Within any even order, 2M,
 - (i) Calculate α_{ij} and β_{ij} by solving equations (15) and (17) simultaneously proceeding in the sequence $(i,j)=(2M,0), (2M-2,1), \dots, (4,M-2)$
 - (ii) Calculate $\alpha_{1,M-1}$, $\beta_{1,M-1}$, $\alpha_{2,M-1}$, and $\beta_{2,M-1}$ by simultaneously solving equations (17) with $j=1, k=M-1$, (15) with $j=2, p=M-1$, (17) with $j=2, k=M-1$, and equations (14) to (18) with $j=M$,
 - (iii) Calculate β_{0M} from equation (18) with $k=M$,
 - (b) Within any odd order, 2M+1,
 - (i) Calculate Δ_M from (15) with $j=1, p=M$
 - (ii) Calculate α_{ij} and β_{ij} by solving equations (15) and (17) simultaneously proceeding in the sequence $(i,j)=(2M+1,0), (2M-1,1), \dots, (3,M-1)$
- 4- Calculate γ_n from (14) with $n=0, 1, \dots, \frac{1}{2}N$

Notice that the odd-order coefficients $\alpha_{1,M-1}$ and $\beta_{1,M-1}$ can not be determined until the next higher order even order, and also that even-order Δ_M can not be determined until the next higher odd order.

After calculation of all coefficients, wave properties can be computed as follows: the wave height,

$$a = \frac{1}{2}H = \sum_{j=1}^{\infty} \frac{1}{2j-1} a_{2j-1} \delta_{2j-1} = \sum_{j=1}^{\infty} \sum_{k=1}^j \frac{1}{2j-1} \alpha_{2j-1,j-1} \delta_{2j-1} \varepsilon^{2j-1} \quad (22)$$

$\bar{\eta}$ the mean elevation of free water surface,

$$\bar{\eta} = \frac{1}{2\pi} \int_0^{2\pi} Y(\Phi, 0) dX = \frac{1}{2} \sum_{j=1}^{\infty} \sum_{k=1}^{j-1} \sum_{n=0}^{j-k-1} \frac{\delta_{j-k-n} \sigma_{j-k-n}}{j-k-n} \alpha_{j-k-n,k} \alpha_{j-k-n,n} \varepsilon^{2j} \quad (23)$$

$$\begin{aligned} \overline{\eta}^2 &= \frac{1}{2\pi} \int_0^{2\pi} Y^2(\Phi, 0) dX = \frac{1}{2} \sum_{j=1}^{\infty} \sum_{k=0}^{j-1} \sum_{n=0}^{j-k-1} \frac{\delta_{j-k-n}}{(j-k-n)^2} \alpha_{j-k-n,k} \alpha_{j-k-n,n} \epsilon^{2j} + \\ &\frac{1}{4} \sum_{j=2}^{\infty} \sum_{m=1}^{j-1} \sum_{k=0}^{j-m-1} \sum_{i=0}^{j-m-k-1} \sum_{n=0}^{j-m-k-i-1} \frac{\delta_{j-m-k-i-n}}{j-m-k-i-n} * \\ &\left(\frac{\delta_m \sigma_{j-k-i-n}}{m} + 2 \frac{\delta_{j-k-i-n} \sigma_m}{j-k-i-n} \right) \alpha_{j-m-k-i-n,k} \alpha_{mi} \alpha_{j-k-i-n,n} \epsilon^{2j} \end{aligned} \quad (24)$$

Table 1 gives all relation required to compute integral properties analytically using the computed coefficients.

Integral propety	Calculation Relation
The circulation per unit length, C	$C = \frac{1}{\lambda} \int_0^{\lambda} u dx = \overline{u}$
The mean momentum or impulse, I	$I = \int_{-d}^{\eta} \overline{\rho u} dy$
The kinetic energy, T,	$T = \int_{-d}^{\eta} \frac{1}{2} \overline{\rho(u^2 + v^2)} dy$
The potential evergy, V	$V = \int_{\eta}^{\eta} \overline{\rho g y} dy$
The radiation stress S_{xx}	$S_{xx} = \int_{-d}^{\eta} \overline{(p + \rho u^2)} dy - \int_{-d}^{\eta} p_0 dy$
The mean energy flux, F	$F = \int_{-d}^{\eta} \left(p + \frac{1}{2} \rho(u^2 + v^2) + \rho g (y - \overline{\eta}) \right) u dy$
The mean squareed velocity at the bottom $\overline{u_b^2}$	$\overline{u_b^2} = \frac{1}{\lambda} \int_0^{\lambda} (u[x, -d])^2 dx$
The mass flux per unit span, Q	$Q = - \int_{-d}^{\lambda} \rho U dY$
The Bernoulli constant, K	$K = 2\rho \overline{\eta} + \overline{u_b^2} + c^2$
The total head R	$R = \frac{1}{2} K + d$
The momentum flux per unit span, S	$S = S_{xx} - 2cI + D \left(c^2 + \frac{1}{2} D \right)$

TABLE 1: Relations of integral properties

Where p_o is the hydrostatic pressure defined as follws:

$$p_o = -\rho g (y - \overline{\eta}) \quad (25)$$

4. NUMERICAL MODEL STRUCTURE

Neural networks (NN) are models of biological neural structures. Abdeen [13] described in a very detailed fashion the structure of any neural network. Briefly, the starting point for most networks is

a model neuron as shown in Fig. 2. This neuron is connected to multiple inputs and produces a single output. Each input is modified by a weighting value (w). The neuron will combine these weighted inputs with reference to a threshold value and an activation function, will determine its output. This behavior follows closely the real neurons work of the human's brain. In the network structure, the input layer is considered a distributor of the signals from the external world while hidden layers are considered to be feature detectors of such signals. On the other hand, the output layer is considered as a collector of the features detected and the producer of the response.

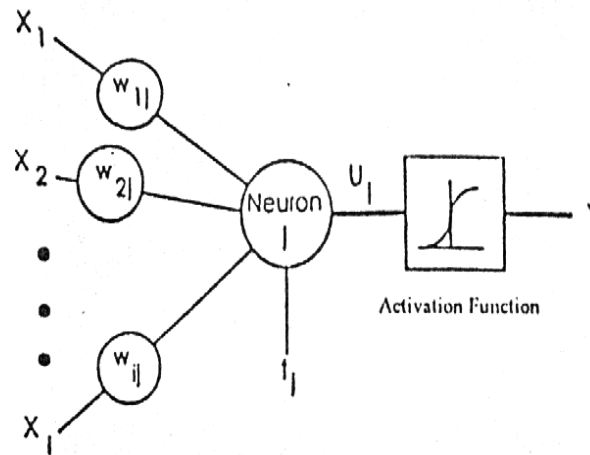


FIGURE 2: Typical picture of a model neuron that exists in every neural network

4.1 Neural Network Operation

It is quite important for the reader to understand how the neural network operates to simulate different physical problems. The output of each neuron is a function of its inputs (X_i). In more details, the output (Y_j) of the j^{th} neuron in any layer is described by two sets of equations as follows:

$$U_j = \sum (X_i w_{ij}) \quad (26)$$

$$Y_j = F_{th}(U_j + t_j) \quad (27)$$

For every neuron, j , in a layer, each of the i inputs, X_i , to that layer is multiplied by a previously established weight, w_{ij} . These are all summed together, resulting in the internal value of this operation, U_j . This value is then biased by a previously established threshold value, t_j , and sent through an activation function, F_{th} . This activation function can take several forms such as Step, Linear, Sigmoid, Hyperbolic, and Gaussian functions. The Hyperbolic function, used in this study, is shaped exactly as the Sigmoid one with the same mathematical representation, as in equation 12, but it ranges from -1 to $+1$ rather than from 0 to 1 as in the Sigmoid one (Fig. 3)

$$f(x) = \frac{1}{1 + e^{-x}} \quad (28)$$

The resulting output, Y_j , is an input to the next layer or it is a response of the neural network if it is the last layer. In applying the Neural Network technique, in this study, Neuralyst Software, Shin [20], was used.

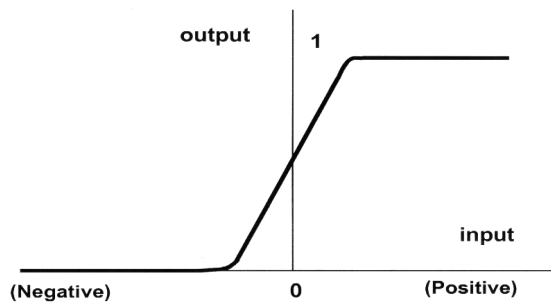


FIGURE 3: The Sigmoid Activation Function

4.2 Neural Network Training

The next step in neural network procedure is the training operation. The main purpose of this operation is to tune up the network to what it should produce as a response. From the difference between the desired response and the actual response, the error is determined and a portion of it is back propagated through the network. At each neuron in the network, the error is used to adjust the weights and the threshold value of this neuron. Consequently, the error in the network will be less for the same inputs at the next iteration. This corrective procedure is applied continuously and repetitively for each set of inputs and corresponding set of outputs. This procedure will decrease the individual or total error in the responses to reach a desired tolerance. Once the network reduces the total error to the satisfactory limit, the training process may stop. The error propagation in the network starts at the output layer with the following equations:

$$w_{ij} = w'_{ij} + LR (e_j X_i) \quad (29)$$

$$e_j = Y_j (1 - Y_j) (d_j - Y_j) \quad (30)$$

Where, w_{ij} is the corrected weight, w'_{ij} is the previous weight value, LR is the learning rate, e_j is the error term, X_i is the i^{th} input value, Y_j is the output, and d_j is the desired output.

5. CONSEQUENCE NUMERICAL MODELS

To fully investigate numerically the wave integral properties for any permanent waves in water of arbitrary uniform depth, five consequence neural network models are designed in this study. Consequence models mean that each model uses the inputs and the outputs of the previous one to be as input variables for the next model to produce another group of outputs and so on until we reach the last one.

5.1 Neural Network Design

To develop neural network models to simulate the water wave integral properties, first input and output variables have to be determined. Input variables are chosen according to the nature of the problem and the type of data that would be collected. To clearly specify the key input variables for each neural network model and their associated outputs, Fig. 4 and Table 2 are designed to summarize all neural network key input and output variables for the five consequence neural network models respectively.

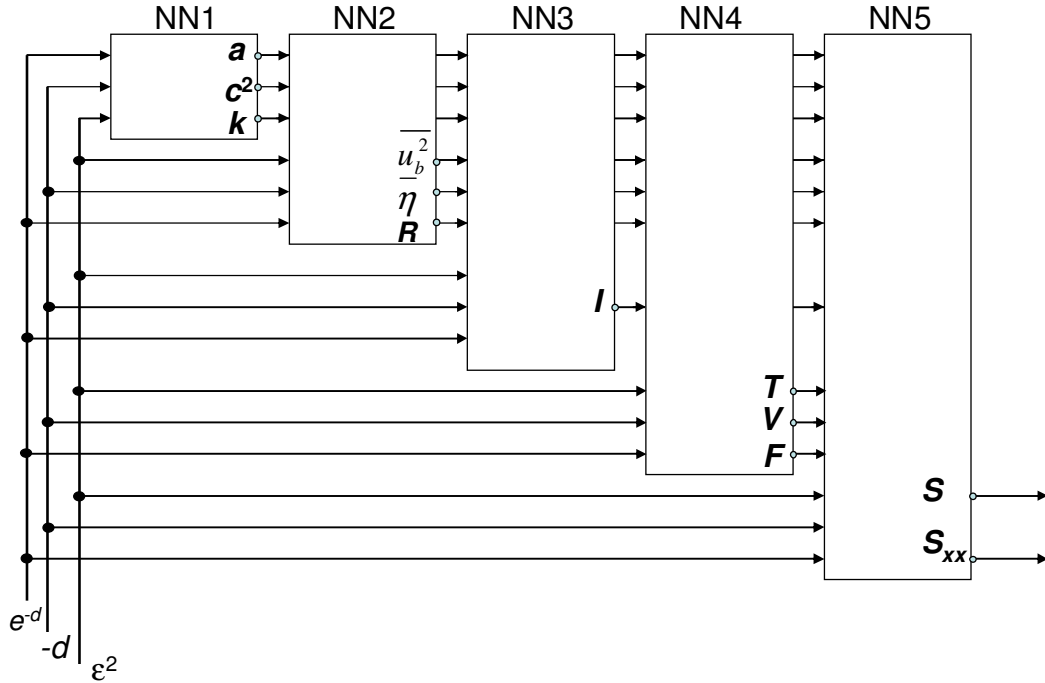


FIGURE 4: Consequence Neural Network Models

Model	e^{-d}	$-d$	ϵ^2	a	c^2	k	\bar{u}_b^2	$\bar{\eta}$	R	I	T	V	F	S	S_{xx}
NN1	/	/	/	O	O	O	-	-	-	-	-	-	-	-	-
NN2	/	/	/	/	/	/	O	O	O	-	-	-	-	-	-
NN3	/	/	/	/	/	/	/	/	/	O	-	-	-	-	-
NN4	/	/	/	/	/	/	/	/	/	/	O	O	O	-	-
NN5	/	/	/	/	/	/	/	/	/	/	/	/	/	O	O

Note: / denotes for Input Variable and O denotes for Output Variable

TABLE 2: Key Input and Output Variables for Neural Network Models

Several neural network architectures are designed and tested for all numerical models investigated in this study to finally determine the best network models to simulate, very accurately, the water wave integral properties based on minimizing the Root Mean Square Error (RMS-Error). Fig. 5 shows a schematic diagram for a generic neural network. The training procedure for the developed NN models, in the current study, uses the data from the results of the analytical model to let the ANN understands the behaviors. After sitting finally the NN models, these models are used to predict the wave properties for different relative fluid depth (d) rather than those used in the analytic solution.

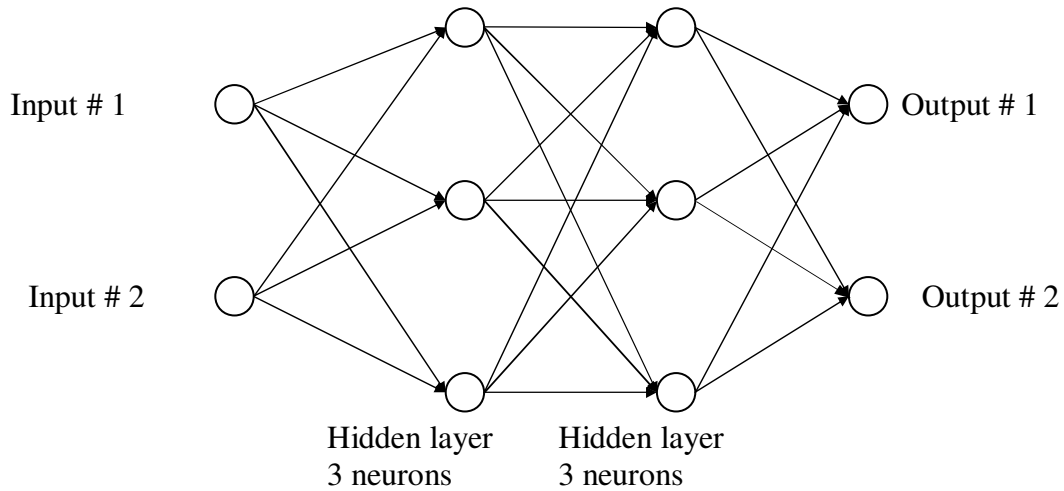


FIGURE 5: General schematic diagram of a simple generic neural network

Table 3 shows the final neural network models for the five consequence models and their associate number of neurons. The input and output layers represent the key input and output variables described previously for each model.

Model	No. of layers	No. of Neurons in each layer			
		Input Layer	First Hidden	Second Hidden	Output Layer
NN1	4	3	5	4	3
NN2	4	6	5	4	3
NN3	4	9	6	4	1
NN4	4	10	8	6	3
NN5	4	13	9	5	2

TABLE 3: The developed Neural Network Models

The parameters of the various network models developed in the current study are presented in Table (4), where these parameters can be described with their tasks as follows:

Learning Rate (LR): determines the magnitude of the correction term applied to adjust each neuron’s weights during training process = 1 in the current study.

Momentum (M): determines the “life time” of a correction term as the training process takes place = 0.9 in the current study.

Training Tolerance (TRT): defines the percentage error allowed in comparing the neural network output to the target value to be scored as “Right” during the training process = 0.01 in the current study.

Testing Tolerance (TST): it is similar to Training Tolerance, but it is applied to the neural network outputs and the target values only for the test data = 0.03 in the current study.

Input Noise (IN): provides a slight random variation to each input value for every training epoch = 0 in the current study.

Function Gain (FG): allows a change in the scaling or width of the selected function = 1 in the current study.

Scaling Margin (SM): adds additional headroom, as a percentage of range, to the rescaling computations used by Neuralyst Software, Shin (1994), in preparing data for the neural network or interpreting data from the neural network = 0.1 in the current study.

Training Epochs: number of trails to achieve the present accuracy.

Percentage Relative Error (PRR): percentage relative error between the numerical results and actual measured value for and is computed according to equation (6) as follows:

$$PRE = (\text{Absolute Value (ANN_PR - AMV)}/\text{AMV}) * 100$$

Where :

ANN_PR : Predicted results using the developed ANN model

AMV : Actual Measured Value

MPRE : Maximum percentage relative error during the model results for the training step (%)

Simulation Parameter	NN1	NN2	NN3	NN4	NN5
Training Epochs	225823	256762	30077	5325	11004
MPRE	3.5	4.4	5.3	4.8	5.7
RMS-Error	0.0038	0.0079	0.0036	0.0035	0.0028

TABLE 4: Parameters used in the Developed Neural Network Models

6. RESULTS AND DISCUSSIONS

Numerical results using ANN technique will be presented in this section for the five consequence neural network models (NN1—NN5) to show the simulation and prediction powers of ANN technique of wave celerity, momentum, energy and other wave integral properties for any permanent wave in water of arbitrary uniform depth.

Figures (6—9) show a comparison between ANN results (dotted lines) and analytical results (symbols) for a , c^2 , K , $\bar{\eta}$, $\overline{u_b^2}$, R , I , T , V , F , S_{xx} and S at different undisturbed fluid depths and wave nonlinearity parameters. Square symbols used in training phase, and triangle symbols used to show the power of prediction of neural network models developed in the present work. It is very clear, from these figures, that the developed neural network models are very efficiently capable of simulating and predicting the non linear properties of permanent steep water waves.

7. CONCLUSIONS

Based on the results of implementing the ANN technique in this study, the following can be concluded:

1. The developed consequence neural network models, presented in this study, are very successful in simulating the non linear properties of permanent steep water waves.
2. The presented neural network models are very efficiently capable of predicting the properties of water waves at different undisturbed fluid depths and wave nonlinearity parameters rather than those used in the training step for developing the models.

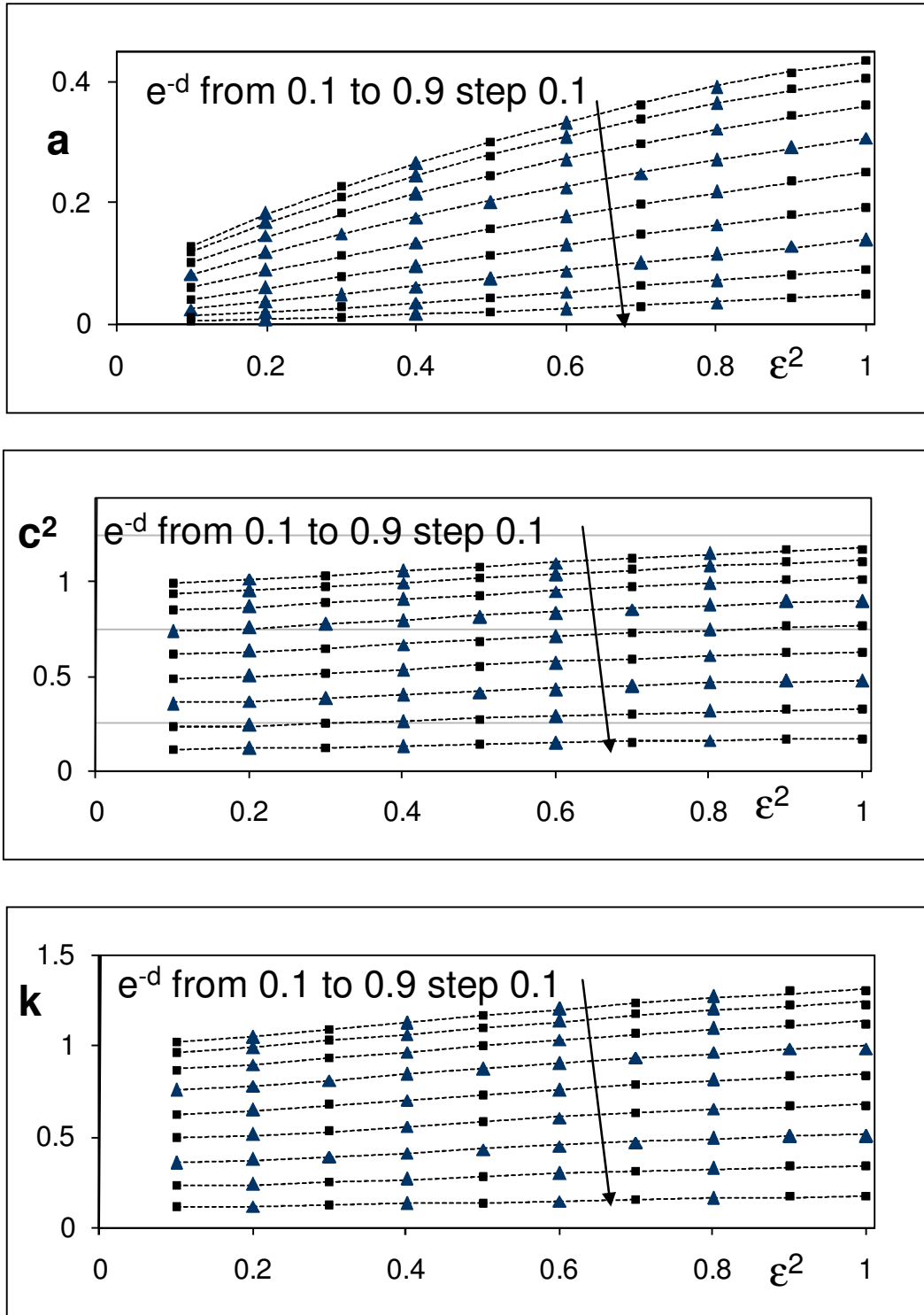


FIGURE 6: Comparison between ANN (dotted lines) and analytical results (symbols) for a , c^2 and K at different undisturbed fluid depths and wave nonlinearity parameters. Square symbols used in training phase, and triangle symbols used only for comparison

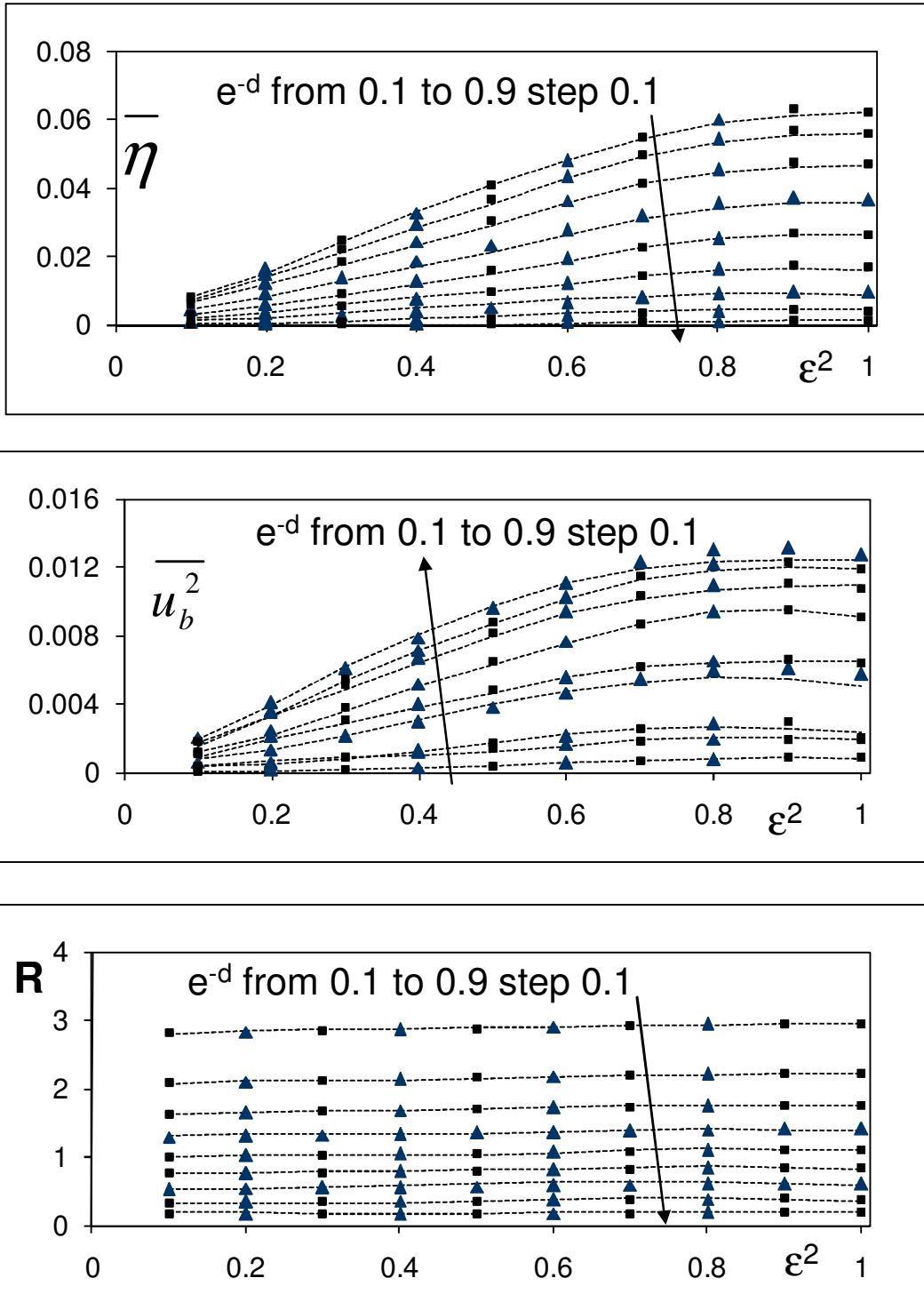


FIGURE 7: Comparison between ANN (dotted lines) and analytical results (symbols) for $\bar{\eta}$, $\overline{u_b^2}$ and R at different undisturbed fluid depths and wave nonlinearity parameters. Square symbols used in training phase, and triangle symbols used only for comparison

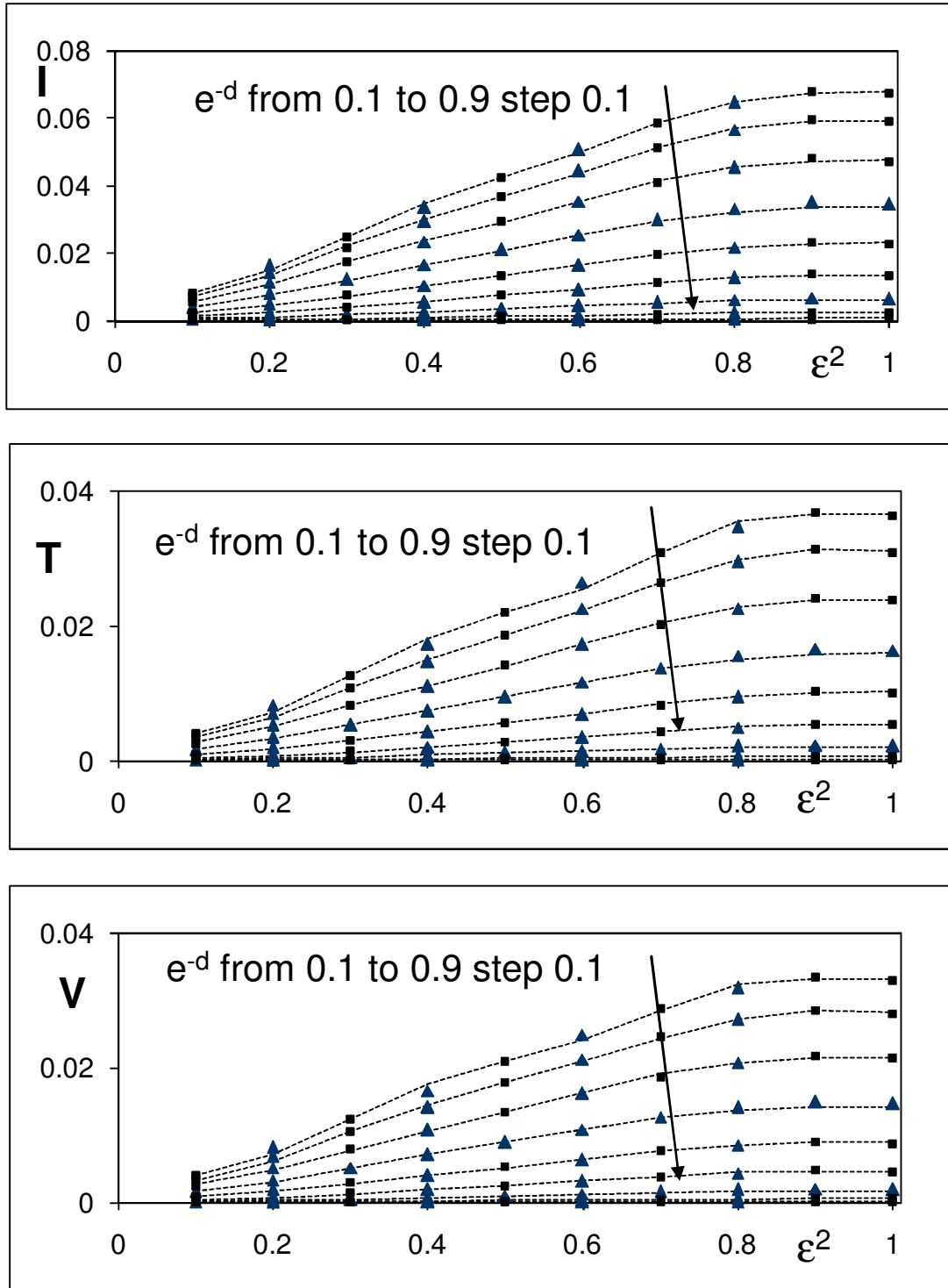


FIGURE 8: Comparison between ANN (dotted lines) and analytical results (symbols) for I , T and V at different undisturbed fluid depths and wave nonlinearity parameters. Square symbols used in training phase, and triangle symbols used only for comparison

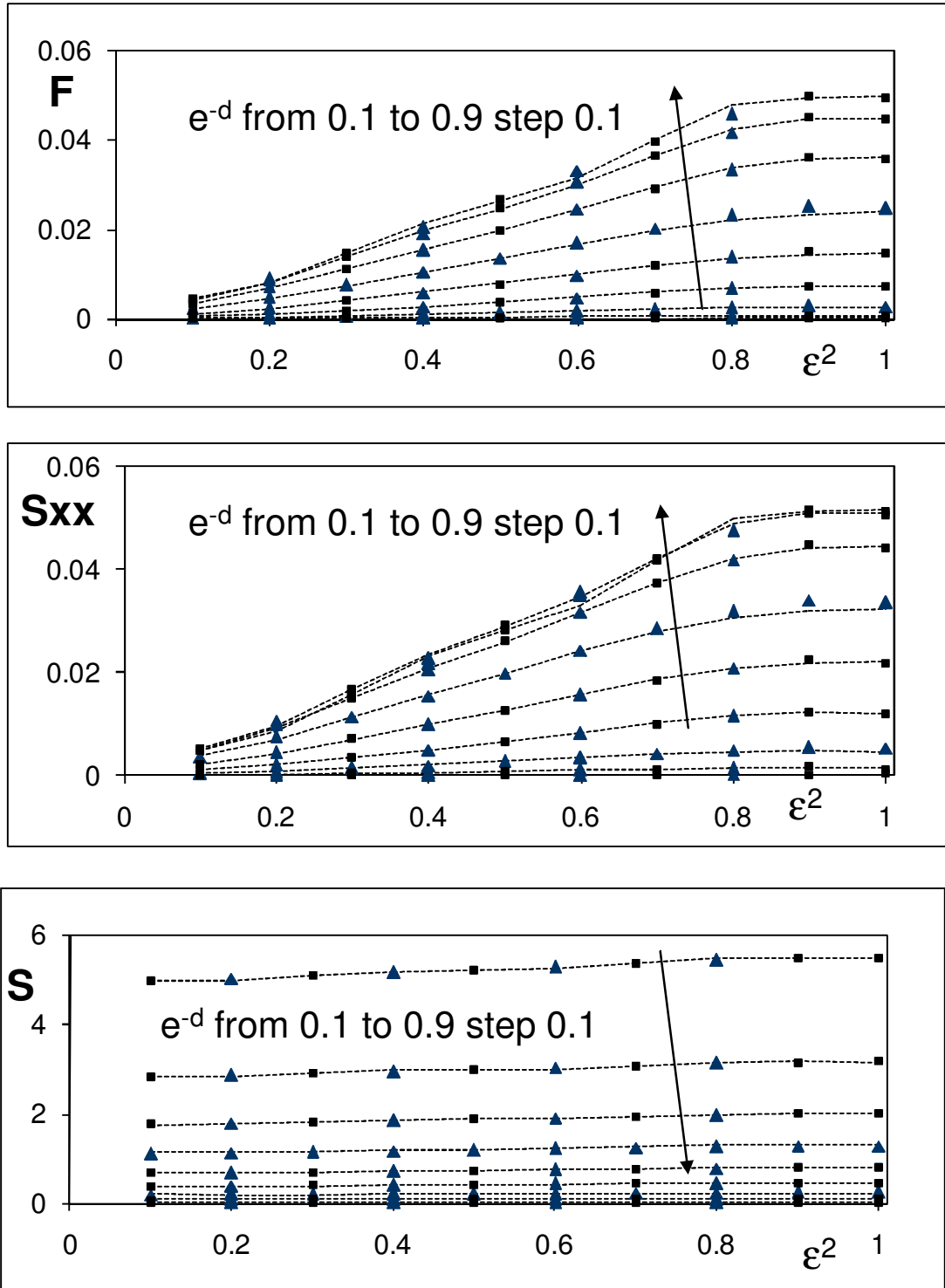


FIGURE 9: Comparison between ANN (dotted lines) and analytical results (symbols) for F , S_{xx} and S at different undisturbed fluid depths and wave nonlinearity parameters. Square symbols used in training phase, and triangle symbols used only for comparison

8. REFERENCES

1. Abohadima, S., Isobe, M., "Limiting criteria of permanent progressive waves", Coastal Eng., Vol. 44/3, pp. 231-237, 2002.
2. Cokelet, E.D., "Steep gravity waves in water of arbitrary uniform depth", Phil. Trans. R. Soc. London A286, pp. 183-230, 1977.
3. Dean, R.G., "Stream function representation of nonlinear ocean waves", J. Geophys. Res. Vol. 70, pp. 4561-4572, 1965.
4. Dean, R.G., "Evolution and development of water wave theories for engineering application", Vols. I and II, Special Rep. No. 1, US Army Coastal Engin. Res. Center, Fort Belvoir, Virginia, 1974.
5. Chaplin, J.R., "Developments of stream function wave theory", Coastal Eng., Vol. 3, pp. 179-205, 1980.
6. Rienecker M. M. and Fenton J. D., "A Fourier approximation methods for steady water waves", J. Fluid Mech., Vol. 104, pp. 119-137, 1981
7. Longuet-Higgins, M. S. and Fenton, J.D., "On the mass, momentum, energy and circulation of a solitary wave II", Proc. R. Soc. London A340, 471-493, 1974.
8. Schwartz, L.W., "Computer extension and analytic continuation of Stokes's expansion for gravity waves", J. Fluid Mech. Vol. 62, pp. 553-578, 1974.
9. Longuet-Higgins, M. S., "Integral properties of periodic gravity waves of finite amplitude", Proc. R. Soc. London A342, 157-174, 1975.
10. Yamada, H. and Shiotani, T., "On the highest water wave of permanent type", Bull. Disas. Prev. Res. Inst. Kyoto Univ., Vol. 18, Part 2, No. 135, pp. 1-22, 1968.
11. Minns, "Extended Rainfall-Runoff Modeling Using Artificial Neural Networks", Proc. of the 2nd Int. Conference on Hydroinformatics, Zurich, Switzerland, 1996.
12. Kheireldin, K. A., "Neural Network Application for Modeling Hydraulic Characteristics of Severe Contraction", Proc. of the 3rd Int. Conference, Hydroinformatics, Copenhagen - Denmark August 24-26, 1998.
13. Abdeen, M. A. M., "Neural Network Model for predicting Flow Characteristics in Irregular Open Channel", Scientific Journal, Faculty of Engineering-Alexandria University, 40 (4), pp. 539-546, Alexandria, Egypt, 2001.
14. Allam, B. S. M., "Artificial Intelligence Based Predictions of Precautionary Measures for building adjacent to Tunnel Rout during Tunneling Process" Ph.D., 2005.
15. Abdeen, M. A. M., "Development of Artificial Neural Network Model for Simulating the Flow Behavior in Open Channel Infested by Submerged Aquatic Weeds", Journal of Mechanical Science and Technology, KSME Int. J., Vol. 20, No. 10, Soul, Korea, 2006.
16. Mohamed, M. A. M., "Selection of Optimum Lateral Load-Resisting System Using Artificial Neural Networks", M. Sc. Thesis, Faculty of Engineering, Cairo University, Giza, Egypt, 2006.

17. Abdeen, M. A. M., "Predicting the Impact of Vegetations in Open Channels with Different Tributaries' Operations on Water Surface Profile using Artificial Neural Networks", Journal of Mechanical Science and Technology, KSME Int. J., Vol. 22, pp. 1830-1842, Seoul, Korea, 2008.
18. Abdeen, M. A. M. and Hodhod, H., "Experimental Investigation and Development of Artificial Neural Network Model for the Properties of Locally Produced Light Weight Aggregate Concrete" Engineering, 2, June 2010, 408-419, Scientific Research Organization, 2010.
19. Hodhod, H. and Abdeen, M. A. M., "Concrete Mix Design Method Based on Experimental Data Base and Predicting the Concrete Behavior Using ANN Technique" Engineering, 2, August 2010, 559-572, Scientific Research Organization, 2010.
20. Shin, Y., "NeuralystTM User's Guide", "Neural Network Technology for Microsoft Excel", Cheshire Engineering Corporation Publisher, 1994

Conceptual Designing and Numerical Modeling of Micro Pulse Jet for Controlling Flow Separation

Zakir Mahfooz

*College of Energy and Power Engineering (CEPE)
Nanjing University of Aeronautics and Astronautics (NUAA)
Nanjing, China*

zakirmehfooz@hotmail.com

M.K.Ahmed

*Institute of Space Technology, Islamabad
Department of Aeronautics and Astronautics
Islamabad, Pakistan.*

mohsinqurashi@gmail.com

Prof. Huang Guoping

*College of Energy and Power Engineering (CEPE)
Nanjing University of Aeronautics and Astronautics (NUAA)
Nanjing, China*

Abstract:

A conceptual design and numerical model of Micro Pulse Jet has been developed to investigate the flow separation. This valve is designed to generate the stream line vortices to suppress the flow separation by enhancing the mixing of the flows between free stream and separated flow of the boundary layer through pitched jet orifice of very small width. This paper describes not only the conceptual modeling of Micro Pulse Jet but also presenting the numerical analysis and results of steady and unsteady pulse of micro jet. The unsteady pulse of the valve is simulated by the periodic inlet boundary condition through a mathematical model. A 2-D ramp with 20 degrees divergence is selected. The divergence of the lower wall of the ramp is large enough to produce a strong adverse pressure gradient causing the boundary layer to separate. A jet orifice is introduced at the upstream of the divergent portion of the ramp and the effect of steady and unsteady jet is analyzed. The main inlet boundary condition is almost of 0.2 Mach. The jet amplitude is characterized by the velocity ratio (V_j/V_∞) in between 0 to 5 and the jet pulse frequency is varying between 0 to 100 Hz. A comparison between the steady and unsteady Micro Pulse Jet is also done, which indicates the mass flow requirement for pulse micro jet is reduced significantly as compare to the steady jet for the flow separation control.

Keywords: Vortex Formation, Mixing Enhancement, Flow Separation, Pulse Frequency, Pressure Ratio, Pitch Angle, Mass Flow Rate, Unsteady and Steady jet, Periodic Behavior

1. INTRODUCTION

Now a day's flow separation control mechanism is largely in practice to enhance the performance of the system in design and off design condition. Generally on the basis of the working principle the flow separation control techniques are classified as Passive and Active control method. In passive control method there is no external source required while there must be an external source for separation control in Active flow control method [1].

The main disadvantage of the passive control method is associated with larger drag value and unable to correspond in time varying action requirement while on the other hand active control method is quite capable of producing good results in design and off design condition. In active flow control technique where separation is controlled by the pulse of the jet, a jet is introduced at the upstream of the effected flow region and the separation is controlled by the jet vortex [2]. The generated vortex enhances the mixing of the flow between the high energy free stream and the low energy separated boundary layer flows [3, 2].

The basic purpose of introducing the new conceptual approach of Micro pulse Jet is to analyze the strength of emitting jet from the valve in order to capture the flow separation effectively. There are many advantages of new conceptual model of Micro Pulse Jet over the traditional methods e.g. it has compact size which can be easily stowed in any system like in internal flows and turbo machinery application, working principle of unsteady valve is very simple and unsteady pulse jet created by the valve having high mach.

In the present study the Micro pulse jet is used for effective control of the flow separation. The conceptual model is applied and analyzed by numerical model of the valve. The unsteady pulse of the jet through the valve is simulated by the periodic inlet boundary condition through mathematical model. The basic working principle of the valve is based on the pressure ratio values. The difference between the total pressure at the lower surface and the static pressure at the upper surface of the valve is providing driving force for unsteady pulse jet. This pressure ratio is responsible for controlling the amplitude of the jet and also defines the velocity ratio. Research starts with conceptual design of micro pulse jet. Two test configurations are devised configuration A and configuration B on the basis of pitch angle.

2. REVIEW OF RELATED RESEARCH WORK

Previous research work for flow separation control is done by the following methods.

- Tangential blowing and suction method. The basic disadvantage of this technique is associated with an external source to avoid the flow separation which increase the complexity level of the system and also increase the parasitic drag value.
- Vortex generators (VGs and Micro VGs) the basic disadvantage of this method is related with larger value of parasite drag as compare to other active flow control techniques [4].
- Acoustic Excitation and It's effect has been observed in delaying the separation and it is well known documented by several researcher like (e.g. Collins & Zelevitz 1975; Mueller & Batill 1982; Ahuja & Burrin 1984 near stall condition was carried out by the group at Lockheed [5]). The main disadvantage of Acoustics excitation is incapable of producing excitation of large intensity for controlling the flow separation. Moreover, these acoustic excitation studies were in most cases facility dependant and therefore, it is of limited use from a practical perspective.
- Synthetic Jet Actuator (SJA) which is based on "zero-net-mass flux flow" in which the energy can be transferred to the flow without adding extra mass [6-10]. The main disadvantage of this method is associated with the strength of jet in small configuration.

Basically all the above techniques are not able to produce a jet of higher energy to suppress the flow separation in highly turbulent and separated environments. This phenomenon is quite evident in AEROMEMS-I and some preliminary work done in AEROMEMS-II in which it was observed that SJA while operating in self contained zero-net-mass-flow mode is not able to produce a jet of velocity of 100 m/sec in small configurations [11]. This problem leads to the importance of Pulsed Jet Actuators [12-14], but in pulse jet actuator there must be an external source for producing pressurized air to open the valve and control the flow separation. In the present research work there is no need of external source for producing the jet. This concept is based on pressure gradient in which total pressure at the lower surface of the valve is greater

than the pressure at the upper surface and consequently separation is controlled through the unsteady pulse of the jet.

3. CONCEPTUAL DESIGN OF MICRO PULSE JET

The conceptual model of Micro Pulse Jet is mainly consists of two parallel plates having pores and voids for the jet. The plate (5) moves over the stationary pate (6) through the force provided by the driving member (10). The driving member is activated by some external source like electric current. The working principal of the valve is based on the pressure gradient between the lower and at the upper surface of the valve. When the pores are aligned with each other due to the motion of moving plat over the fixed plat, gives the passage for unsteady pulse jet. The unsteady jet is further accelerated in convergent duct in the form of nozzle, as shown in the fig [1].

The conceptual model of the valve is shown in fig [1] and due to simplicity of the design and its compact configuration; it can be easily accommodated in any system. The basic principal of separation control through unsteady jet is shown in fig [2].

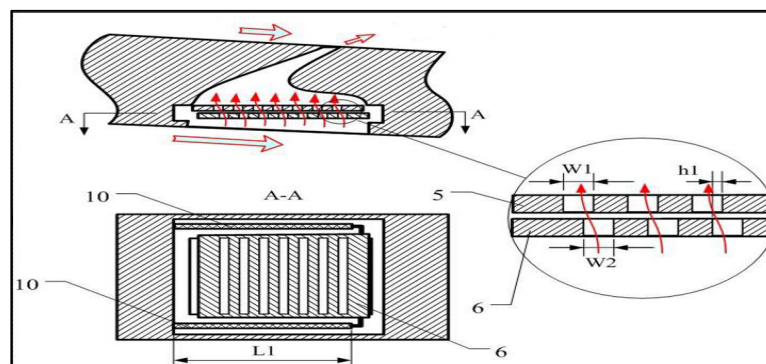


FIGURE 1: Conceptual model of Micro Pulse Jet

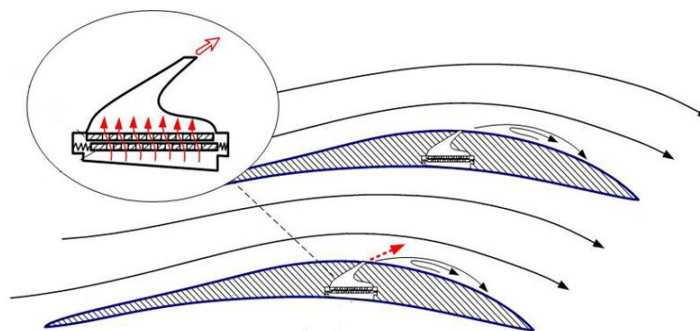


FIGURE 2: Conceptual Model of Flow Separation Control by Micro Pulse Jet

4. MODELING OF FLUID DYNAMICS

A computational study has been carried out in order to investigate the effectiveness of the conceptual model in controlling the flow separation. The unsteady valve is simulated by the periodic inlet boundary condition though CFD-ACE+ software. In order to validate the new conceptual model of micro Pulse Jet, a 2-D ramp channel is selected due to severe separation in the flow, caused by existence of adverse pressure gradient due to the lower wall divergence of the ramp channel.

4.1 Case Discription

2-D channel with 20 degrees of divergence is selected for numerical analysis of Micro Pulse jet. The jet of 2mm is placed at the upstream of ramp. The jet amplitude is varied by using various

value of K . The various velocity ratios have been analyzed with different pitchy angle (α) and jet pulse frequency. The reference case for the validation, with and without the valve is shown in the following figures.

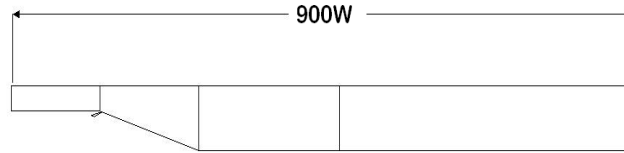


Figure 3: Baseline case geometry



FIGURE 4: Baseline case geometry with valve

4.2 Mesh

2-D ramp is discretised with H- type structured mesh with almost 100,000 mesh cells. The RNG K-E turbulence model is used with viscous spacing of $1e-05$ in order to keep the Y_+ values in between the recommended values for capturing the flow separation and unsteadiness of the flow. The mesh of the ramp channel with unsteady valve is shown in the fig [5].

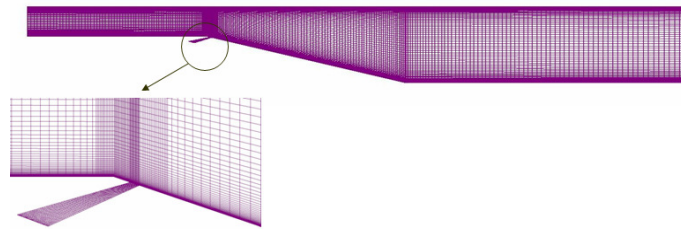


FIGURE 5: Mesh of 2-D ramp with almost 100,000 cells

4.3 Boundary Condition

In order to simulate Micro Pulse Jet with the Ramp 2-D model four types of boundary conditions are used. Inlet with Mach no. 0.2 is used for the free stream condition, at the end of the ramp the Outlet fixed pressure is used while the ramp has no slip wall condition. The valve is simulated through periodic Inlet boundary condition having transient normal total pressure condition as shown in mathematical model

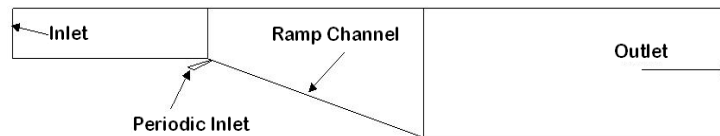


FIGURE 6: Detail of Boundary Condition

4.4 Mathematical Model

Basic purpose of this research is to simulate the valve for generating the micro pulse jet for controlling the flow separation. The functionality of the valve which consists on a converging duct is based upon the pressure gradient between the lower surface and the upper surface of the

valve. The flow is accelerated due to the pressure gradient and the convergent duct of the valve. The Mach of the jet and velocity ratio is controlled by the pressure ratio (K). The transient behavior of the valve is modeled with the help of the mathematical model. The following mathematical function is used to simulate the valve with periodic inlet boundary condition for the unsteady micro pulse Jet.

$$P_o = P_{st} \left[\left(\frac{\cos wt + 1}{2} \right) * K + 1 \right] \quad [1]$$

Where K is the pressure ratio factor

5. EXPERIMENTAL VALIDATION

The present research work is based on computational analysis of a new conceptual design of the valve through periodic inlet boundary condition by using above mentioned mathematical model. So, it is mandatory to validate the computational scheme and discretization methodology through some experimental work. As this research work is based on new conceptual approach so for validation purpose a 2-D ramp case is selected having the experimental results available in ref [2]. In order to correlate the numerical results with the experimental data, the same environments of experimental conditions are tried to simulate with inlet velocity of 11.5 m/sec only. New conceptual model of the valve is analyzed with different inlet conditions. The non dimensional velocity ratio at various points as shown in fig [7], plotted against wind tunnel data shows good agreement. Dimensions are in cm.

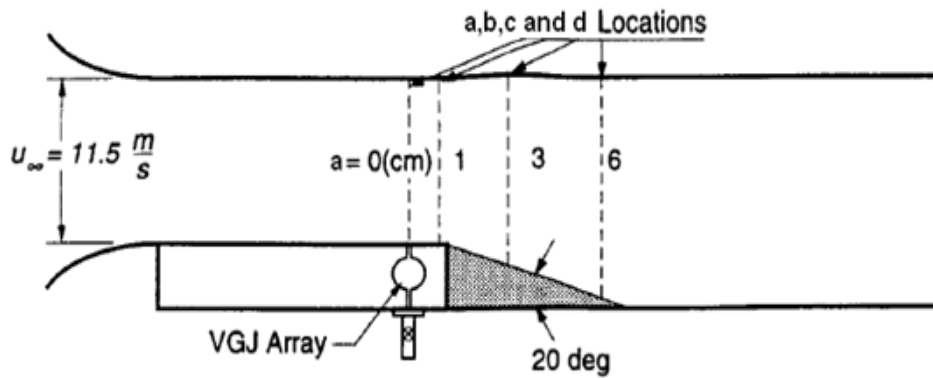


FIGURE 7: Experimental setup and Position of Velocity Profiles
(Reprinted with permission from American Institute of Aeronautics and Astronautics (AIAA))

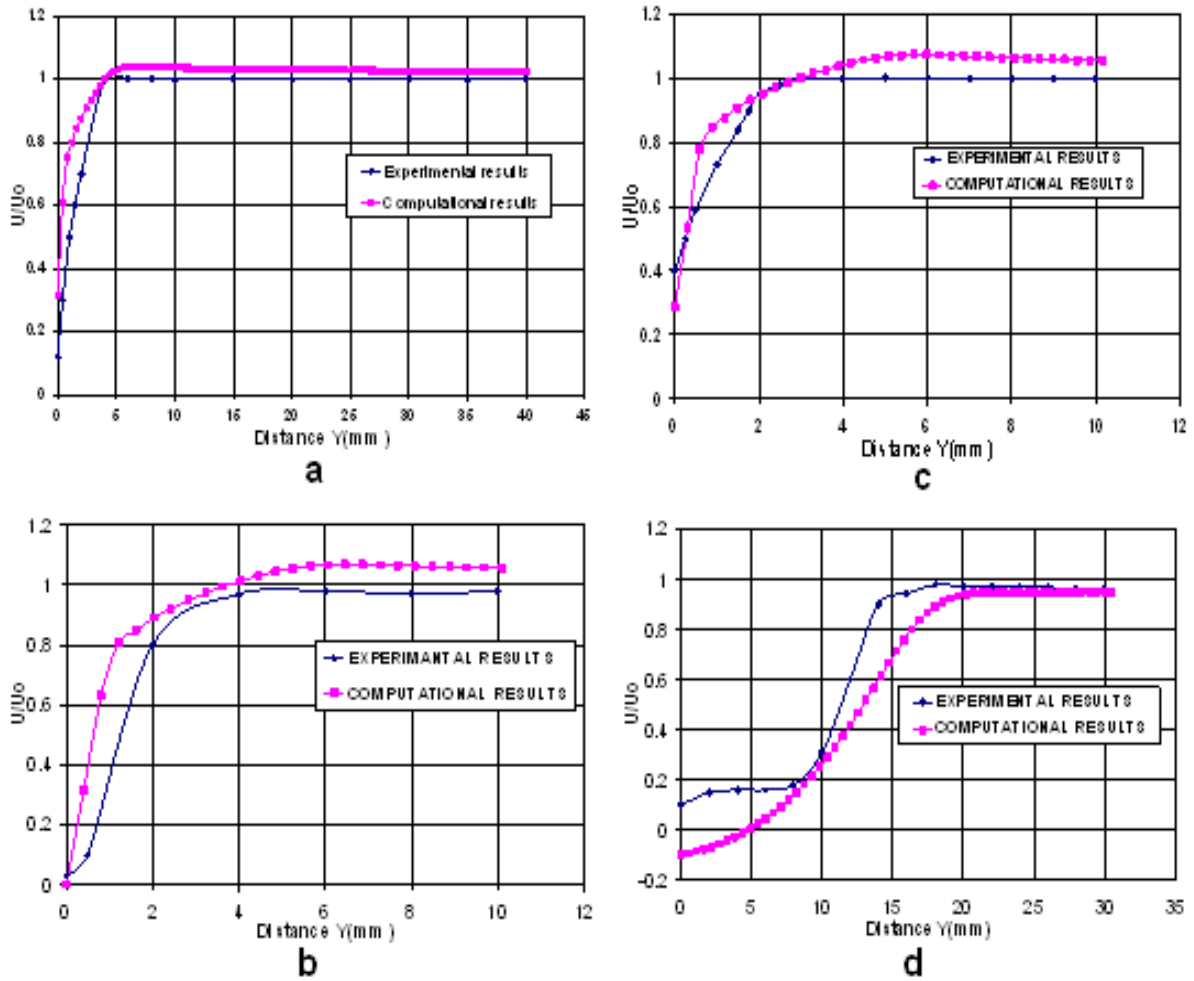


FIGURE 8: Velocity profile at various locations
(Experimental data reprinted with permission from American Institute of Aeronautics and Astronautics (AIAA))

The trend line of velocity ratio shows a good agreement of computational results with experimental. Overall the percentage variation in the results is less than 10%. The behavior of velocity ratio depicts the presence of separated boundary layer adjacent to the lower wall of ramp as shown in fig [8(d)], where U_0 is inlet velocity (11.5 m/sec) is selected for correlation purpose only while the rest of research work is conducted at Mach 0.2.

6. BASELINE FLOW FIELD CHARACTERISTIC

A baseline analysis shows that the flow has high turbulent separated structure near the lower wall of the ramp channel, due to the adverse pressure gradient. The behavior of v component of velocity contour shows that the flow is not attached with the wall. The rotating vortex in without valve configuration is not able to overcome the separation in the flow, as there is no mechanism of crating unsteady pulse jet, as shown below.

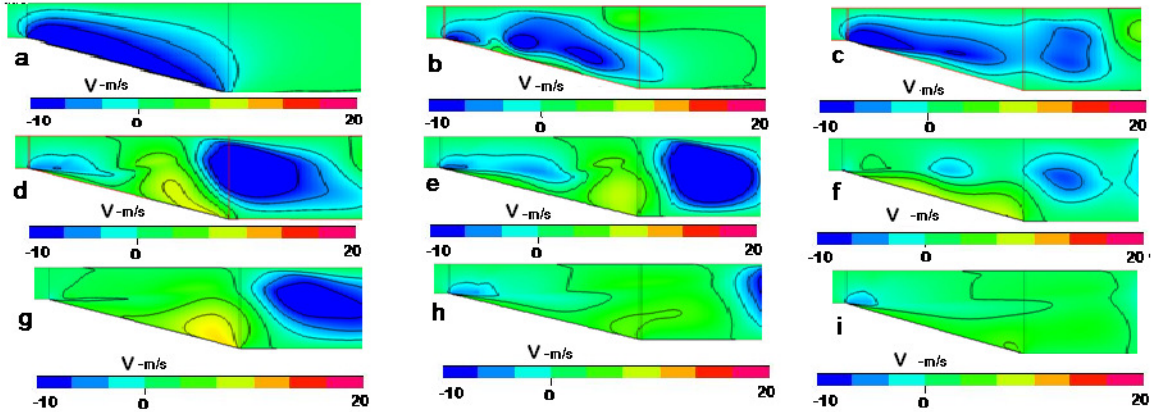


FIGURE 9: Velocity v -contour at (a) Time=0.01 sec, (b) Time=0.02 sec, (c) Time=0.03 sec, (d), Time=0.04 sec (e) Time=0.05 sec, (f) Time=0.06 sec, (g) Time=0.07 sec, (h) Time=0.08sec (l) Time=0.1sec

The results of Velocity (v) contour clearly describe the existence of separation with the lower wall of the ramp channel. The rotating vortices is not able to control the separation in the flow rather the separation is growing with time, as shown by the behavior of the stream traces in the following figure[10].

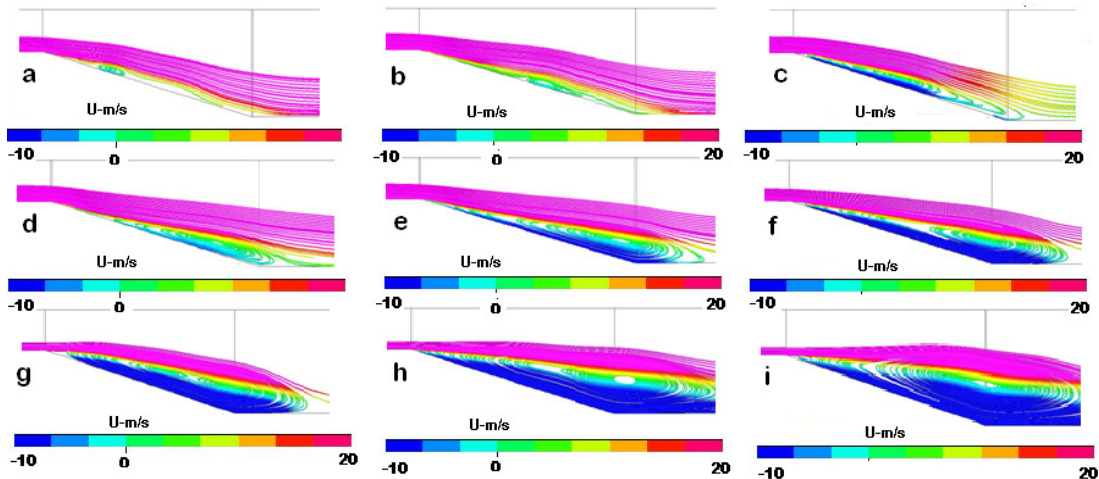


FIGURE 10: Velocity u traces at (a) Time=0.01 sec, (b) Time=0.02 sec, (c) Time=0.03 sec, (d), Time=0.04 sec. (e) Time=0.05 sec, (f) Time=0.06 sec,(g) Time=0.07 sec, (h) Time=0.08sec (l)Time=0.1sec

The stream traces of x component of velocity (u) show the flow behavior at various time intervals. The separation is growing with time in without control environment as shown by the following [10].

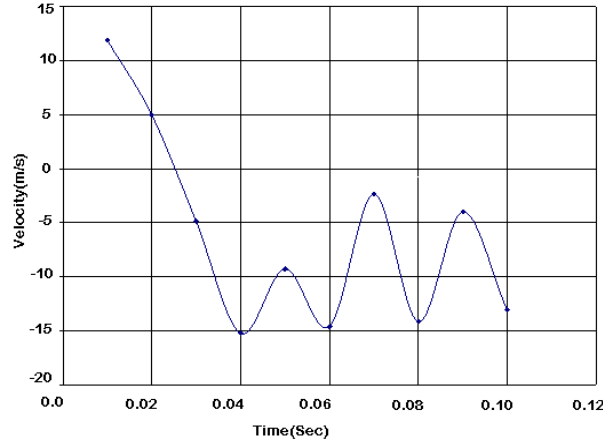


FIGURE 11: Velocity plot at various time intervals

The periodic behavior of the separation is observed at almost 72% ramp channel length, as shown in the fig [11]. The magnitude of the velocity clearly indicates the existence of the separation in the flow.

In order to estimate the frequency of separated flow, various points are introduced at different location in the computational domain of the ramp channel and it was investigated that the unsteady flow has the frequency of 40 HZ.

7. EFFECT OF MICRO PULSE JET ON FLOW SEPARATION

The effect of Micro pulse jet on flow separation is investigated with the various test parameters including different velocity ratio (VR), pitch angle (α) and various set of unsteady pulse frequencies. The flow characteristics under the control environment of Micro pulse Jet valve operating at various combinations of test parameters are analyzed with the help of the following table.

Test Configuration	VR	Pitch Angle (α)	Unsteady Frequencies (HZ)
A	2.3	45	20,40,80,100 HZ
	2.5	45	20,40,80,100 HZ
	3	45	20,40,80,100 HZ
B	2.3	30	20,40,80,100 HZ
	2.5	30	20,40,80,100 HZ
	3	30	20,40,80,100 HZ

TABLE 1: Test parameters for Micro Pulse Jet

7.1 Flow Visualization and Results

The results from all above mentioned configuration will discuss in this section. The results are described on the basis of velocity contour, flow quality which shows the separation existence, mass flow requirement to control the flow separation at steady and unsteady jets and velocity plots at various points in the flow field. For the flow visualization and qualitative results the best combination of pitch angle with different velocity ratio and frequencies are selected. Overall four

test configuration are selected which include the worst and the best combination of pitch angle and different frequencies at two different velocity ratios.

1. Test configuration (A)

The test configuration A has the combination of different velocity ratio, constant pitch angle and various set of frequencies, from these test configurations on the bases of the quality of the results the two cases are selected for the results discussion in the following manner.

a) Results (VR=2.3, $\alpha=45^\circ$)

Micro Pulse Jet operating at above mentioned test parameters are analyzed in detail. This section of paper restrain the flow characteristics results in the form of velocity contours and stream traces through the pulse jet valve at unsteady frequency of 80 HZ. The unsteady pulse frequency of the jet is selected on the basis of the quality of the results.

When the Micro Pulse valve is operating with the combination of pitching angle 45 degrees, velocity ratio 2.3 and the pulse frequency 80 HZ, the results of velocity contour and the stream traces show that the valve is not able to control the flow distortion effectively. The results of stream traces are described below,

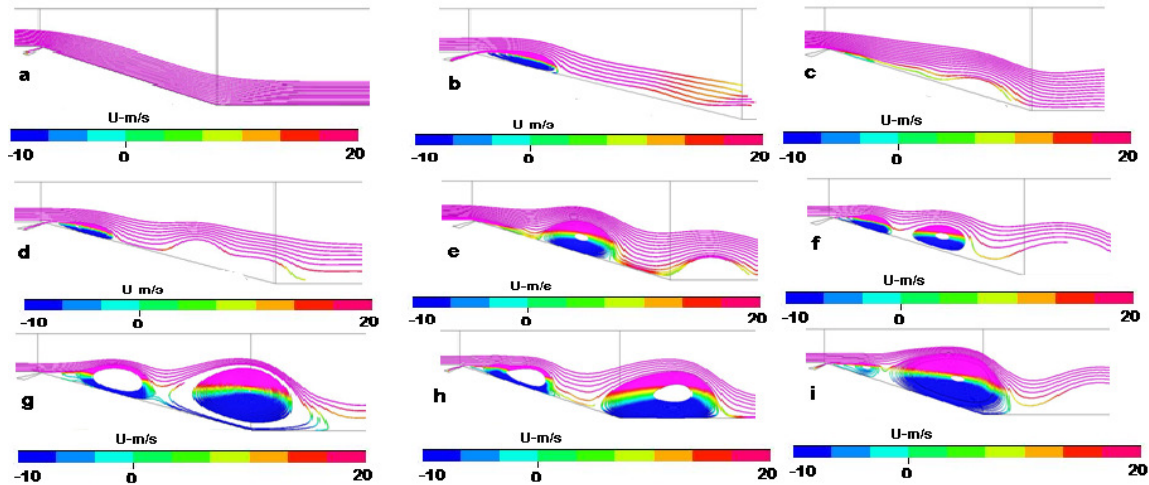


FIGURE 12: Velocity u traces at pitch angle=45, VR=2.3 and 80HZ (a) Time=0.01 sec, (b) Time=0.02 sec, (c) Time=0.03 sec, (d), Time=0.04 sec (e) Time=0.05 sec, (f) Time=0.06 sec, (g) Time=0.07 sec, (h) Time=0.08sec (l) Time=0.1sec

Initially it was investigated that due to the pulse of the jet, separation is removed by the rotating vortex. There is a small portion of the separated flow just under the pulse of the jet, when the valve is operating at 80 HZ, as shown in fig [12(b)]. The separation in the flow is growing with the passage of time as shown in fig [12(c) and (d)]. Actually the valve is creating the rotating vortex continuously and the separation is controlled to some extent at the initial level of time interval, as shown by the fig [12(a) to (c)]. There is a severe separation observed at the time interval of 0.05 sec of the simulation as shown by the fig [12(e)], it may be due to the jet operating angle or the velocity ratio which is not allowing the unsteady jet to control the separation in the flow in an effective manner. This phenomenon of controlling the flow separation and internal flow behavior is also visible in the velocity contour plot as shown in the following figures,

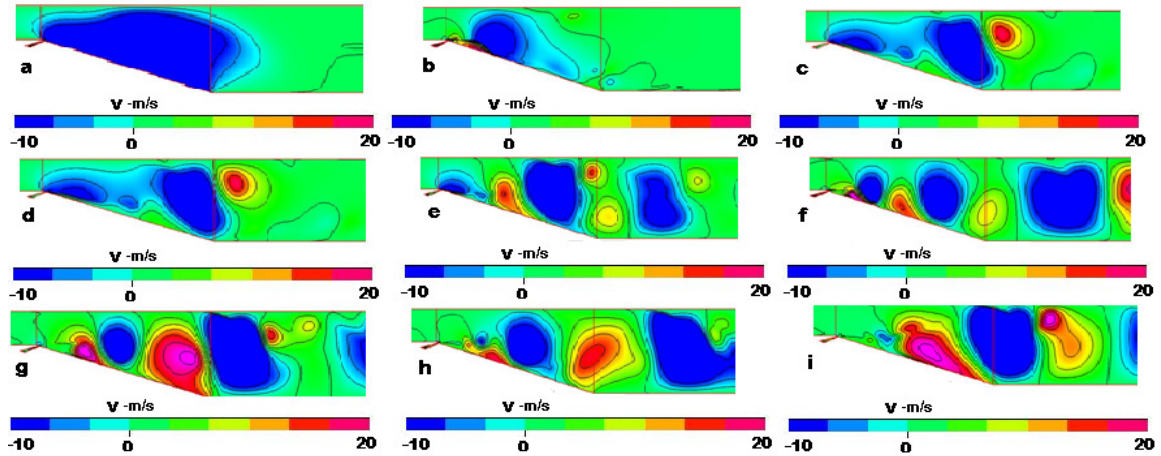


FIGURE 13: Velocity v -contour at pitch angle=45, VR=2.3 and 80HZ (a) Time=0.01 sec, (b) Time=0.02 sec, (c) Time=0.03 sec, (d), Time=0.04 sec (e) Time=0.05 sec, (f) Time=0.06 sec, (g) Time=0.07 sec, (h) Time=0.08sec (l) Time=0.1sec

The significance of created rotating vortex for controlling the flow separation is quite visible in velocity contour plot. There is a visible separation in the flow at the time of 0.05 sec as shown in the fig [13(e)]. The valve operating at 80 HZ is not capable of reducing and removing the separation in the flow along the wall of the ramp rather the effected portion is growing and separation becomes more and more severe with the time.

In order to investigate the effective control of the separation by the unsteady pulse jet operating at test configuration (A), the data of velocity are obtained at a point almost 72 % downstream of the ramp channel.

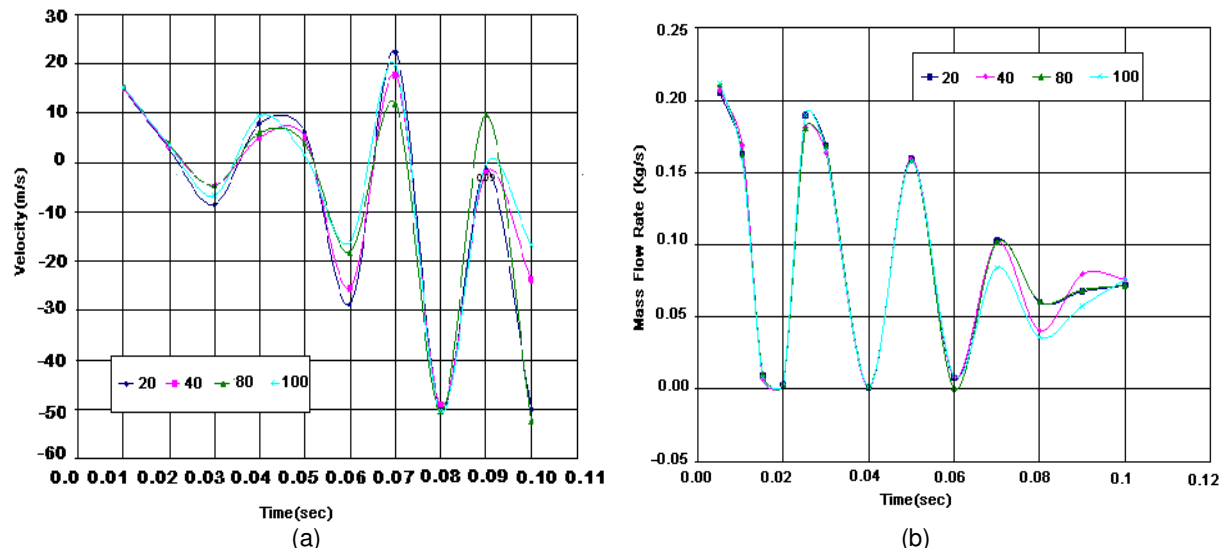


FIGURE 14: Plots at (VR=2.3, $\alpha=45$) (a) Velocity plots at 72 % ramp length, (b) Mass flow rate requirement at various frequencies of 20,40,80,100 HZ.

The periodic behavior of velocity plot clearly indicate that in the beginning the separation is controlled by the pulse of the jet while operating at velocity ratio of 2.3 and at a pitch angle of 45 degrees but with the passage of the time the magnitude of the velocity even at higher frequencies becomes negative, indicates the existence of separation in the flow as shown in fig [14(a)].

Mass flow requirement for the valve to control the separation is also plotted in fig [14(b)] which shows there is no significant difference between the mass flow requirements at various

frequencies. It was investigated that the mass flow requirement for the steady jet is significantly larger as compare to the unsteady frequencies in order to capture the flow separation in the flow.

b) Results (VR=3, $\alpha=45^\circ$)

The results for the test configuration at Pitch angle 45 degrees with the velocity ratio 3, shows the effective control of Micro Pulse Jet as compare to the unsteady pulse jet operating at velocity ratio 2.3. The pulse jet of the valve is controlling the flow separation quite effectively while operating at 80 HZ. The flow behavior under the control action of Micro pulse Jet is shown by the following figure

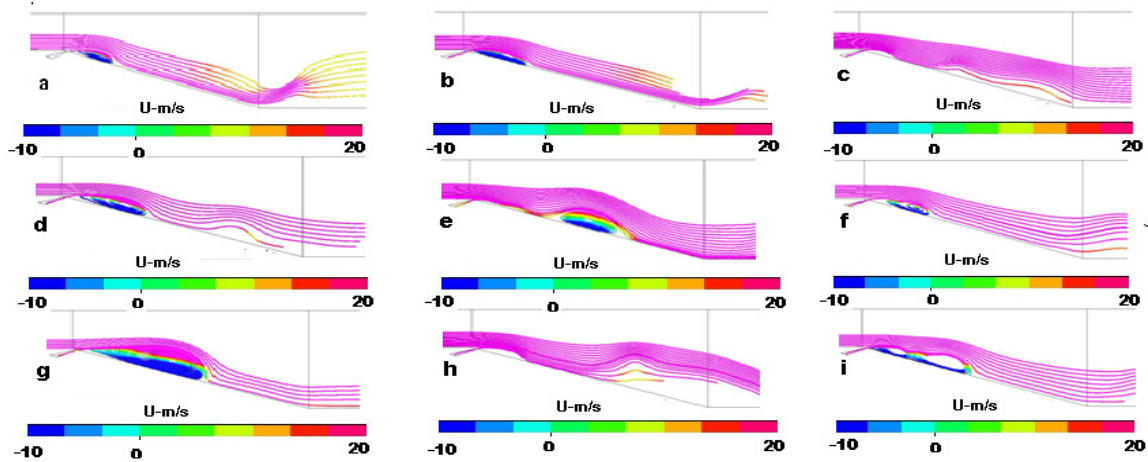


FIGURE 15: Velocity u-contour at pitch angle=45, VR=3and 80HZ (a) Time=0.01 sec, (b) Time=0.02 sec, (c) Time=0.03 sec, (d), Time=0.04 sec (e) Time=0.05 sec, (f) Time=0.06 sec, (g) Time=0.07 sec, (h) Time=0.08sec (l) Time=0.1sec

The flow picture under the control environment of micro Pulse Jet operating at above mentioned parameters show that the valve is quite capable of controlling the separation in the flow. The pulse of the jet is not allowing the separation to grow with time as shown by the fig [15 (a) to (i)]. The same phenomenon is also quite evident from the velocity contour plot, as shown by the following figure.

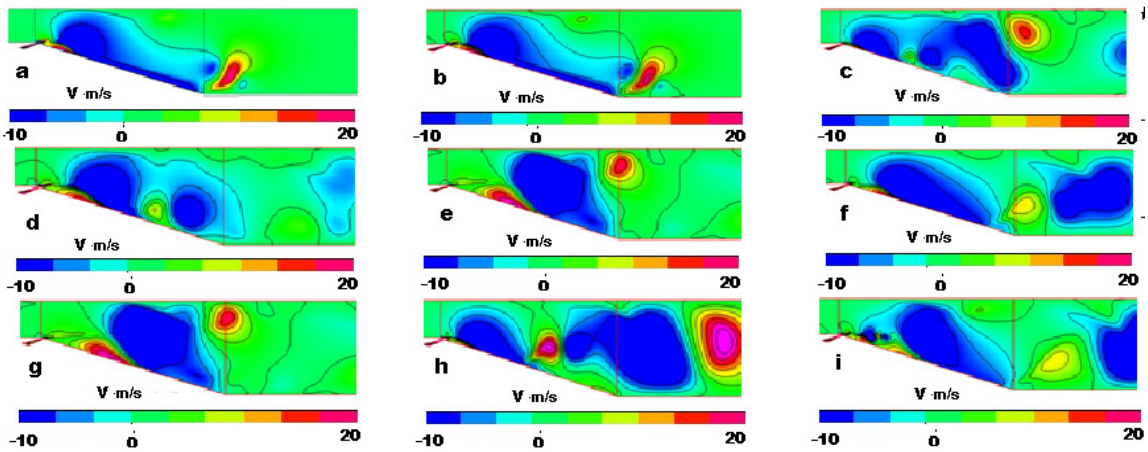


FIGURE 16: Velocity v traces at pitch angle=45, VR=3and 80HZ (a) Time=0.01 sec, (b) Time=0.02 sec, (c) Time=0.03 sec, (d), Time=0.04 sec (e) Time=0.05 sec, (f) Time=0.06 sec, (g) Time=0.07 sec, (h) Time=0.08sec (l) Time=0.1sec

The effectiveness of the unsteady pulse frequency in controlling the flow separation is quite visible in velocity contour plot, shown in fig [16]. Overall the flow characteristics in term of separation control for the unsteady jet operating at velocity ratio 3 at constant pitch angle and unsteady frequency of 80 HZ is better than the velocity ratio 2.3.

The velocity plot at the 72 % downstream length of the ramp channel shows that the valve is quite capable of controlling the separation at 80 HZ in an efficient manner as compare to the unsteady jet operating at same pitch angle with the velocity ratio 2.3, as shown by the periodic behavior of velocity in fig [17 (a)].

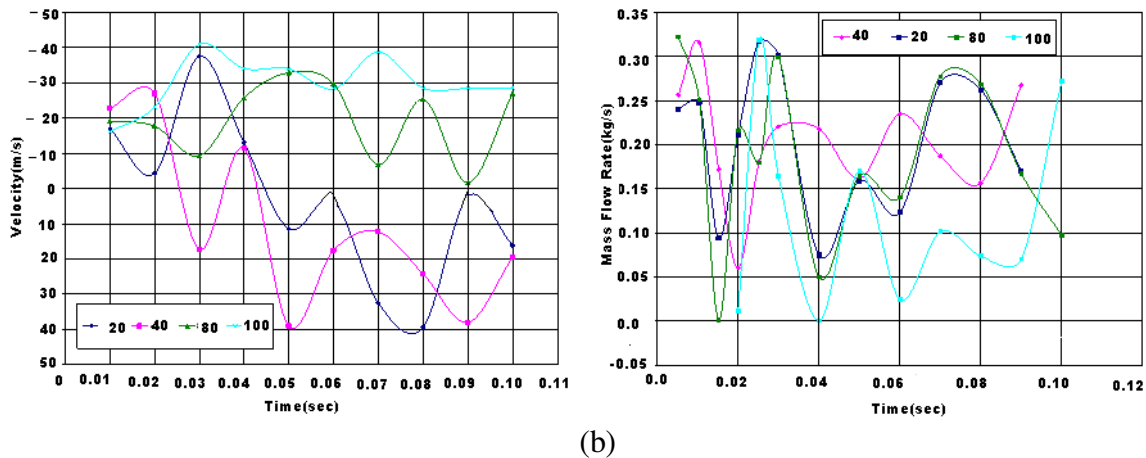


FIGURE 17: Plots at (VR=3, $\alpha=45$) (a) Velocity plots at 72 % ramp length, (b) Mass flow rate requirement at various frequencies of 20, 40, 80, 100 HZ

The mass flow rate requirement while operating with these parameters, is significantly increase as compare to the previous test parameters case as shown in the fig [17(b)], but having the lesser requirement for the unsteady case as compare to the steady jet operating under the same test parameters of configuration (A).

2. Test configuration (B)

A detailed numerical study has been conducted to investigate the effectiveness of Micro Pulse Jet operating at test condition, described in configuration B. Two test cases are selected on the bases of the results obtained at constant pitch angle 30 degrees, different velocity ratios and with the same unsteady jet frequency of 80 HZ, in the following manner.

a) Results (VR=2.3, $\alpha=30^\circ$)

It is investigated through comprehensive numerical study that the unsteady Micro Pulse Jet operating at pitch angle 30 degrees, velocity ratio 2.3 and with the unsteady frequency 80 HZ, controlling the separation in the flow quite effectively. Overall results obtained from the flow visualization and the velocity plot at a certain point, downstream of the ramp show that the pulse of the jet is controlling the separation in efficient manner. The stream traces of velocity contour at different time intervals are shown below.

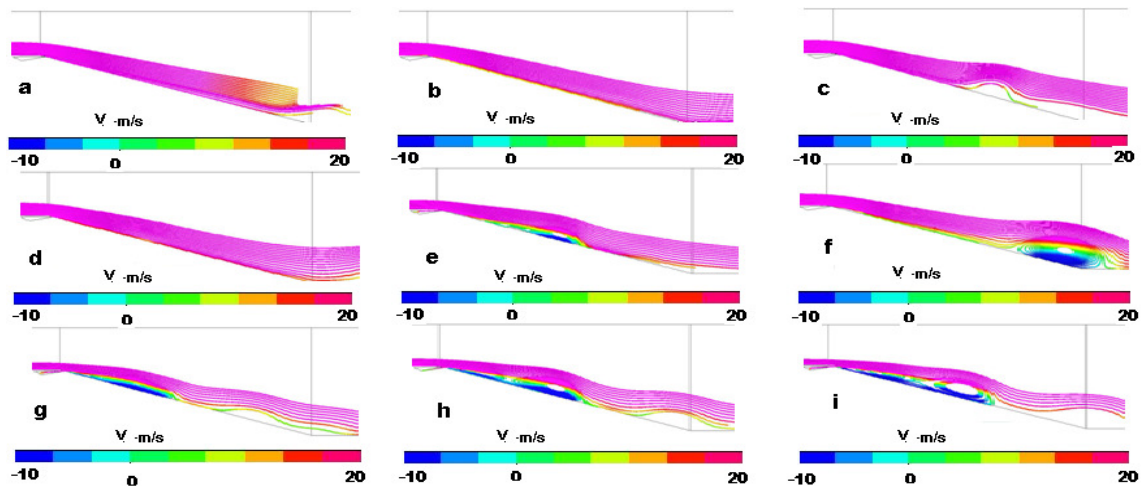


FIGURE 18: Velocity v-contour at pitch angle=30, VR=2and 80HZ (a) Time=0.01 sec, (b) Time=0.02 sec, (c) Time=0.03 sec, (d), Time=0.04 sec (e) Time=0.05 sec, (f) Time=0.06 sec, (g) Time=0.07 sec, (h) Time=0.08sec (l) Time=0.1sec

The behavior of stream traces show that the pulse of the jet is effectively controlling the separation in the flow, there is a small separation observed at time interval of 0.03 sec shown by the fig [18(c)] but it is removed by the pulse of the valve. There is another separation zone in the flow very close to the valve, is moved further downstream to the ramp as shown by the fig [18(e) and (f)]. The pulse of the valve is controlling the separation by rotating vortex generation and separation area is reduced as shown by the fig [18(g)] ,but it is not removed completely from the flow as shown by the fig [18(h) and (l)].

The Micro Pulse Jet is controlling the separation well, while operating at above mentioned test parameters but not able to suppress the separation completely from the flow. The reason for that may be the valve is not able to produce enough energetic pulse of the jet which can remove the separation from the wall of the ramp. Overall results on the bases of controlling the flow separation and the quality of the flow are better than the results obtained from the pitch angle 45 degrees while operating at the same parameters. The velocity contours of the flow at various time intervals are shown below.

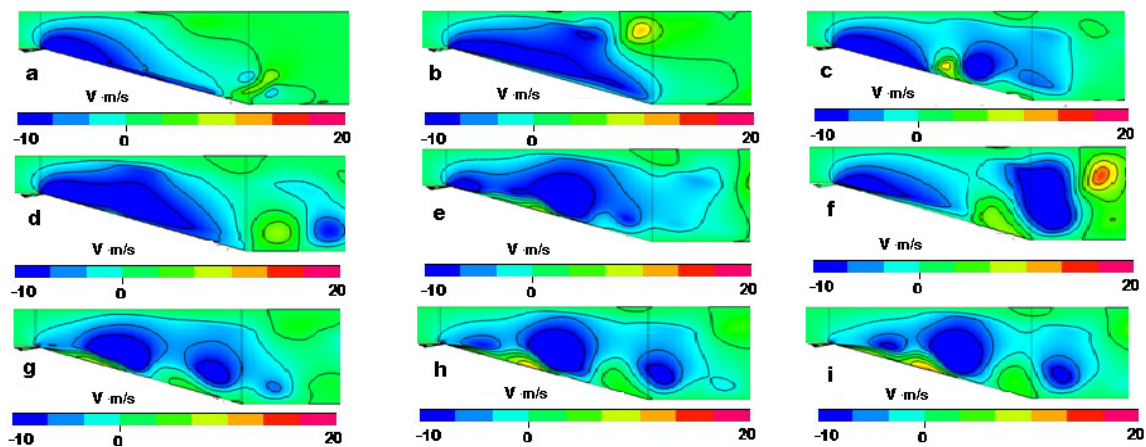


FIGURE 19: Velocity v traces at pitch angle=30, VR=2and 80HZ (a) Time=0.01 sec, (b) Time=0.02 sec, (c) Time=0.03 sec, (d), Time=0.04 sec (e) Time=0.05 sec, (f) Time=0.06 sec, (g) Time=0.07 sec, (h) Time=0.08sec (l) Time=0.1sec

The trend of the velocity (v) contour shows that how effectively the separation is controlled by the pulse of the jet while operating at test parameter (B). Initially there is no significant separation observed in the flow except at 0.03 sec as shown by the fig [19(c)] but removed by the pulse of the jet as shown by the fig [19(d)]. It was investigated in all the test cases that due to the pulse of the jet there is separation just beneath the jet but the pulse of the jet is quite capable in removing and controlling the flow separation, as was observed in the case of test configuration (B).

A point is placed at 72 % downstream of the ramp in order to investigate the flow quality and magnitude of the velocity in more detail. The trend of the velocity magnitude is shown below,

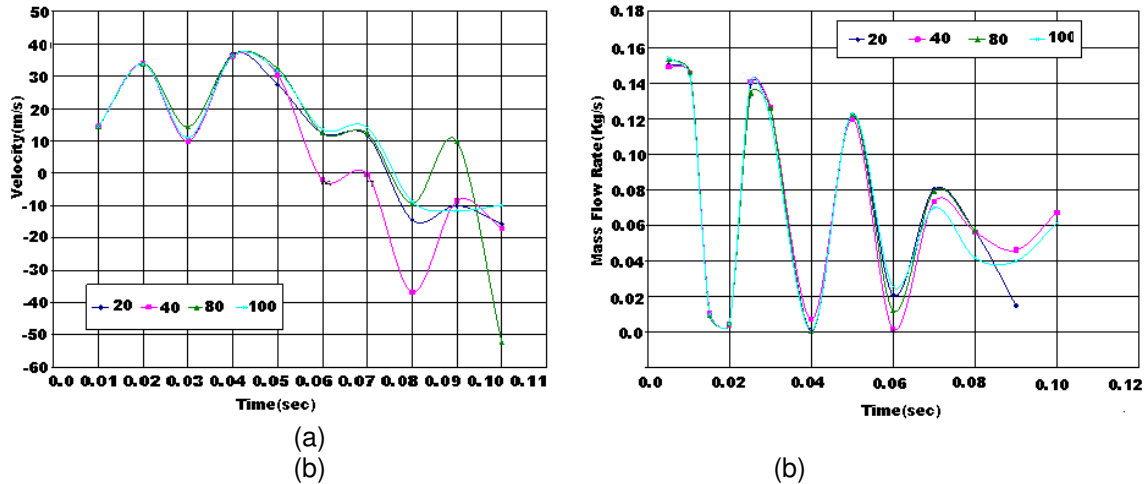


FIGURE 20: Plots at (VR=2, $\alpha=30$) (a) Velocity plots at 72 % ramp length, (b) Mass flow rate requirement at various frequencies of 20, 40, 80, 100 HZ

The trend line of the velocity plots show that the separation is controlled at the downstream of the ramp most of the time but at the end the separation is not removed by the pulse of the jet completely as shown by the fig [20(a)] and the magnitude of the velocity becomes negative which shows the existence of the separation. The separation is controlled though not removed completely but the results are better than the valve operating at pitch angle of 45 degrees with the same test parameters.

The mass flow rate requirement for suppressing the flow separation in case of pulse jet is significantly reduced from the steady jet. The mass flow rate requirement while operating at pitch angle of 30 degrees is appreciably reduces from the valve operating at 45 degrees, shown in the fig [20(b)].

b) Results (VR=3, $\alpha=30^\circ$)

This section of the document describes either the pulse of the jet at pitching angle 30 degrees, velocity ratio 3 with unsteady frequency of 80 HZ is capable of controlling and removing the separation in flow or not. A detailed study has been done to investigate the control action taken by the pulse of the jet, presented below,

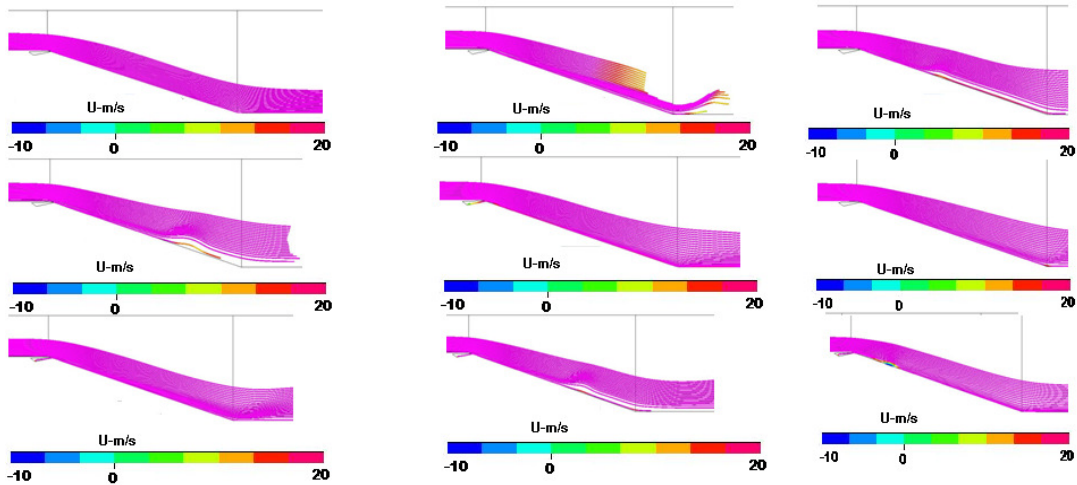


FIGURE 21: Velocity u -contour at pitch angle=30, VR=3and 80HZ (a) Time=0.01 sec, (b) Time=0.02 sec, (c) Time=0.03 sec, (d), Time=0.04 sec (e) Time=0.05 sec, (f) Time=0.06 sec, (g) Time=0.07 sec, (h) Time=0.08sec (i) Time=0.1sec

The result for the Micro pulse jet at pitch angle 30 degrees shows the effective separation control. The valve while operating with this combination of condition is effectively in not only controlling the separation but also removing it completely from the flow. Under this optimum conditions there is no separation observed except at 0.03 sec which was a very thin portion as shown in fig [21(c)]. The pulse of the jet is quite energetic that it didn't allow the separation to grow and remove it completely from the flow as shown by the fig [21(g) to (i)].

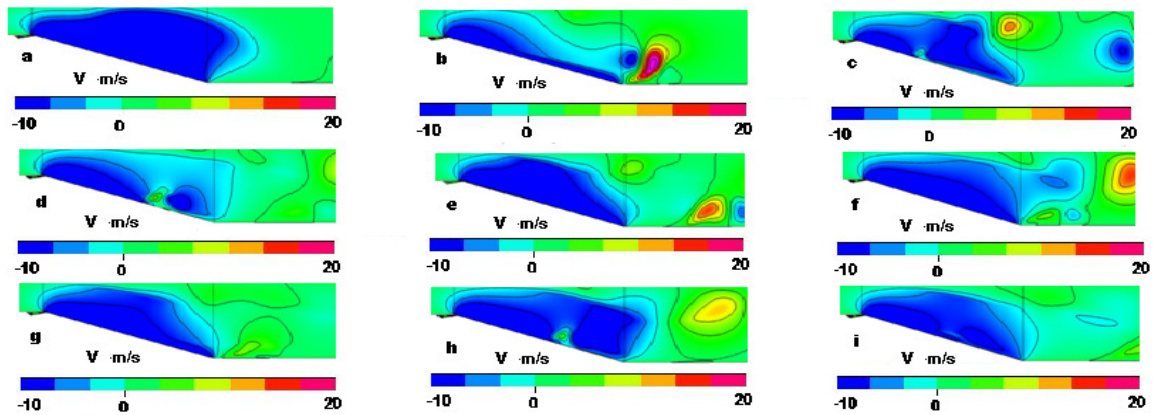


FIGURE 22: Velocity v traces at pitch angle=30, VR=3and 80HZ (a) Time=0.01 sec, (b) Time=0.02 sec, (c) Time=0.03 sec, (d), Time=0.04 sec (e) Time=0.05 sec, (f) Time=0.06 sec, (g) Time=0.07 sec, (h) Time=0.08sec (i) Time=0.1sec

The trend of velocity contour shows the effect of micro pulse Jet in separation control by the pulse of the jet operating at above mentioned parameters. The valve is operating with an optimum set of test condition in order to reduce and remove the separation completely from the flow as shown by the fig [22].

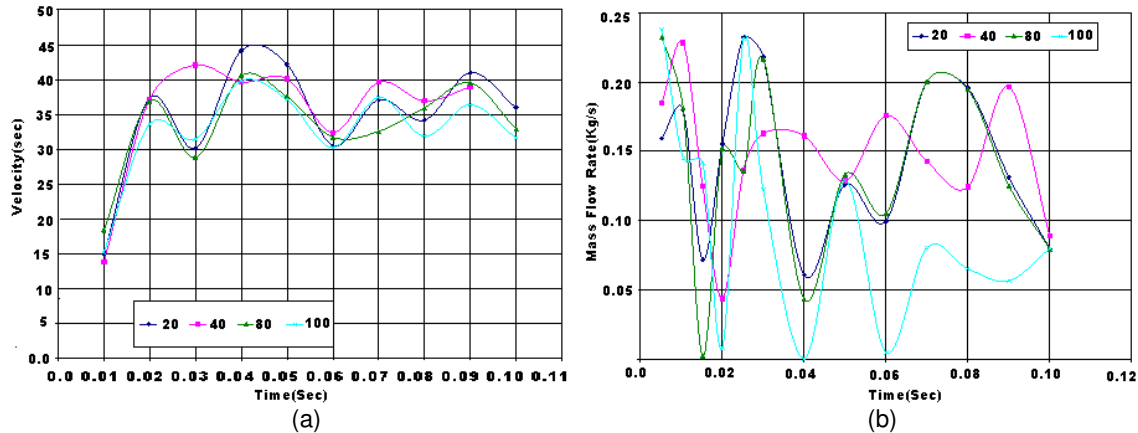


FIGURE 23: Plots at (VR=3, $\alpha=30$) (a) Velocity plots at 72 % ramp length, (b) Mass flow rate requirement at various frequencies of 20, 40, 80, 100 HZ

The velocity plots indicate an ideal and optimum condition of the test parameters for the Micro Pulse Jet to control the flow separation effectively. The velocity at the 72 % downstream length of the ramp is shown by the fig [23(a)] and indicates that the velocity magnitude is positive throughout, reflects there is no existence of the separation in the flow. These results also show that the micro jet valve is operating at velocity ratio 3 with pitch angle 30 degrees at any frequency of the pulse is controlling the flow separation very effectively as compare to all the previous numerical results analyzed for the valve at pitch angle 45 degrees.

Same observation is found in all the test cases that mass flow rate requirement for controlling the flow separation in micro pulse jet is significantly reduce as compare to the steady jet case. The mass flow rate is reduce as compare to the same case at pitch angle of 45 degrees but higher than the valve operating at velocity ratio of 2 with same pitch angle. The trend of mass flow rate is shown in fig [23(b)].

8. SUMMARY OF RESEARCH WORK

A comprehensive numerical study has been done to show the effectiveness of the conceptual modeling of Micro Pulse Jet to control the flow separation. The Micro Pulse jet valve is modeled through periodic Inlet boundary condition with the help of mathematical function. The basic purpose of the valve is to suppress the separation by creating the rotating vortex which enhances the mixing between the energetic free stream flows with the separated boundary layer flow through the pulse of the jet. The results presented in the paper clearly indicate the Micro pulse jet is capable of reducing the flow separation in a severe separated flow.

The other finding of this paper is that the conceptual model of Micro Pulse Jet can generate the jet up to Mach 0.5 with only 20 % pressure ratio i.e. the total pressure is more than the atmospheric pressure.

In order to validate the effective control of separation by Micro Pulse Jet a 2-D ramp with 20 degrees of divergence is selected. The lower wall of the ramp is diverged enough to create the adverse pressure gradient and hence having a severe separated permanent region in the flow. The unsteady frequency of the flow is estimated by introducing various points in the separated region and then from the unsteady behavior the frequency of unsteadiness is calculated. A jet of 2 mm width is introduced at the upstream of divergent portion and flow is suppressed completely by the pulse of the jet as shown in the results. The jet amplitude is varied by the pressure ratio which ultimately controlling the velocity ratio (V_j / V^∞), ranging from 0 to 5 and the unsteady frequency is changed from 0 to 100 HZ.

The Optimum Condition for the Control of Flow Separation Through Micro Pulse Jet is estimated by analyzing four different test configurations. These configurations can easily be classified into two groups according to the Pitch angle i.e.45 and 30 degrees and then further classified each group in two sub groups according to the velocity ratio i.e. 2 and 3.

The results can be summarized as follows

- The velocity contour plot suggests that the flow quality and the separation for the valve operating at velocity ratio of 3 with pitching angle of 45 degrees at 80 HZ is better than the valve operating at velocity ratio 3 with pitching angle of 30 degrees at 80 HZ.
- The stream traces plots indicate that the flow separation is reduce when the valve is functioning at velocity ratio 3 with pitching angle of 45 degrees as compare to the flow at pitch angle of 30 degrees with velocity ratio of 2, but the separation is not removed completely. For a qualitative analysis the valve is reducing 50 % more separation as compare to the condition at velocity ratio 2.3 and pitching angle of 45 degrees at 80 HZ.
- The data of the velocity for the certain points in the computational domain suggest that the flow control by the valve at pitch angle of 45 degrees is better than the valve operating at velocity ratio 2 and pitching angle value of 30 degrees. Though the velocity plot for velocity ratio of 3 has the positive value throughout the simulation as compare to the velocity ratio 2 clearly suggest a good control on separation but still there is some separation as the value of velocity ratio 3 is touching almost zero velocity line as shown by the following figure [24].

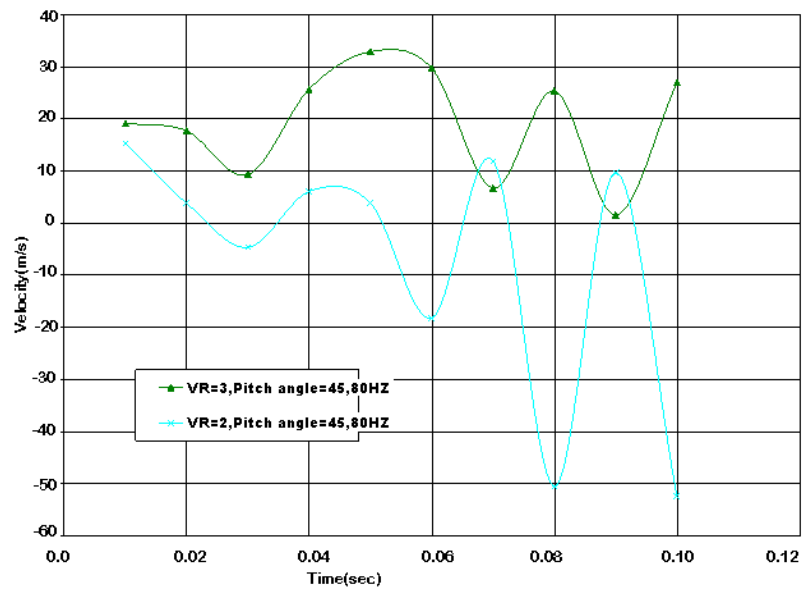


FIGURE 24: Comparison of velocity plots at different test configuration (A)

- The mass flow rate requirement for controlling the flow separation is almost 50% less than the valve while operating at velocity ratio of 2 and pitching angle 45 degrees at 80 HZ but the mass flow requirement of unsteady jet is significantly reduce than the steady jet as shown in following figure[25].

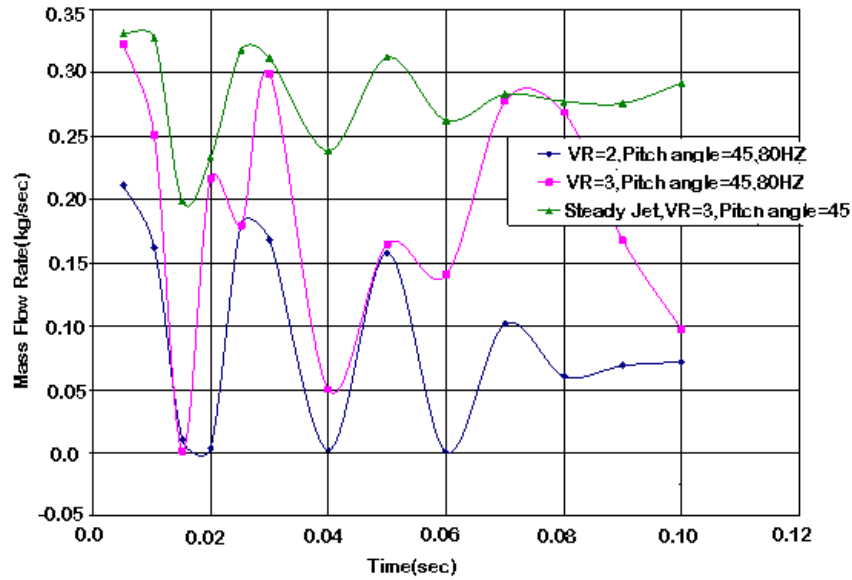


FIGURE 25: Comparison of Mass flow rate at test configuration (A)

- The velocity contour indicates better results of the valve operating at pitch angle 30 degrees, velocity ratio 3 at unsteady frequency of 80 HZ than the valve operating at velocity ratio of 2.
- Flow visualization for the stream traces indicate better results of the flow in controlling the flow separation for the pulse of the valve while operating at $\alpha=30$, VR=3 and frequency of 80 HZ as compare to the valve operating at velocity ratio 2. For the qualitative analysis it reduces the flow separation almost 100 % as compare to the case with velocity ratio of 2.
- The velocity data of the point in the computational domain suggests that there is no separation zone for the test parameters of the valve operating at 30 degrees of pitch angle, velocity ration 3 and unsteady frequency 80HZ because the velocity magnitude is positive as compare to the valve operating at velocity ratio 2 having negative velocity as shown in the fig [26].

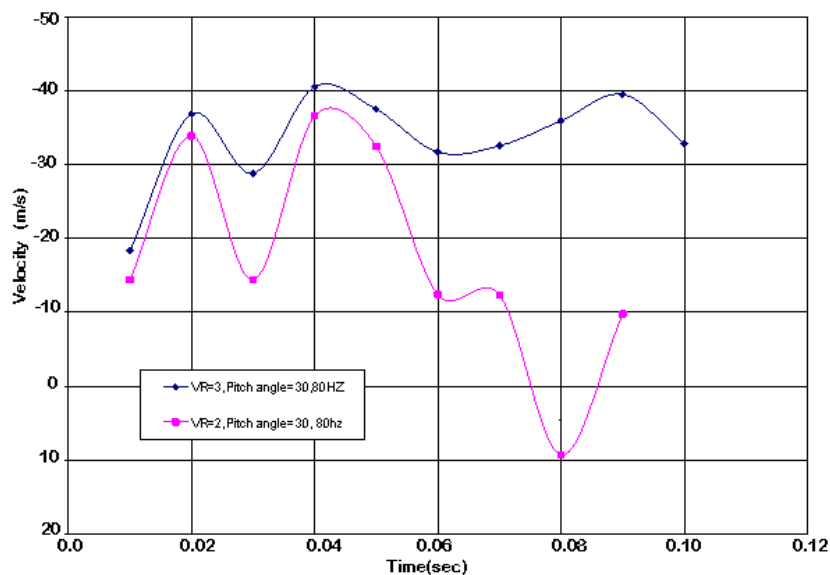


FIGURE 26: Velocity plots comparison for the test configuration (B)

- The mass flow rate requirement for the test case with pitch angle 30 degrees, velocity ratio 3 with pulsing frequency of 80 HZ is almost 50 % more than the valve operating at velocity ratio 2. The mass flow rate for the unsteady jet significantly reduced for the unsteady test cases as shown in the fig [27].

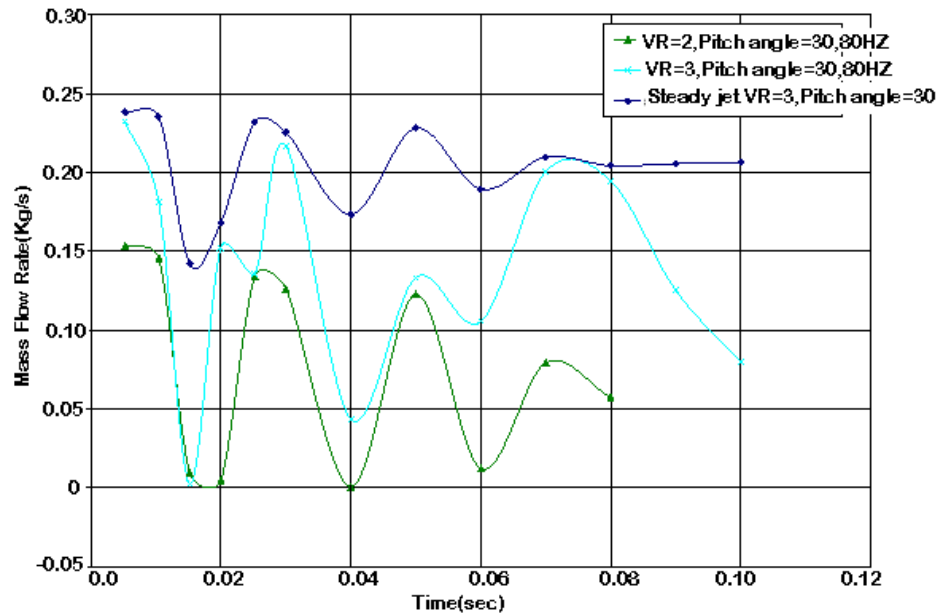


FIGURE 27: Comparison of Mass flow rate at test configuration (B)

From the flow visualization and comprehensive numerical analysis suggest that the flow separation is completely removed by the valve with the optimum test parameters setting of velocity ratio 3, pitch angle of 30 degrees with the unsteady frequency equal to 80 HZ. This optimum frequency is almost double from the calculated unsteady frequency for the base line case.

So on the bases of the results it is quite clear that the Micro Pulse Jet is completely feasible. Due to the compact size of the valve and less power requirement, it can be easily accommodated in any system for controlling the flow separation either in an external Aerodynamic application e.g. in aircraft wing, MAU'S wing or in canard or high lifting device or in an internal flow like in turbo machinery etc.

9. CONCLUSION

The basic aim of this paper is to describe the new conceptual approach of controlling the flow separation by Micro Pulse Jet. The effectiveness of this new method is validated by the numerical modeling of the valve by periodic Inlet boundary condition. The key finding of this research work describe as follows

- Practical designing of Micro Pulse Jet is completely feasible.
- In order to control the flow separation, various combinations of test configuration were analyzed and it was found for effective control of flow separation the velocity ratio, Pitch angle and the pulse frequency play an important role.
- It was investigated in all the test cases that the mass flow rate requirement for controlling the flow separation is reduced significantly for the unsteady jet as compare to steady jet.
- The optimum condition for Micro pulse Jet operating at pitch angle 45 degrees must have velocity ratio 3 with unsteady frequency of 80 HZ

- It can be concluded from the analysis that when the unsteady jet is operating at pitch angle 30 degrees, it should have velocity ratio 3 and unsteady frequency of 80 HZ.
- The overall optimum set of test parameters for the valve in controlling the flow separation completely, should operate at the velocity ratio 3, pitch angle 30 degree and pulse frequency of 80 HZ.
- The optimum pulse frequency is almost 2 times from the unsteady frequency which was calculated in base line reference case.

The overall efficiency of Micro pulse Jet can be easily compared with the other methods for controlling the flow separation in the following manner

- The working principal of Micro Pulse Jet is very simple and comparable with the other active flow techniques in the form of Pulsed Jet actuator in which there must be an external source for producing the pressure gradient across the valve instead of using the existing pressure difference as in case of Micro pulse Jet.
- As there is no external source is required in Micro Pulse Jet for creating the pressure difference which reduces the complexity of the system and having low value of the parasite drag as compared with the other active flow control techniques.
- The efficiency of the valve is higher as compare to other passive flow control methods like in VGS and Micro VGS due to the timely action of control for suppressing the separation in the flow.
- The jet of higher velocity can easily achievable in compact and small configuration of the Micro Pulse Jet valve as compare to zero net mass flow technique (SJA) and tangential blowing and suction method.

Acknowledgement:

This research work is conducted by the College of Energy and Propulsion Engineering (CEPE), Nanjing University of Aeronautics and Astronautics (NUAA) China, under the supervision of Professor Huang Guoping.

10. References

1. H. Shan a, L. Jiang , C. Liu , M. Love and Brant Maines, "Numerical study of passive and active flow separation control over a NACA0012 airfoil", *Computers & Fluids* 37 (2008) 975–992.
2. K. McManus, H. H. Lengner, , and S. J. Davis , "Pulsed Vortex Generators Jets for Active Control of Flow Separation", AIAA 94-2218.
3. D. A. Compton, J. P. Johnston, "Streamwise vortex production by pitched and skewed jets in a turbulent boundary layer," *AIAA J.* 30 (3) (1992) 640–647
4. J. P. Johnston, M. Nishi, "Vortex generator jets—a means for flow separation control," *AIAA J.* 28 (6) (1990) 989–994
5. Aman, K. B. M. Q., Bar Sever, A., Mangalam, S. M. "Effect of acoustic excitation on the flow over a lower airfoil". *J Fluid Mech.* 182, 127–148 (1987)
6. J. Gilarranz, L. Traub, and O. Rediniotis, "Characterization of a compact, high-power synthetic jet actuator for flow separation control," *AIAA Paper*, no. 2002-0127, pp. 1–28, 2002.
7. M. Amitay, D. Smith, V. Kibens, D. Parekh, and A. Glezer, "Aerodynamic flow control over an unconventional airfoil using synthetic jet actuators" *AIAA Journal*, vol. 39, pp. 361–370, 2001.
8. C. Lee and D. Goldstein, "Two-dimensional synthetic jet simulation," *AIAA Journal*, vol. 40, no. 3, pp. 510–516, 2002
9. L. Kral, J. Donovan, A. Cain, and A. Cary, "Numerical simulation of synthetic jet actuators"

AIAA Paper, no. 97-1824, pp. 1–13, 1997.

10. M. Amitay, M. Horvath, M. Michaux, and A. Glezer, "Virtual aerodynamic shape modification at low angles of attack using synthetic jet actuators," AIAA Paper, no.2001-2975, pp. 1–11, 2001.
11. K. L. Kudar & P. W. Carpenter, "Numerical Investigation and Feasibility Study of a PZT-driven Micro-valve pulsed-jet Actuator," *Flow Turbulence Combust* (2007) 78:223–254, Received: 21 April 2006/Accepted: 24 October 2006 /Published online: 2 March 2007
12. C Warsop , M Hucker & A J. Press & Paul, "Pulsed Air-jet Actuators for Flow Separation Control", *Flow Turbulence Combust* (2007) 78:255–281
13. K.McManus, A.Ducharme, C.Goldey, and J.Magill , "Pulsed Jet Actuators for Suppressing Flow Separation", AIAA 96-0442
14. K.McManus, H.H Lengner, , and S.J Davis , "Pulsed Vortex Generators Jets for Active Control of Flow Separation", AIAA 94-2218

HW/SW Partitioning Approach on Reconfigurable Multimedia System on Chip

Kais Loukil

*CES Laboratory/ENIS National Engineering School
University of Sfax
Sfax, 3062, Tunisia*

kais_loukil@yahoo.fr

Nader Ben Amor

*CES Laboratory/ENIS National Engineering School
University of Sfax
Sfax, 3062, Tunisia*

nader.benamor@enis.rnu.tn

Mohamed Abid

*CES Laboratory/ENIS National Engineering School
University of Sfax
Sfax, 3062, Tunisia*

mohamed.abid@enis.rnu.tn

Abstract

Due to the complexity and the high performance requirement of multimedia applications, the design of embedded systems is the subject of different types of design constraints such as execution time, time to market, energy consumption, etc. Some approaches of joint software/hardware design (Co-design) were proposed in order to help the designer to seek an adequacy between applications and architecture that satisfies the different design constraints. This paper presents a new methodology for hardware/software partitioning on reconfigurable multimedia system on chip, based on dynamic and static steps. The first one uses the dynamic profiling and the second one uses the design trotter tools. The validation of our approach is made through 3D image synthesis.

Keywords: Partitioning, Design Trotter, Profiling, Reconfigurable System.

1. INTRODUCTION

Today's demanding consumer multimedia applications has created new challenges for system on chip (SoC) developers. Due to their complexity, they require high performance architectures. Their integration in a portable and battery operated system impose stringent constraints about energy consumption and final cost. This makes that dedicated architectures the best choice a priori for their integration. This limits the flexibility of the final product which is an important feature for multimedia systems. Indeed, media applications are often changing due to the norm evolution itself (from MPEG2 to MPEG4 to H.264). The same application in the same norm can be executed with different modes and parameters values. For example MPEG4 can be executed with simple or main profile. On the other hand, the mobility of the target system imposes flexibility that permits to the system the use of different norms depending of its location (Bluetooth or Wifi for example). The download of new services according to the context variation. As those media systems are rapidly evolving, the time to market became more and more shorter witch impose reuse concept. All those constraints make flexible architectures an ideal architectural choice for multimedia systems provided that will be enhanced with powerful multimedia capabilities. Several industrials propose processors and platform for multimedia applications. Those architectures are optimized for the application that were designed for (typically video treatment) and are not necessarily sufficient powerful for incoming or other applications (such as 3D image synthesis).

Some approaches of joint software/hardware design (Co-design) were proposed in order to help the designer to seek an adequacy between application and architecture that satisfies the many design constraints (cost, performance, surface, consumption, flexibility...). Currently, with the rapid evolution of reconfigurable architectures like FPGA, new co-design techniques must be investigated due to the variability of the mobile system. In this paper, we present a new approach for multimedia system design based on mixed static and dynamic strategy.

This paper is organized as follows: the first part is devoted for the presentation of the state of the art and positioning of our work compared to the community. The second part describes our approach for HW/SW partitioning. The third part presents the validation through the 3D image synthesis. Finally, we conclude about our work and present some perspectives.

2. STATE OF THE ART

The goal of profiling is to analyze the program statically and/or dynamically in order to determine relevant information for design exploration, hardware/software partitioning and parallelization. Multiple profiling techniques are developed to analyze the input application behavior for different criteria such as performance, memory, power consumption etc[AP].

The methods proposed in the literature can be classified in three categories: statics, dynamic and mixed [1].

Static method estimate of performance of a design solution using static analysis of an input specification, (example: analyze ways in a specification). Dynamic method permit the measurements of performance of a solution are the result of a dynamic analysis of a specification (suing simulation for example).

Mixed Dynamic/static method: It is the use of some elements of the two preceding approaches for the analysis of performance of a solution [12]. The static approaches are in general very fast, but they present an average precision considering the distance which separates the implementation and the specification [1]. The dynamic approaches are more precise but slower considering the time taken for obtaining both simulation model and time [13]. These disadvantages limit the use of these two methods. The majority of the existing tools for estimation use mixed methods to profit from the advantages of the two preceding methods.

The method described in [3] is based on static analyzes (calculation of the execution time based on the assembler code) and dynamic (profiling). Whereas in [5] [4], they calculate the metric separate ones for the software, the hardware and the communication. Then, they use these metrics in particular equations. For the software part, they calculate the execution time in the worst case by using techniques of analysis of way. [18] [6] estimates the performance by using the execution time techniques on low level for the software, the hardware and the communication. The authors of [7] tackle the problem from a generic point of view. They analyze, on the level system, the interaction between the various processes by giving best and the worst time for each one of them. Then, on the basis of an acyclic graph representing the dependences of data between the processes, they calculate the execution time, in the worst case, for the whole system. In [2],[9] they describe a method of mixed static/dynamic estimation. It is made in two stages. The first one is Pre-estimate: A profiling of the description of the system is carried out to obtain execution times for various levels (process, basic block, communication).

On line estimation: The results obtained during the phase of pre-estimate are used in complex expressions for the calculation of the total performance of the system.

The majority of these tools offer a good estimate for the software part; but, for the hardware part, we always finds values considered different from the actual values: what influences the estimate of the execution time of the complete system considering the distance which separates the specification from the system of the hardware implementation. In more quoted work are based on estimation techniques by high level abstract analysis (analyzes critical ways).

Make tradeoff between the offered criteria. In our methodology, we combine both static and dynamic approaches for efficient profiling tool in terms of accuracy and speed for hardware/software partitioning. During the profiling phase, relevant execution and data storage information are collected. In addition, preliminary estimations of the hardware and the software costs of the application's kernels are performed.

3. APPROACH

The main goal of hardware/software co-design is to shorten time to market while reducing the design effort and costs of designed products. Moreover, the increasing heterogeneous nature of embedded system platform and application make necessary a good hardware/software partitioning and optimization. Design Space Exploration of embedded system allows rapid performance evaluation of different design parameters and application hardware/software partitioning.

In our work we use two steps methodology Figure 1: profiling and a static analysis using the Design Trotter environment.

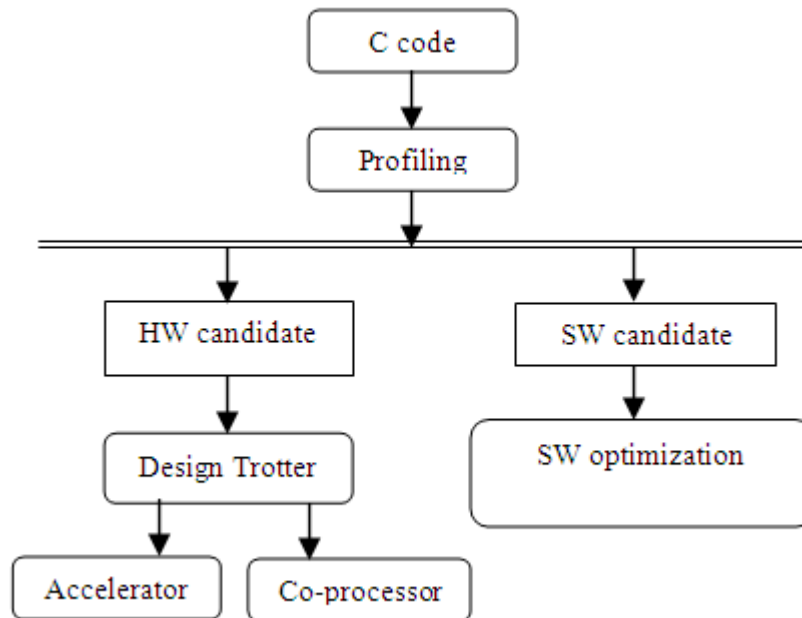


FIGURE 1: Proposed approach

3.1 Profiling

It is obvious that a hardware task is carried out more quickly than software. Thus to accelerate the treatment of a task it is advised to implement it in the form of HW accelerator. In order to determine which part of the application must be optimized of speed of execution, we chose a dynamic analysis of the application software.

Dynamic profiling is a performance analysis technique that measures the behavior of a running program particularly measuring the frequency and duration of function calls. This investigates the program's behavior using information gathered as the program runs [AP]. The output is a stream of recorded events (a trace) or a statistical summary of the events observed (a profile). Dynamic profiling involves obtaining the execution time and percentage call of various functions. This gives us an idea of where the processor is spending most of its time. Dynamic analysis is performed with executing programs. The most called functions are the privileged candidates for hardware implementation. Those HW candidates are then analyzed using the Design Trotter codesign tool.

3.2 Design Trotter tool

The aim of this analysis is the characterization of the first step candidates to detect if they are suitable for HW acceleration. A often called function with many control structure (like while loop) is not suitable for HW acceleration. Functions with intrinsic parallelism are also not suitable for HW accelerations.

Design Trotter (DT) is a set of cooperative tools which aim at guiding embedded system designers early in the design flow by means of design space exploration, as summarized in Figure 2. It operates at a high-level of abstraction (algorithmic-level). Firstly the different functions of the applications are explored separately. For each function, the two first steps (presented in

this paper) include the construction of the graph (HCDFG model) and the characterization by means of metric computations. Then a scheduling step, presented in [10] is performed for all the data-flow graphs and loop nests within the functions. The design space exploration is performed by means of a large set of time constraints (e.g., from the critical path to the sequential execution). Finally, the results are combined to produce trade-off curves (number of resources vs. number of cycles). The scheduling process offers different options including the balance between data-transfers and data-processings and the use of loop unrolling to meet time constraints.[9]

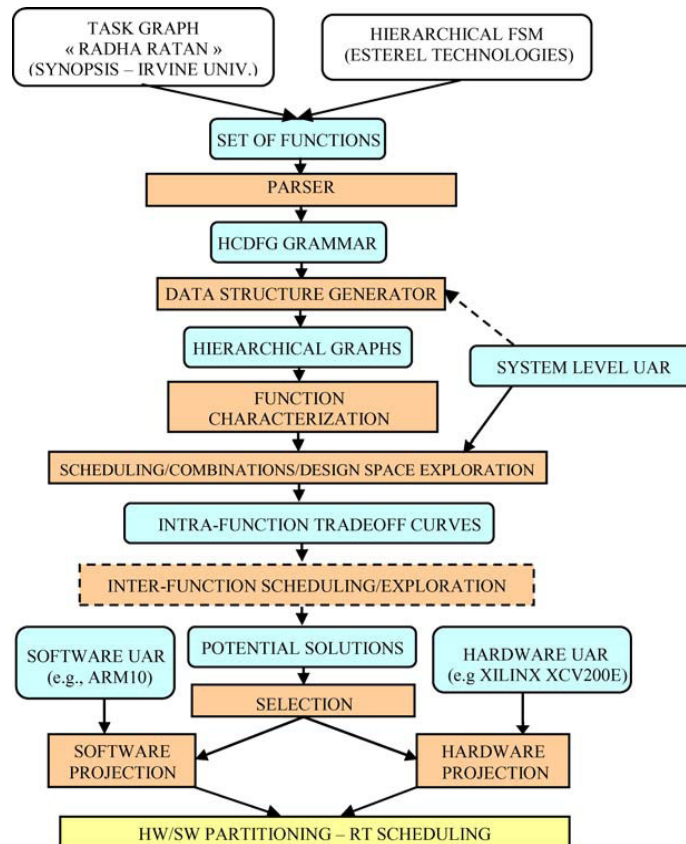


FIGURE 2: Design trotter tools

The entries of the environment Design Trotter are appeared as functions described in C high-level language or using the HCDFG model. (Hierarchical and Control Data Flow Graph) Each C function of the specification is a node at the top level of the hierarchical control and data flow graph (HCDFG). A function is a HCDFG. A HCDFG is a graph that contains only HCDFGs and CDFGs. A CDFG contains only elementary conditional nodes and DFGs. A DFG contains only elementary memory and processing nodes. Namely, it represents a sequence of non-conditional operations. There are three kinds of elementary (i.e. non hierarchical) nodes of which the granularity depends on the architectural model: a processing node represents an arithmetic or logic operation. A memory node represents a data transfer (memory operation). Its parameters are the transfer mode (read/write), the data format and the hierarchy level that can be fixed by the designer. A conditional node represents a test operation (if, case, loops, etc.) [10]. In our work, we use the “function characterization” module of the DT tool. Four metrics are defined for function orientation characterization. : γ (Parallelism Upper Bound Metric), MOM (Memory Orientation Metric) and COM (Control Orientation Metric).

TABLE 1: METRIC DEFINITION

Metric definition		
Metric name	Type of graph	Formula
γ	General definition	$\gamma = \frac{\text{Nb of global memory accesses and processing operations}}{\text{Critical Path}} \quad (1)$
γ	IF graph	$\gamma = P_{\text{true}} \frac{\text{Nop}_{\text{true}}}{\text{CP}_{\text{true}}} + P_{\text{false}} \frac{\text{Nop}_{\text{false}}}{\text{CP}_{\text{false}}} + \frac{\text{Nop}_c}{\text{CP}_c} \quad (2)$
γ	Combination of sequential graph	$\gamma_{\text{equivalent}} = \frac{\sum_i^{\text{total subgraphs}} \text{Nop}_i}{\sum_i^{\text{total subgraphs}} \text{CP}_i} \quad (3)$
γ	Combination of parallel graph	$\gamma_{\text{equivalent}} = \frac{\sum_i^{\text{total subgraphs}} \text{Nop}_i}{\text{Max}_i\{\{\text{CP}_i\}\}} \quad (4)$
MOM	General definition	$\text{Mom} = \frac{\text{Nb of global memory accesses}}{\text{Nb of processing operations} + \text{Nb of global memory accesses}} \quad (5)$
COM	General definition	$\text{Com} = \frac{\text{Nb of test operations}}{\text{Nb of processing operations} + \text{Nb of global memory accesses}} \quad (6)$

For a DFG graph g is defined by formula (1) in Table 1. The critical path, noted CP, in a DFG graph, is the longest sequential chain of operations (processing, control, memory) expressed in terms of cycle number. CP is computed for each hierarchical level with a data and control dependency analysis. MOM metric is defined by the general formula (5) in Table 1. MOM indicates the frequency of memory accesses in a graph. MOM values are normalized in the interval. The closer to 1 MOM is, the more the function is considered as data-access dominated. Therefore, in the case of hard time constraints, some high performance memories are required (large bandwidth, dual-port memory, etc.) as well as an efficient use of memory hierarchy and data locality [11]. To calculate this metric, test operations, namely the following operators: $<$, $>$, $!=$, must be identified. COM is defined by the general formula (6) in Table 1. It indicates the appearance frequency of control operations (i.e. tests that can be eliminated at compilation time) in a graph. The designer can refer to this metric to evaluate the need for complex control structures to implement a function. For example functions with high COM values are most likely to better implemented on a GPP processor rather than on a DSP processor since, the latter is not well suited for control-dominated algorithms. It also indicates that implementing such functions in hardware would require rather large state machines.

4. VALIDATION

4.1 3D synthesis overview

The 3D pipeline is a whole of the necessary stages to the creation and the visualization of a 3D object. This chain is broken up into a whole of necessary operations to post a 3D object observed from a position and with a given orientation. The whole stages are presented in figure 3.

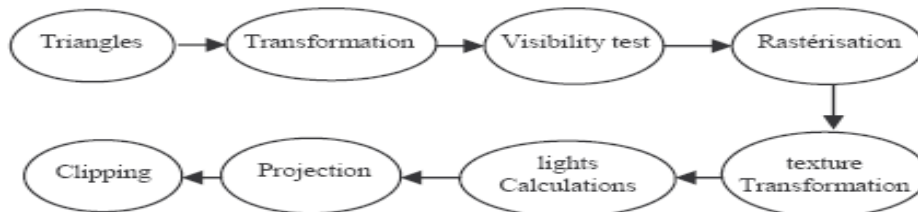


FIGURE 3: 3D graphic pipeline

Transformations: The different transformations consist on translations, rotations and homotheties of the triangles to convert them from their local reference marks to the total scene reference mark and then to the camera reference mark.

visibility test: The visibility test of a triangle is made to determine if it is visible or not.

lights calculations: The models of illumination, taking into account only the interactions between a surface and the source of light, determines the intensity of the color in a point.

textures transformations: This step makes it possible to transform textures before being applied to the triangle in the Rasterisation step.

Clipping: In this step, we eliminate the triangles which do not belong to the volume of sight and we cut out those which have visible parts according to their intersections with the sight volume.

Projection: The projection is the transformation which makes it possible to give the position of the point image on the plan starting from a point in the space.

Rasterisation: The rasterisation is the step responsible for transforming the 3D geometrical forms into pixels on the screen while giving a real aspect to the 3D object in question. In this part, we deal with the shade model.

The figure 4 shows the tasks graph associated with the 3D image synthesizes application. The entry of this graph is a set of local references of the various polygons summits that constitute the 3D object.

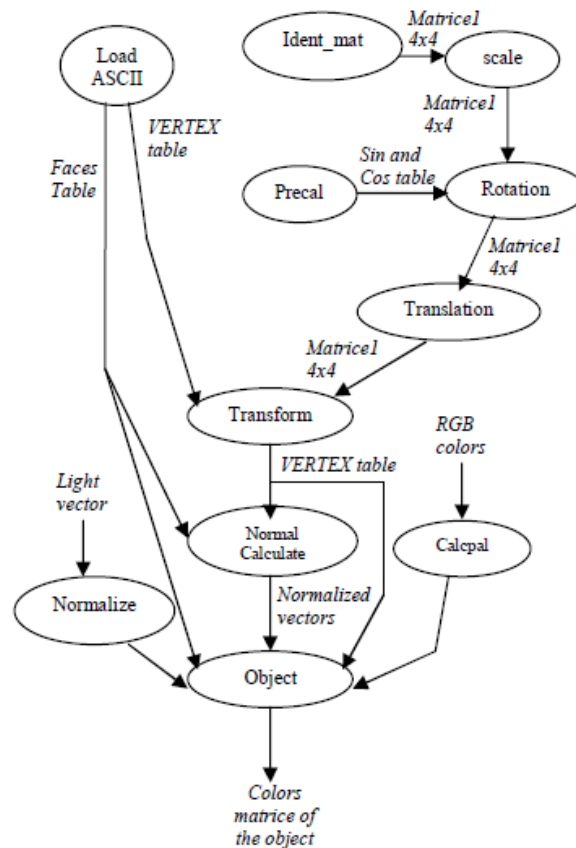


FIGURE 4: Task graph of the synthesis 3D application

4.2 3D Synthesis Application Analysis

To identify the critical (often-called) functions which require a hardware implementation, it is necessary to analyze the 3D synthesis application using profiling technique and high level complexity analysis to each function. As we plan the use of the NIOS embedded processor for the configurations set up, we adopt its associated profiling tool “NIOS IDE”. It has a “Performance Counter” that determines the different functions execution time, their percentage as well as the call number of each function. This will enable us to identify the critical functions requiring

hardware modules for their execution. Table 2 shows the profiling results of the synthesis 3D application. Using the task Graph in the figure 4, we can identify the most really most called functions. The most critical function is "Object_draw". We analyse them using the "Design Trotter" tool which enables to know more precisely their orientations.

TABLE 2: Profiling result of the 3D synthesis

Section	%	Time(sec)	Occurrences
Transform	6.03	26.875	360
Normal_Calculate	13.5	58.966	360
Translation	0.165	0.726	360
Load_ASCII	0.013	0.0566	1
Object_draw	77.6	340.79	360
Rotation	0.479	2.103	360
normalize	2.23	9.787	12960
scale	0.144	0.62963	360

The hardware candidates tasks are analyzed using a high level co-design tool called "Design Trotter" in order to better analyze their inherent parallelism and orientation (memory, treatment or control). Such analysis is useful to define the most suitable implementation for critical functions so that the application-architecture matching goal can be reached. For example, often-called functions with high inherent parallelism are ideal candidates for hardware accelerators. Critical functions with small local data exchange are ideal candidates for coprocessors. Design Trotter tool analyses of separate functions written in C language and computes three metrics. "Gamma" metric is used for inherent parallelism determination. MOM computes the ratio of data exchanges on the total operations executed by the function. COM metric computes the control operation (do while loops, test operations, switch tests ...) on the total operations executed by the function. Table 3 represents the results of the "Design Trotter" analysis.

TABLE 3: Results OF METRIC BY DESIGN TROTTER

Function	Gamma	MOM	COM
transform	3.8750	0.3939	0.000
Normal_Calculate	3.3244	0.6527	0.0425
Object_draw	1.2429	0.8298	0.0038

According to table 3, we note that the "transformation", "normal_Calculate", functions have a relatively high value of gamma; therefore they have an important average parallelism. "Object_draw" function has a high value of MOM metric and a low value of Gamma metric it is a candidate for implementation in coprocessor.

4.3 Architecture Design

Based system using the NIOS II processor and the AVALON bus figure5.

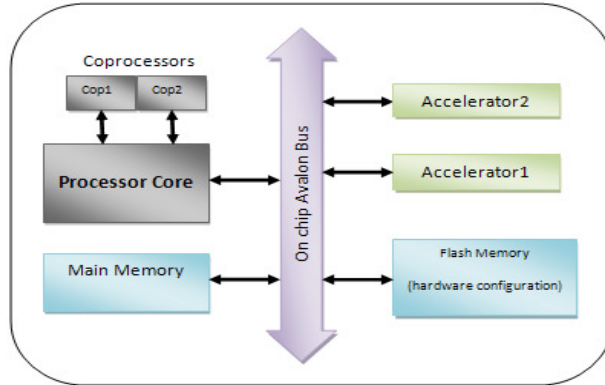


FIGURE 5: Hardware architecture

We realize a system composed of a NIOS II Processor that communicates with HW accelerator through the Avalon bus. The accelerator treats the data while the Avalon Bus supports the control and runs the data tradeoff between HW blocks and memories.

The accelerator communicates with Avalon bus using the “user defined interface”. It is a customizable interface that is automatically generated by the Altera design tool. It supports both slave and master accelerator may.

The slave accelerator (unlike the master one) cannot access directly to the memory to read / write data. It receives data sequentially from the main processor and sends back the result.

The master accelerator can reach the memory via a master port with a DMA mechanism. The HW accelerator receives base address of RAM from the processor via the slave port. It accesses in the external RAM to read data via the master port. Computations are done in combinatorial process. The accelerator accesses again in external RAM via the master port to write the results. This process is repeated until the end of computation. At the end the HW module sends an interruption signal (IRQ) to the processor. Slave accelerators are more ease to design but are slower.

Choosing a method or the other depends on the target application and the desired performance and HW resources occupation. If the processor has to do parallel processing master method is used if else we use the slave method, since it consumes fewer resources on the FPGA.

When the HW accelerator is fully tested, we conduct necessary modifications on the C original code to obtain a new functional code that supports the HW components.

4.4 Accelerator implementation

According to the result of profiling and design trotter tool, we chose to implement (calculates normal, scalar, vector, normalization and transformation) functions as hardware accelerators. For reasons of simplicity the function transformation was implemented using the master method, and other functions are implemented by the slave method.

The figure 6 shows the schematic block of the normal accelerator.

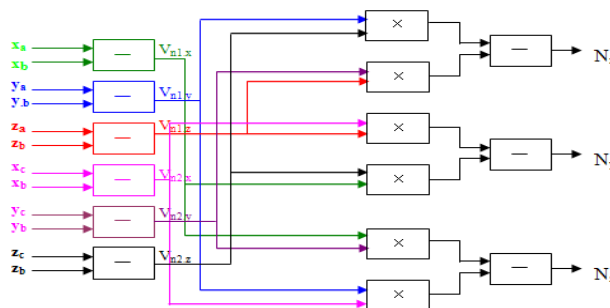


FIGURE 6: schematic block of the normal accelerator

The outputs of the normal calculate circuit can be redirected to the normalization circuit (figure 7) for normalizing the normal vector.

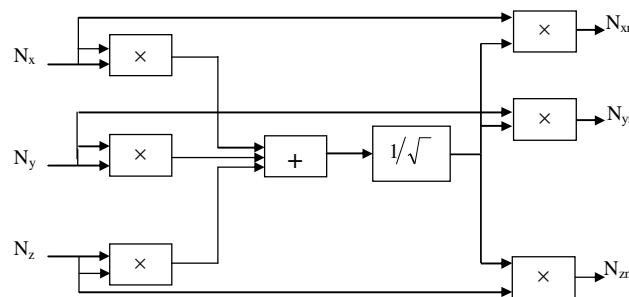


FIGURE 7: schematic block of the normalization accelerator

To ensure the communication between the accelerator and the Nios processor, an interface was developed. Figure 8 describes the overall interface with the signals. This interface consists of different signals I/O accelerators allow to communicate with the rest of the system through the bus Avalon. If we use a slave accelerator, all the master signals can be deleted.



FIGURE 8 : Schematic of the accelerator interface

The following table shows the used FPGA resources for each implemented hardware component. Table 4: ALUT consumed of Hardware component vaut mieux ajouter un pourcentage ou indiquer le total disponible sur le circuit.

Component	Total ALUT
CPU+MEM	11075
CPU+MEM+scal	11109
CPU+MEM+vector	11261
CPU+MEM+normalization	15513
CPU+MEM+normal	15793
CPU+MEM+coprocessors	15297
CPU+MEM+coprocessors+normal	19881
CPU+MEM+transformation	14873

4.5 Experimental results

According to the table 3, obtained by the prototyping phase, we notice that the “Object_Draw” function is the most favored with the hardware implementation. Whereas the results obtained by

design trotter, support the functions “Transformation” and “Normal_calculate”. The following table represents the profit of three functions implemented in hardware. We notice that each one of them has an influence over the total execution time of the 3D images synthesis application.

TABLE 5: execution time for 3d synthesis application executed with different architectures

	Execution time	Benefit %
Transformation SW Normal_calculate SW Object_Draw SW	556,032	0
Transformation HW Normal_calculate SW Object_Draw SW	539,742	3%
Transformation SW Normal_calculate HW Object_Draw SW	507,36	9%
Transformation SW Normal_calculate SW Object_Draw HW	400,954	28%
Transformation HW Normal_calculate HW Object_Draw SW	491,07	12%
Transformation HW Normal_calculate SW Object_Draw HW	384,664	37%
Transformation SW Normal_calculate HW Object_Draw HW	352,282	31%
Transformation HW Normal_calculate HW Object_Draw HW	335,992	40%

We note that if we use only the two functions “transformation” and “Normal_Calculate” in the form of hardware accelerator (result of design trotter) we attend 12% of the benefit, while the “Object_draw” function (result of profiling) offers a profit of 28%. In other hand, combining the two solutions offered by the two methods gives a profit of 40%.

5. CONCLUSION

This article deals with the problem related to the hardware/software partitioning of reconfigurable multimedia system on chip. We proposed a new method of HW/SW partitioning. Indeed, our method is based on a static/dynamic mixed approach. For the static part, we used the design trotter tool and for the dynamic part we used the dynamic profiling of the application.

We presented all the steps used for the validation of the method by using the environment of Altera and the 3D images synthesis application.

This method presents interesting results. However, it can be refined by taking account of the data exchanged between the tasks and of the parallelism with the level of the accelerator.

6. REFERENCES

1. A.Baghdadi, exploration et conception systématique d'architectures multiprocesseur monopuces dédiées à des applications spécifiques, thèse PhD, Mai 2002, TIMA France.
2. D.Gajski, F.Vahid, S.Narayan and J.Gong System-level Exploration with SpecSyn. Design Automation Conference, Juin 1998.
3. H.J.Eikerling, W.HARDT, J.Gerlack, W.Rosenstiel: A Methodology for Rapid Analysis and optimization of Embedded Systems. International IEEE Symposium and workshop on ECBS, D-friedrichshafen, Mars 1996
4. J.Grode and J.Madsen Performance Estimation for Hardware/Software Codesign using Hierarchical Colored Petri Nets. Proceedings of Jigh Performance Computing'98, in Special Session on Petri Net Applications and HPC, Boston, Avril 1998.
5. J.henkel and R. Ernst, High-level Estimation Techniques for usage in hardware/software codesign. Asia and south Pasific Automation Conference Yokohama, Japan, Fevrier 1998
6. J.Liu, M.Lajolo and A.Sangiovanni-Vincentelli, Software Timing Analysis Using HW/SW Cosimulation and Instruction Set Simulator. International Workshop on Hardware-Software Codesign, Mars 1998.
7. T-Y.Yen and W.Wolf, Communication Synthesis for Distributed Embedded Systems. International Conference on Computer-Aided Design,1995.
8. S. Rouxel Modélisation et Caractérisation de Plates-Formes SoC Hétérogènes : Application
9. Y.le moullec, J.P.Diguet, N. Ben amor, T.gourdeaux, and J.L.Philippe: Algorithmic-level Specification and Characterization of Embedded Multimedia Applications with Design Trotter. Journal of VLSI Signal Processing 42, 185–208, 2006
10. N. Ben Amor, Y. Le Moullecc, J. P. Diguet, J.L. Philippe, M.Abid: Design of a multimedia processor based on metrics computation. Advances in Engineering Software 36 (2005) 448–458
11. S. Wuytack, J.P. Diguet, F. Catthoor, H. De Man. Formalized methodology for data reuse exploration for low-power hierarchical memory mappings. IEEE Trans VLSI Syst 1998;6(4):529–37.
12. K. Bertels, G. Kuzmanov, E. M. Panainte, G. N. Gaydadjiev, Y. D. Yankova, V. Sima, K. Sigdel, R. J. Meeuws, and S. Vassiliadis, "Profiling, compilation, and hdl generation within the hartes project," in FPGAs and Reconfigurable Systems: Adaptive Heterogeneous Systems-on-Chip and European Dimensions (DATE 07 Workshop), April 2007, pp. 53–62.
13. A. Srivastava and A. Eustace, "Atom: a system for building customized program analysis tools," SIGPLAN Not., vol. 39, no. 4, pp. 528–539, 2004.
14. R. J. Meeuws, Y. D. Yankova, K. Bertels, G. N. Gaydadjiev, and S. Vassiliadis, "A quantitative prediction model for hardware/software partitioning," in Proceedings of 17th International Conference on Field Programmable Logic and Applications (FPL07), August 2007, p. 5.

A New Paradigm in User Equilibrium-Application in Managed Lane Pricing

Asapol Sinprasertkool

Research Associate/Department of Civil Engineering
University of Texas at Arlington
Arlington, 76019-0308, Texas, USA

asapol.sinprasertkool@mavs.uta.edu

Siamak A. Ardekani

Professor/Department of Civil Engineering
University of Texas at Arlington
Arlington, 76019-0308, Texas, USA

ardekani@uta.edu

Stephen P. Mattingly

Associate Professor/Department of Civil Engineering
University of Texas at Arlington
Arlington, 76019-0308, Texas, USA

mattingly@uta.edu

Abstract

Ineffective use of the High-Occupancy-Vehicle (HOV) lanes has the potential to decrease the overall roadway throughput during peak periods. Excess capacity in HOV lanes during peak periods can be made available to other types of vehicles, including single occupancy vehicles (SOV) for a price (toll). Such dual use lanes are known as "Managed Lanes." The main purpose of this research is to propose a new paradigm in user equilibrium to predict the travel demand for determining the optimal fare policy for managed lane facilities. Depending on their value of time, motorists may choose to travel on Managed Lanes (ML) or General Purpose Lanes (GPL). In this study, the features in the software called Toll Pricing Modeler version 4.3 (TPM-4.3) are described. TPM-4.3 is developed based on this new user equilibrium concept and utilizes it to examine various operating scenarios. The software has two built-in operating objective options: 1) what would the ML operating speed be for a specified SOV toll, or 2) what should the SOV toll be for a desired minimum ML operating speed.

A number of pricing policy scenarios are developed and examined on the proposed managed lane segment on Interstate 30 (I-30) in Grand Prairie, Texas. The software provides quantitative estimates of various factors including toll revenue, emissions and system performance such as person movement and traffic speed on managed and general purpose lanes. Overall, among the scenarios examined, higher toll rates tend to generate higher toll revenues, reduce overall CO and NOx emissions, and shift demand to general purpose lanes. On the other hand, HOV preferential treatments at any given toll level tend to reduce toll revenue, have no impact on or reduce system performance on managed lanes, and increase CO and NOx emissions.

Keywords: Managed Lanes, User Equilibrium, Pricing Policy

1. INTRODUCTION

Raising the capacity on congested corridors can be achieved geometrically by several means such as building a parallel elevated section or a tunnel along the corridors. Such approaches are generally very costly. Building completely new roads through congested urban corridors is also usually not viable due to a lack of right-of-way availability. As such, when new capacity is added, transportation planners use lane management strategies to manage flows on freeway networks

such as express lanes, high-occupancy-vehicle (HOV) lanes, high-occupancy-toll (HOT) lanes and managed lanes (ML).

Recently, managed lanes have become the primary option in attempts to reduce traffic congestion by many agencies. During the past few years, an improvement in traffic throughput is indicated when this lane management strategy is implemented [2], [4], [6], [7], [10], [15], [16], [26], [27]. This improvement results in reductions in travel time, fuel consumption and emissions and an increase in revenue [5].

The managed lane concept is suitable for implementing congestion pricing in corridors, for instance, a highway through a downtown area where adding new general purpose lanes (GPL) is not feasible. Instead, part of GPL is converted for a special use, called the managed lane. The TxDOT Research Monitoring Committee has given a definition of managed lane as "A managed lane facility is one that increases freeway efficiency by packaging various operational and design actions. Lane management operations may be adjusted at any time to better match regional goals." [18]. Unlike the conventional toll facilities, the managed lane offers the flexibility of adjusting the tolls and policies depending on the traffic demands and regional objectives.

In the past, all motorists were allowed to use toll facilities and were charged a fixed toll rate. Many economists suggested other approaches and constraints for establishing a toll rate [14]. For example, on uncongested roads, Sharp et al. [25] proposed a toll rate to be set equal to operating costs. Ragazzi [24] suggested that the operations-plus-capital-cost toll can subsidize the general lane users and taxpayers. As a result, these average-cost pricing models set a toll at a certain amount. This operating policy, which allows all vehicle classes to enter the toll road and pay a single rate, would simplify the operational requirements such as the toll setting, operating strategy, system complexity, operating cost, and technology deployment. However, allowing all travelers to access the toll lanes would eventually reduce the facility performance [28].

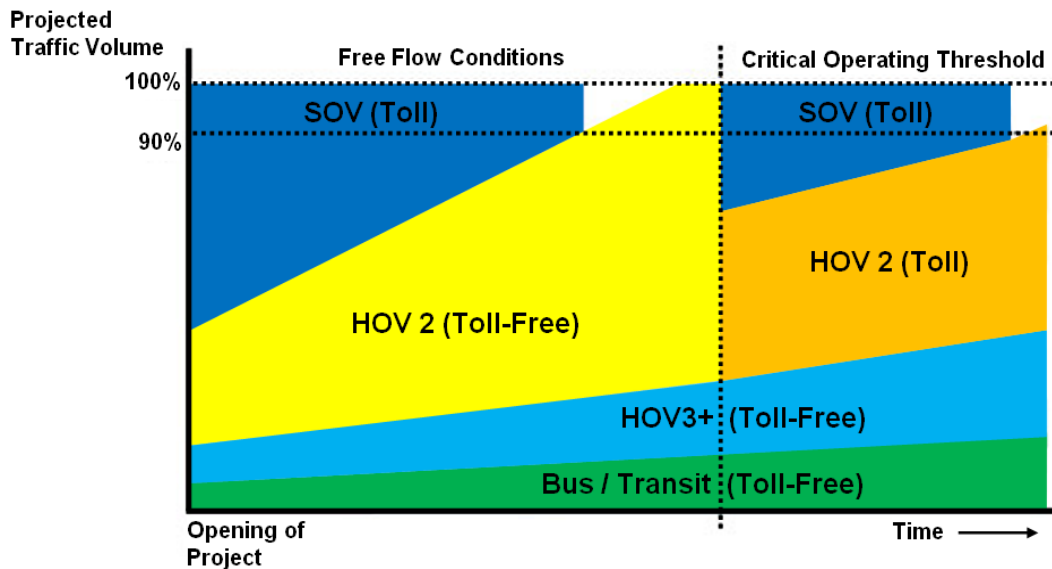


FIGURE 1: Life span of a managed lane.

Figure 1 [9] illustrates the HOV traffic growth over time on managed HOV lanes. The study shows that the projection of managed lanes users increases over time and eventually reaches the road capacity. In other words, a managed lane facility that operates by giving free access to HOV2+ and charging the SOV will eventually become congested due to capacity being exceeded by the HOV2+. As a result, a new policy is needed to solve traffic congestion on managed lanes. In this

case, a lack of ability to predict the potential users for each mode in the previous models make planning an optional operating policy difficult. Therefore, a pricing strategy should be capable of analyzing a plan that combines several toll policies among the modes. For examples, as proposed by some transportation agencies, HOV2 could be charged less than SOV; and HOV3+ could get free access [21]. If congestion problems continue on the corridor due to increases in the HOV2 volume, preferential access could only be provided to HOV3+ vehicles.

Due to the underutilization of the HOV facilities, toll pricing strategies have been implemented to utilize the excess capacity on the managed lane facility. However, a number of questions must still be addressed, including how many additional users should be allowed on managed lanes without reaching an unacceptable level of performance, and what should the toll value be corresponding to this level of additional users. These questions pose a challenge for toll pricing studies that attempt to predict the potential users based on toll charges.

Especially, the challenge increases for the facilities that operate using a variety of toll pricing scenarios. Examples may include allowing three classes of vehicles to access the ML and tolling them differently, as well as varying the toll amount by time of day and even day of week. Since flow rates on managed lanes are affected by dynamic toll rates, the pricing strategies become more complex and require a good understanding of changes in demand with respect to toll amounts. Even though previous pricing studies have proposed concepts for pricing the managed lanes to effect a desired level of demand, such concepts are not practical for facilities with various toll rates by class of vehicle and time of day.

Many of the previous studies incorporate an average value of time (VOT) to predict demands and tolls in their respective models. Parsons Brinckerhoff [23] uses the average wage rate to determine the VOT. In their study, the overall network travel time is optimized. Then, one third the average is used as the "low VOT" and one-half the average wage rate is used as the "base VOT" to generate the toll rates for toll roads in Washington State.

Li and Govind et al. [19] developed a tool for the evaluation of pricing strategies using users' willingness to pay as derived from survey data. Their study has shown that the willingness to pay differs among vehicle classes. Therefore, the assumption that all vehicle classes will have the same response at a certain toll rate seems unreasonable and thus does not allow an accurate prediction of the level of utilization of managed lanes.

He et al. [15] presents a model to assess the impact of the managed lanes on the I-394 corridor in Minnesota. The proposed model is an analytical multiclass stochastic dynamic transportation network model with Monte Carlo simulation and the method of successive averages. They assume a homogenous population of users, so the differences in VOT between the modes are not captured. To achieve an accurate prediction for various classes, the specific VOT distribution of each vehicle class must be used to predict the travel demands.

Wilbur Smith has conducted a toll revenue estimation study for the I-30 Reversible Managed Lanes in the Dallas, TX region [32]. Their estimates are based on the travel demand model databases developed under basic assumptions provided by NCTCOG and micro-simulation using VISSIM. After the model is built, the median VOT is used and several scenarios are examined to measure the impact of different toll rates.

The Toll Pricing Model (TPM-3.1) [1] is developed based on the concepts of price elasticity and the speed-flow-concentration model. TPM-3.1 uses the values for the percentage of users' willing to pay a certain toll based on data from "stated-preference" surveys. The software can do demand analysis based on one of two objectives. One objective is maintaining a minimum operating speed at a certain level while another is estimating the ML demand and the corresponding operating speed based on a pre-specified toll charge.

More recently, Yin and Lou [34] proposed two toll pricing approaches for managed lane facilities. The first approach applies the concept of a feedback control to determine a toll rate. This concept is easy to implement and requires only one loop-detector. The second concept learns the managed lane users' willingness to pay and determines the pricing strategies to meet the facilities' objectives. This approach requires two sets of loop-detectors to measure the flow rates to be used in calibrating the model parameters.

The objective of this research is to develop a simulation model for volume assignment between managed lanes and general purpose lanes as a function of toll charged for various vehicle classes. As a result, this study proposes a new paradigm in user equilibrium for managed lane networks in order to examine the various operating scenarios to meet operating objectives. A software package known as the Toll Pricing Modeler version 4.3 (TPM-4.3) is developed based on this framework for determining the dynamic toll rates.

This paper has a total of six sections. The next section proposes the concept of a new paradigm in user equilibrium and its components. Section 3 demonstrates a description of the VOT distribution estimates and inputs. Section 4 presents the details of a traffic demand model software package (TPM 4.3) that is developed based on this user equilibrium concept. Section 5 proposes a number of scenarios examined and shows their results. Finally, the conclusions and recommendations are presented in section 6.

2. A NEW PARADIGM IN USER EQUILIBRIUM

In traffic theory, Wardrop's first principle [31] applies to a network where all the used routes between an origin-destination (O-D) pair have the same travel costs under equilibrium conditions. In other words, no one can decrease their travel costs by unilaterally switching to another route. If time spent to drive on each route is the cost, all routes have an equal travel time under equilibrium. In a managed lane network, however, Wardrop's first principle cannot apply directly to determine the equilibrium flows because managed lanes are intended to have a lower travel time when compared to general purpose lanes. Therefore, a new user equilibrium paradigm for managed lanes is needed for incorporation into managed lane demand models.

2.1 Basic Concept and Components

Managed lanes are intended to provide a better level of service in the travel corridor. A typical managed lane travel corridor consists of two types of lanes: general purpose lanes and managed lanes. All travelers can use the general purpose lanes without paying tolls while the managed lanes are tolled with an occupancy restriction. However, the benefit of paying tolls is that the ML travelers are able to experience a higher speed (a lower travel time) relative to GPL travelers in the same travel corridor.

A new paradigm entails two important components: Cost of Time Saving (CTS) and Value of Time (VOT). When commuters travel on managed lane networks, they can choose to travel on either managed lanes or general purpose lanes. CTS is the amount per mile that motorists pay for saving one unit of time (usually measured in minutes) if they choose to take the managed lanes. Mathematically, CTS for the ML can be stated as:

$$CTS = \frac{\textit{Toll per mile}(\$)}{\textit{Travel Time Saving per mile}} \quad (1)$$

$$CTS = \frac{T}{[(L_{GPL} \times t_{GPL}) - (L_{ML} \times t_{ML})] / L_{ML}} \quad (2)$$

In Equation 1, travel time saving per mile is an average travel time saving per mile that motorists can expect to gain when they travel on managed lanes. In Equation 2, T is a managed lane toll per mile. L_{GPL} and L_{ML} are corridor lengths of general purpose lanes and managed lanes, respectively. Due to this variable (L), this concept can be utilized to examine an impact of toll

pricing on alternative toll versus free highway. Both facilities may have the same origin and destination with the different lengths. In this case, GPL inputs are used for the free highway and ML inputs are used for the alternative toll.

In Equation 2, t_{GPL} is the travel time spent for one mile if one chooses to travel on the general purpose lanes and t_{ML} is the travel time spent for one mile if one chooses to travel on managed lanes and pay a toll. The travel times are forecasted based on demand levels using the most common function called the Bureau of Public Roads (BPR) function [11]. If V is the volume per lane and C is the respective capacity per lane on either general purpose or managed lanes, the travel time (t) for each lane can be computed by the following equations:

$$t_{GPL} = 0.8 \times \left[1 + \left(\frac{V_{GPL}}{C_{GPL}} \right)^4 \right] \quad (3)$$

$$t_{ML} = 0.8 \times \left[1 + \left(\frac{V_{ML}}{C_{ML}} \right)^4 \right] \quad (4)$$

The second component is the Value of Time (VOT). VOT is the amount that users are willing to pay for one unit of time saved. In the current study, VOT data derived from previous studies in Texas [12], [20] are utilized. Those studies determine the VOT of the potential users of proposed managed lanes on the I-30 segment in Grand Prairie, Texas, between the cities of Arlington and Dallas. In general, the VOT distribution can be derived by using survey data or other methods to estimate the value of time of the toll users [3], [17].

2.2 Initial and Equilibrium States

The basic concept and components involved in this new paradigm are presented in the previous section. These primary components are the significant factors controlling the volume assignments on the managed lane networks. At an initial state, when a toll is not charged on the managed lanes, the volume is assumed to be equally assigned on both managed lanes and general purpose lanes. In this case, the cost of time savings (CTS) of corridors does not play a role. Later, when a charge is implemented on the tolled lanes, drivers who have a value of time (VOT) higher than the CTS will use the managed lanes in order to save time. On the other hand, drivers who have a VOT lower than CTS will not use the managed lanes and will switch to the general purpose lanes. Due to the change in travel time savings when a motorist switches from ML to GPL or vice versa, CTS is recalculated and compared with the remaining ML users' VOT. The decision rules can be stated as follows:

- Zero toll (CTS = 0) $\rightarrow V_{ML} = V_{GPL}$, where V_{ML} and V_{GPL} are the volumes of ML and GPL, respectively (Initial loading condition)
- CTS < VOT_i \rightarrow ML is the choice
- CTS \geq VOT_i \rightarrow ML is not chosen

An individual decision (i^{th}) based on their VOT will continually be made on the corridor until the network is stable, i.e., no one else will switch to another lane. At this point, the network's equilibrium is reached and the conditions are satisfied. Under equilibrium conditions, the users' VOT will be equal to the corridor's CTS, i.e., the condition of equilibrium becomes,

$$CTS = VOT \quad (5)$$

The general concept of this new paradigm is that *under user equilibrium conditions, traffic arranges itself in such a way that managed lane users' VOT are equal to or higher than the corridor's CTS and the general purpose lane users' VOT are lower than the corridor's CTS*. If homogeneous travelers (No distinction between vehicle classes such as SOV, HOV2, or HOV3+)

are assumed on the corridor, an average VOT distribution can be used to estimate the volume assignments. In reality, however, various vehicle classes are allowed to travel on the managed lane facility. To approximate the volumes at the equilibrium condition on the managed lane networks, the users' VOT distribution has to be defined for each vehicle class and incorporated into the model.

2.3 Incorporation of Multiple Vehicle Classes

In general, a managed lane facility can operate using different toll policies for multiple vehicle classes. In order to integrate multiple vehicle classes to the new equilibrium concept, additional procedures are developed as follows.

2.3.1 Value of Time Adjustment

Previous researchers [12] have found that the characteristics of the VOT distributions are different among the vehicle classes. Many studies estimate the value of time functions in term of price and travel time saving. These can be converted into a term of VOT and their respective population by applying a travel time saving (see section three). Thus, the proportions of population (a, b, c, \dots, z) based on their VOT can be generated for different vehicle classes (A, B, C, ..., Z) and VOT ranges (1, 2, 3, ..., n) as shown schematically in Table 1.

No.	VOT Range (\$/hr)	Vehicle Class A	Vehicle Class B	Vehicle Class C	...	Vehicle Class Z
1	$0 - VOT_1$	a_1	b_1	c_1	...	z_1
2	$VOT_1 - VOT_2$	a_2	b_2	c_2	...	z_2
3	$VOT_2 - VOT_3$	a_3	b_3	c_3	...	z_3
.
.
.
N	$VOT_{n-1} - VOT_n$	a_n	b_n	c_n	...	z_n

TABLE 1: Value of Time distributions

Theoretically, in the scenarios where tolls are charged differently for different vehicle classes, CTS must be separately calculated for each class due to unequal tolls (T) (Equation 2). However, the VOT distributions can be modified in order to utilize only one equilibrium equation by adjusting the percentages of population in each vehicle class. For example, if R_A is a ratio of toll rate of class A compared to the highest toll rate on the facility, an adjusted VOT percentage (a_{1Adj}) can be calculated as follows:

$$a_{1Adj} = a_1 \times R_A \tag{6}$$

Accordingly, a_{2Adj} , a_{3Adj} , ..., a_{nAdj} can be computed as follows:

$$a_{nAdj} = \left[\frac{(VOT_n \times R_A) - VOT_{k-1}}{VOT_k - VOT_{k-1}} (a_k) + \sum_{i=1}^{k-1} a_i \right] - a_{n-1Adj} \tag{7}$$

k is the range number where the result of $VOT_n \times R_A$ falls into this range.

After the percentages of population in each vehicle class are adjusted, as shown in Table 2, an equilibrium state can be calculated by using one equation (Equation 5).

No.	VOT Range (\$/hr)	Vehicle Class A	Vehicle Class B	Vehicle Class C	...	Vehicle Class Z
1	$0 - VOT_1$	a_{1Adj}	b_{1Adj}	c_{1Adj}	...	Z_{1Adj}
2	$VOT_1 - VOT_2$	a_{2Adj}	b_{2Adj}	c_{2Adj}	...	Z_{2Adj}
3	$VOT_2 - VOT_3$	a_{3Adj}	b_{3Adj}	c_{3Adj}	...	Z_{3Adj}
.
.
.
n	$VOT_{n-1} - VOT_n$	a_{nAdj}	b_{nAdj}	c_{nAdj}	...	Z_{nAdj}

TABLE 2: Adjusted Value of Time distributions

2.3.2 Vehicle Conversion

To simulate the behavior of drivers on the managed lane facility, the actual number of vehicles must be known. In this model, the vehicles in all classes are converted into passenger car equivalents. When the passenger-car-equivalency (PCE), the total travel demand, and the percent of vehicles in the mix are given, a number of vehicles in each cell can be computed by the following equation:

$$Z_n = Demand \times Percent\ of\ Class\ Z\ Vehicles\ in\ the\ Mix \times PCE_Z \times z_{nAdj} \quad (8)$$

where Z_n is the number of class Z vehicles in range n. This actual number of vehicles is computed by multiplying the percentage in each cell by the respective demand, vehicle mix percentage, and PCE. The resulting calculations are summarized in Table 3. For example, A_1 in this table would be the number of class A vehicles with a value of time range of $0 - VOT_1$ dollars per hour.

No.	VOT Range (\$/hr)	Vehicle Class A	Vehicle Class B	Vehicle Class C	...	Vehicle Class Z
1	$0 - VOT_1$	A_1	B_1	C_1	...	Z_1
2	$VOT_1 - VOT_2$	A_2	B_2	C_2	...	Z_2
3	$VOT_2 - VOT_3$	A_3	B_3	C_3	...	Z_3
.
.
.
n	$VOT_{n-1} - VOT_n$	A_n	B_n	C_n	...	Z_n

TABLE 3: Vehicle conversion

2.3.3 Equilibrium Reaching Concept

The previous sections describe how the VOT percentages of multiple vehicle classes are adjusted and converted into an actual number of passenger car equivalents. This process is key to preparing the data for the model simulation. In this model, when a toll is charged on the managed lanes, a random vehicle from the lowest VOT range among vehicle classes is shifted from the ML to GPL until the equilibrium is reached. This vehicle is randomly selected from a random vehicle class. Internally, CTS and VOT are recalculated, and an equilibrium state is verified every time that a vehicle is shifted from ML to GPL. In conditions where the final volumes

fall between the VOT ranges, the model linearly interpolates the VOT between the lower bound and upper bound based on the volumes. However, if all the vehicles in this VOT range are shifted to the general purpose lanes and equilibrium is still not reached, the model will proceed to the next VOT range and continues to shift vehicles from ML to GPL until the equilibrium condition (VOT=CTS) is reached. The equilibrium reaching procedure can be demonstrated as shown in Table 4.

Iteration No.	Total number of vehicles shifted to GPL			ML Volume	GPL Volume	CTS (\$/hr)		VOT (\$/hr)
	Vehicle Class A	Vehicle Class B	Vehicle Class C					
1	0 (0)	1 (1)	0 (0)	Demand (D) - 1	1	CTS ₁	>	VOT ₁
2	1 (1)	1 (0)	0 (0)	D - 2	2	CTS ₂	>	VOT ₂
3	1 (0)	2 (1)	0 (0)	D - 3	3	CTS ₃	>	VOT ₃
⋮	⋮	⋮	⋮	⋮	⋮	⋮	⋮	⋮
n	x (0)	y (0)	z (1)	D - (x+y+z)	x+y+z	CTS _n	=	VOT _n

Note: Vehicles shifted to GPL in each iteration are shown in ()

TABLE 4: Equilibrium reaching procedure

2.4 Application of Flow-Density-Speed (q-k-u) Model

Theoretically, drivers choose to travel on toll lanes when their VOT is higher than the CTS. These decisions directly impact the facility performance. To characterize the performance impact, the flow, density and speed relationship should be derived for the proposed facility. In this study, the result from a traffic flow model study by Nepal [22] is utilized for this purpose. He has found that the Drake [8] model has the best fit on the data collected for freeways in the DFW area. Therefore, the Drake Model is utilized to characterize the relationship between speed, flow, and concentration in the TPM-4.3. The general equation of the Drake Model is shown as Equation 9. However, the model parameters, -0.5 and 2, can also be calibrated through the model calibration process. If a model with new parameters shows a better result (higher R²), the parameter values can be changed, but is expected to be in the -0.5 and +2 range.

$$u = u_f e^{[-0.5(k/k_c)^2]} \tag{9}$$

Where:

- u* = speed (mph)
- u_f* = free flow speed (mph)
- k* = concentration (pcpmp)
- k_c* = concentration at capacity (pcpmp)

The concentration at capacity (*k_c*) can be computed by Equation 10 with the given parameters including capacity per lane (*q_c*) and free-flow speed (*u_f*). The Drake Model (Equation 9) can be calibrated by obtaining the concentration value from Equation 10 and a given free-flow speed. The Drake Model also yields Equation 11 to estimate the flow (*q*) as a function of speed and concentration. After a model is calibrated, the TPM-4.3 utilizes Equation 11 to calculate the speed from the flow or the flow from a given speed.

$$k_c = \frac{q_c}{u_f e^{-0.5}} \quad (10)$$

$$q = uk_c \sqrt{-2 \ln(u/u_f)} \quad (11)$$

In conditions where demand is higher than capacity but less than twice the capacity, speeds are expected to vacillate between $u = u_f e^{-0.5}$ (at $q = q_c$) and $u = 0$ (at $q = 2q_c$). In those cases, the TPM-4.3 model interpolates the speed between $u_f e^{-0.5}$ and zero for volumes between q_c and $2q_c$. For demands higher than $2q_c$, speed is considered to be zero due to the jam condition.

2.5 Solutions of Analysis Objectives

The operating objectives will vary from one facility to another. In this model, there are two operational objective options. One option is to estimate demands and operating speeds on ML and GPL for a proposed SOV toll charge. A second option is to estimate what the toll charge should be for a desired minimum operating speed on the ML facility.

2.5.1 Toll Objective

In order to measure the impact of toll policies on demand and operating speeds, various SOV toll charges can be examined in the toll objective module. In general, an initial toll rate may be specified based on an existing toll facility in the area. Then, other toll scenarios can be examined to assess the impact on measures of effectiveness such as speeds, emissions and toll revenues. Under this option, the model uses the specified VOT distribution to determine the operational outcomes based on the toll amount specified in the objective option. In conjunction with the facility and user information, the software can then estimate the volumes and speeds on the managed lanes and general purpose lanes. Revenue is accordingly calculated by multiplying the ML volumes by the respective toll rates. Finally, the speed and volume estimates for each respective lane type are used to estimate the expected emissions.

2.5.2 Speed Objective

A second option is to specify a desired average operating speed on managed lanes to determine the corresponding toll charge. For example, in the proposed scenarios, one of the operating objectives could be to maintain the minimum speed on the ML during peak period at 50 mph. This will limit the volume on ML so that the ML will maintain the speed at or above 50 mph. In this case, the model computes toll values, which maintain the desired average speed on the ML. The program output includes the toll amounts to be charged for each vehicle class, the expected volumes and speeds on the both lane types, and the emissions estimates for the travel corridor.

In this option, the model uses the VOT to determine the impact based on the minimum desired speed specified in the objective option. In conjunction with the facility and user information, the software can estimate the corresponding ML volume and GPL volume. The GPL speed can then be computed from the volume. As before, revenue is calculated by multiplying the volumes by the respective tolls. Finally, the speed and volume estimates for each respective lane type are used to estimate expected emissions.

2.6 Emission Estimations

Emission estimates, except for the SO₂ emissions, are based on a number of regression equations which use the average speed as the predictor variable [33]. The SO₂ emission rates are obtained from the information provided by vehicle manufacturers and built into MOBILE6.2 [29]. The regression models for CO, VOC and NO_x are developed from the MOBILE6.2 run results. The regression equations for CO₂ are developed based on tailpipe field data from on-board measurements in a passenger car. After the regression equation for passenger cars (SOV&HOVs) is generated, the equations for remaining classes are developed based on the multiplying factors used in MOBILE6.2. To improve emission estimates, future model can incorporate emission modules called Motor Vehicle Emission Simulator (MOVES) [30]. MOVES provides more accurate results and will replace MOBILE6 for all official analyses.

3. VALUE OF TIME DISTRIBUTION

This research was not focused on the accuracy of the value of time (VOT) distribution; however, in order to present a new paradigm for the managed lane networks, a known or assumed distribution must be used. This study used a VOT distribution derived from a stated-preference survey as part of a Texas Department of Transportation (TxDOT) project to study the travel choice behavior of single occupancy vehicle (SOV) travelers between high-occupancy-toll (HOT) lanes and free lanes [20]. This project surveyed a sample of potential HOT lane users in the Dallas-Fort Worth (DFW) area. A total of fifteen mode choice stated-preference questions based on hypothetical travel time savings and toll scenarios were utilized. The scenarios varied tolls at values of one, two, three, four and five dollars per ten miles and travel time savings at values of five, ten and twenty minutes. Each respondent was asked to choose between traveling on HOT lanes or free lanes; and those who chose to use HOT lanes would either pay the toll or convert to high occupancy vehicles (HOV).

Mattingly et al. [20] used logistic regression models to predict the value of a binary dependent variable from a set of independent utility variables. These models estimated the probability that a driver made a decision to travel on a HOT lane under a given price and travel time scenario. The dependent variables in this model were the choice of HOT lane or free lane. The critical variables (travel time savings and toll) for this distribution were derived directly from the stated-preference survey. The SOV binary logit model from the HOT lane study is shown in Table 5. The distribution described by this model is used for generating the VOT input for the SOV class.

Description	Estimated Value
<i>Constant</i>	0.139
<i>Travel Time Saving (mins/10 miles)</i>	0.128
<i>Toll (\$/10 miles)</i>	-0.785
-2Log Likelihood	6510.02
Chi-Square	1913.49
ρ^2	0.227
Percentage Correct Estimation	75.7
Percentage Correct Validation	78.8

TABLE 5: SOV binary logit model

The VOT distributions for the HOV class were derived from another TxDOT study [12]. The potential managed lane users in the DFW and Houston areas participated in an Internet survey conducted from May to July, 2006. The survey, tailored to two different cities, was available in both English and Spanish on separate DFW and Houston web sites. The survey asked respondents questions regarding their current travel patterns, reasons for choosing their travel modes, propensity towards managed lanes, as well as socio-demographic characteristics. An adaptive survey ensured that each respondent only received relevant questions. The policy scenarios were also randomized within the context of a previously selected structure for each respondent.

The research also used a stated-preference experiment to assess the decision-making behavior of drivers when choosing between the managed lane (ML) or general purpose lane (GPL). The study presented hypothetical travel time and toll scenarios through four stated-preference questions on mode choice. Each respondent was asked to choose one of six potential travel options: three involved traveling on managed lanes and three on general purpose lanes. The travel time and toll rate would vary in these six alternatives for each of the four scenarios presented to the respondents.

In the stated-preference questions, travel time savings were calculated depending on the input travel distance and randomly assigned speeds for both ML and GPL. A similar technique as for

SOV was used to analyze the VOT distributions for HOV [12]. Table 6 displays the results of the high occupancy vehicle with two occupants (HOV2) and high occupancy vehicle with three or more occupants (HOV3+) binary logit models. In general, except for travel distance, the significant variables included in the HOV2 and HOV3+ models are similar, namely the travel time saving and the toll amount.

Description	HOV2	HOV3+
Constant	-0.553	0.142
Travel Distance (mile)	0.011	-
Travel Time Saving (mins/mile)	1.042	0.868
Toll(\$/mile)	-7.132	-8.803
Number of Observation	860	212
-2LL only constant	1182.35	264.51
-2LL with variable	1075.99	247.70
ρ^2	0.091	0.064
Percent Correct	66.2%	70.8%

TABLE 6: HOVs binary logit model estimate results

The representative values of time distributions used for the model input are calculated from the binary logit model estimate results. Generally, the VOT distributions for SOV, HOV2 and HOV3+ can be written as Equations 12, 13 and 14, respectively:

$$P_T = \frac{1}{(1 + e^{-(0.139 + (0.128 \times t) - (0.785 \times T))})} \tag{12}$$

$$P_T = \frac{1}{(1 + e^{-(0.553 + (1.042 \times t) - (7.132 \times T) + (0.011 \times D))})} \tag{13}$$

$$P_T = \frac{1}{(1 + e^{-(0.142 + (0.868 \times t) - (8.803 \times T))})} \tag{14}$$

P_T represents a proportion of population who choose to pay a toll T dollars for travel time saving t minutes with travel distance D miles. In order to convert these equations in terms of VOT inputs, the researchers assume a travel time saving of one minute per mile and reformulate the equations in the form of Equations 15, 16 and 17, respectively:

$$P_T = \frac{1}{(1 + e^{-1.419 + (7.85 \times VOT)})} \tag{15}$$

$$P_T = \frac{1}{(1 + e^{-0.5 + (7.132 \times VOT)})} \tag{16}$$

$$P_T = \frac{1}{(1 + e^{-1.01 + (8.803 \times VOT)})} \tag{17}$$

VOTs in the above equations are in dollars per minute. The proportion of population who choose to pay a toll T dollars for a travel time saving of one minute on a one-mile section can now be defined as the proportion of population P who has a value of time greater than VOT assumed in the analysis. Equations 15, 16 and 17 specify the VOT distributions, and they are used to generate the VOT inputs in this study. As a result, the percentages of population are calculated for a total of ten intervals with the bandwidth of three dollars per hour, as shown in Table 7.

The absence of previous studies on the VOT distribution for the other vehicle classes is noted through the literature review. This study assumes HOV3+'s VOT distribution for the remaining classes. However, if transportation planners are interested in analyzing impact of the other vehicle classes on the managed lane, a similar survey of SOV and HOVs should be conducted to obtain the VOT distribution for those modes.

VOT (\$/hr)	Percentage of Population	HOV2	HOV3+
0.00 - 3.00	26.4%	46.4%	36.1%
3.01 - 6.00	8.3%	8.9%	10.6%
6.01 - 9.00	9.3%	8.6%	10.9%
9.01 - 12.00	9.8%	7.8%	10.2%
12.01 - 15.00	9.5%	6.7%	8.8%
15.01 - 18.00	8.6%	5.5%	6.9%
18.01 - 21.00	7.2%	4.3%	5.2%
21.01 - 24.00	5.8%	3.3%	3.7%
24.01 - 27.00	4.4%	2.4%	2.5%
> 27.00	10.7%	6.2%	5.0%

TABLE 7: VOT inputs

4. THE TOLL PRICING MODEL

A toll pricing model (TPM-4.3) is developed based on the user equilibrium concept for managed lanes described in section two. This section describes the software features to estimate the demands on the managed lane and general purpose lane, among other performance outcomes.

4.1 Facility Information

The facility information includes all the necessary details about the GPL and ML facilities such as number of lanes, corridor length and parameters to utilize the calibrated flow-density-speed models. A number of input parameters must be specified, as follows:

- **Flow-Density-Speed ($q-k-u$) model.** The (model) option is chosen to characterize the performance impact. The specified flow-density-speed relationship should be calibrated for the facility under study or a similar facility.
- **Number of Lanes.** The number of lanes is a total number of lanes for each lane type on the corridor. The inputs are separated for managed lanes and general purpose lanes.
- **Free-Flow Speed.** Free-flow speed is an average free-flow speed (in mph) in the study corridor. This value should be established when calibrating the flow-density-speed model.
- **Capacity Per Lane.** Capacity per lane is a maximum lane flow (in pcphpl) for freeway conditions.
- **Jam Density.** Jam density is the concentration at which speeds approach zero (in pcpmpl). This value is required only when the Greenshields model [13] is specified.
- **Corridor Length.** The corridor length is a total length (in miles) of the roadway segment. Although the lengths of the ML and the GPL are the same, this is not an absolute requirement. The ability to specify different lengths allows for analysis of two alternative travel corridors unequal in length, one toll and one non-toll.

4.2 User Information

User information requires all the necessary details related to the corridor users such as the vehicle mix, Passenger Car Equivalency (PCE), toll policy, demand, and dead setter percentages. These input variables can be specified as follows:

- **Vehicle Mix.** Vehicle mix is the percentage of each vehicle type in the travel corridors. It defines the total number of vehicles for each vehicle type presented in the traffic stream under investigation.
- **Passenger Car Equivalency (PCE).** The passenger car equivalency factor (PCE) is a multiplier used to convert a mixed vehicle flow into an equivalent passenger car flow.
- **Toll Policy.** Toll policy defines the toll amount for each vehicle class allowed to travel on managed lanes. Toll policies for different classes of vehicles can be specified as a percent of the SOV toll.
- **Corridor Demand.** Corridor demand is an expected total directional demand (in vph) including all vehicles in the ML and GPL regardless of vehicle type.
- **Dead Setters.** Dead setters are defined as the percent of each vehicle class, except SOV, choosing to use GPL regardless of the amount of toll on ML. This could be due to their specific origin-destinations or other driver behavioral reasons.

4.3 Value of Time Distributions

VOT distributions reveal the time values for study areas and estimate the potential managed lane users. The value of time distribution is entered separately for each vehicle class. The VOT inputs were presented in section three.

4.4 Analysis Objectives

In the TPM-4.3, the user can select one of two proposed managed lane operational objectives. One option is to set a SOV toll to estimate demands and operating speeds on the ML and GPL. A second option is to set a desired minimum operating speed on the ML facility to estimate the toll amount that should be charged to maintain the desired speed.

4.5 Software Output

After specifying the objective, the results are computed and presented in the output summary. The outputs are road performances, revenues, and emissions, as follows:

- **Volume.** Volume is a measure of the demand (in vph). Volumes are shown for each lane type when the equilibrium is reached.
- **Speed.** Speed is an average speed (in mph) computed for each lane. Speeds are computed based on the estimated volumes at equilibrium if the toll objective is chosen.
- **Percentage Share.** Percentage ML share is the percentage of total users who use the ML. It is calculated for each vehicle class separately.
- **Toll Charge.** Toll charges are based on the SOV toll and the toll policies for other vehicle classes. Tolls are calculated according to the percentage of SOV charges specified.
- **Total Revenue.** Total revenue is the total toll amount collected from all managed lane users. It is computed based on the toll users estimates.
- **Emission Summary.** Emission estimates including CO, HC, NO_x, CO₂ and SO₂ are presented for each vehicle class.

5. CASE STUDY AND IMPACT ESTIMATES

The main purpose of the impact analysis is to provide quantitative estimates of how different high occupancy vehicle (HOV) preferential treatments impact toll revenue, air quality, and system performance for the managed lanes and general purpose lanes. The Toll Pricing Model (TPM-4.3) developed under the new user-equilibrium paradigm described in the previous section, is used as a tool to estimate impacts of twenty-four pricing scenarios.

5.1 Case Study

As a case study, a future managed lane segment on I-30 in Grand Prairie, Texas, between the cities of Dallas and Arlington, is modeled to examine a set of proposed operating scenarios. The required inputs, including geometric configuration and the user composition of the facility, are presented below.

- The Drake model is used with free-flow speed of 80 mph and a lane capacity of 2200 pcphpl.
- Corridor demand is assumed to be 11,000 vph and the dead setters are set at 5 percent.
- This study section is five-miles long with two toll lanes and four free lanes.
- The vehicle mix includes 76.4% SOV, 10% HOV2, 5% HOV3+, 1.5% Van-Pool, 0.5% Para-Transit, 0.2% Bus, 0.8% Light Freight truck, 5.2% Single Trailer truck and 0.4% Double Trailer truck [12].
- The PCE for SOV, HOV2, HO3+, Van-Pool, Para-Transit, Bus, Light Freight, Single Trailer and Double Trailer are 1, 1, 1, 1.2, 1.5, 1.2, 1.2, 1.5, 2.0 and 3.0, respectively [12].
- SOV is charged at full toll rates based on the scenarios. HOV2, HOV3+ and Van-Pools are either half-price or free, and Para-Transit and Buses are free.
- The VOTs are based on the values presented in section three.

Scenario	Corridor Length (miles)	Toll Amount (\$/mile)				ML Speed (mph)
		SOV	HOV2	HOV3+	Trucks	
1	5	\$0.10	SOV	SOV	Not on ML	-
2	5	\$0.10	Free	Free	Not on ML	-
3	5	\$0.10	0.5xSOV	0.5xSOV	Not on ML	-
4	5	\$0.10	0.5xSOV	Free	Not on ML	-
5	5	\$0.10	SOV	0.5xSOV	Not on ML	-
6	5	\$0.10	SOV	Free	Not on ML	-
7	5	\$0.25	SOV	SOV	Not on ML	-
8	5	\$0.25	Free	Free	Not on ML	-
9	5	\$0.25	0.5xSOV	0.5xSOV	Not on ML	-
10	5	\$0.25	0.5xSOV	Free	Not on ML	-
11	5	\$0.25	SOV	0.5xSOV	Not on ML	-
12	5	\$0.25	SOV	Free	Not on ML	-
13	5	\$0.50	SOV	SOV	Not on ML	-
14	5	\$0.50	Free	Free	Not on ML	-
15	5	\$0.50	0.5xSOV	0.5xSOV	Not on ML	-
16	5	\$0.50	0.5xSOV	Free	Not on ML	-
17	5	\$0.50	SOV	0.5xSOV	Not on ML	-
18	5	\$0.50	SOV	Free	Not on ML	-
19	5	-	SOV	SOV	Not on ML	65
20	5	-	Free	Free	Not on ML	65
21	5	-	0.5xSOV	0.5xSOV	Not on ML	65
22	5	-	0.5xSOV	Free	Not on ML	65
23	5	-	SOV	0.5xSOV	Not on ML	65
24	5	-	SOV	Free	Not on ML	65

TABLE 8: Policy scenarios

A total of 24 policy scenarios are tested on the proposed managed lane section. The policies can be divided into four subsets: 1 to 6, 7 to 12, 13 to 18, and 19 to 24 as shown in Table 8. Each subset includes six different pricing scenarios with various preferential treatments for HOV2 and HOV3+ vehicles. Subsets one to three are analyzed by toll objectives, which cover prices ranging from \$0.10/mile to \$0.50/mile. The fourth subset is run by maintaining the managed lane speed at 65 mph, with the same preferential treatment scenarios as the first three subsets. These inputs will be entered into TPM-4.3 to estimate outcomes such as traffic volume, speed, revenue and emissions for the ML and GPL.

5.2. Impact Estimates

Table 9 displays the impact estimates of various HOV preferential treatment policies presented in Table 8. The first two scenarios for each subset begin with a scenario of the least preferential treatment (tolled same as SOV) and the most preferential treatment (free) for HOV followed by four more scenario variations for intermediate HOV preferential treatments.

5.2.1 Policy Scenarios 1 to 18

In Table 9, scenarios 1 to 6 have a SOV toll of \$0.10/mile, scenarios 7 to 12 are at \$0.25 /mile and scenarios 13 to 19 specify a SOV toll of \$0.50/mile. CO and NO_x emissions show little to no change within each subset regardless of the preferential treatment for HOV2 and HOV3+, but they are significantly reduced when toll amounts increase (Table 5.2). When compared with the first two subsets, subset three, which includes scenarios 13 to 18 results in an increase in CO₂ and VOC. Scenarios 13 and 17, which have ML volumes less than 1800 vehicles per hour, result in the lowest NO_x emission, and a decrease in CO emissions when compared to other scenarios.

System performance varies little within scenario subsets, but it differs greatly across the scenarios. The peak-hour average speeds on the ML increase with larger charges. As expected, the GPL becomes more congested under higher toll scenarios due to decreasing use of ML. For ML, volumes vary from 1,723 to 3,472 vph. For GPL, volumes vary from 7,528 to 9,278 vph (Table 5.2). Scenarios 13 to 18, with tolls of \$0.50/mile, show significant differences in the level of performance between ML and GPL. Among scenarios with a full toll price of \$0.50/mile, the charge-all scenario (scenario 13) has the highest impact on speeds, with 77 mph for ML and 30 mph for GPL, and results in the lowest CO (76.9 kilograms/mile) and NO_x (4.34 kilograms/mile) emissions, and the highest toll revenue of \$4,115 per hour.

Peak hour revenues range from \$832 to \$4,115. Exempting the HOVs from paying tolls would, as expected, result in the lowest peak revenue. Conversely, charging HOV the same toll as SOV results in the highest revenue. The second greatest peak hour revenue in each subset is attained by charging the HOV2s the same toll as the SOV and charging the HOV3+ half as much. Naturally, as the scenarios become more preferential towards the HOV2 and HOV3+, toll revenues decrease.

5.2.2 Policy Scenarios 19 to 24

Policy scenarios 19 to 24, with tolls as low as \$0.02/mile and as much as \$0.03/mile, are aimed at maintaining the ML speed at 65 mph. These scenarios result in the same GPL speed at 62 mph. They show little difference in VOC emission, and no change is observed for other emissions. Scenario 19 results in the highest ML volume of 3,757 vph. Scenario 20, with the maximum HOV preferential treatment, yields the lowest peak hour toll revenue of \$289. Scenario 24 which charges SOV and HOV2 at \$0.03/mile and HOV3+ at half price yields the maximum peak hour revenue of \$445.

TABLE 9: Impact estimates using the TPM-4.3

Scenario	Toll Amount (\$/mile)			Peak Hr. Volume (vph)		Peak Hr. Avg. Speed (mph)		Peak Hr. Emissions (Kilograms/mile)					Peak Hr. Corridor Revenue (\$/peak hr)
	SOV	HOV2	HOV3+	ML	GPL	ML	GPL	CO	VOC	NOx	CO ₂	SO ₂	
1	\$0.10	SOV	SOV	3344	7656	69	58	114.4	0.983	4.77	1,987	0.084	\$1,634
2	\$0.10	Free	Free	3472	7528	67	60	117.2	0.983	4.80	1,977	0.084	\$832
3	\$0.10	0.5xSOV	0.5xSOV	3381	7619	68	59	115.7	0.983	4.79	1,982	0.084	\$1,478
4	\$0.10	0.5xSOV	Free	3404	7596	68	59	115.8	0.985	4.79	1,982	0.084	\$1,224
5	\$0.10	SOV	0.5xSOV	3357	7642	69	58	114.4	0.984	4.77	1,987	0.084	\$1,562
6	\$0.10	SOV	Free	3380	7620	68	59	115.7	0.984	4.79	1,982	0.084	\$1,308
7	\$0.25	SOV	SOV	2622	8378	73	40	88.0	0.972	4.44	2,199	0.084	\$3,182
8	\$0.25	Free	Free	2959	8041	71	52	104.6	0.970	4.64	2,034	0.084	\$1,438
9	\$0.25	0.5xSOV	0.5xSOV	2714	8286	73	41	89.5	0.972	4.46	2,178	0.084	\$2,925
10	\$0.25	0.5xSOV	Free	2791	8209	72	43	91.8	0.968	4.48	2,144	0.084	\$2,327
11	\$0.25	SOV	0.5xSOV	2660	8340	73	40	88.1	0.973	4.44	2,198	0.084	\$3,062
12	\$0.25	SOV	Free	2739	8261	73	42	90.8	0.970	4.48	2,160	0.084	\$2,469
13	\$0.50	SOV	SOV	1723	9278	77	30	76.9	1.016	4.34	2,503	0.084	\$4,115
14	\$0.50	Free	Free	2179	8821	75	35	82.1	0.986	4.38	2,322	0.084	\$925
15	\$0.50	0.5xSOV	0.5xSOV	1853	9147	77	31	78.1	1.012	4.35	2,459	0.084	\$3,772
16	\$0.50	0.5xSOV	Free	2014	8986	76	33	80.1	0.997	4.36	2,385	0.084	\$2,770
17	\$0.50	SOV	0.5xSOV	1779	9221	77	31	77.9	1.010	4.34	2,463	0.084	\$3,959
18	\$0.50	SOV	Free	1936	9064	76	32	78.9	1.004	4.35	2,420	0.084	\$2,930
19	\$0.02	SOV	SOV	3757	7243	65	62	120.0	0.982	4.83	1,970	0.084	\$368
20	\$0.03	Free	Free	3733	7267	65	62	120.0	0.981	4.83	1,970	0.084	\$289
21	\$0.02	0.5xSOV	0.5xSOV	3751	7249	65	62	120.0	0.983	4.83	1,970	0.084	\$330
22	\$0.03	0.5xSOV	Free	3733	7267	65	62	120.0	0.982	4.83	1,970	0.084	\$406
23	\$0.02	SOV	0.5xSOV	3750	7250	65	62	120.0	0.983	4.83	1,970	0.084	\$350
24	\$0.03	SOV	Free	3733	7267	65	62	120.0	0.982	4.83	1,970	0.084	\$445

5.3 Sensitivity Analysis

In this section, sensitivity analysis is performed and the results are graphically presented to better explain the relationship between various operational outcomes and toll rates as well as demand levels.

5.3.1 Toll Rate Sensitivity

Figures 2 through 7 illustrate the toll sensitivity curves under various toll policies. The figures show the effects that toll rates have on average speed on both managed lanes (ML) and general purpose lanes (GPL), revenue and emissions. Graph (a) in each figure presents the average operating speeds on ML and GPL. As seen, the speeds between ML and GPL slightly differ at low toll rate ($< \$0.10$) and the difference increases when toll is increased. This also shows that increasing the average operating speed on the ML can be achieved by implementing a higher toll rate.

Graph (b) in each figure shows the estimated revenue collected from the proposed managed lane facility. As toll increases, revenue also increases to a point where the maximum revenue is reached (Figure 3) or the curve slope starts decreasing.

Graphs (c) through (f) in each figure show the relationship between toll rate and emissions. As seen, CO (graphs (c)) and NO_x (graph (e)) decrease when toll increases. In contrast, CO₂ (graphs (f)) increases as toll increases. An increase in CO₂ is associated with a reduction in CO and NO_x. Interestingly, as toll increases, VOC (graphs (d)) drops to the minimum level at toll rate between \$0.20 and \$0.25.

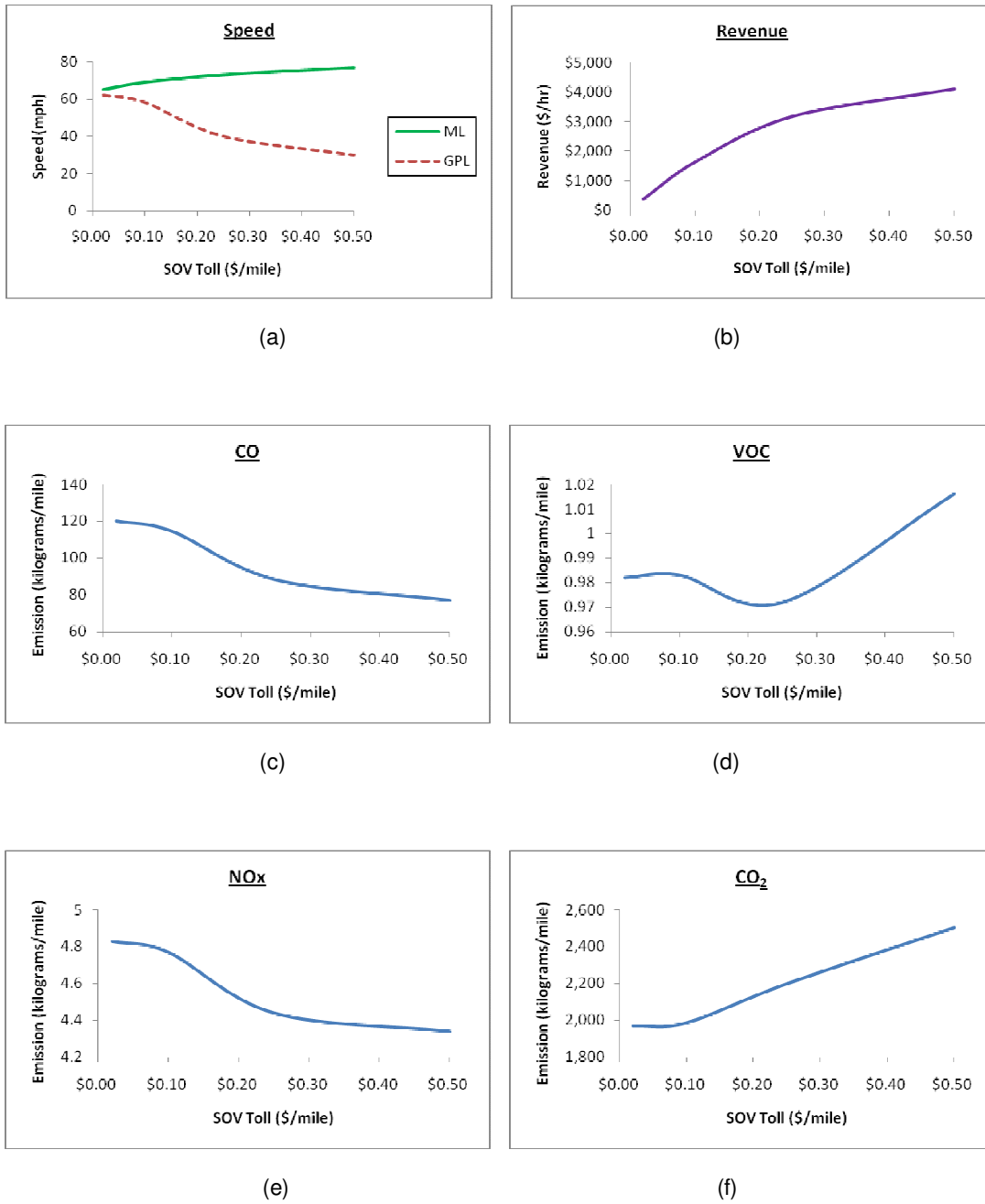


FIGURE 2: Operational outcomes for policy: HOV2 toll = SOV and HOV3+ = SOV; (a) Speed, (b) Revenue, (c) CO, (d) VOC, (e) NOx, (f) CO₂.

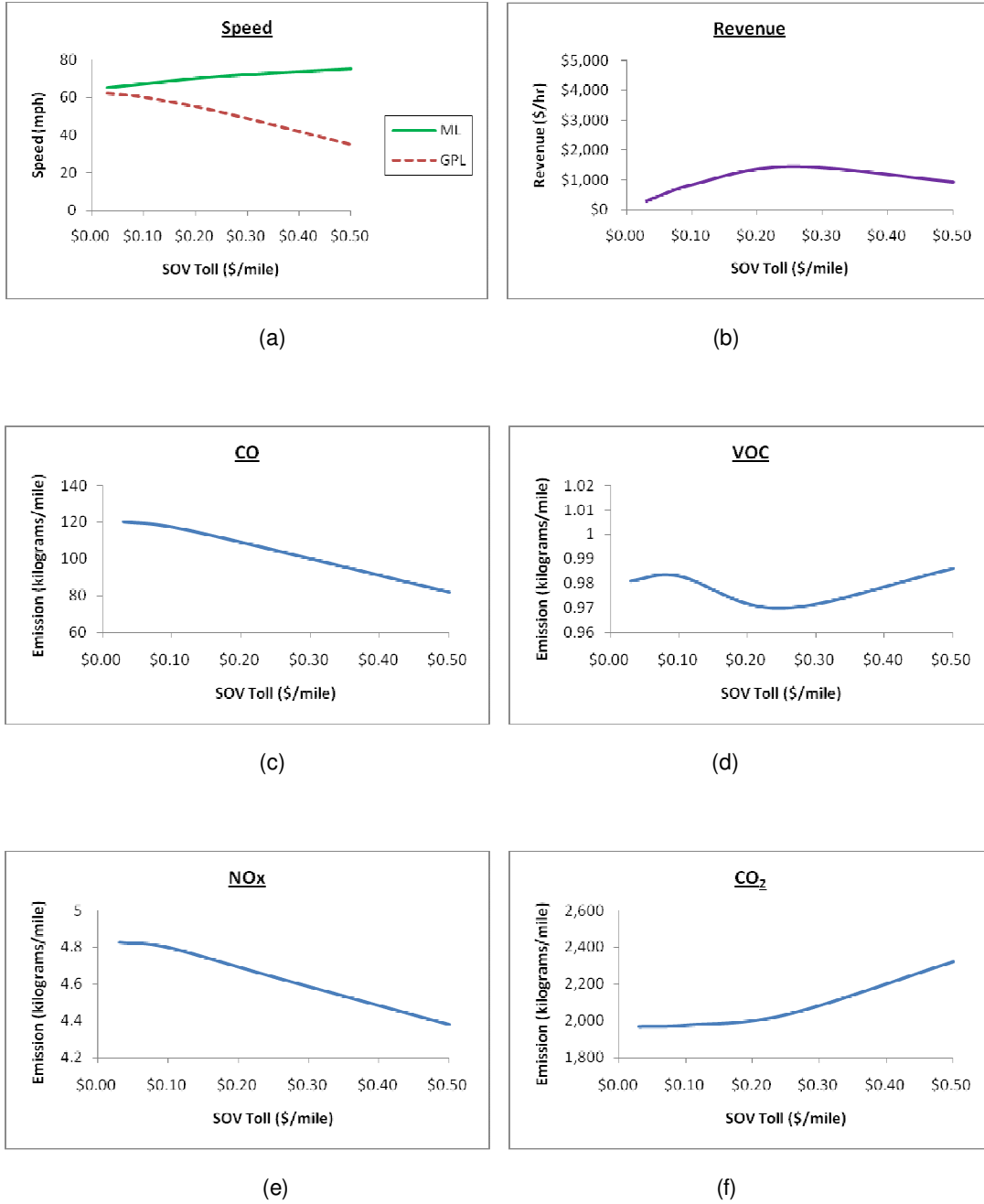


FIGURE 3: Operational outcomes for policy: HOV2 toll = Free and HOV3+ = Free; (a) Speed, (b) Revenue, (c) CO, (d) VOC, (e) NOx, (f) CO₂.

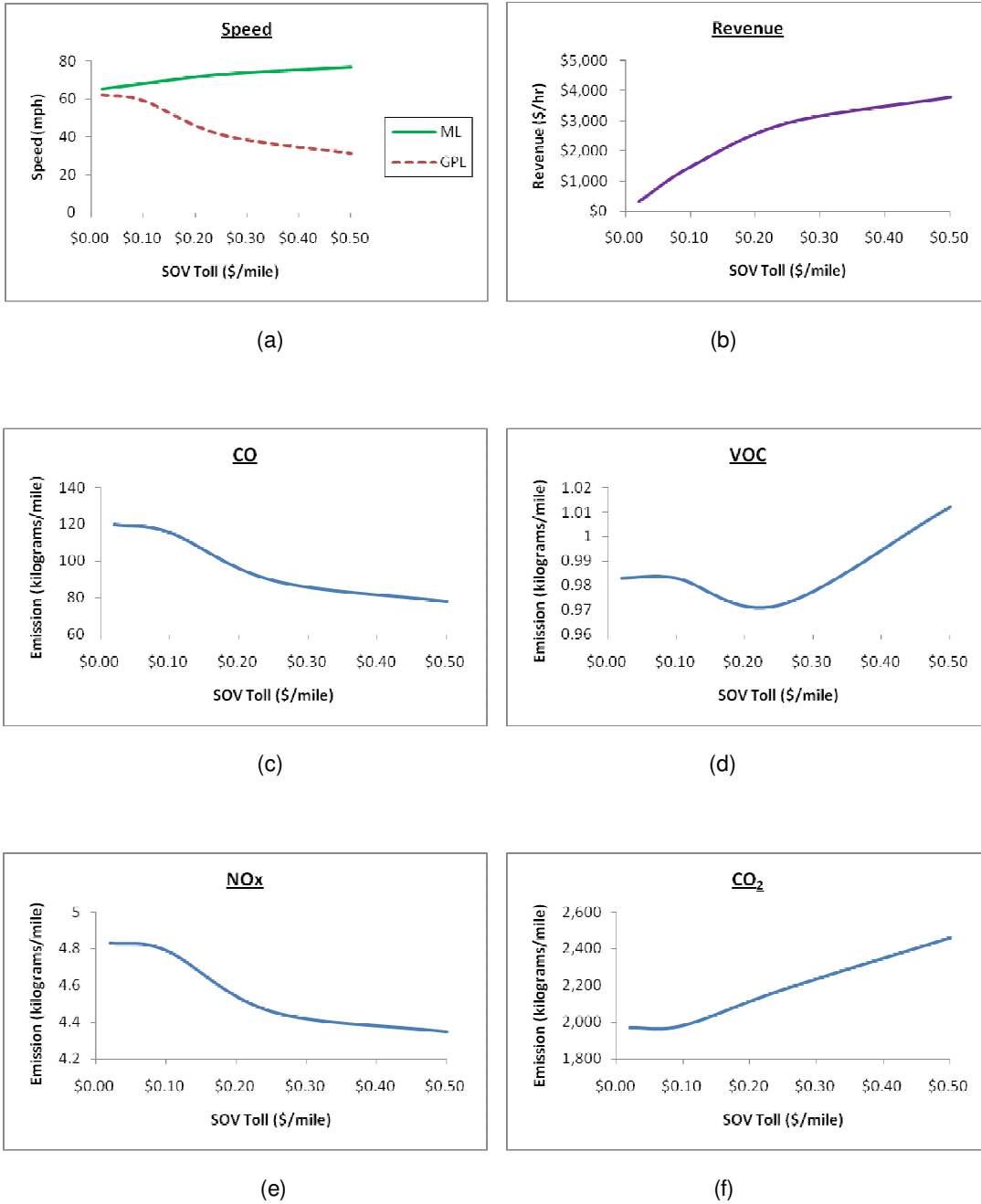


FIGURE 4: Operational outcomes for policy: HOV2 toll = 50%SOV and HOV3+ = 50%SOV; (a) Speed, (b) Revenue, (c) CO, (d) VOC, (e) NOx, (f) CO₂.

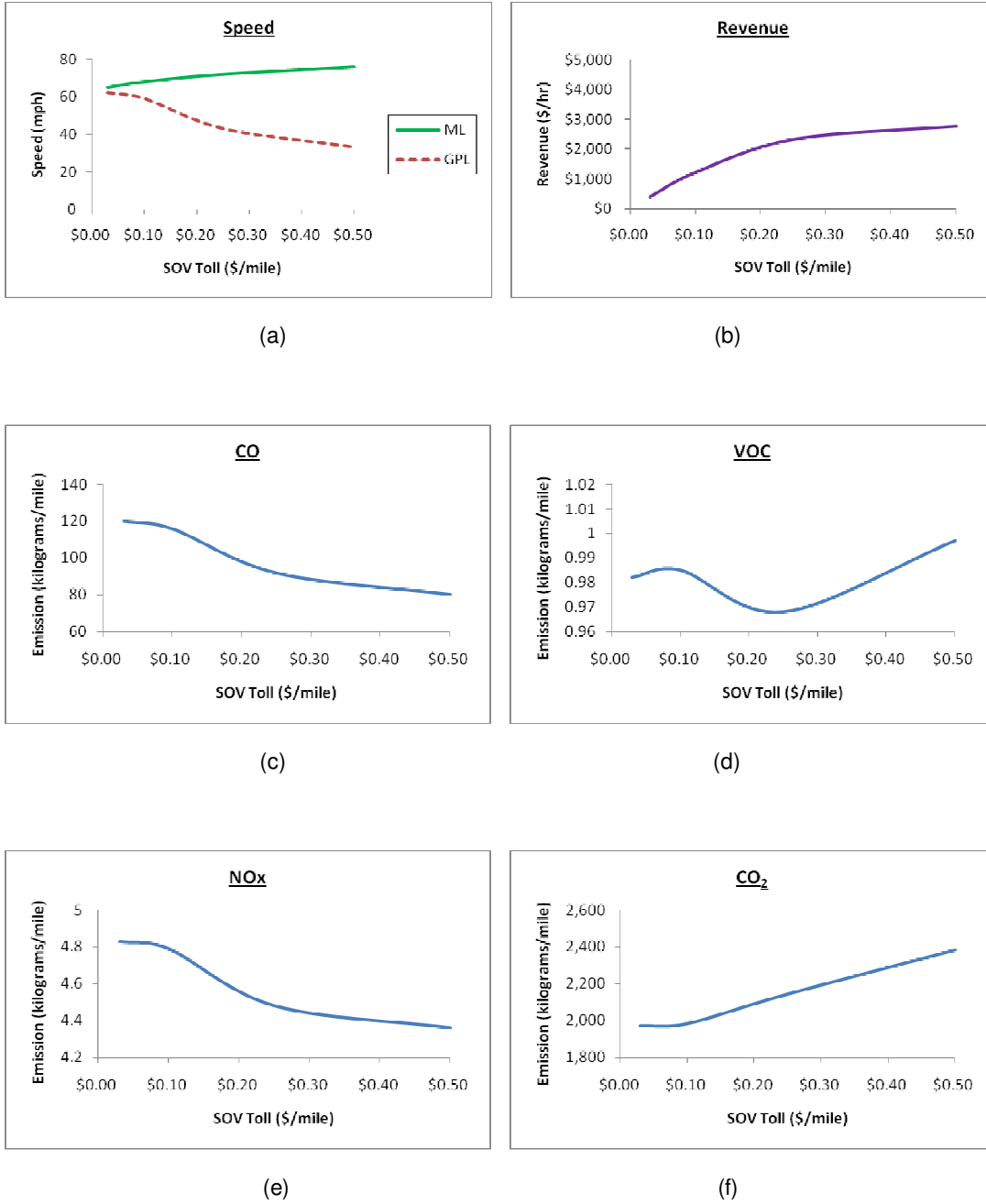


FIGURE 5: Operational outcomes for policy: HOV2 toll = 50%SOV and HOV3+ = Free; (a) Speed, (b) Revenue, (c) CO, (d) VOC, (e) NOx, (f) CO₂.

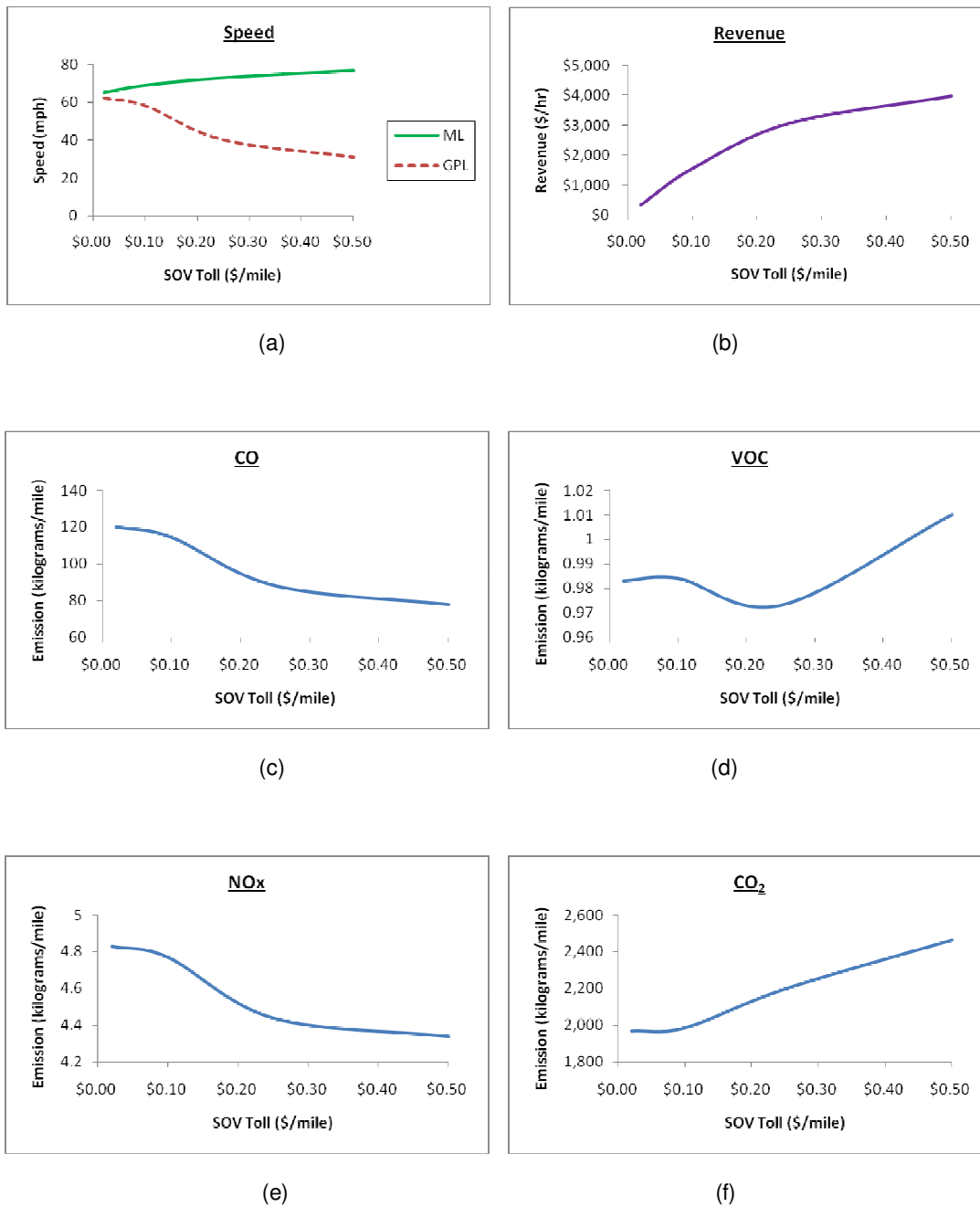


FIGURE 6: Operational outcomes for policy: HOV2 toll = SOV and HOV3+ = 50%SOV; (a) Speed, (b) Revenue, (c) CO, (d) VOC, (e) NOx, (f) CO₂.

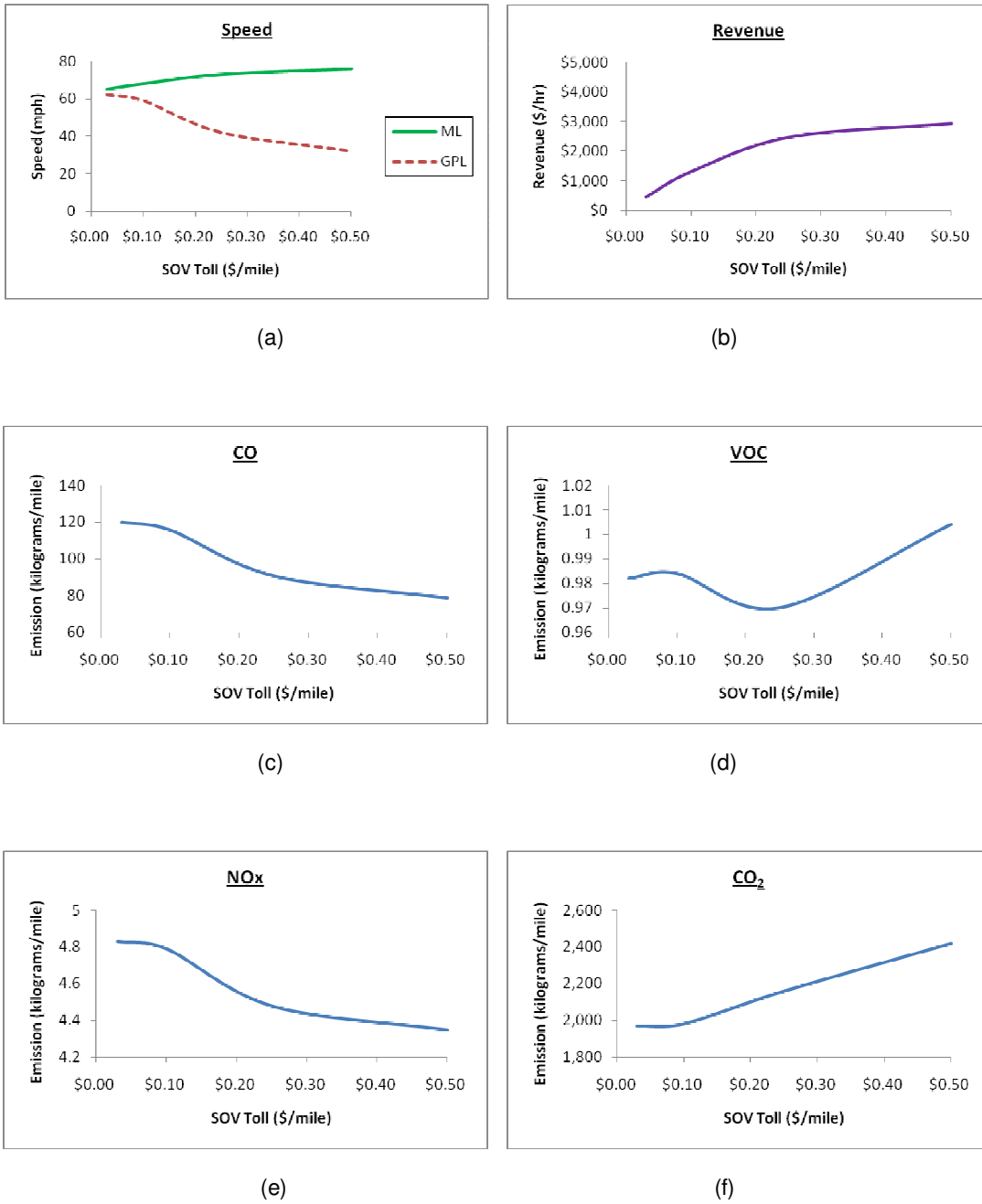


FIGURE 7: Operational outcomes for policy: HOV2 toll = SOV and HOV3+ = Free; (a) Speed, (b) Revenue, (c) CO, (d) VOC, (e) NOx, (f) CO₂.

5.3.2 Demand Sensitivity

Figure 8 shows the demand sensitivity curves based on the per mile policy of SOV toll = \$0.25, HOV2 toll = \$0.125 and HOV3+ = Free. Graphs (a), (b), (c) and (d) illustrate the relationship between demand level (v/c) and the amounts of CO, VOC, NOx and CO₂, respectively. As seen, the amounts of all emissions increase as demand increases, except for CO. In general, lesser speed emits lower CO. When demand is greater than 75% of the capacity, speeds on both GPL and ML drop. This results in reduction in CO.

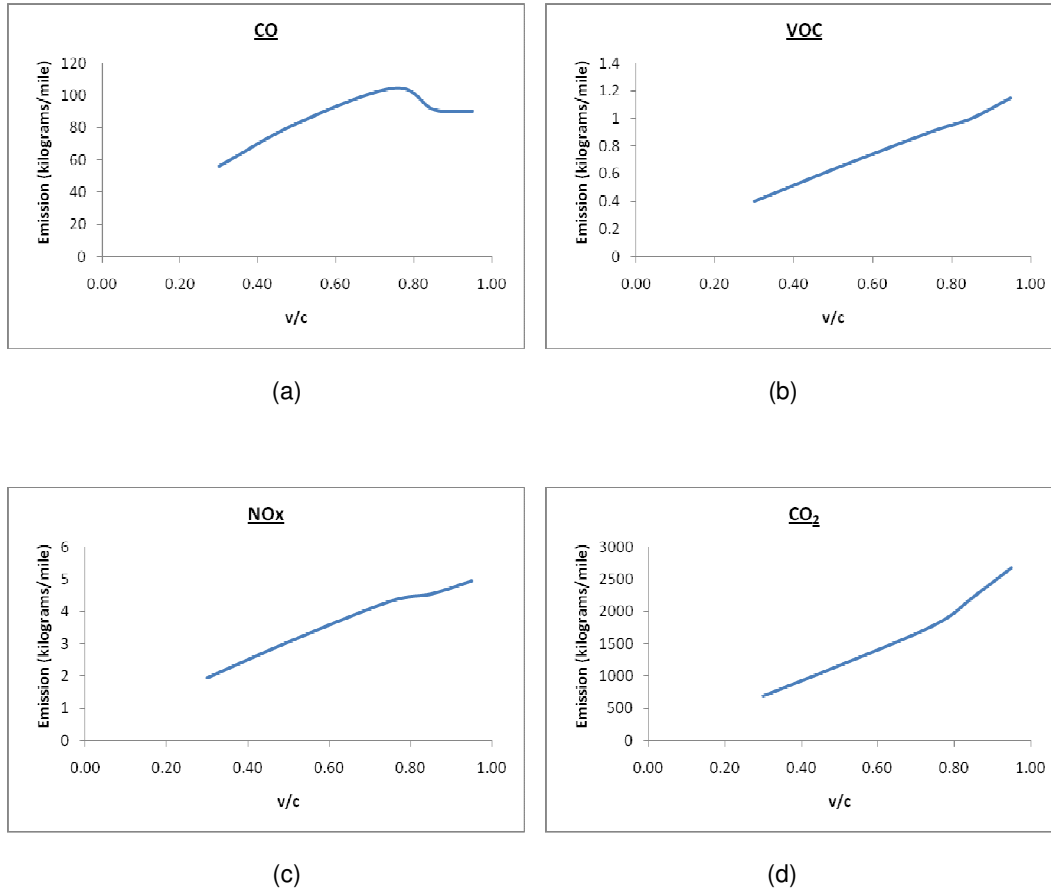


FIGURE 8: Emissions emitted at different demand levels (v/c) based on the policy of SOV toll = \$0.25, HOV2 toll = \$0.125 and HOV3+ = Free; (a) CO, (d) VOC, (e) NOx, (f) CO₂.

5.4 Impact Summary

Based on the results, impacts on system performance, emissions and revenue can be summarized as follows:

5.4.1 System Performance Impacts

Based on the stated-preference price sensitivities derived from previous studies for Texas drivers, tolls below \$0.10/mile tend to equally spread out vehicles in both the GPL and ML. As a result, there would be no significant difference in speeds between the GPL and ML. Charging a toll of \$0.25/mile or higher would increase system performance on the ML and reduce system performance on the GPL. In each subset, HOV preferential treatments have little impact on the overall system performance. However, lower HOV preferential treatment (higher tolls) would increase system performance on the ML.

Maintaining a speed of 65 mph on the ML requires a tradeoff between toll rate and HOV preferential treatment, namely, either a SOV toll rate of \$0.02/mile with no HOV preferential treatment, or a toll rate of \$0.03/mile with free HOV access, or some combination of these pricing policies.

5.4.2 Emissions Impacts

As seen, the most preferential treatment scenario generates the most CO and NO_x emissions. Regardless of the toll policy, no change in the amount of peak hour SO₂ emissions is observed. Trucks are by policy not allowed on the ML. Scenarios 13 to 18 have the greatest CO₂ emissions followed by scenarios 7 to 12. The greatest reduction in CO and NO_x emissions occurs in scenarios at the toll level of \$0.50/mile. Among all scenarios, the policy with a toll rate of \$0.50/mile and no HOV preferential treatment results in the least CO and NO_x emissions. It is observed that a reduction in NO_x is generally associated with an increase in VOC.

5.4.3 Revenue Impacts

Although HOV preferential treatments do not significantly affect peak hour system performance, they do negatively impact the peak hour revenue. In general, a lower HOV preferential treatment (higher tolls) results in an increase in overall toll revenues. In scenarios where HOV has free access to ML, revenue is observed to be the smallest for every subset. The maximum revenue of \$4,115 per peak hour is obtained in scenario 13 at a toll of \$0.50 with the least preferential treatment for HOV, followed by \$3,959 and \$3,772 for scenarios 17 and 15, respectively.

Overall, except for the highest preferential treatment scenarios for HOV, higher toll rates tend to generate higher toll revenues, reduce overall CO and NO_x emissions, and shift travel demand to GPL. HOV preferential treatments at any given toll level tend to reduce toll revenue, either have no impact or reduce system performance on ML, and increase CO and NO_x emissions.

6. CONCLUSIONS AND RECOMMENDATIONS

This research developed and implemented the Toll Pricing Modeler version 4.3 (TPM-4.3) for a dynamic toll pricing study for multiple vehicle classes based on a new paradigm in user equilibrium. The TPM-4.3 was utilized to estimate impacts of toll pricing scenarios on system performance, toll revenue and emissions on the proposed I-30 managed lane facility in Texas by using value of time (VOT) distributions derived in the Dallas-Fort Worth area. For each vehicle class, different VOT distributions were used to estimate the impact on user equilibrium assignment.

6.1 Conclusions

The impact analysis results indicate that various toll pricing policies could have substantial impacts on the volume assignment, system performance, total revenue and emissions. A number of key conclusions can be drawn from this analysis, as follows:

1. In the low volume conditions, the managed lanes (ML) become less-attractive to single occupancy vehicles (SOV) if the ML travel times do not differ or are only slightly lower than the

general purpose lane (GPL) travel times and SOVs are likely to continue using the GPLs. As the volume increases to the point where volumes can greatly increase the travel time on the GPLs, the probability of using MLs will also increase.

2. Based on the stated-preference price sensitivities for Dallas-Fort Worth drivers, tolls above \$0.10/mile tend to spread vehicles across the GPLs and MLs in such a way to generate significant ML travel time improvements. At this toll rate (\$0.10/mile), more than 30% of travelers on the corridor would pay a toll to use managed lanes.

3. In the scenarios where SOVs and high occupancy vehicles (HOV) are charged the same price, the predicted ML shares are different because characteristics of the VOT distribution of the SOVs differ from those of the HOVs.

4. HOV preferential treatments (lower HOV tolls) have little impact on system performance. However, lower HOV preferential treatment (higher HOV tolls) would increase system performance on the ML.

5. A tradeoff between SOV toll rate and HOV preferential treatment can be used to maintain a speed on the ML at or above a threshold value.

6. The HOV preferential treatment (lower HOV tolls) on the managed lanes increases the level of CO and NO_x emissions.

7. There is no difference in the amount of peak hour SO₂ emissions across the various policies since SO₂ does not depend on the speed. In general, SO₂ is emitted by trucks using diesel fuel and trucks are not allowed on ML under any of the policies examined.

8. The greatest reduction in CO and NO_x emissions occurs at a high toll rate. A policy with a high toll rate and no HOV preferential treatment results in the least CO and NO_x emissions. Also, a reduction in NO_x is generally associated with an increase in VOC and CO₂.

9. HOV preferential treatments do not significantly affect peak hour system performance but they do negatively impact the peak hour revenue. In general, lower HOV preferential treatment and higher toll rate result in an increase in toll revenues.

6.2 Future Directions

In this version, the TPM-4.3 software does not include a conversion between modes. If HOV preferential treatments (lower HOV tolls or free) are implemented on the ML to encourage carpooling, a SOV may become a HOV. In this case, mode change can occur but it cannot be captured in the software. Also, when the managed lane concept is implemented on the corridor, travelers may change their commute route. A possibility of route change (increase or decrease in demand) is also not accommodated in the TPM-4.3 model. A future version should include modules to capture potential mode and route changes.

As mentioned previously, the TPM-4.3 has potential application in analysis of alternative toll versus free highway that has a same origin-destination pair with different lengths. However, further validation of this analysis type should be performed to ensure the model applicability. Additionally, the model validation using I-30 or Katy freeway data is needed when it is available because various components in the TPM-4.3 are based on the results from previous studies using Texas data.

Finally, in the TPM-4.3, the last VOT range for the VOT input is assumed to have a same interval as the previous range. This assumption may lead to prediction errors. This group of motorists (high VOT) has an important role on the ML utilization since they will influence the toll charge when available capacity for SOV is low. In order to improve the results, actual characteristic of

VOT distributions at upper limits must be better known. Thus, a future study should be conducted to capture this characteristic for inclusion in the model.

ACKNOWLEDGMENTS

Various elements of the TPM-4.1 software are based on results from a number of previous research studies sponsored by the Texas Department of Transportation (TxDOT). Authors in particular wish to acknowledge contribution of Dr. Jianling Li at the UTA School of Urban and Public Affairs and Dr. Khaled Abdelghany at the SMU Department of Environmental and Civil Engineering for their contributions to the earlier versions of the TPM software as well as their general contributions to the afore-mentioned TxDOT studies. Additional acknowledgment goes to Michael Vickers for his assistance in writing and testing the software codes.

REFERENCES

1. S. A. Ardekani, F. Kashefi, K. Abdelghany, and A. Hassan. *"User Guide to Toll Pricing Model v3.1: TPM-3.1"*. 2007
2. J. T. Berg, K. Kawada, M. Burris, C. Swenson, L. Smith and E. Sullivan. *"Value Pricing Pilot Program"*. TR News 204, pp. 3-10, 1999
3. D. Brownstone, A. Ghosh, T. F. Golob, C. Kazimi and D. V. Amelsfort. *"Drivers' Willingness-to-Pay to Reduce Travel Time: Evidence from the San Diego 1-15 Congestion Pricing Project"*. Transportation Research Part A: Policy and Practice, Vol. 37, Issue 4, pp. 373-387, May 2003
4. M. W. Burris, M. C. Pietrzyk and C. R. Swenson. *"Observed Traffic Pattern Changes Due to the Introduction of Variable Tolls"*. Paper presented at the 79th Annual Meeting of the Transportation Research Board, Washington, D.C., 2000
5. M. W. Burris and E. Sullivan. *"Benefit-Cost Analysis of Variable Pricing Projects: QuickRide HOT Lanes"*. Journal of Transportation Engineering, pp. 183- 190, March 2006
6. Cambridge Systematics, Inc. and Short-Elliott-Hendrickson, Inc. *"I-394 MNPASS Technical Evaluation: Final Report"*. Project report to the Minnesota Department of Transportation, Minnesota, 2006
7. Cambridge Systematics, Inc. and URS Corporation. *"MNPASS System Study: Final Report"*. Project report to the Minnesota Department of Transportation, Minnesota, 2005
8. J. S. Drake, J. L. Schofer and A. D. May. *"A Statistical Analysis of Speed Density Hypotheses"*. Highway Research Record, Vol. 154, Highway Research Board, NRC, Washington, 1967
9. Federal Highway Administration *"Managed Lanes: A Primer"*. U.S. Department of Transportation, 2008
10. G. Fielding and D. Klein. *"High Occupancy/Toll Lanes: Phasing in Congestion Pricing a Lane at a Time"*. Policy Study No. 170, Reason Foundation, Los Angeles, 1993
11. J. D. Fricker and R. K. Whitford. *"Fundamentals of Transportation Engineering: A Multimodal Systems Approach"*. Pearson Prentice Hall, 2004
12. D. G. Goodin, M. W. Burris, C. M. Dusza, D. H. Ungemah, J. Li, S. A. Ardekani and S. P. Mattingly. *"Role of Preferential Treatment of Carpools in Managed Lane Facilities"*. Texas Transportation Institute, The Texas A&M University System, College Station, Texas, Project Summary Report 0-5286-2, 2009

13. B. Greenshields. *"A Study of Traffic Capacity"*. Proceedings of the Highway Research Board, Highway Research Board, Washington D.C., Vol. 14, pp. 468-477, 1933
14. M. E. Gross and M. J. Garvin. *"Approaches for Structuring Concession Lengths and Toll Rates for Transportation Infrastructure PPPs"*. Proceedings of the Construction Research Congress, pp. 191-200, 2009
15. R. He, B. Ran, K. Choi and A. L. Kornhauser. *"Evaluation of Value Pricing Using a Multiclass Dynamic Network Model"*. Journal of Transportation Engineering, ASCE, pp. 617-624, November/December 2003
16. M. Hickman, Q. Brown and A. Miranda. *"An Evaluation of the Demand for the Katy Freeway HOV lane Value Pricing Project"*. Paper presented at the 79th Annual Meeting of the Transportation Research Board, Washington, D.C., 2000
17. D. H. Kang and W. Stockton. *"Estimation of Toll Road Users Value of Time"*. Texas Transportation Institute, The Texas A&M University System, College Station, Texas, Report No. SWUTC/08/473700-00084-1, 2008
18. B. Kuhn, G. Goodin, A. Ballard, M. Brewer, R. Brydia, J. Carson, S. Chrysler, T. Collier, K. Fitzpatrick, D. Jasek, C. Toyce and G. Ullman. *"Managed Lanes Handbook"*. Texas Transportation Institute, The Texas A&M University System, College Station, Texas, 2005
19. J. Li, S. Govind, J. C. Williams, S. A. Ardekani and C. R. Richard. *"Assessing Pricing Strategies and Users' Attitudes Towards Managed Lanes: Executive Summary"*. Project Summary Report 4009-S, 2002
20. S. P. Mattingly, A. Upayokin and J. Li. *"A Driver's Dilemma: Main Lane or HOT Lane"*. Proceedings of the 4th International Conference on Decision Making in Urban and Civil Engineering, 2004
21. NCTCOG. *"Managed Lanes: Improved Mobility Through Choice"*. North Central Texas Council of Governments, 2009
22. S. M. Nepal. *"Traffic Flow Models for Freeway Traffic Operation"*. Master of Science Thesis, Department of Civil Engineering, The University of Texas at Arlington, Texas, 2008
23. Parsons Brinckerhoff *"Regional toll revenue feasibility study"*. Working draft prepared for Washington State Department of Transportation Urban Corridors Office, 2002
24. G. Ragazzi. *"Tolls and Project Financing: a Critical View"*. Research in Transportation Economics, Vol. 15(1), pp. 41-53, 2005
25. C. Sharp, K. Button and D. Deadman. *"The Economics of Tolled Road Crossings"*. Journal of Transportation Economics and Policy, Vol. 20(2), pp. 255-274. 1986
26. E. Sullivan. *"Continuation Study to Evaluate the Impacts of the SR91 Value-Priced Express Lanes: Final Report"*. Project report to the California Department of Transportation, Traffic Operation Program, HOV System Branch, Sacramento, CA, 2000
27. J. Supernak, J. M. Golob, K. Kawada and T. F. Goob. *"San Diego's I-15 Congestion Pricing Project – Preliminary Findings"*. Paper presented at the 78th Annual Meeting of the Transportation Research Board, Washington, D.C., 1999

28. M. Swisher, W. L. Eisele, D. Ungemah and G. D. Goodin. *"Life-Cycle Graphical Representation of Managed HOV Lane Evolution"*. Submitted for the 11th International HOV conference, Seattle, Washington, October 2002
29. USEPA (2009). *"MOBILE6 Vehicle Emission Modeling Software"*. U.S.Environmental Protection Agency, Website available at:
<http://www.epa.gov/OMS/m6.htm>. [Accessed: November 29, 2009]
30. USEPA (2009). *"Motor Vehicle Emission Simulator (MOVES)"*. U.S. Environmental Protection Agency, Website available at:
<http://www.epa.gov/otag/models/moves/index.htm>. [Accessed: November 29, 2009]
31. J. G. Wardrop. *"Some Theoretical Aspects of Road Traffic Research"*. Proceedings of the Institution of Civil Engineers, Part II, Vol. I, pp. 325-362, 1952
32. WSA. *"Level 2 Traffic and Toll Revenue Study: IH 30 Reversible Managed Lanes- June 2007"*. Wilbur Smith Associates, 2007
33. A. Yerramalla. *"Vehicular Emissions Models Using MOBILE6.2 and Field Data"*. Master of Science Thesis, Department of Civil Engineering, The University of Texas at Arlington, Texas, 2007
34. Y. Yin and Y. Lou. *"Dynamic Tolling Strategies for Managed Lanes"*. Journal of Transportation Engineering, Vol. 135, No. 2, pp. 45-52, 2009

Design and Simulation of a Modified Architecture of Carry Save Adder

Chakib Alaoui

*College of Computers and Information Technology
Taif University, KSA*

chakib@tu.edu.sa

Abstract

This paper presents a technology-independent design and simulation of a modified architecture of the Carry-Save Adder. This architecture is shown to produce the result of the addition fast and by requiring a minimum number of logic gates. Binary addition is carried out by a series of XOR, AND and Shift-left operations. These operations are terminated with a completion signal indicating that the result of the addition is obtained. Because the number of shift operations carried out varies from 0 to n for n-bit addends, a behavioral model was developed in which all the possible addends having 2- to 15-bits were applied. A mathematical model was deduced from the data and used to predict the average number of shift required for standard binary numbers such as 32, 64 or 128-bits. 4-bit prototypes of this adder were designed and simulated in both synchronous and asynchronous modes of operation.

Keywords: Carry Save Adder, Synchronous Adder, Asynchronous Adder, VHDL Simulation.

1. INTRODUCTION

Addition is the most important operation in any digital system. All other arithmetic operations, such as subtraction, multiplication and division are deeply related to the addition; hence, the design of a fast, accurate and low power binary adder translates to a gain in simulation speed and an increase in battery life for portable computing systems [1-3]. Many circuits for binary arithmetic addition exists, such as the ripple carry adder, the carry skip adder, the carry look-ahead adder, the carry select adder, Manchester chain adder, prefix adder among others [4-8]. The performance of these adders has been evaluated in several publications in terms of speed, area and power consumption [4-8].

Arithmetic transformations using carry-save adders (CSAs) have been exploited recently in [9]. Variations of the techniques proposed in [9] have also been reported [10-13]. Carry-save transformations across non-addition operators were proposed in [10]. The timing and area trade-offs of carry-save implementation for multiple addition trees were exploited in [11]. However, all these transformation techniques [9-11] optimize combinatorial circuits only. They are obviously limited by the register boundaries and cannot be applied to optimize synchronous data-path circuits. Arithmetic operations other than addition have been implemented by using CSAs in [12-14].

This paper presents a new modification to the carry-save-adder (CSA) for fast addition. An algorithm was first developed and checked with several arithmetic additions to verify its correctness. Since the number of binary operations needed to compute the addition varies from 0 to n for n-bit addends, a behavioral model was developed in Matlab in order to check all possible binary operations that exist between two n-bit binary numbers. Finally, 4-bit synchronous and asynchronous prototypes were designed and implemented by using Quartus II design Software. These prototypes were chosen to be technology-independent at first. They can be re-simulated by using any technology process such as 0.18 μ m, 0.13 μ m or others.

2. CARRY-SAVE ADDERS

Carry save adder is used to compute sum of three or more n-bit binary numbers. Carry save adder is same as a full adder. Figure 1 shows the sum of two 32-bit binary numbers, so 32 full adders are used at first stage. Carry save unit consists of 32 full adders, each of which computes single sum and carry bit based only on the corresponding bits of the two input numbers. Let X and Y are two 32-bit numbers and produces partial sum and carry as S and C as shown in the following example:

$$S_i = X_i \text{ xor } Y_i$$

$$C_i = X_i \text{ and } Y_i$$

The final addition is then computed as:

1. Shifting the carry sequence C left by one place.
2. Placing a 0 to the front (MSB) of the partial sum sequence S.
3. Finally, a ripple carry adder is used to add these two together and computing the resulting sum.

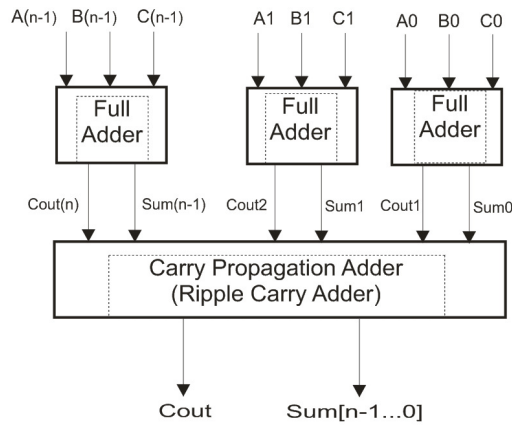


FIGURE 1: Computation Flow of Carry Save Adder

3. BEHAVIORAL ANALYSIS OF THE MODIFIED ARCHITECTURE

Figure 2 shows the algorithm of the proposed parallel adder with a completion signal.

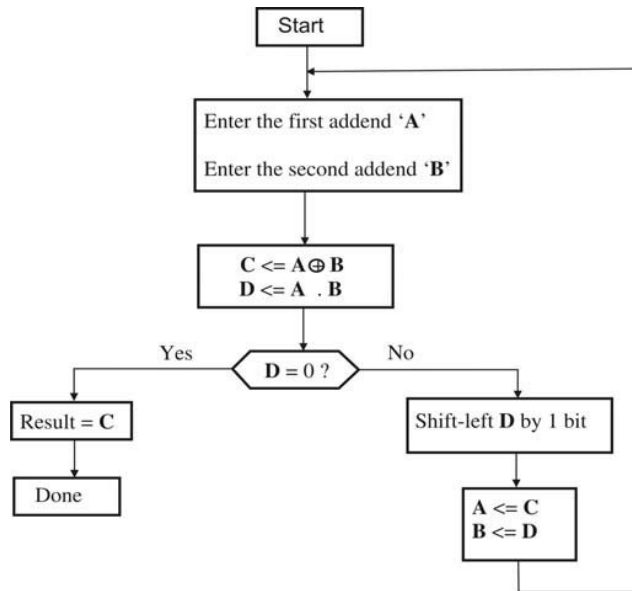


FIGURE 2: Adder Algorithm

Once the two addends are entered into the registers A and B, a XOR operation and an AND operation are performed between the two registers. If the result of the AND operation equals zero

(this indicates that the addition has completed), then the final outcome of the addition is the result of the XOR operation. If the result of the AND operation is different from zero, then it is shifted to the left by 1 bit and sent back to the register B, and the result of the XOR operation is sent to the register A, and the algorithm is applied again until the completion signal is active (this corresponds to the result of AND operation equal to zero). This algorithm was applied to Matlab in order to deduce a mathematical model that predicts the average, the maximum, the minimum number of shifts needed for operands having any number of bits 'n'. Table 1 shows the total number of shift operations required for addends having 2 bits to 15 bits.

3.1 Simulation

The performance of the parallel adder was evaluated in terms of number of number of shifts. A behavioral model was developed because this adder uses a different number of shifts for different addends. This depends on sequence of 0's and 1's in the addends that influences on the result of the AND operation.

Actual ALU's use 8, 16, 32, 64 or 128-bit addends. But in order to study this adder, a behavioral simulation was made on 2, 3, 4, 5, 6, 7, 8, 9, 10, 11, 12, 13, 14 and 15-bit addends. Table 1 shows all the possible combinations for 2 to 15-bit addends distributed in terms of number of shift operations.

The number of shift operations varies from 0 to 'n', 'n' being the number of bits, the results show that:

1.) The total number of additions is:

$$\sum_{i=1}^{2^n} i \quad (1)$$

2.) The maximum number of shift operations is 'n', and has the least number of occurrences, and can be approximated by

$$2^{n-2} \quad (2)$$

3.) For any $n > 2*m$, (n - m) shift operations occur:

$$(m + 2) * 2^{(n+m-3)} \text{ Number of times} \quad (3)$$

4.) The highest number of occurrences happens about 30% of the total additions. Table 2 shows the number of shifts that happen 30% of the occurrences.

Figure 3 shows the average number of shift operations vs. the number of bits.

# of bits	2	3	4	5	6	7	8	9	10	11	12	13	14	15
0 Shift	5	14	41	122	365	1094	3281	9842	29525	88574	265721	797162	2391485	7174454
1 Shift	4	14	49	174	623	2234	7991	28462	100891	355970	1250599	4376982	15268355	53108426
2 Shifts	1	6	30	136	588	2464	10104	40768	162448	640896	2508128	9750144	37691456	1.45E+08
3 Shifts	0	2	12	64	312	1440	6432	28064	120320	508928	2129536	8832512	36366336	1.49E+08
4 Shifts	0	0	4	24	128	650	3040	13952	62592	275968	1200384	5165056	22028288	93255680
5 Shifts	0	0	0	8	48	256	1280	6144	28544	129536	578048	2545664	11091968	47908864
6 Shifts	0	0	0	0	16	96	512	2560	12288	57344	261632	1173504	5195776	22765568
7 Shifts	0	0	0	0	0	32	192	1024	5120	24576	114688	524288	2357248	10461184
8 Shifts	0	0	0	0	0	0	64	384	2048	10240	49152	229376	1048576	4718592
9 Shifts	0	0	0	0	0	0	0	128	768	4096	20480	98304	458752	2097152
10 Shifts	0	0	0	0	0	0	0	0	256	1536	8192	40960	196608	917504
11 Shifts	0	0	0	0	0	0	0	0	0	512	3072	16384	81920	393216
12 Shifts	0	0	0	0	0	0	0	0	0	0	1024	6144	32768	163840
13 Shifts	0	0	0	0	0	0	0	0	0	0	0	2048	12288	65536
14 Shifts	0	0	0	0	0	0	0	0	0	0	0	0	4096	24576
15 Shifts	0	0	0	0	0	0	0	0	0	0	0	0	0	8196

TABLE 1: Number of shift operations per number of bits

Number of bits	Number of shifts that happen 30% of total occurrences
2	0
3 to 6	1
7 to 14	2
15 to 30	3
31 to 62	4

TABLE 2: Number of shifts that happen 30% of total occurrences

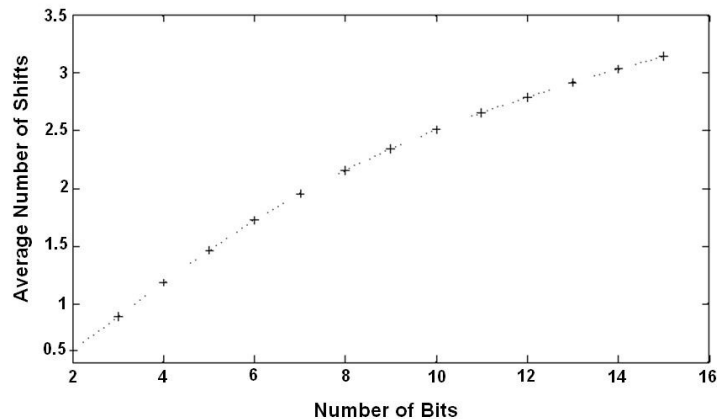


FIGURE 3: Average number of shifts vs. Number of bits

3.2 Modeling

The data shown in figure 2 was injected into Matlab' Curve fitting tool in order to deduct a mathematical model that gives the average number of shifts for addends having up to 128 bits. The model obtained is shown in (4)

$$ANS = 1.759 n^{0.3801} - 1.744 \quad (4)$$

With ANS: Average Number of Shifts, and n: Number of bits. The Goodness of fit was as follows:

- Sum of squares due to errors (SSE): 0.01361 ≈ 0
- R-square: 0.9984 ≈ 1
- Adjusted R-square: 0.9982 ≈ 1
- RMSE: 0.03518 ≈ 0

These results show that the fit was of a good quality. Figure 4 shows the average number of shifts vs. the numbers of bits for addends having up to 128 bits according to the mathematical model obtained.

Table 3 shows the average number of shifts for standard adders having 8, 16, 32, 64 or 128 bits

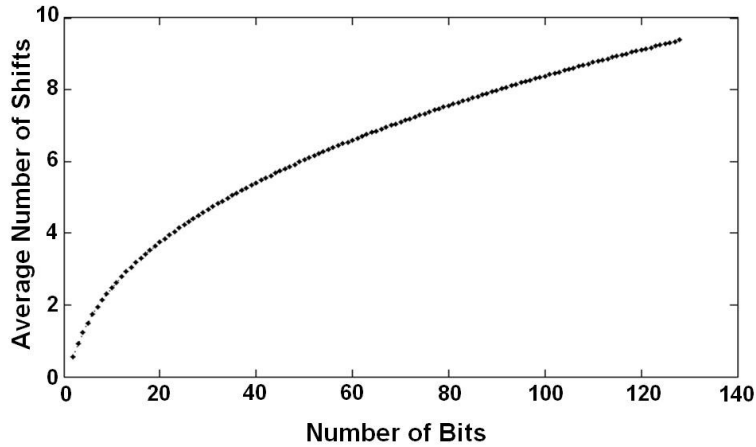


FIGURE 4: Average number of shifts vs. number of bits according to the mathematical model.

n-bit addends	ANS
8	2.1578
16	3.3021
32	4.8231
64	6.8026
128	9.3789

TABLE 3: Average number of shifts for standard adders

4. DESIGN AND IMPLEMENTATION OF THE SYNCHRONOUS PARALLEL ADDER WITH A COMPLETION SIGNAL

4.1 Synchronous Shift-left Register Design

The shift-left operation is critical to the performance of this adder. In order to minimize the hardware needed for its implementation, the same register that stores the result of the AND operation ($D \leq A \cdot B$) was modified in order to accommodate the shift operation. A 2-to-1

multiplexer was added to each D flip-flop. The selection bit of these multiplexers allow either the loading of D when Load/Shift = '1' or the shift to the left of D by 1 bit when Load/Shift = '0'. These actions happen at the rising edge of the clock since this circuit works in synchronous mode of operation. Figure 5 shows the logic circuit for the synchronous shift-left operation.

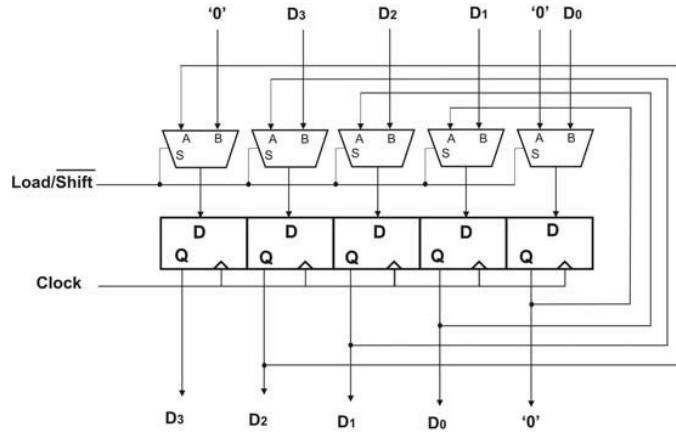


FIGURE 5: Shift-Left Register Logic Circuit

4.2 Shift-left Register Simulation

The logic circuit of figure 4 was simulated with Quartus II design software. Figure 6 shows the output waveforms. For testing purposes, a binary data of D[3..0]=1111 was sent to the register D. This value was first loaded into the register (Load/Shift = '1'), then it was shifted to the left by 1 bit after each rising edge of the clock. Table 4 shows the timing and the bit values of the D registers.

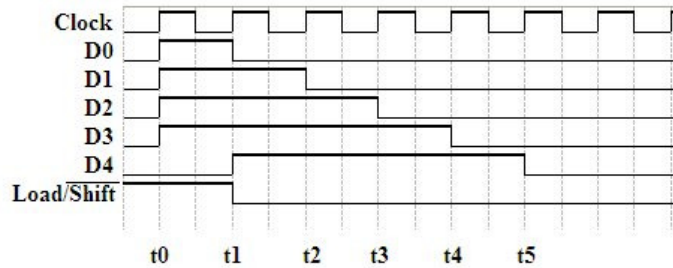


FIGURE 6: Output waveforms of the Shift-left register

Timing	Action	Load/Shift	D4&D[3..0]
t0	Load data	1 (Load)	01111
t1	Shit-left by 1 bit	0 (Shift)	11110
t2	Shit-left by 1 bit	0 (Shift)	11100
t3	Shit-left by 1 bit	0 (Shift)	11000
t4	Shit-left by 1 bit	0 (Shift)	10000
t5	Shit-left by 1 bit	0 (Shift)	00000

TABLE 4: Timing of shift-left logic circuit

4.3 Synchronous Parallel Adder Design

Figure 6 shows the logic circuit of the proposed synchronous adder. For simulation purposes, the circuit was designed for 4-bit addends. The same principle can be easily extended to 32, 64-bit or more addends. An extra bit is needed as the carry bit.

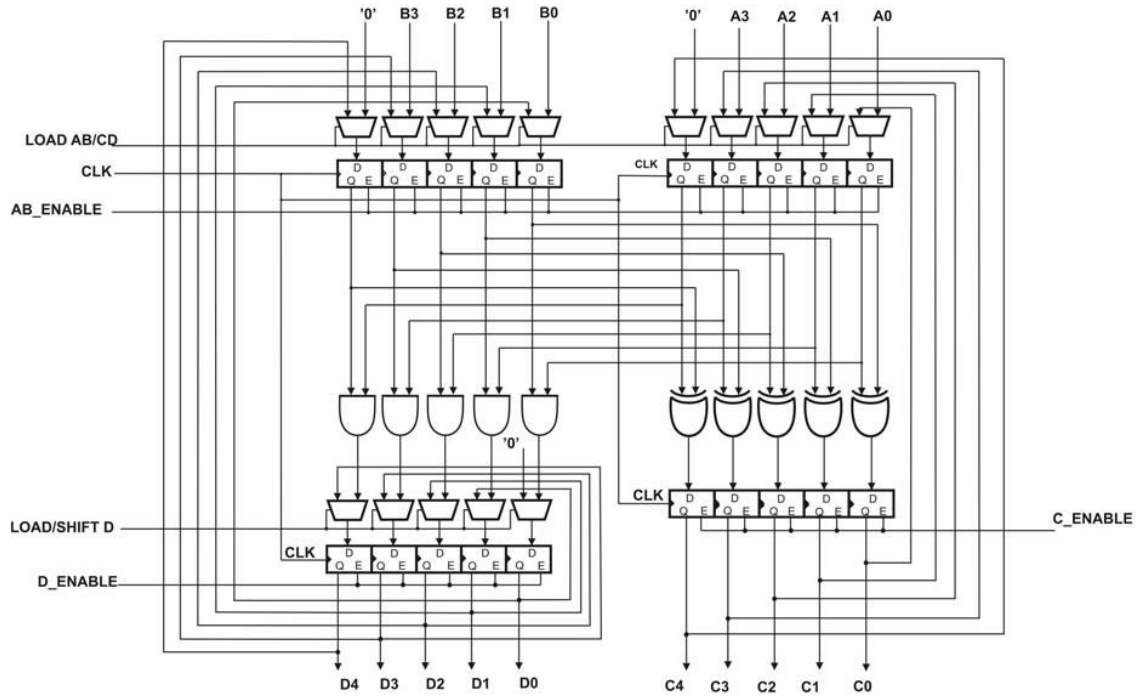


FIGURE 7: Logic Circuit of the Synchronous Adder

The logic circuit of figure 7 is made of 4 registers: A and B to load the addends, C and D to store the results of XOR and AND logic operations. The registers A and B have 2-to-1 multiplexers connected at their inputs used to select either the addends A and B or to reload C and D after the XOR and AND logic operations.

This logic circuit stops shifting the register D and reloading the registers A and B when the register D is equal to 0. In order to keep the logic circuit of figure 8 simple, it does not show a “zero-detector” at the output of register D (Basically a 5-input NOR gate).

4.4 Synchronous Parallel Adder Simulation

The logic circuit of figure 7 was simulated with Quartus II design software. D-flip-flops with Enable signal were used to make the registers A, B, C and D. For testing purposes, a binary value of ‘1011’ was loaded into the register A, and ‘0110’ was loaded into the register B. A manual execution of the algorithm of figure 1 using these addends shows that three shift operations are needed to obtain the result. Table 5 shows the control signals used for the synchronous parallel adder.

Figure 8 shows the input and output wave forms, and table 6 shows the timing and the values of the signals.

Signal	Function
AB_Enable	Enable Signal for A and B registers
C_Enable	Enable Signal for C register
D_Enable	Enable Signal for D register
Load AB/CD	If =‘1’ load A and B into registers A and B If =‘0’ load C=A+B into register A, and load D=A.B into register B
Load/Shift D	If=‘1’ load A.B into register D if ‘0’ Shift D to the left

TABLE 5: Control signals

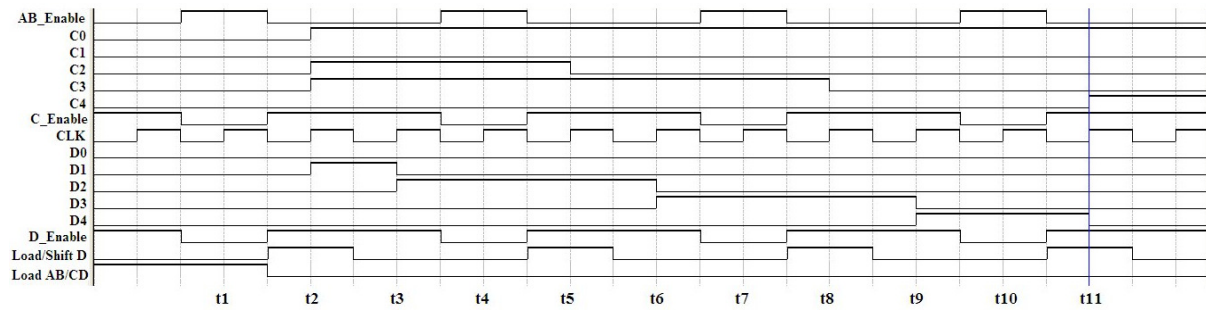


FIGURE 8: Wave forms of the Synchronous Adder

Timing	Action	Values
t1	Load A, Load B	A = '1011' B = '0110'
t2	$C \leq A + B, D \leq A \cdot B$	C = '01101' D = '00010'
t3	Shift D to the left	D = '00100'
t4	Load C into A, Load D into B	A = '01101' B = '00100'
t5	$C \leq A + B, D \leq A \cdot B$	C = '01001' D = '00100'
t6	Shift D to the left	D = '01000'
t7	Load C into A, Load D into B	A = '01001' B = '01000'
t8	$C \leq A + B, D \leq A \cdot B$	C = '00001' D = '01000'
t9	Shift D to the left	D = '10000'
t10	Load C into A, Load D into B	A = '00001' B = '10000'
t11	$C \leq A + B, D \leq A \cdot B$	C = '10001' D = '00000'

TABLE 6: timing of synchronous adder circuit

Table 6 shows that at t11, the register D has zero, and the register C has the result of the addition. Three shift operations were needed to obtain the result of this addition in this example.

5. DESIGN AND IMPLEMENTATION OF ASYNCHRONOUS PARALLEL ADDER WITH A COMPLETION SIGNAL

5.1 Asynchronous Shift-left Register Design

The shift-left operation is critical in the asynchronous mode of operation as well. Figure 9 shows the shift-left operation logic circuit in asynchronous mode. Similarly to the synchronous mode, 2-to-1 multiplexers were used to select either new data into the D register (Load/Shift D = '1') or to shift the existing data in the register D (Load/Shift D = '0'). In order to remove the clock signal, additional registers were added to work in 'master-slave' mode.

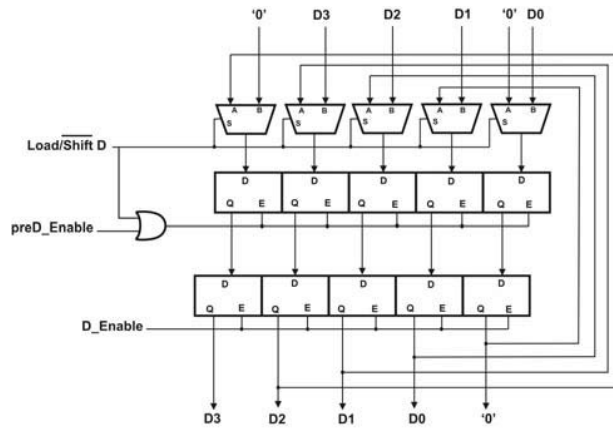


FIGURE 9: Asynchronous Shift Register

5.2 Asynchronous Shift-left Register Simulation

Figure 9 shows the Quartus II simulation of the asynchronous shift register of figure 8. For testing purposes, a value of D=[1111] was first loaded into the register D (t1 in figure 11, Load/Shift = '1'). In order to shift the data by 1 bit to the left, Load/Shift = '0', and send an impulse to the register preD (master) '1' →'0', followed by a second impulse to the register D (slave) '0' →'1'. This is illustrated at (t2, t3), (t4, t5), (t6, t7) etc. in figure 10. Table 7 shows the asynchronous shift register simulation results and control signals in greater detail.

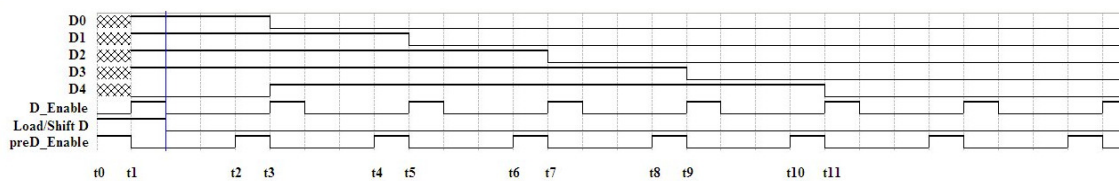


FIGURE 10: Asynchronous Shift Register

Timing	Action	Control Signals	D4&D[3..0]
t0→t1	Load data	Load/Shift D <= '1' preD_Enable <= '1'→'0' D_Enable <= '0'→'1'	01111
t2 →t3	Shit-left by 1 bit	Load/Shift D <= '0' preD_Enable <= '1'→'0' D_Enable <= '0'→'1'	11110
t4 →t5	Shit-left by 1 bit	Load/Shift D <= '0' preD_Enable <= '1'→'0' D_Enable <= '0'→'1'	11100
t6 →t7	Shit-left by 1 bit	Load/Shift D <= '0' preD_Enable <= '1'→'0' D_Enable <= '0'→'1'	11000
t8 →t9	Shit-left by 1 bit	Load/Shift D <= '0' preD_Enable <= '1'→'0' D_Enable <= '0'→'1'	10000
t10 →t11	Shit-left by 1 bit	Load/Shift D <= '0' preD_Enable <= '1'→'0' D_Enable <= '0'→'1'	00000

TABLE 7: Timing of shift-left logic circuit

5.3 Asynchronous Parallel Adder Design

Figure 10 shows the logic circuit for the 4-bit asynchronous adder. This logic circuit is very similar to its synchronous version. It contains four registers A, B, C and D. 4-bit addends were used in figure 11, plus an extra bit as carry.

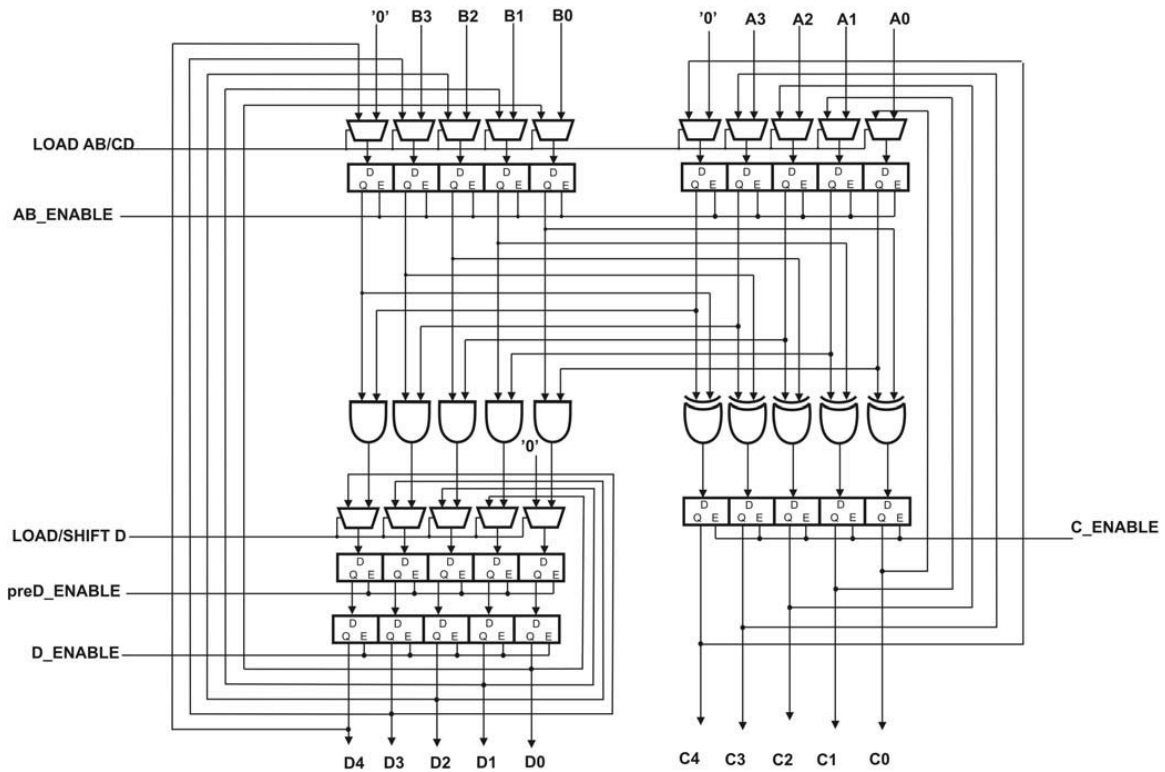


FIGURE 11: 4-bit Asynchronous Parallel Adder

5.4 Asynchronous Parallel adder Simulation

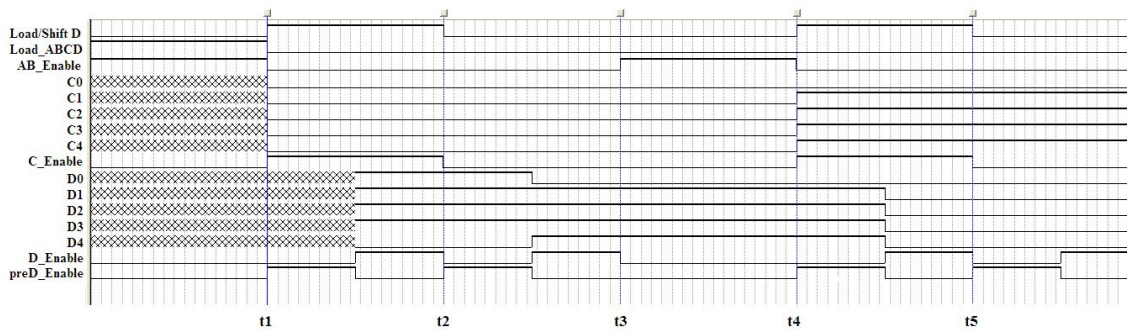


FIGURE 12: 4-bit Asynchronous Parallel Adder Simulation Results

Figure 12 shows the Quartus II simulation results of the 4-bit asynchronous parallel adder. This circuit was simulated with addends $A = [1111]$ and $B = [1111]$. First the addends values were loaded into the registers A and B ($Load_ABCD = '1'$ and $AB_Enable = '1'$). Then the results of $C \leftarrow (A \text{ AND } B)$ and $D \leftarrow (A \text{ XOR } B)$ were loaded into the registers C and D ($Load/ShiftD \leftarrow '1'$, $preD_Enable \leftarrow '0' \rightarrow '1'$, $D_Enable \leftarrow '1' \rightarrow '0'$ and $C_Enable \leftarrow '1'$). Since the register D is not equal to zero, its contents are shifted to the left by 1 bit ($Load/ShiftD \leftarrow '0'$ and $preD_Enable \leftarrow '0' \rightarrow '1'$, $D_Enable \leftarrow '1' \rightarrow '0'$). The contents of registers C and D are loaded into the registers A and B ($Load_ABCD = '0'$ and $AB_Enable = '1'$) and the procedure is repeated again. Table 8 shows the asynchronous simulation in greater detail.

Timing	Action	Control Signals	Values
0 → t1	Load A, Load B	AB_Enable <= '1', Load_ABCD <= '1'	A = '01111', B = '01111'
t1 → t2	C <= A + B, D <= A . B	Load/Shift D <= '1', C_Enable <= '1' preD_Enable <= '1'→'0', D_Enable <= '0' →'1'	C = '00000', D = '01111'
t2 → t3	Shift D to the left	Load/Shift D <= '0', preD_Enable <= '1'→'0' D_Enable <= '0' →'1'	D = '11110'
t3 → t4	Load C into A, Load D into B	Load_ABCD <= '0', AB_Enable <= '1'	A = '00000', B = '11110'
t4 → t5	C <= A + B, D <= A . B	Load/Shift D <= '1', C_Enable <= '1' preD_Enable <= '1'→'0', D_Enable <= '0' →'1'	C = '11110', D = '00000'

TABLE 8: Timing of asynchronous adder circuit

The execution of the algorithm stopped at t5, where D='00000' and C='11110' which represents the final result of the binary addition.

6. CONCLUSION

A modified architecture of parallel binary addition based on a series of logic XOR, AND and Shift operations was introduced in this paper. Its behavioral analysis was simulated with Matlab. The results show that for 128-bit addends, an average of 9.3789 shift operations is needed. Its structural analysis was simulated using Quartus II, where the synchronous and asynchronous technology-independent logic circuits were designed and simulated. For n-bit addends, and for synchronous mode of operation, (n+1) XOR gates, (n+1) AND gates, 4 x (n+1) D flip-flops and 3 x (n+1) 2-to-1 multiplexers are needed. For the asynchronous mode of operation, (n+1) XOR gates, (n+1) AND gates, 5 x (n+1) D flip-flops and 3 x (n+1) 2-to-1 multiplexers are needed.

REFERENCES

1. Bruce Gilchrist, J. H. Pomerene, and S. Y. Wong, "Fast Carry Logic for Digital Computers," IRE Transactions on Electronic Computers, vol. EC-4, pp. 133-136, 1955.
2. E.E. Swartzlander, "Computer Arithmetic", volume I, IEEE computer society press, 1990
3. I. Koren, "Computer arithmetic algorithms", Prentice-Hall, 1993
4. F.C Cheng, S. H. Unger, "Self-Timed Carry-Look Ahead Adders", IEEE Transactions on Computers, Vol. 49, No. 7, July 2000
5. M. Alioto, G. Palumbo, "Analysis and Comparison on Full Adder Block in Submicron Technology", IEEE Transactions on Very Large Scale Integration (VLSI) Systems, Vol. 10, No. 6, December 2002
6. M. D. Ercegovic, T. Lang, "Digital Arithmetic", Morgan Kaufmann Publishers. An imprint of Elsevier Science, 2004.
7. B. Parhami, "Computer Arithmetic, Algorithm and Hardware Design", Oxford University Press, New York, pp. 91-119, 2000.
8. R. P. P. Singh, P. Kumar, B. Singh, "Performance Analysis of 32-bit Array Multiplier with a Carry Save Adder and with a Carry Look Ahead Adder", International Journal of Recent Trends in Engineering, Vol. 2, No. 6, November 2009.
9. T. Kim, W. Jao, and S. Tjiang, "Arithmetic optimization using carry-save-adders", in Proc. Design Automation Conf., Jun. 1998, pp. 433-438.

10. T. Kim and J. Um, "A *timing-driven synthesis of arithmetic circuits using carry-save-adders*", in Proc. Asia and South Pacific Design Automation Conf., Jan. 2000, pp. 313–316.
11. Y. Kim and T. Kim, "An *accurate exploration of timing and area trade-offs in arithmetic optimization using carry-save adder cells*", in Proc. Midwest Symposium on Circuit and Systems, Aug. 2000.
12. T. Kim, W. Jao, and S. Tjiang, "Circuit Optimization using Carry-Save-Adder Cells", IEEE TCAD, October 1998.
13. J. Um, T. Kim, C. L. Liu, "Optimal Allocation of Carry-Save-Adders in Arithmetic Optimization", Proc. ICCAD, 1999.
14. B. Ramkumar, H. M. Kittur, P. Mahesh Kannan, "ASIC implementation of Modified Faster Carry Save Adder". European Journal of Scientific Research. ISSN 1450-216X, Vol.42 No.1, 2010, pp.53-58.

Peltier Thermoelectric Modules Modeling and Evaluation

Chakib Alaoui

College of Computers and Information Technology
Taif University, KSA

chakib@tu.edu.sa

Abstract

The purpose of this work is to develop and experimentally test a model for the Peltier effect heat pump for the transient simulation in Spice software. The proposed model uses controlled sources and lumped components and its parameters can be directly calculated from the manufacturer's data-sheets. In order to validate this model, a refrigeration chamber was designed and fabricated by using the Peltier modules. The overall system was experimentally tested and simulated with Spice. The simulation results were found to be compatible with the experimental results. This model will help designers to better design thermal systems using the Peltier modules.

Keywords: Peltier Effect thermoelectric Heat Pumps; Heat sink; Spice Model.

1. INTRODUCTION

The Peltier effect thermoelectric heat pump is a semiconductor based electronic component that functions as a heat pump. Just by applying a low DC voltage to this module, one surface gets cold and the other surface gets hot. And just by reversing the applied DC voltage, the heat moves to the other direction. Thus this thermoelectric device works as a heater or a cooler.

The Peltier thermoelectric heat pumps have been used for medical devices [1,2], sensor technology [3,4], cooling integrated circuits [5], automotive applications and military applications. This project is about the validation of a Spice model of the Peltier thermoelectric heat pump suitable for transient simulations. In order to verify this model, a cooling chamber was designed and fabricated. Its inside temperature was measured under different rates of input power and its performance was calculated. This Spice compatible model will help designers predict the thermal behavior of system using Peltier thermoelectric heat pumps.

2. PRINCIPLE OF OPERATION AND MODELING

The thermoelectric heat pump was discovered by a French watchmaker during the 19th century. It is described as a solid state method of heat transfer generated primarily through the use of dissimilar semiconductor material (P-type and N-type).

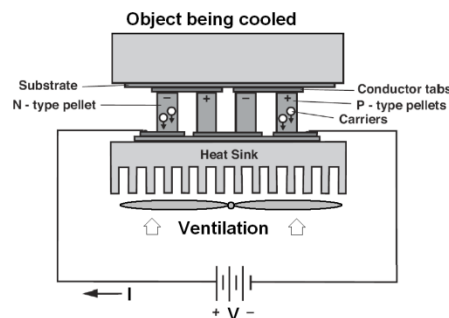


FIGURE 1: Peltier effect heat pump electrical and mechanical installation.

Figure 1 shows a Peltier effect heat pump typical mechanical and electrical installation. Like conventional refrigeration, Peltier modules obey the laws of thermodynamics. Basically the refrigerant in both liquid and vapor form is replaced by two dissimilar conductors. The solid junction (evaporator surface) becomes cold through absorption of energy by the electrons as they pass from the low energy level to the high energy level. The compressor is replaced by a DC

power source that pumps the electrons from one semiconductor to another one. A heat sink replaces the conventional condenser fins, discharging the accumulated heat from the system. The following table outlines the differences and similarities between the thermoelectric module and the conventional refrigerator.

The evaporator	Allows the pressurized refrigerant to expand, boil and evaporate (The heat is absorbed during the change of state from liquid to gas)	At the cold junction, heat is absorbed by the electron as they pass from a low energy level (P-type) to a high energy level (N-type)
The compressor	Acts on the refrigerant and recompresses the gas to liquid. The refrigerant leaves the compressor as a vapor.	The power supply provides the energy to move the electrons
The condenser	Expels the heat absorbed at the evaporator to the environment plus the heat produced during compression into the ambient. Also, the refrigerant returns to the liquid phase.	At the hot junction, heat is expelled to the heat sink as the electrons move from high energy level to the low energy level

TABLE 1: Comparison between the conventional and the solid state refrigeration

The absorbed heat q_a , the emitted heat q_e and the input electrical power P used to operate the modules can be described from equations (1). The heat pumped is the sum of the Peltier effect term ($\alpha m.T.I$), the heat conduction term ($\Delta T/\Theta m$) and the Joule effect term ($I^2 R m$). It is conventional to leave out the effect of the Thompson phenomena because it is negligibly small. Additionally, it is common practice to apply equivalent electrical circuit scheme in one-dimensional heat transfer problems [7].

$$\begin{aligned}
 q_a &= \frac{\Delta T}{\Theta m} + \alpha m.T_a.I - \frac{I^2 R m}{2} \\
 q_e &= \frac{\Delta T}{\Theta m} + \alpha m.T_e.I + \frac{I^2 R m}{2} \\
 P &= V.I = I(\alpha m.\Delta T + R m.I)
 \end{aligned}
 \tag{1}$$

Where: $R m$ is the resistance of the module, αm is the Seebeck-coefficient of the pn junction, Θm is the thermal resistance, T_e is the absolute temperature of the heat emitted, T_a is the absolute temperature of the heat absorbed and $\Delta T = T_e - T_a$. q_a and q_e represent the amount heat absorbed and emitted from the module. Finally, V and I are the voltage and the current from the input power supply. The Coefficient Of Performance, or COP in short, describes the efficiency of the heat pump when working in cooling and in heating modes. The COP is expressed by equations (2).

$$COP = q_a / P \tag{2}$$

2.1 Previous Models

Various equivalent circuits have been developed to model the behavior of the Peltier heat pump. The purpose of these models is to simulate the behavior of Peltier modules in CAD tools like Spice, and hence to predict the amount of heat that it can transfer. Figure 2 proposes a thermal network [6]. In this scheme, the Peltier effect is represented by the flow source $P_s = \alpha m.T_c.I$, the Joule effect by $P_{J/2} = R m I^2/2$ and a thermal resistance term by $R_{th} = \Theta m$.

Figure 3 shows an equivalent circuit of the Peltier effect heat pump based on a Cauer-type network as it is described by [7]. Finally Figure 4 shows a proposed circuit from [8]. It consists of with two dependent sources instead of three and lumped parameters instead of distributed ones as described in previous model.

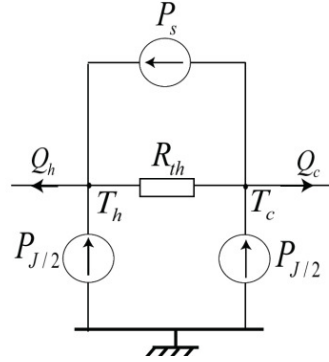


FIGURE 2 : Peltier effect model from [6].

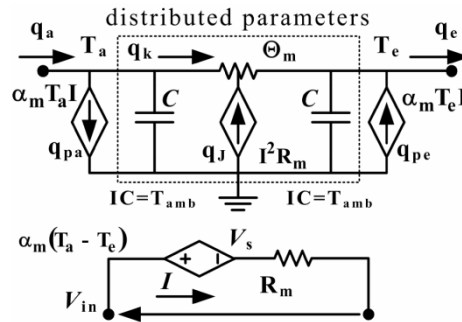


FIGURE 3 : The Equivalent Peltier from [7]

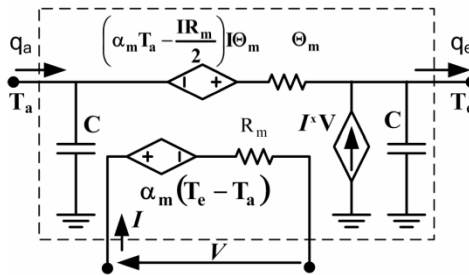


FIGURE 4 : The Equivalent Peltier from [8]

2.2 The Proposed Model

Figure 5 shows a modified equivalent circuit of the Peltier module. This model is made of two current dependent voltage sources, two current dependent current sources and two lumped parameters. It can be easily implemented on Spice since all the elements exist on its library. The parameters am , Θm and Rm can be directly calculated from the manufacturers data sheet according to equations (3).

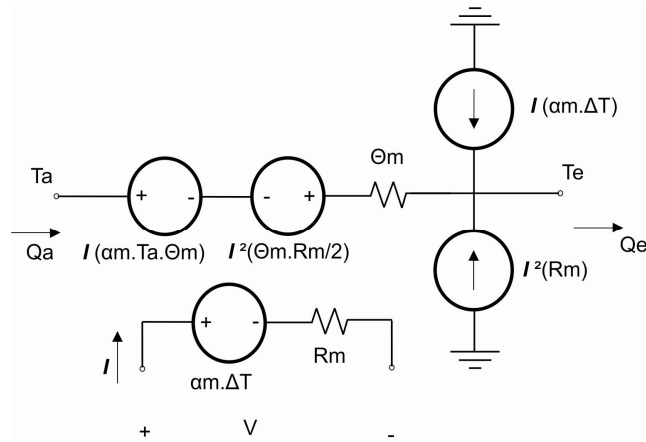


FIGURE 5: Proposed model of Peltier module.

$$Rm = \frac{Vmax}{Imax} * \frac{(Th - \Delta Tmax)}{Th}$$

$$\Theta m = \frac{\Delta Tmax}{Imax * Vmax} * \frac{2Th}{(Th - \Delta Tmax)} \tag{3}$$

$$am = \frac{Vmax}{Th}$$

Where $\Delta Tmax$ is the largest temperature differential that can be obtained with $Imax$ and $Vmax$. Th being the temperature in the hot side.

3. EVALUATION OF THE PROPOSED MODEL

3.1. Design and Fabrication of a Refrigeration Chamber

The main body of the refrigeration chamber has a dimension of: 0.11x0.29x0.33 m³ strongly insulated to minimize heat loss to the ambient air. In the cross section of this chamber, three layers exist: two walls of aluminum separated by an insulating material of 3 cm of thickness. Refer to figure 2.

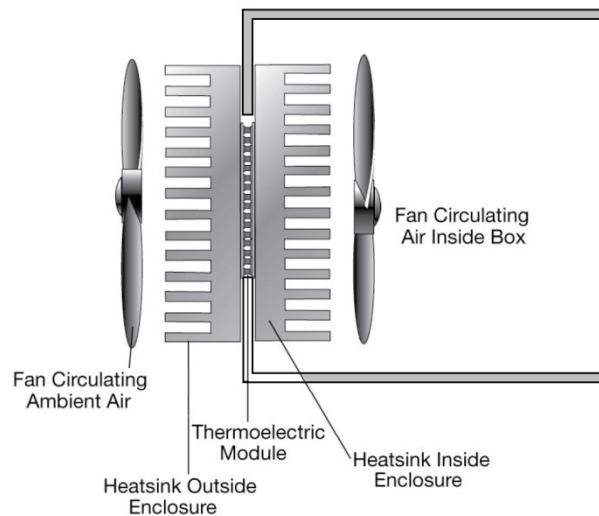


FIGURE 6: Main body of the refrigeration chamber

High density heat sinks were specially fabricated for this project. They are made of Aluminum and are 350 x 75 x 39 mm³, with 21 fins along their length and weight is 1500 Grams. Their specific heat is 0.963 J/g. °C. The “hot” surface of the thermoelectric heat pump must be attached to a heat sink that is capable of carrying away both the heat pumped by the modules and the heat generated by the Joule effect.

The “cold” surface is also attached to another heat sink that will carry away the cold air, hence decreasing the temperature differential ΔT , and then making the thermoelectric more efficient.

A “spacer block” is also put between the modules and the heat sinks. Its thickness, of 18 mm, separates the “hot” heat sink from the “cold” one, which yields to a maximum heat transfer.

Peltier modules from Ferrotec [9] were used in this experiment. Their specifications are $I_{max}=8.5A$, $Q_{max}=80W$, $V_{max}=17.5V$, $DT_{max}=72^{\circ}C$.

Their thermal resistance, Seebeck coefficient and internal resistance were calculated according to equations (3). $R_m = 1.6\Omega$, $\Theta_m = 1.25 K/W$ and $am = 0.054 V/K$ for $T_h = 300K$.

3.2. Simulation of the Refrigeration Chamber

The equivalent circuit of the chamber was implemented on Spice according to figure 3. The lumped parameters R's and C's are defined as follows:

- R1: Thermal resistance of the chamber's wall
- R2, R5: Thermal resistance of the heat sink + fan
- R3, R4: Assembly's thermal resistance
- C3, C4: Heat capacity of alumina ceramic plates and pellets of the Peltier modules.
- C2, C5: Heat capacity of the heat sinks
- C1: Heat capacity of the chamber
- TSSHC: Temperature inside the chamber
- Ta/Te: Cooling/Heating temperature at Peltier module
- Ta'/Te': Cooling/Heating temperature at Peltier module after assembly

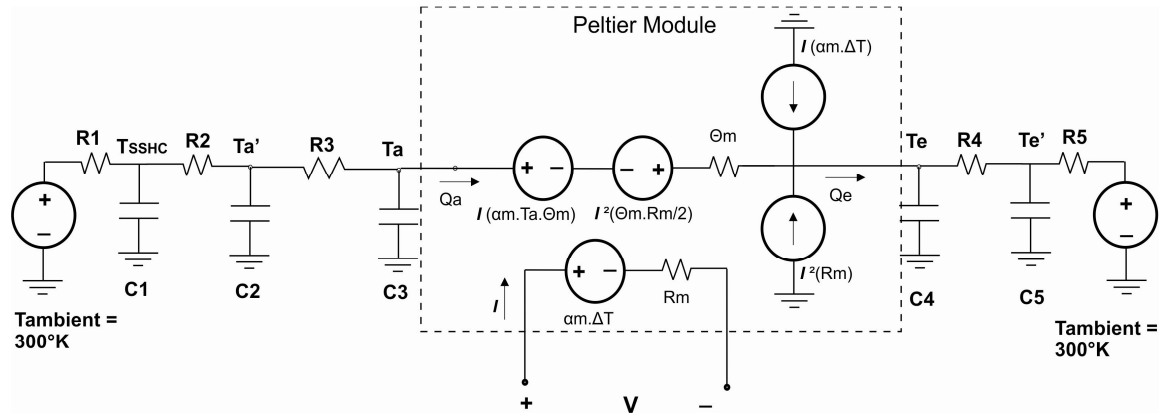


FIGURE 7: Spice equivalent circuit of the refrigeration chamber

3.3. Experimental Evaluation of Refrigeration Chamber

The thermal output power was calculated by using the laws of thermodynamics [10, 11, 12]:

Heat given by modules = [Heat gained by aluminum chamber + Heat gained by the air inside + Heat gained by heat sinks + Outside losses]. First order equations were used to calculate the COP. The outside losses are neglected at the beginning of the experiment when the temperature increases linearly with time.

Heat gained by the air: $P(\text{air})$

$$P(\text{air}).dt = n.c'.dT \tag{4}$$

with:

$P(\text{air})$: Output power (W)

n: Number of moles (0.4616 mole)

c' : Molar heat capacity (20.93 j/mole. °K)

dt : $t_2 - t_1$ (sec)

Then:

$$P(\text{air}) = 9.65 \, dT/dt \text{ (W)}$$

Heat gained by the chamber and the heat sinks: $P(\text{Aluminum})$

$$H = m.c.dT \tag{5}$$

with

H : The gained energy (J)

m : Total mass (Chamber = 2200g, Heat sinks = 1875.75g) = 4048.75 g

c : Specific heat (0.963 J/g. °C for Aluminum)

$$P(\text{Aluminum}) = H / dt = 3908.6 \, dT/dt$$

3.4. Experimental Results

The refrigeration chamber was run for many values of input current. The temperature, time and input electrical power were measured. The simulation and experimental results are shown in figure 4. The obtained COP for the different current is shown in table 3. The experimental results show a good fit of the Spice simulation with the experimental data.

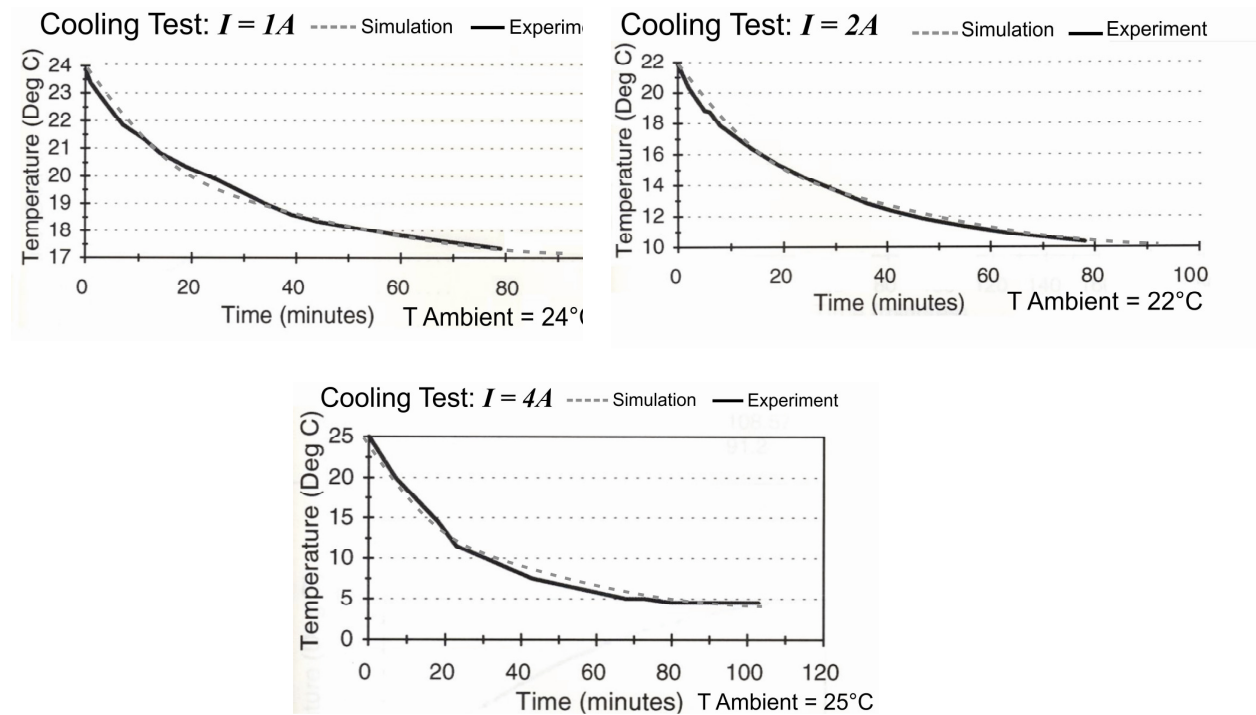


FIGURE 8: Simulation and Experimental Results for 1A, 2A and 4A Cooling

Input Current (A)	Input Power (W)	Output Power (W)	COP(Experimental)	COP(Simulation)
1	12.89	24.61	1.91	2.04
2	52.62	43.06	0.818	0.98
3	119.58	55.37	0.463	0.51
4	216.56	55.38	0.255	0.32

TABLE 2: Cooling Performance Results

4. CONCLUSION

A model has been developed to simulate the transient state for a Peltier thermoelectric module. This model uses controlled sources and lumped parameters, hence can be easily simulated with simulation software like Spice. The model parameters were calculated by using the manufacturer's datasheet.

In order to validate this model, a refrigeration chamber that uses Peltier modules was designed and fabricated. The overall system was tested and simulated with Spice under various values of input currents. The result is a good fit between the simulation and the experimental data.

This model can easily extended with lumped parameters R's and C's representing the thermal resistance and the heat capacity of a thermal system.

REFERENCES

1. C. Alaoui, Z. Salameh, "Solid State Heater Cooler: Design and Evaluation", Large Engineering Systems Conference on Power Engineering (July 2001).
2. J. C. Reynaud, F. Martini, "A new interface chamber for the study of mammalian nervous tissue slices", Journal of Neuroscience Methods 58(1995) , pp. 203-208.
3. P. Ancy, M. Gshwind, "New concept of integrated Peltier cooling device for the preventive detection of water condensation", Sensors and Actuators B 26-27 (1995) pp. 303-307.
4. H. Stachowiak, S. Lassue, "A thermoelectric sensor for fluid flow measurement. Principles, calibration and solution for self temperature compensation". Flow, measurement and instrumentation 9 (1998) pp. 135-141.
5. E. D. Baetselier, W. Goedertier, "A survey of the thermal stability of an active heat sinks", Microelectron reliability, Vol 37. No. 12 (1997), pp. 1805-1812.
6. G. Selliger, J. Stephan and S. Lange, "Hydroadhesive gripping by using Peltier effect", ASME International Mechanical Engineering Congress & Exposition (IMECE), pp.3-8, Florida USA, November 2000.
7. J. Chavez, J. Ortega, J. Salazar, A. Turo, and J. Garcia, "Spice model of thermoelectric elements including thermal effects," Proceedings of the Instrumentation and Measurement Technology Conference, 2000, pp. 1019 - 1023.
8. S. Lineykin, S. B. Yaakov, "Pspice Equivalent Circuit of Thermoelectric Coolers", Power Electronics Specialists Conference, PESC '05. IEEE 36th, (2005).
9. ITI Ferrotec: "Thermoelectric product catalog and technical reference manual", catalog No. 100.
10. J. P. Holman, "Heat transfer", 7th ed., London: McGraw-Hill, (1992)
11. P. Atkins, "Physical Chemistry", W.H. Freeman and Company, (1994).

12. Warren L. McCabe, "*Chemical Engineering Series*", McGraw-Hill Inc. (1993).

Margin Parameter Variation for an Adaptive Observer to a Class of Systems

Elleuch Dorsaf

*Industrial Processes Control Unit
Sfax University, ENIS
Sfax, BP W3038, Tunisia*

dorsafelleuch@yahoo.fr

Damak Tarak

*Industrial Processes Control Unit
Sfax University, ENIS
Sfax, BP W3038, Tunisia*

tarak.damak@enis.rnu.tn

Abstract

In this paper, adaptive observer robustness is studied. The adaptive observer is proposed to a nonlinear system linearized by output injected for variable structure systems. Despite, the adaptive observer is suggesting to supply the parameter variation but it isn't usually verified. Unfortunately, the parameter uncertainty impact state convergence. For that a margin parameter variation is determined which the convergence of the state is guaranty. Simulation results show that the adaptive observer is robust only in the definite parameter margin variation.

Keywords: Nonlinear Systems, Adaptive Observer, Margin Parameter Variation, Robustness.

1. INTRODUCTION

During the running, it is not usually possible for some systems to know about the exact value of the system parameters. These kinds of systems have two proposed methods to be studied. The first is to augment the state vector which will include the state and the unknown parameters [15]. The second is to build an adaptation law depending only on measured and estimated state variables. Indeed, in literature ([1], [2], [3], [4]), adaptive observers using parameter adaptation law to estimate state variables are considered.

In [5] the authors have compared these two methods and they conclude that these two techniques have the same results and the adaptive observer is more robust for nominal systems. In [6] an adaptive observer is defined as a recursive algorithm which allows state and parameter estimation. These parameters can be assumed as unknown inputs [7].

To determine the adaptation law for some class systems, the following techniques are proposed:

- Linearization by output injected for variable structure systems [6],
- Linearization by feed forward [7],
- Systems transformed into a canonical form in which the error becomes linear at the new coordinate ([8], [9], [10], [11]),
- Lipschitz nonlinear systems [12],

The studied adaptive observer made to a constant unknown parameter of system. But, really, the parameter varied in time. Recently, the authors in ([12], [13], [14]) studied the robustness of an adaptive observer. For that a set of parameter are determined which the state estimation are improved.

The aims contribution of this paper is to determine the parameter variation margin which the adaptive observer build to systems linearization by output injected for variable structure systems ([6]) remains still robust.

2. ADAPTIVE OBSERVER FOR SYSTEMS TRANSFORMED INTO A CANONICAL FORM ([8], [9], [10], [11])

2.1. Observer architecture:

Consider the nonlinear system:

$$\begin{cases} \dot{x} = f(x) + q_0(x, u) + \sum_{i=1}^p \theta_i q_i(x, u) \\ \dot{x} = f(x) + q_0(x, u) + \theta^T Q(x, u) \\ y = h(x) \end{cases} \quad (1)$$

Where:

$$x \in R^n; u \in R^m; q_i \in R^n * R^m \rightarrow R^n \text{ for all } 1 \leq i \leq p; Q(x, u) \in R^{p*n};$$

$$\theta \in [\theta_1 \ \theta_2 \ \dots \ \theta_p]^T \in R^p; y \in R$$

In ([8], [9], [10], and [11]) the authors present the different steps to change the system (1) into the form (2) in which the error becomes linear. The system is transformed in a canonical form if there exists a global state space diffeomorphism and the parameters become independent as such:

$$\begin{cases} \xi = T(x), T(x_0) = 0 \\ \dot{\xi} = A_c \xi + \psi_0(x, u) + \sum_{i=1}^p \theta_i \psi_i(x, u) \\ \dot{\xi} = A_c \xi + \psi_0(x, u) + \Psi(x, u)\theta \\ y = C_c \xi \end{cases} \quad (2)$$

With:

$$A_c = \begin{bmatrix} 0 & 1 & 0 & \dots & 0 \\ 0 & 0 & 1 & \dots & 0 \\ \vdots & \vdots & 0 & \ddots & 0 \\ \vdots & \vdots & \vdots & & 1 \\ 0 & 0 & 0 & 0 & 0 \end{bmatrix}; C_c = [1 \ 0 \ \dots \ 0]$$

The parameter adaptation algorithm designed for the systems can be in this form:

$$\begin{cases} \dot{z} = A_c z + \gamma(y, u) + b \sum_{i=1}^p \beta_i(t) \theta_i \\ \dot{z} = A_c z + \gamma(y, u) + b \beta^T(t) \theta \quad ; z \in R^n \\ y = C_c z \end{cases} \quad (3)$$

Where:

$$z = \xi - M(t)\theta \quad ; M = \begin{bmatrix} 0 \\ N \end{bmatrix} \tag{4}$$

With N functioning as the solution of the matrix equation (5):

$$\dot{N} = \begin{bmatrix} -b_2 & 1 & 0 & \dots & \dots & 0 \\ \vdots & 0 & \dots & \dots & \dots & 0 \\ \vdots & \dots & \dots & \dots & \dots & \dots \\ -b_{n-1} & \dots & \dots & \dots & \dots & 1 \\ -b_n & \dots & \dots & \dots & \dots & 0 \end{bmatrix} N + \begin{bmatrix} -b_2 & 1 & 0 & \dots & \dots & 0 \\ \vdots & 0 & \dots & \dots & \dots & 0 \\ \vdots & \dots & \dots & \dots & \dots & \dots \\ -b_{n-1} & \dots & \dots & \dots & \dots & 1 \\ -b_n & \dots & \dots & \dots & \dots & 0 \end{bmatrix} \Psi(y,u) \tag{5}$$

The functions $\Psi(y,u)$ and N are bounded, b_i are the coefficients of a Hurwitz polynomial:

$$s^{n-1} + b_2 s^{n-2} + \dots + b_n .$$

$$\beta^T(t) = [\beta_1(t) \quad \beta_2(t) \dots \beta_p(t)] = C_c A_c M + C_c \Psi(y,u)$$

The adaptive observer is revealed by the following equations [8]:

$$\begin{aligned} \dot{\hat{z}} &= (A_c + kC_c)\hat{z} + \gamma(y,u) + b\beta^T(t)\hat{\theta} - ky \\ \dot{\hat{z}} &= A\hat{z} + \gamma(y,u) + b\beta^T(t)\hat{\theta} - ky \\ \dot{\xi}_i &= A\xi_i + b\beta_i(t) \quad ; \xi_i \in R^n, \xi_i(0) = \xi_{i0} \\ \dot{\xi}_0 &= A\xi_0 + b\beta^T(t)\hat{\theta} \quad ; \xi_0 \in R^n, \xi_0(0) = \xi_{00} \\ \eta^T &= C_c [\xi_1 \quad \xi_2 \quad \dots \quad \xi_p] \\ \dot{W} &= -\alpha W + \eta\eta^T, W \in R^p * R^p, W(0) = W_0 \\ \dot{w} &= -\alpha w - \eta(C_c \xi_0 + y - C_c \hat{z}), w \in R^p, w(0) = w_0 \\ \dot{\hat{\theta}} &= -\Gamma(W\hat{\theta} + w), \hat{\theta}(0) = \hat{\theta}_0 \end{aligned} \tag{6}$$

Where:

The gain k is determined so that the matrix $A = A_c + kC_c$ is Hurwitz.

The vector $\beta(t)$ is bounded.

α is a positive reel.

W_0 is symmetric and semi defined positive.

$\eta(t)$ satisfy the existence condition if there exists $k > 0$ and $\delta > 0$ such as:

$$\int_t^{\delta+t} \eta(\tau)\eta^T(\tau)d\tau \geq k\tau$$

This type of observer is characterized by simplicity to implement it even though it is limited to a class of systems [11] and the error converges exponentially to an arbiter rate [8].

This observer is very robust when the parameters are constant. The efficiency of this architecture will be studied with a linear parameter variation in time. The maximal margin variation of the parameter is determined so that the convergence of the desired state is guaranteed.

2.2. Parameter Margin Variation

During the running the parameters of systems vary, to overcome this parameter variation an adaptive observer is used to estimate joint parameter and unmeasured state. In [16], the author's proved that the adaptation law isn't usually robust to estimate the state for all parameter variation.

In [13] the author's suppose that the unknown parameter is bounded for that the adaptive observer gives a good performance. In this section, a maximal margin of variation is defined for which the adaptation law is still robust, we will study the adaptive observer presented in ([8], [9], [10], [11]) in the case of varied parameter when the following assumptions are satisfied.

Assumptions:

The matrix $A = A_c + kC_c$ is invertible and stable.

$b\beta^T(t)$ is stable.

$$e^T b\beta^T(t)\hat{\theta} \geq 0 \quad \text{and} \quad \tilde{\theta}^T \Gamma^{-1} \dot{\hat{\theta}} > 0$$

$$|\theta_i| > 1 \quad \text{for all } i = 1 \dots p$$

If the vector of parameters varies in time, the nonlinear system transformed will have the form (7) however the observer has the same architecture as (6):

$$\dot{z} = A_c z + \gamma(y, u) + b\beta^T(t)\theta' \tag{7}$$

With

$$\theta' = \theta + \Delta\theta; \Delta\theta = n\theta; n \in R$$

When $\Delta\theta$ is the parameter variation, it is proportionally into the nominal parameters.

The new vector of unknown parameters can be written as such $\theta' = (n + 1)\theta$. We express the theorem:

Theorem:

If the assumptions are satisfied, the observers (6) still robust to estimate the state of systems (1) for all values of n satisfying this relation:

$$n \leq \frac{\|y\|}{\|\max(\theta_i)\|}$$

Proof:

Defining:

$$\text{The error parameter } \tilde{\theta}' = \theta' - \hat{\theta} \Rightarrow \dot{\tilde{\theta}}' = -\dot{\hat{\theta}}$$

$$\text{The error state } e = z - \hat{z}$$

The error dynamics is:

$$\begin{aligned} \dot{e} &= A_c(z - \hat{z}) + b\beta^T(t)(\theta' - \hat{\theta}) + ky - kC_c \hat{z} \\ \dot{e} &= (A_c + kC_c)e + b\beta^T(t)(\theta' - \hat{\theta}) \\ \dot{e} &= (A_c + kC_c)e + b\beta^T(t)\tilde{\theta}' \end{aligned} \tag{8}$$

The stability of the observers (6) with varying parameters is developed with a Lyapunov function defined as:

$$V = \frac{1}{2} e e^T + \frac{1}{2} \tilde{\theta}'^T \Gamma^{-1} \tilde{\theta}' \tag{9}$$

The derived function of V is:

$$\begin{aligned} \dot{V} &= \dot{e} e^T - \tilde{\theta}'^T \Gamma^{-1} \dot{\hat{\theta}} \\ \dot{V} &= (A_c + kC_c) e e^T + b\beta^T(t) \tilde{\theta}' e^T - \tilde{\theta}'^T \Gamma^{-1} \dot{\hat{\theta}} \\ \dot{V} &= A e e^T + b\beta^T(t) (\theta + \Delta\theta - \hat{\theta}) e^T - (\theta + \Delta\theta - \hat{\theta})^T \Gamma^{-1} \dot{\hat{\theta}} \end{aligned}$$

As defined in assumptions $e^T b\beta^T(t)\hat{\theta} \geq 0$ and $\tilde{\theta}^T \Gamma^{-1} \dot{\hat{\theta}} > 0$ we have:

$$\dot{V} \leq Aee^T + b\beta^T(t)\theta e^T + b\beta^T(t)\Delta\theta e^T - \Delta\theta^T \Gamma^{-1} \dot{\hat{\theta}} + \hat{\theta}^T \Gamma^{-1} \dot{\hat{\theta}} \leq 0$$

Since

$$\Delta\theta^T \Gamma^{-1} \dot{\hat{\theta}} = (\Gamma^{-1} \dot{\hat{\theta}})^T \Delta\theta$$

Then:

$$\Delta\theta(b\beta^T(t)e^T - (\Gamma^{-1} \dot{\hat{\theta}})^T) \leq -(Aee^T + b\beta^T(t)\theta e^T + \hat{\theta}^T \Gamma^{-1} \dot{\hat{\theta}})$$

$$\Delta\theta \leq \frac{-(Aee^T + b\beta^T(t)\theta e^T + \hat{\theta}^T \Gamma^{-1} \dot{\hat{\theta}})}{(b\beta^T(t)e^T - (\Gamma^{-1} \dot{\hat{\theta}})^T)} \leq \frac{1}{b\beta^T(t)e^T - (\Gamma^{-1} \dot{\hat{\theta}})^T}$$

$$\Delta\theta \leq \frac{1}{(\Gamma^{-1} \dot{\hat{\theta}})^T}$$

By including the equation (6) in this inequality we obtain:

$$\dot{\hat{\theta}} = -\Gamma(W\hat{\theta} + w)$$

$$\Delta\theta \leq \frac{1}{(-\Gamma^{-1}\Gamma(W\hat{\theta} + w))^T} \leq w^T$$

$$\Delta\theta \leq w^T$$

(10)

$$\dot{w} = -\alpha w - \eta(C_c \xi_0 + y - C_c \hat{z})$$

This implies

$$w = \frac{1}{\alpha}(-\dot{w} + \eta(C_c \xi_0 + y - C_c \hat{z}))$$

$$w \leq \eta(C_c \xi_0 + y - C_c \hat{z})$$

Where $t \rightarrow \infty \quad e_y \rightarrow 0$

Then:

$$w^T \leq \xi_0^T C_c^T \eta^T \tag{11}$$

Or $\eta^T = C_c [\xi_1 \ \xi_2 \ \dots \ \xi_p]$

Therefore (11) becomes:

$$w^T \leq \xi_0^T C_c^T C_c [\xi_1 \ \xi_2 \ \dots \ \xi_p] \tag{12}$$

If A is invertible and stable then:

$$\dot{\xi}_i = A\xi_i + b\beta_i(t)$$

$$\xi_i = A^{-1}(\dot{\xi}_i - b\beta_i(t)) \leq \lambda_{\max}(A^{-1})(\dot{\xi}_i - b\beta_i(t))$$

With $\lambda_{\max}(A^{-1}) \leq 0$

This implies

$$\begin{aligned} \xi_i &\leq \lambda_{\max}(A^{-1})b\beta_i(t) \\ [\xi_1 \ \xi_2 \ \dots \ \xi_p] &\leq \lambda_{\max}(A^{-1})b\beta_i(t) \end{aligned} \tag{13}$$

$$\dot{\xi}_0 = A\xi_0 + b\beta^T(t)\hat{\theta}$$

$$\xi_0 = A^{-1}(\dot{\xi}_0 - b\beta_i^T(t)\hat{\theta})$$

$$\xi_0^T \leq \lambda_{\max}(A^{-1})\hat{\theta}^T \beta(t)b^T \tag{14}$$

With:

$$\dot{\hat{z}} = (A_c + kC_c)\hat{z} + \gamma(y, u) + b\beta^T(t)\hat{\theta} - ky$$

This implies

$$\hat{\theta}^T \beta(t) = (\dot{\hat{z}} - (A_c + kC_c)\hat{z} - \gamma(y, u) + ky)(b^{-1})^T$$

$$\hat{\theta}^T \beta(t) \leq (\dot{\hat{z}} + ky)^T (b^{-1})^T \quad (15)$$

But:

$$\dot{\hat{z}} = C_c^{-1} \dot{y}$$

According to (13), (14) and (15) the equation (12) becomes:

$$w^T \leq \lambda_{\max}(A^{-1})(\dot{\hat{z}} + ky)^T (b^{-1})^T b^T C_c^T C_c \lambda_{\max}(A^{-1}) b \beta(t)^T$$

Then:

$$w^T \leq \left| \lambda_{\max}(A^{-1}) \right|^2 (\dot{\hat{z}} + ky)^T C_c^T C_c b \beta(t)^T \quad (16)$$

The matrix $b\beta(t)^T$ is stable; this implies that $\lambda_{\max}(b\beta(t)^T) \leq 0$, the equation (16) becomes:

$$w^T \leq \left| \lambda_{\max}(A^{-1}) \right|^2 (\dot{\hat{z}} + ky)^T C_c^T C_c \lambda_{\max}(b\beta(t)^T)$$

$$w^T \leq \left| \lambda_{\max}(A^{-1}) \right|^2 (ky)^T C_c^T C_c \lambda_{\max}(b\beta(t)^T) \quad (17)$$

Since

$$y = z_1 \text{ And } C_c^T C_c = \begin{bmatrix} 1 & 0 & \dots & 0 \\ 0 & 0 & \dots & 0 \\ \vdots & \vdots & \dots & \vdots \\ 0 & \dots & \dots & 0 \end{bmatrix}$$

$$w^T \leq \left| \lambda_{\max}(A^{-1}) \right|^2 k_1 z_1 \lambda_{\max}(b\beta(t)^T) \leq z_1$$

The equation (10) will have the new form $\Delta\theta \leq \|z_1\|$. Or $z_1 = y$ due to

$$\Delta\theta \leq \|y\| \quad (18)$$

From (18), it becomes clear that the margin parameter variation depends only on the output. With proportional to the nominal parameter θ , $\Delta\theta = n\theta$. The number n verifies the relation:

$$n \leq \frac{\|y\|}{\|\max(\theta_i)\|} \quad (19)$$

3. EXAMPLE

To verify and to make valid the robustness of the proposed adaptive observer when the parameter varies, one considers the robot arm motion equation of the robot arm studied in [8].

$$I\ddot{q} + \frac{1}{2}mgl \sin(q) = u$$

In which q : angle, u : the input torque; I : the moment of inertia of the link, g : the gravity constant, m : mass of link, l : the length of the link.

It is clear that the system can be put directly in the form (7) when choosing:

$$z_1 = q; z_2 = \dot{q}; y = q; \rho_1 = \frac{mgl}{2I}; \rho_2 = \frac{1}{I}$$

The equations in the state space are:

$$\begin{cases} \dot{z}_1 = z_2 \\ \dot{z}_2 = -\rho_1 \sin(y) + \rho_2 u \\ y = z_1 \end{cases}$$

The adaptive observer designed in the robot arm model is given by the following equations:

$$\begin{bmatrix} \dot{\hat{z}}_1 \\ \dot{\hat{z}}_2 \end{bmatrix} = \begin{bmatrix} -k_1 & 1 \\ -k_2 & 0 \end{bmatrix} \begin{bmatrix} \hat{z}_1 \\ \hat{z}_2 \end{bmatrix} + \begin{bmatrix} k_1 \\ k_2 \end{bmatrix} y + \begin{bmatrix} 0 \\ 1 \end{bmatrix} (-\hat{\rho}_1 \sin(y) + \hat{\rho}_2 u)$$

$$\dot{\xi}_1 = \begin{bmatrix} -k_1 & 1 \\ -k_2 & 0 \end{bmatrix} \xi_1 + \begin{bmatrix} 0 \\ 1 \end{bmatrix} (-\sin(y))$$

$$\dot{\xi}_2 = \begin{bmatrix} -k_1 & 1 \\ -k_2 & 0 \end{bmatrix} \xi_2 + \begin{bmatrix} 0 \\ 1 \end{bmatrix} u$$

$$\dot{\xi}_0 = \begin{bmatrix} -k_1 & 1 \\ -k_2 & 0 \end{bmatrix} \xi_0 + \begin{bmatrix} 0 \\ 1 \end{bmatrix} (-\hat{\rho}_1 \sin(y) + \hat{\rho}_2 u)$$

$$\dot{W} = -\alpha W + \begin{bmatrix} \xi_{11}^2 & \xi_{11}\xi_{21} \\ \xi_{11}\xi_{21} & \xi_{21}^2 \end{bmatrix}$$

$$\dot{w} = -\alpha w + \begin{bmatrix} \xi_{11} \\ \xi_{21} \end{bmatrix} (C_c \xi_0 + y - \hat{z}_1)$$

$$\begin{bmatrix} \dot{\hat{\rho}}_1 \\ \dot{\hat{\rho}}_2 \end{bmatrix} = -\Gamma(W \begin{bmatrix} \hat{\rho}_1 \\ \hat{\rho}_2 \end{bmatrix} + w)$$

In simulation, the nominal parameters and simulation parameters used are as follows [8]:

$$m = 1Kg ; g = 9.8 ; l = 1m \text{ and } I = 0.5$$

In literature the margin parameter variation is determined under a real application. In ([12], [14], [17]), the parameter variation is a percentage of the nominal parameter determined by the practical test or the constructor which the adaptive observer show a best performances. But the proposed bound of the external parameter margin variation can be enough or very large. To justify the robustness of the proposed margin parameter variation, the adaptive observer robustness (6) is tested through out the robot arm example under a variations on ρ_1 and ρ_2 are considered which the margin parameter variation taken is $n < 12$.

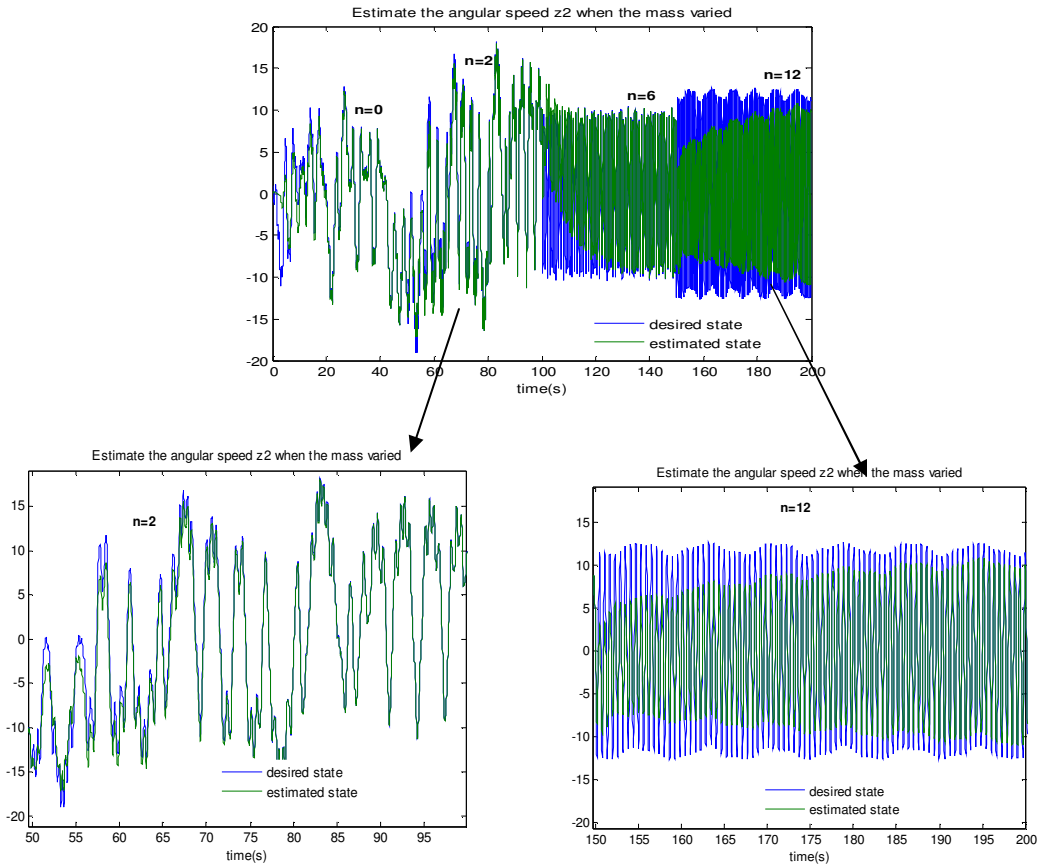
The results obtained are reported as follows:

If the link mass varied such as $m=1Kg$ ($n=0$) at $t < 50s$, $m=3Kg$ ($n=2$) at $50 < t < 100s$, $m=7Kg$ ($n=6$) at $100 < t < 150s$ and $m=13Kg$ ($n=12$) at $t > 150s$. The angular speed z_2 and the estimated parameter converge to the desired values at each variation after a time delay which is proportional to the margin variation applied (figure (1)). For a little variation of mass ($n=2$), the state and the parameter converge at the same time ($t_c=80s$). But, if n is maximal ($n=12$) the estimated parameters and state take more time to converge to the reached value.

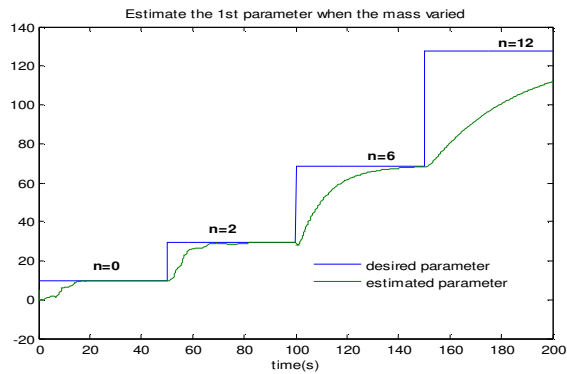
for that, if the inertia varied slowly, such as: $I=0.5$ at $0 < t < 70s$, $I=1$ at $70s < t < 140s$ and $I=2$ and $t > 140s$, the state z_2 and the parameter ρ_2 converges rapidly to the reached values (figure (2.a), figure (2.c)) . Due to the inertia depend on m the parameter ρ_1 did not usually converges which is requires more time than ρ_2 to converge (figure (2.b)).

When the mass and the inertia vary simultaneously , to $I=0.5$ at $0 < t < 70s$, $I=1$ at $70s < t < 140s$, $I=2$ at $t > 140s$ and for the mass $m=1Kg$ at $0 < t < 50s$, $m=3Kg$ at $50s < t < 100s$, $m=7Kg$ at $100s < t < 150s$ and $m=13Kg$ at $t > 150s$, we show that only the instance of the mass varying. In this case, it is clear that the state lasts longer time to converge to the desired values than the inertia (figure(3.a)). Thus, the parameter variation and the time converge become more efficient with the

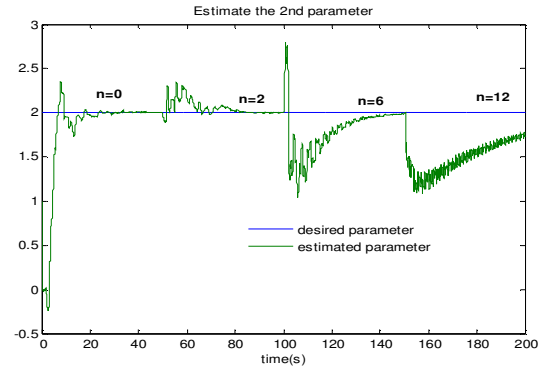
mass variation rather than with the inertia (figure(3.c)). This is also shown in the estimation of the parameter (figure (3.b)).



a. Estimation of the angular speed z_2 when the mass varied

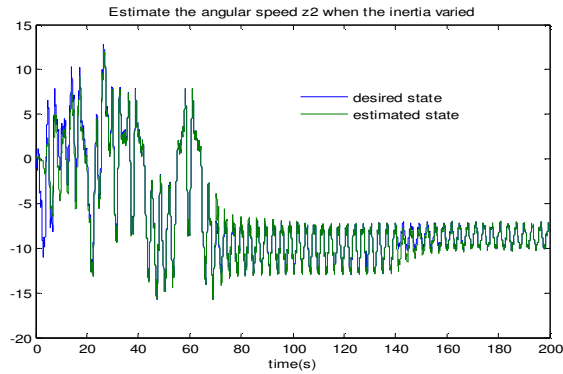


b. Estimation of the 1st parameter ρ_1

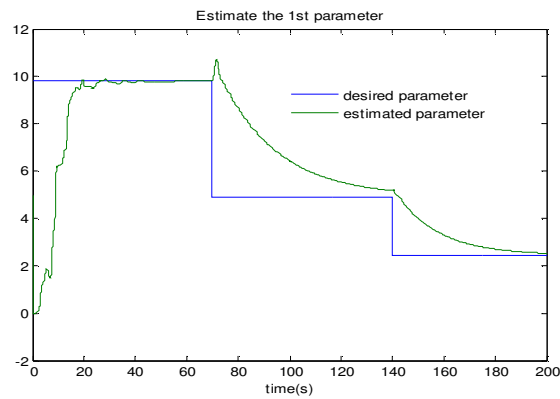


c. Estimation of the 2nd parameter ρ_2

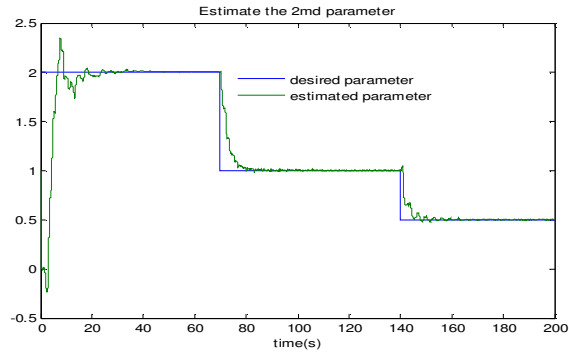
FIGURE1: Estimation of the angular speed z_2 and the parameter when the mass varied



a. Estimation of the angular speed z_2 when the inertia varied

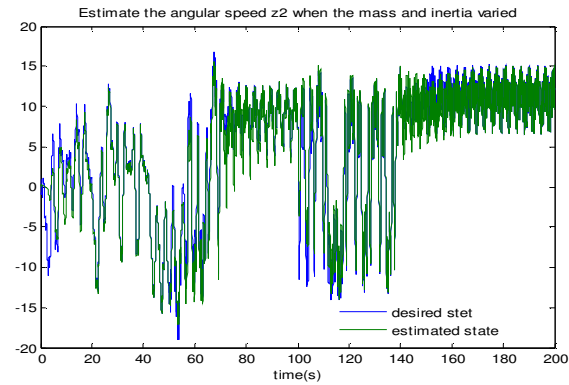


b. Estimate the 1st parameter ρ_1

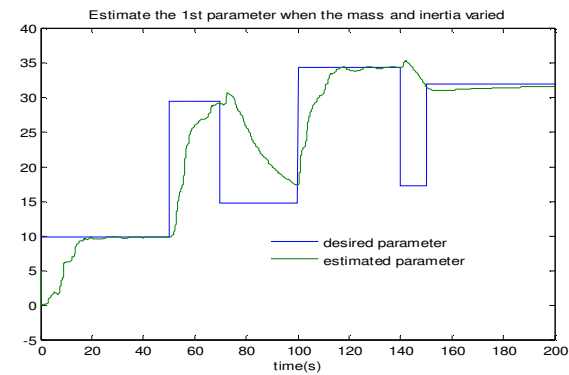


c. Estimate the 2nd parameter ρ_2

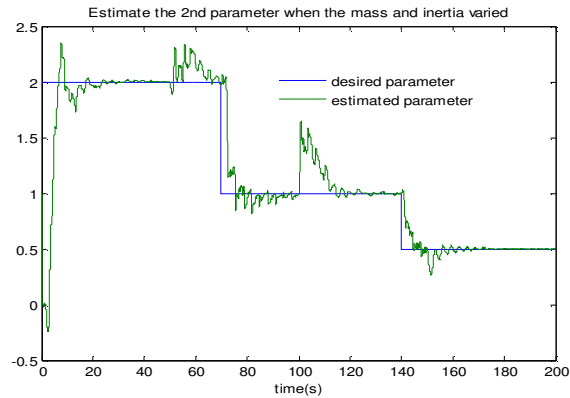
FIGURE 2: Estimation of the angular speed and the parameter when the inertia I varied



a. Estimation of the angular speed z2 when the inertia and mass varied



b. Estimate the 1st parameter ρ_1



c. Estimate the 2nd parameter ρ_2

FIGURE 3: Estimation of the angular speed z_2 and the parameter when the mass and inertia varied

We find that the studied adaptive observer is robust to estimate the state and the parameter only if parameter variations verify the inequality (18) and (19). The rapidity of convergence depends only on the varied parameter

4. CONCLUSION

In this paper, we have studied the robustness of the adaptive observer proposed in ([8], [9], [10], [11]) in the case of linear parameter variation of the system. A parameter variation margin is determined which the state convergence is guaranteed. In fact, the architecture of this adaptive observer shows good performance in the estimation of the state and of the unknown varied parameter.

4. REFERENCES

1. R.Rajamani, "Adaptive observers for active automotive Suspensions: theory and experiment". IEEE transaction on control systems technology,32(1), 1995
2. S.Tatiraju and M. Soroush, "Parameter estimation via inversion with application to a reactor". Proceeding of the American control conference Albuquerque, New Mexico, 1997.
3. N. M.Iyer and A. E. Forell, "Design of stable adaptive nonlinear observer for an exothermic stirred Tank reactor". Computers Chem.Engng, 20(9): 1141-1147, 1996.
4. C.M.Astorga-Zaragoza, A.Zavala-Rio, V.M.Alvarado, R.M Mendez and J.Reyes-Reyes, "Performance monitoring of heat ex-changers via adaptive observers". Measurement, 40, 2007.
5. G.Besaçon, "nonlinear observers and applications". Springer-verlag Berlin Heidelberg (2007)
6. H.Saadaoui, De leon, M.djemai and J.P Barbo, "High order sliding mode and adaptive observers for a class of switched systems with unknown parameter: A comparative study". Proceeding of the 45th IEEE conference on decision and control, San Diego, CA, USA, 2006.
7. F. Zhu, "The design of full order and reduced-order adaptive observers for nonlinear systems". IEEE international conference on control automation, China, 2007.
8. R. Marino, P. Tomei, "Adaptive observers with arbitrary exponential rate of convergence for nonlinear systems". IEEE transaction on automatic control,40(7), 1995

9. R. Marino, P. Tomei, “*observer-based adaptive stabilization for a class of nonlinear systems*”. *Automatica*, 28(4): 787-793, 1992
10. R. Marino, P. Tomei, “*Global adaptive observers for nonlinear systems via filtered transformations*”. *IEEE transaction*, 37(8): 1239-1245, 1992
11. R. Marino, “*Adaptive observers for single output nonlinear systems*”. *IEEE transaction on automatic control*, 35(9), 1990
12. A.B. Proca and A. Keyhani “*Sliding-Mode Flux Observer with Online Rotor Parameter Estimation for Induction Motors*” *IEEE transactions on industrial electronics*, 54(2), 2007.
13. Ph. Garimella, B.Yao “*Nonlinear Adaptive Robust Observer Design for a Class of Nonlinear Systems*” *Proceedings of the American Control Conference*, Denver, Colorado, 2003.
14. Ph. Garimella, B.Yao “*Fault detection of an electro-hydraulic cylinder using adaptive robust observers*” *Proceedings of IMECE04 ASME International Mechanical Engineering Congress and Exposition*, Anaheim California, USA, 2004.
15. P. Moireau, D. Chapelle and P. Le Tallec “*Joint state and parameter estimation for distributed mechanical systems*” *Computer methods in applied mechanics and engineering*, 197: 659–677, 2008.
16. Elleuch,D.and Damak,T.(2009) “*Adaptive sliding mode observer for Lipchitz nonlinear systems with varying parameters*” *10th International conference on Sciences and Techniques of Automatic control & computer engineering*, December 20-22, Hammamet, Tunisia, pp.1821–1833.
17. A. S. TLILI and E. BENHADJ BRAIEK “*A reduced-order robust observer using nonlinear parameter estimation for induction motors*” *IEEE International Conference on Systems, Man and Cybernetics*, 2002

Cluster Based Web Search Using Support Vector Machine

Rita. S. Shelke

*Department of Computer Engineering
Bharati Vidyapeeth University, COE
Pune-43, India.*

ritashelke@gmail.com

Devendra Singh Thakore

*Department of Computer Engineering
Bharati Vidyapeeth University, COE
Pune-43, India*

deventhakore@yahoo.com

Abstract

Now days, searches for the web pages of a person with a given name constitute a notable fraction of queries to Web search engines. This method exploits a variety of semantic information extracted from web pages.

The rapid growth of the Internet has made the Web a popular place for collecting information. Today, Internet user access billions of web pages online using search engines. Information in the Web comes from many sources, including websites of companies, organizations, communications and personal homepages, etc. Effective representation of Web search results remains an open problem in the Information Retrieval community. For ambiguous queries, a traditional approach is to organize search results into groups (clusters), one for each meaning of the query. These groups are usually constructed according to the topical similarity of the retrieved documents, but it is possible for documents to be totally dissimilar and still correspond to the same meaning of the query. To overcome this problem, the relevant Web pages are often located close to each other in the Web graph of hyperlinks. It presents a graphical approach for entity resolution & complements the traditional methodology with the analysis of the entity-relationship (ER) graph constructed for the dataset being analyzed. It also demonstrates a technique that measures the degree of interconnectedness between various pairs of nodes in the graph. It can significantly improve the quality of entity resolution.

Using Support Vector Machines (SVMs) which are a set of related Supervised learning methods used for classification of load of user queries to the sever machine to different client machines so that system will be stable. Cluster web pages based on their capacities stores whole database on server machine.

Keywords: SVM, Cluster, ER.

1. INTRODUCTION

Web search is difficult because it is hard for users to construct queries that are both sufficiently descriptive and sufficiently discriminating to find just the web pages that are relevant to the user's search goal. Queries are often ambiguous: words and phrases are frequently polysemantic and user search goals are often narrower in scope than the queries used to express them. This ambiguity leads to search result sets containing distinct page groups that meet different user search goals. Often users must refine their search by modifying the query to filter out the irrelevant results. Users must understand the result set to refine queries effectively; but this is time consuming, if the result set is unorganized. Web page clustering is one approach for assisting users to both comprehend the result set and to refine the query. Web page clustering identifies semantically meaningful groups of web pages and presents these to the user as clusters. The clusters provide an overview of the contents of the result set and when a cluster is selected the result set is refined to just the relevant pages in that cluster. After clustering

whatever the load of queries on a single machine which is treated as server will get distributed over the network using Support Vector Machine, which act as load classifier or distributor. Depending upon the capacities of machines each can handle the specific load & return unstable when it exceed the limit. It is useful to determine whether the machine is stable or not.

1.1 Present Theories & Practices

There has been a large body of work on web search, unambiguation, entity resolution. Here we review some of the main work, but the review is not exhaustive. In Web people search application [1] the main techniques used are unambiguation & entity resolution. The authors have overviewed several existing entity resolution approaches, pointing out that they rely primarily on analyzing object features for making their co reference decisions. As compared it with existing unambiguation works. The Authors have developed a novel algorithm for unambiguating among people that have the same name which is based on extracting "significant" entities such as the names of other persons, organizations, and locations on each web page, forming relationships between the person associated with the web page and the entities extracted, and then analyzing the relationships along with features such as TF/IDF, as well as other useful content including hyperlink information to disambiguate the pages. Then design a cluster-based people search approach based on the disambiguation algorithm. In Disambiguation Algorithm for People Search on the Web [2], the authors have concentrated on disambiguation algorithm which exist for a variety of data management applications. The proposed disambiguation algorithm is based on analyzing two types of information. First, it analyzes object features, like many other techniques. Second, (most important) it also analyzes the Entity-Relationship Graph (ER graph) for the dataset. The idea behind analyzing features of objects u, v is based on the assumption that similarity of features of two objects defines certain affinity/attraction between those objects $f(u, v)$. If this attraction $f(u, v)$ is sufficiently large, then the objects are likely to be the same (co-refer). The intuition behind analyzing paths in the ER graph is similar. The assumption is that each path/connection/link p between two objects u, v can serve as evidence that they co-refer. So if the combined evidence, stored in all the u - v paths, is sufficiently large, the objects are likely to be the same. Formally, the attraction between two nodes u and v via paths is measured using the connection strength measure $c(u, v)$ which is defined as the sum of attractions contributed by each path:

$$c(u, v) = \sum_{p \in P_{uv}} w_p.$$

Here P_{uv} denotes the set of all simple paths between u and v (of limited length), and $c(p)$ is the contribution of path p .

1.2 The Limitations Of Web Search

With an enormous growth of the Internet it has become very difficult for the users to find relevant documents. In response to the user's query, currently available search engines return a ranked list of documents along with their partial content. If the query is general, it is extremely difficult to identify the specific document which the user is interested in. The users are forced to sift through a long list of off-topic documents. Moreover, internal relationships among the documents in the search result are rarely presented and are left for the user. Standard information retrieval systems rely on two orthogonal paradigms: the textual similarity with the query (e.g., tf-idf-based cosine similarity) on one hand and a query independent measure of each web page's importance (e.g., link authority ranking) on the other hand. However, these systems generally lack user modeling and thus are far from being optimal i.e Different users may submit exactly the same query even though they have different intentions. The most famous examples of such ambiguous queries include bass (fish or instrument), java (programming language, island or coffee), jaguar (animal, car or Apple software) and IR application (Infrared application or Information Retrieval application) For example assume we have two users, one of whom is a computer science student, and the other is geography student. Figure 1 represents the top-6 results returned by Google when the query "java map" is submitted. The result set spans two categories, namely the java map collection classes and maps for the Indonesian island java. Generally speaking, the computer science student would be most likely interested in the java map collection classes,

where as the geography student would be interested in locating maps for the Indonesian island java.

[An Introduction to Java Map Collection Classes](#)

Learn the basics of one the most commonly used collection types, Maps, and how to optimize Maps for your application specific data.

www.oracle.com/technology/pub/articles/maps1.html - 69k -
Cached - Similar pages

[Map \(Java 2 Platform SE v1.4.2\)](#)

For further API reference and developer documentation, see [Java 2 SDK SE Developer Documentation](#). That documentation contains more detailed, ...

java.sun.com/j2se/1.4.2/docs/api/java/util/Map.html - 37k - Cached - Similar pages

[Java Technology Concept Map](#)

The [Java Technology Concept Map 1.0](#) is an interactive diagram.

java.sun.com/developer/onlineTraining/new2java/javamap/intro.html - 15k -
Cached - Similar pages

[More results from java.sun.com]

[Map of Java - Lonely Planet](#)

You'll soon be zipping around like a local, thanks to this [map of Java](#) provided by Lonely Planet.

www.lonelyplanet.com/mapshells/south_east_asia/java/java.htm - 8k -
Cached - Similar pages

[Indonesia Map - interactive map of Indonesia and area maps of ...](#)

[Indonesia Map & Travel Guide - interactive map of Indonesia and area maps of Indonesia, with locations of major tourist attractions and ...](#) [Central Java Map ...](#)

www.hoteltravel.com/indonesia/maps.htm - 42k - Cached - Similar pages

[Java world map projections - by Henry Bottomley.](#)

An interactive [java](#) applet for exploring different [map](#) projections of the world, with the ability to change the projection, scale and center of the [map](#).

www.btinternet.com/~se16/js/mapproj.htm - 10k - Cached - Similar pages

FIGURE 1: Overview of query processing

1.3 Cluster _Based Web Search

Clustering of Web search results has been in the focus of IR community since the yearly days of the Web. There are two reasons for clustering of search results. The first is that the IR research community has long recognized the validity of the clustering approach in top ranked documents; I. e. similar documents tend to be relevant to the same request. A second reason is that the ranked list is usually too large and contains many documents that are irrelevant to the particular meaning of the query the user had in mind. Thus it would be beneficial to group search results by various meanings of the query. The attempts have made the clustering of search results for many web users. However, it is still not accurate enough to attract an average user. The main drawback of many Web page clustering methods is that they take into account only the topical similarity between the documents in the ranked list. Topical similarity metrics between Web pages would not help solving the clustering problem in at least two cases: (a) when there is not enough contextual information on a page (b) When Websites are contextually different but actually refer to the meaning of the query.

The limitations are as follows:

- a. Users must sift through a long list of documents, some of which are irrelevant
- b. The reason a document was included in the results is not explicit
- c. The relation of a document to the query is not explicit
- d. No explicit information is provided about the relationships between documents on the list
- e. All documents on the list must be sorted even though some of them may not relate to each other and are thus not comparable.

The solution is that for each such web page, the search-engine could determine which real entity the page refers to. This information can be used to provide a capability of clustered search, where instead of a list of web pages of (possibly) multiple entities with the same name, the results are clustered by associating each cluster to a real entity. The clusters can be returned in a ranked order determined by aggregating the rank of the web pages that constitute the cluster. With each cluster, we also provide a summary description that is representative of the real entity associated with that cluster.

2. QUERY PROCESSING

To overcome these limitations, the goal is to group all the entity descriptions that refer to the same real world entities. A user submits a query to the middle ware via a specialized Web-based interface. The middle ware queries a search engine with this query via the search engine API and retrieves a fixed number (top K) of relevant web pages. The result is a set of clusters of these pages with the aim being to cluster web pages based on association to real entity. Each resulting cluster is then processed. A set of keywords that represent the web pages within a cluster is computed for each cluster. The goal is that the user should be able to find the person of interest by looking at the sketch. The proposed work has been divided into four modules which are 1. Web pages retrieval for the query 2. Preprocessing of web pages 3. Clustering & its Processing 4. Graph Creation.

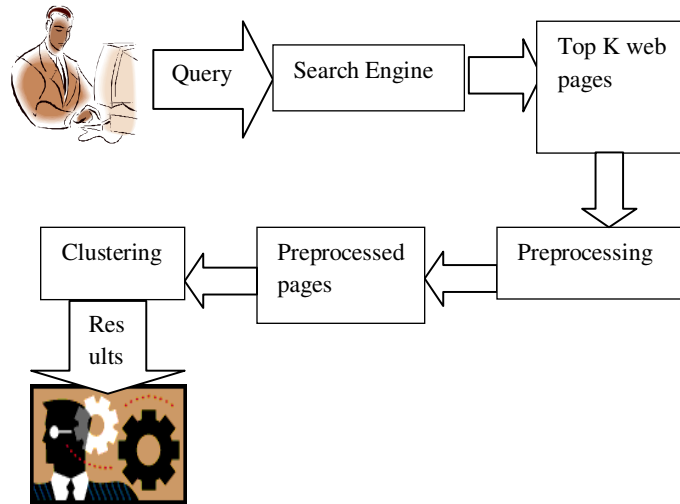


FIGURE 2: Overview of query processing

Web search applications can be implemented in two different settings.

1. Server-side setting
2. Middle ware setting

In server-side setting, the disambiguation mechanism is integrated into the search engine directly. On other hand in a middle ware approach, build entity search capabilities on top of an existing

search-engine such as Google by “wrapping” the original engine. The middle ware would take a user query, use the search engine API to retrieve top K web pages most relevant to the user query, and then cluster those web pages based on their associations to real people. The middle-ware approach is more common, as it is difficult to conduct realistic testing of the server-side approach due to the lack of direct access to the search engine internal data. The architecture is a pipeline that receives the input query, obtains search results from a search engine, filters the results applying a clustering algorithm and then gets the clusters. The steps of overall approach are illustrated in Figure 3.

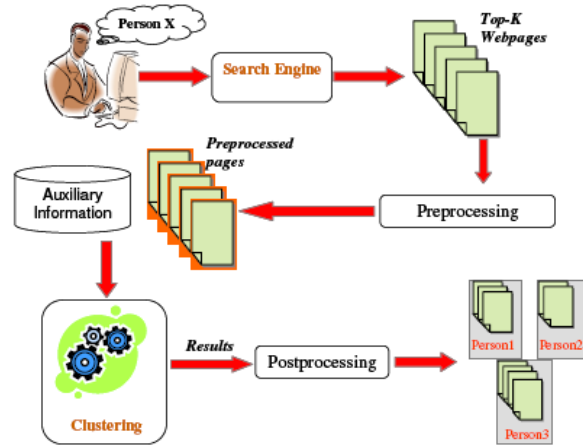


FIGURE 3: Overview of processing steps

2.1 Design Of Web Pages Retrieval For Query

Web Pages retrieval for query can be implemented in many ways. There are many algorithms to process Top-k retrieval, for example: Fagins Threshold Algorithm (TA), No Random Access Algorithm (NRA) and Combined Algorithm (CA). All these threshold algorithms work on inverted indices for query terms. Assuming the vector space model, the way to fetch the top-k documents would be to compute the textual similarity of all the documents present in the corpus with the query vector, order them according to this similarity score and then fetch the top-k documents from this ordered list. However taking into consideration the huge size of the web corpus, this process becomes very unfeasible. The *HttpServlet* component seeks to fill this void by providing an efficient, up-to-date, and feature-rich package implementing the client side of the most recent HTTP standards and recommendations. The features are standards based, pure Java, implementation of HTTP versions 1.0 and 1.1. It is the full implementation of all HTTP methods. The figure 4, shows the process of retrieving the top pages from the search engine.

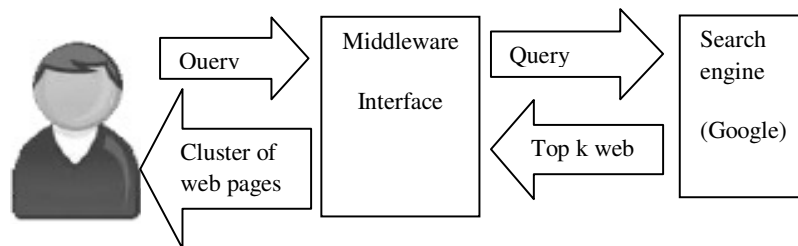


FIGURE 4: Web pages retrieval

2.2 Design of Preprocessing Of Web Pages

After retrieving the top pages related to the query, the pages are processed by using IR techniques. There are various algorithms which are simply a set of instructions, usually mathematical, used to calculate a certain parameter and perform some type of data processing.

The job is to generate a set of highly relevant documents for any search query, using the available parameters on the web. The task is challenging because the available parameters usable by the algorithm are not necessarily the same as the ones web users see when deciding if a webpage is relevant to their search. The figure 5 shows the preprocessing of the web pages which include the two processes named as stemming & stop word removal.

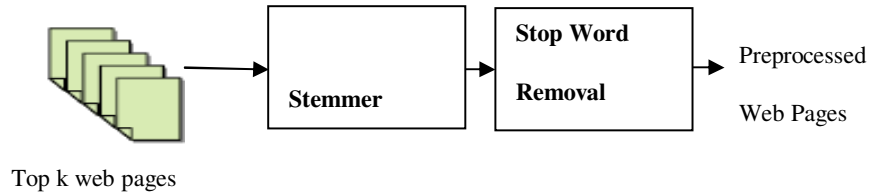


FIGURE 5: Processing of Web Pages

2.2.1 Stemming

Stemming algorithms are used to transform the words in texts into their grammatical root form, and are mainly used to improve the Information Retrieval System's efficiency. To stem a word is to reduce it to a more general form, possibly its root. For example, stemming the term interesting may produce the term interest. Though the stem of a word might not be its root, we want all words that have the same stem to have the same root. The effect of stemming on searches of English document collections has been tested extensively. Several algorithms exist with different techniques. The most widely used is the Porter Stemming algorithm. In some contexts, stemmers such as the Porter stemmer improve precision/recall scores [3]. The stemmer operations are classified into rules where each of these rules deals with a specific suffix and having certain condition(s) to satisfy. A given word's suffix is checked against each rule in a sequential manner until it matches one, and consequently the conditions in the rule are tested on the stem that may result in a suffix removal or modification. Using $(VC)^m$ to denote VC repeated m times, this may again be written as $[C](VC)^m[V].m$ will be called the measure of any word or word part when represented in this form. The case $m = 0$ covers the null word. The algorithm now follows:

Step 1a

Rules	Illustrations
SSES -> SS	caresses ->caress
IES -> I	ponies -> poni, Ties ->ti
SS -> SS	caress -> caress
S ->	cats -> cat

Step 1b

Rules	Illustrations
$(m>0)$ EED -> EE	feed -> feed, agreed ->agree
$(*v^*)$ ED ->	plastered -> plaster, bled -> bled
$(*v^*)$ ING ->	motoring -> motor, sing -> sing

If the second or third of the rules in Step 1b is successful, the following is done:

AT -> ATE	conflat(ed) -> conflate
BL -> BLE	troubl(ed) -> trouble
IZ -> IZE	siz(ed) -> size

(*d and not (*L or *S or *Z))

-> single letter

hopp(ing) -> hop, tann(ed) -> tan

(m=1 and *o) -> E fail(ing) -> fail, fil(ing) -> file

The rule to map to a single letter causes the removal of one of the double letter pair. The -E is put back on -AT, -BL and -IZ, so that the suffixes -ATE, -BLE and -IZE can be recognized later. This E may be removed in step 4.

Step 1c

Rule	Illustrations
(*v*) Y -> I	happy -> happi, sky -> sky

Step 1 deal with plurals and past participles. The subsequent steps are much more straightforward.

Step 2

Rules	Illustrations
(m>0) ATIONAL -> ATE	relational -> relate
(m>0) TIONAL -> TION	conditional -> condition, rational->rational
(m>0) ENCI -> ENCE	valenci -> valence
(m>0) ANCI -> ANCE	hesitanci -> hesitance
(m>0) IZER -> IZE	digitizer -> digitize
(m>0) ABLI -> ABLE	conformabli -> conformable
(m>0) ALLI -> AL	radicalli -> radical
(m>0) ENTLI -> ENT	differentli -> different
(m>0) ELI -> E	vileli -> vile
(m>0) OUSLI -> OUS	analogousli -> analogous
(m>0) IZATION -> IZE	vietnamization -> vietnamize
(m>0) ATION -> ATE	predication -> predicate
(m>0) ATOR -> ATE	operator -> operate
(m>0) ALISM -> AL	feudalism -> feudal
(m>0) IVENESS -> IVE	decisiveness -> decisive
(m>0) FULNESS -> FUL	hopefulness -> hopeful
(m>0) OUSNESS -> OUS	callousness -> callous

(m>0) ALITI -> AL	formaliti -> formal
(m>0) IVITI -> IVE	sensitiviti -> sensitive
(m>0) BILITI -> BLE	sensibiliti -> sensible

Step 3

Rules	Illustrations
(m>0) ICATE -> IC	triplicate -> triplic
(m>0) ATIVE ->	formative -> form
(m>0) ALIZE -> AL	formalize -> formal
(m>0) ICITI -> IC	electriciti -> electric
(m>0) ICAL -> IC	electrical -> electric
(m>0) FUL ->	hopeful -> hope
(m>0) NESS ->	goodness -> good

Step 4

Rules	Illustrations
(m>1) AL ->	revival -> reviv
(m>1) ANCE ->	allowance -> allow
(m>1) ENCE ->	inference -> infer
(m>1) ER ->	airliner -> airlin
(m>1) IC ->	gyroscopic -> gyroscop
(m>1) ABLE ->	adjustable -> adjust
(m>1) IBLE ->	defensible -> defens
(m>1) ANT ->	irritant -> irrit
(m>1) EMENT ->	replacement -> replac
(m>1) MENT ->	adjustment -> adjust
(m>1) ENT ->	dependent -> depend
(m>1 and (*S or *T)) ION ->	adoption -> adopt
(m>1) OU ->	homologou -> homolog
(m>1) ISM ->	communism -> commun
(m>1) ATE ->	activate -> activ

(m>1) ITI -> angulariti -> angular
 (m>1) OUS -> homologous -> homolog
 (m>1) IVE -> effective -> effect
 (m>1) IZE -> bowdlerize -> bowdler

The suffixes are now removed. All that remains is a little tidying up.

Step 5a

Rules	Illustrations
(m>1) E ->	probate -> probat, rate->rate
(m=1 and not *o) E ->	cease -> ceas

Step 5b

Rules	Illustrations
(m > 1 and *d and *L) -> single letter	control->control

The algorithm is careful not to remove a suffix when the stem is too short, the length of the stem being given by its measure, m. It was merely observed that m could be used quite effectively to help decide whether or not it was wise to take off a suffix.

2.2.2 Elimination of Stop Words

After stemming it is necessary to remove unwanted words. There are 400 to 500 types of stop words such as “of”, “and”, “the,” etc., that provide no useful information about the document’s topic. Stop-word removal is the process of removing these words. Stop-words account for about 20% of all words in a typical document[4]. These techniques greatly reduce the size of the search engine’s index. Stemming alone can reduce the size of an index by nearly 40%. To compare a webpage with another webpage, all unnecessary content must be removed and the text put into an array. The Sam Allen has proposed the stop word dictionary on Dot Net Perls but this is not sufficient for some of the applications. For this reason, static dictionary is modified.

2.3 Design of Clustering & Its Processing

When designing a Cluster Based Web Search, special attention must be paid to ensuring that both content and description (labels) of the resulting groups are meaningful to humans. As stated, “a good cluster—or document grouping—is one, which possesses a good, readable description”. There are various algorithms such as K means, K-medoid but this algorithm require as input the number of clusters. A Correlation Clustering (CC) algorithm is employed which utilizes supervised learning. The key feature of Correlation Clustering (CC) algorithm is that it generates the number of clusters based on the labeling itself & not necessary to give it as input but it is best suitable when query is person names. For general query, the algorithms are Query Directed Web Page Clustering (QDC), Suffix Tree Clustering (STC), Lingo, and Semantic Online Hierarchical Clustering (SHOC).The focus is made on Lingo because the QDC considers only the single words. The STC tends to remove longer high quality phrases, leaving only less informative & shorter ones. So, if a document does not include any of the extracted phrases it will not be included in results although it may still be relevant. To overcome the STC’s low quality phrases problem, in SHOC introduce two novel concepts: complete phrases and a continuous cluster definition. The drawback of SHOC is that it provides vague threshold value which is used to describe the resulting cluster. Also in many cases, it produces unintuitive continuous clusters. The majority of open text clustering algorithms follows a scheme where cluster content discovery

is performed first, and then, based on the content, the labels are determined. But very often intricate measures of similarity among documents do not correspond well with plain human understanding of what a cluster's "glue" element has been. To avoid such problems Lingo reverses this process—first attempt to ensure that we can create a human-perceivable cluster label and only then assign documents to it. Specifically, extract frequent phrases from the input documents, hoping they are the most informative source of human-readable topic descriptions. Next, by performing reduction of the original term-document matrix using Singular Value Decomposition (SVD), try to discover any existing latent structure of diverse topics in the search result. Finally, match group descriptions with the extracted topics and assign relevant documents to them.

LINGO – Main phase's pseudo-code

Phase 1: Preprocessing

for each document

{

apply stemming;

mark stop words;

}

Phase 2: Frequent Phrase Extraction

discover frequent terms and phrases;

Phase 3: Cluster label induction

use LSI to discover abstract concepts;

for each abstract concept

{

find best-matching phrase;

}

prune similar cluster labels;

Phase 4: Cluster content discovery

for each cluster label

{

use VSM to determine the cluster contents;

}

Phase 5: Final cluster formation

calculate cluster scores;

apply cluster merging;

3. FREQUENT PHRASE EXTRACTIONS

The frequent phrases are defined as recurring ordered sequences of terms appearing in the input documents. Intuitively, when writing about something, we usually repeat the subject-related keywords to keep a reader's attention. Obviously, in a good writing style it is common to use synonymy and pronouns and thus avoid annoying repetition. The Lingo can partially overcome the former by using the SVD-decomposed term document matrix to identify abstract concepts—single subjects or groups of related subjects that are cognitively different from other abstract concepts. To be a candidate for a cluster label, a frequent phrase or a single term must:

1. Appear in the input documents at least certain number of times (term frequency threshold),
2. Not cross sentence boundaries,
3. Be a complete phrase (see definition below),
4. Not begin nor end with a stop word.

A complete phrase is a complete substring of the collated text of the input documents, defined in the following way: Let T be a sequence of elements $(t_1, t_2, t_3 \dots t_n)$. S is a complete substring of T when S occurs in k distinct positions $p_1, p_2, p_3 \dots p_k$ in T and $\exists i, j \in 1 \dots k : t_{p_i-1} \neq t_{p_j-1}$ (left-completeness) and $\exists i, j \in 1 \dots k : t_{p_i+|S|} \neq t_{p_j+|S|}$ (right-completeness). In other words, a complete phrase cannot be "extended" by adding preceding or trailing elements, because at least one of these elements is different from the rest. An efficient algorithm for discovering complete phrases was proposed in [5], although it contained one mistake that caused the frequency of some phrases to be miscalculated. It does not affect further discussion of Lingo because any algorithm capable of discovering frequent phrases could be used at this stage. Figure 6 presents the whole phrase extraction phases.

LINGO – phrase extraction phase pseudo-code

Phase 2: Frequent phrases extraction

Conversion of the representation

for each document

```
{ convert the document from the character-based to  
the word-based representation;  
}
```

Document concatenation

concatenate all documents;

create an inverted version of the concatenated documents;

Complete phrase discovery

discover right-complete phrases;

discover left-complete phrases;

sort the left-complete phrases alphabetically;

combine the left- and right-complete phrases into a set of complete phrases;

Final selection

for further processing choose the terms and phrases whose frequency exceed the Term Frequency Threshold;

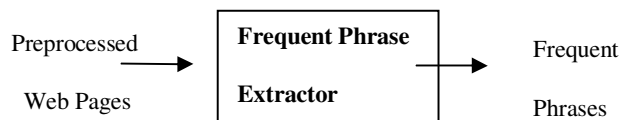


FIGURE 6: Frequent phrase extraction

3.1 Cluster Label Induction

Once frequent phrases (and single frequent terms) that exceed term frequency thresholds are known, they are used for cluster label induction. There are three steps to this: term-document matrix building, abstract concept discovery, phrase matching and label pruning.

The term-document matrix is constructed out of single terms that exceed a predefined term frequency threshold. Weight of each term is calculated using the standard term frequency, inverse document frequency (tf-idf) formula [7], terms appearing in document titles are additionally scaled by a constant factor. In abstract concept discovery, Singular Value Decomposition method is applied to the term-document matrix to find its orthogonal basis. The vectors of this basis (SVD’s U matrix) supposedly represent the abstract concepts appearing in the input documents. We estimate the value of k by selecting the Frobenius norms of the term-document matrix A and its k-rank approximation A_k . Let threshold q be a percentage-expressed value that determines to what extent the k-rank approximation should retain the original information in matrix A. We hence define k as the minimum value that satisfies the following condition: $\|A_k\|_F / \|A\|_F \geq q$, where $\|X\|_F$ symbol denotes the Frobenius norm of matrix X. Clearly, the larger the value of q the more cluster candidates will be induced. The choice of the optimal value for this parameter ultimately depends on the users’ preferences. Therefore make it one of Lingo’s control thresholds—Candidate Label Threshold.

Phrase matching and label pruning step, where group descriptions are discovered, relies on an important observation that both abstract concepts and frequent phrases are expressed in the same vector space—the column space of the original term-document matrix A. Thus, the classic cosine distance can be used to calculate how “close” a phrase or a single term is to an abstract concept. Let us denote by P a matrix of size $t \times (p+t)$ where t is the number of frequent terms and p is the number of frequent phrases. P can be easily built by treating phrases and keywords as pseudo-documents and using one of the term weighting schemes. Having the P matrix and the i^{th} column vector of the SVD’s U matrix, a vector m_i of cosines of the angles between the i^{th} abstract concept vector and the phrase vectors can be calculated: $m_i = U_i^T P$. The phrase that corresponds to the maximum component of the m_i vector should be selected as the human-readable description of i^{th} abstract concept. Additionally, the value of the cosine becomes the score of the cluster label candidate. A similar process for a single abstract concept can be extended to the entire U_k matrix—a single matrix multiplication $M = U_k^T P$ yields the result for all pairs of abstract concepts and frequent phrases. On one hand we want to generalize information from separate documents, but on the other we want to make it as narrow as possible at the cluster description level. Thus, the final step of label induction is to prune overlapping label descriptions. Let V be a vector of cluster label candidates and their scores. We create another term-document matrix Z, where cluster label candidates serve as documents. After column length normalization calculates $Z^T Z$, which yields a matrix of similarities between cluster labels. For each row we then pick columns that exceed the Label Similarity Threshold and discard all but one cluster label candidate with the maximum score.

LINGO – cluster label induction phase pseudo-code

Phase 3: Cluster label induction

Term-document matrix building

build the term-document matrix A for the input snippet collection.

as index terms use the non-stop words that exceed the predefined

term frequency threshold. use the tf-idf weighting scheme;

Abstract concept discovery

perform the Singular Value Decomposition of the term-document matrix to obtain U , S and V matrices;

based on the value of the q parameter and using the S matrix -

calculate the desired number k of abstract concepts;

use the first k columns of the U matrix to form the U_k matrix;

Phrase matching

using the tf-idf term weighting create the phrase matrix P ;

for each column of the U_k matrix

{

multiply the column by the P matrix;

find the largest value in the resulting vector to determine

the best matching phrase;

}

Candidate label pruning

calculate similarities between all pairs of candidate labels;

form groups of labels that exceed a predefined similarity threshold;

for each group of similar labels

{

```

select one label with the highest score;
}

```

3.2. Cluster Content Discovery

In the cluster content discovery phase, the classic Vector Space Model (VSM) is used to assign the input documents to the cluster labels induced in the previous phase. In a way, re-query the input document set with all induced cluster labels. The assignment process resembles document retrieval based on the VSM model. Let us define matrix Q , in which each cluster label is represented as a column vector. Let $C = Q^T A$, where A is the original term-document matrix for input documents. This way, element c_{ij} of the C matrix indicates the strength of membership of the j^{th} document to the i^{th} cluster. A document is added to a cluster if c_{ij} exceeds the Snippet Assignment Threshold, yet another control parameter of the algorithm. Documents not assigned to any cluster end up in an artificial cluster called others.

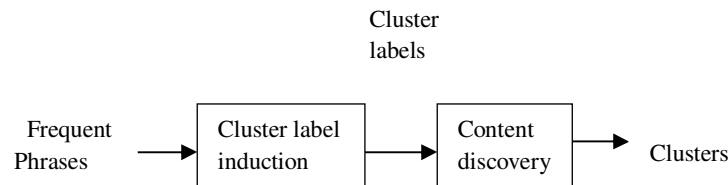


FIGURE 7: Cluster Formation

3.3 Final Cluster Formation

Finally, clusters are sorted for display based on their score, calculated using the following simple formula: $C_{\text{score}} = \text{label score} \times ||C||$, where $||C||$ is the number of documents assigned to cluster C . The scoring function, although simple, prefers well-described and relatively large groups over smaller, possibly noisy ones. For the time being, no cluster merging strategy or hierarchy induction is used for Lingo.

3.4 Design of Graph Creation

It is a graphical approach, as it visualizes the dataset as the standard entity-relationship graph. There are other graphical disambiguation approaches, which visualize different graphs: Web Graph, Co-reference dependence graph, Entity-relationship graph (ER graph). Existing techniques are frequently based on probabilistic methodologies, application rely primarily on the mathematical apparatus from the area of Operation Research. The suitable visualization is the ER graph. By using JGraph class objects and their relations are displayed. A JGraph object doesn't actually contain the data; it simply provides a view of the data. Like any non-trivial Swing component, the graph gets data by querying its data model. Table1 shows the expected results/cluster names for various categories of queries.

Type of query	Query	Clusters
Ambiguous	Mouse	Computer mouse, Magic mouse, Cursor, gene, House Mouse, Mickey Mouse
General	Music	New music, music news, pop music, songs, Albums, Games
Compound Query	Travel to shimla	Tourism Travels, Travel Guide, shimla Tour Packages, Map, Hotels, Resorts
People Name	Pratibha Patil	Female President, President of India, Governor of Rajasthan, Photos, Videos, Visit

TABLE 1: Clusters

4. TOOLS USED

For many reasons we have decided to implement the system in Java (JDK 1.6). Firstly, with its emphasis on Object Oriented Programming (OOP), Java enforces the much needed good software practices such as the use of interfaces and proper code organization. Finally, Java comes with a package of optimized ready-to-use data structures (such as hash tables or lists) that make programming faster and less error-prone.

4.1 Public Interface HttpServletRequest

The `HttpServletRequest` is an abstract class that simplifies writing HTTP servlets. It extends the `GenericServlet` base class and provides a framework for handling the HTTP protocol. Because it is an abstract class, servlet writers must subclass it and override at least one method. The methods normally overridden are `doGet`, `doPost`, `doPut`. The `doGet` Performs the HTTP GET operation; the default implementation reports an HTTP BAD_REQUEST error. Overriding this method to support the GET operation also automatically supports the HEAD operation. (HEAD is a GET that returns nobody in the response; it just returns the request HEADER fields.) Servlet writers who override this method should read any data from the request, set entity headers in the response, access the writer or output stream, and, finally, write any response data. The headers that are set should include content type, and encoding. If a writer is to be used to write response data, the content type must be set before the writer is accessed. In general, the servlet implementer must write the headers before the response data because the headers can be flushed at any time after the data starts to be written. Setting content length allows the servlet to take advantage of HTTP "connection keep alive". If content length cannot be set in advance, the performance penalties associated with not using keep alive will sometimes be avoided if the response entity fits in an internal buffer. Entity data written for a HEAD request is ignored. Servlet writers can, as a simple performance optimization, omit writing response data for HEAD methods. If no response data is to be written, then the content length field must be set explicitly. The GET operation is expected to be safe: without any side effects for which users might be held responsible. For example, most form queries have no side effects. Requests intended to change stored data should use some other HTTP method. The GET operation is also expected to be idempotent: it can safely be repeated. This is not quite the same as being safe, but in some common examples the requirements have the same result. For example, repeating queries is both safe and idempotent (unless payment is required!), but buying something or modifying data is neither safe nor idempotent.

protected void doGet ([HttpServletRequest](#) req,
[HttpServletResponse](#) resp) throws [ServletException](#), IOException

Parameters:

req - [HttpServletRequest](#) that encapsulates the request to the servlet

resp - [HttpServletResponse](#) that encapsulates the response from the servlet

Throws: [IOException](#)

if detected when handling the request

Throws: [ServletException](#)

if the request could not be handled

4.2 JGraph

JGraph is a mature, feature-rich open source graph visualization library written in Java. JGraph is written to be a fully Swing compatible component, both visually and in its design architecture. JGraph can be run on any system supporting Java version 1.4 or later. JGraph provides a range of graph drawing functionality for web applications. JGraph has a simple, yet powerful API enabling you to visualize, interact with, automatically layout and perform analysis of graphs. JGraph, through its programming API, provides the means to configure how the graph or network is displayed and the means to associate a context or metadata with those displayed elements. JGraph visualization is based on the mathematical theory of networks, graph theory. The main package is JGraph itself which comprises the basic JGraph swing component:

Java Package Name	Functionality
org.jgraph	Basic JGraph class
org.jgraph.event	Graph Event Models
org.jgraph.graph	Graph Structure and nodes
org.jgraph.plaf	Graph UI delegate component
org.jgraph.util	General purpose utilities
com.jgraph.algebra	Graph Analysis Routines
com.jgraph.layout	JGraph Facade and utilities
com.jgraph.layout.organic	Force directed layouts
com.jgraph.layout.tree	Tree layouts
com.jgraph.layout.routing	Edge routing algorithms
com.jgraph.layout.hierarchical	Hierarchical layouts

TABLE 2: JGraph Package

5. ADVANTAGES

1. Readable cluster labels: - The use of phrases in the process of cluster label induction guarantees that group descriptions can be easily understood by the users. As argued in [8], frequent phrases significantly increase the overall quality of clustering, not only of the phrase-based algorithms (such as Suffix Tree Clustering) but also of other approaches such as k-means. Similar effects can be observed also in Cluster Based Web Search.

2. Diverse cluster labels: - Apart from the general abstract concepts related to fairly large groups of documents, Latent Semantic Indexing discovers narrower, more-specific ones. In this way meaningful clusters can be created whose labels are not necessarily the highest-frequency phrases. Additionally, the orthogonality of the SVD-derived abstract concept vectors makes the diversity among cluster labels even wider.

3. Overlapping clusters:- Placing the same document in a larger number of clusters increases the chances that, viewing only selected groups, the user is able to identify all relevant documents. Moreover, some snippets may be related to two or more topics and thus should be placed in all respective clusters.

4. Modular design: - As all the phases of system are easily separable. Thus, it is possible to provide alternative implementations of some of them, improving the quality or time-efficiency of the algorithm as a whole.

6. RESULTS

The system was implemented using Netbean 6.5.1 as development tool & Jdk 1.6 development Platform .Also it was tested for variety of queries under following four categories and the results obtained where satisfactory.

6.1 System Interface

This module gives the facilities for specifying the various queries to the middleware. The front end developed so far is as follows. The Figure 8 shows user interface, by using that the user enters the query to the middleware. Along with the query, user can also select the number of results (50/100/150/200) to be fetched from source. In Figure 8, query entered is "mouse" & result selected is 100.

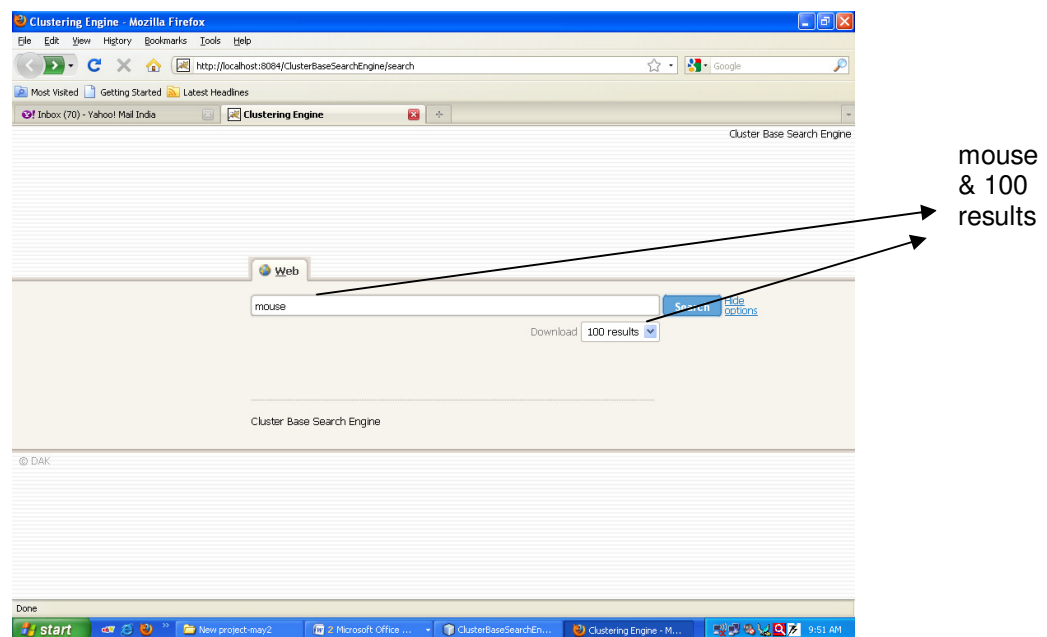


FIGURE 8: System Interface

6.2 Web Pages Retrieval for the Query

The user issues a query to the system (middleware) sends a query to a search engine, such as Google, and retrieves the top-K returned web pages. This is a standard step performed by most of the current systems. The figure 9 shows that the 200 results were fetched from the source Google for query “mouse”.

Input: Query “mouse” & k=50/100/150/200 pages Output: Web pages of Query “mouse”

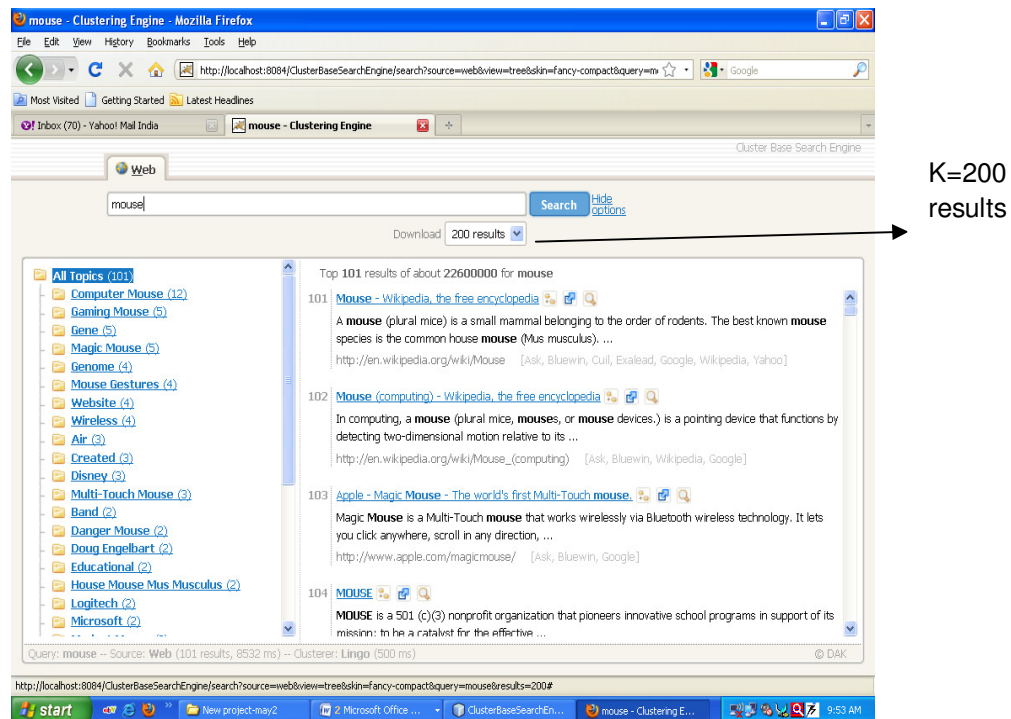


FIGURE 9: Clustering results for a ambiguous query “mouse” & k=200 result

6.3 Preprocessing Of Web Pages

The Porter stemming algorithm (or ‘Porter stemmer’) is a process for removing the commoner morphological and in flexional endings from words in English. Its main use is as part of a term normalization process that is usually done when setting up Information Retrieval systems.

Input:-connected/connecting/connection/connections

Output:-connect

The stop word removal algorithm:-To remove useless words from a search query string, in the Framework. These words, such as "the", "because" and "how", are considered stop words and can usually be safely ignored.

Input: I saw a cat and a horse.

Output: saw cat horse

6.4 Clustering & Its Processing

1. Sample results for General & specific Query

The system was assessed for a number of real-world queries; also analyzed the results obtained from our system with respect to certain characteristics of the input data. The queries are mainly categorized in four types such as

- 1 Ambiguous Query
- 2 General Query
- 3 Compound Query
- 4 People Name

The system was tested for all these queries & the result obtained is satisfactory. The figure 10 shows the clusters obtained for query “mouse” whereas the figure 11 shows the relevant pages under the cluster “Computer Mouse”.

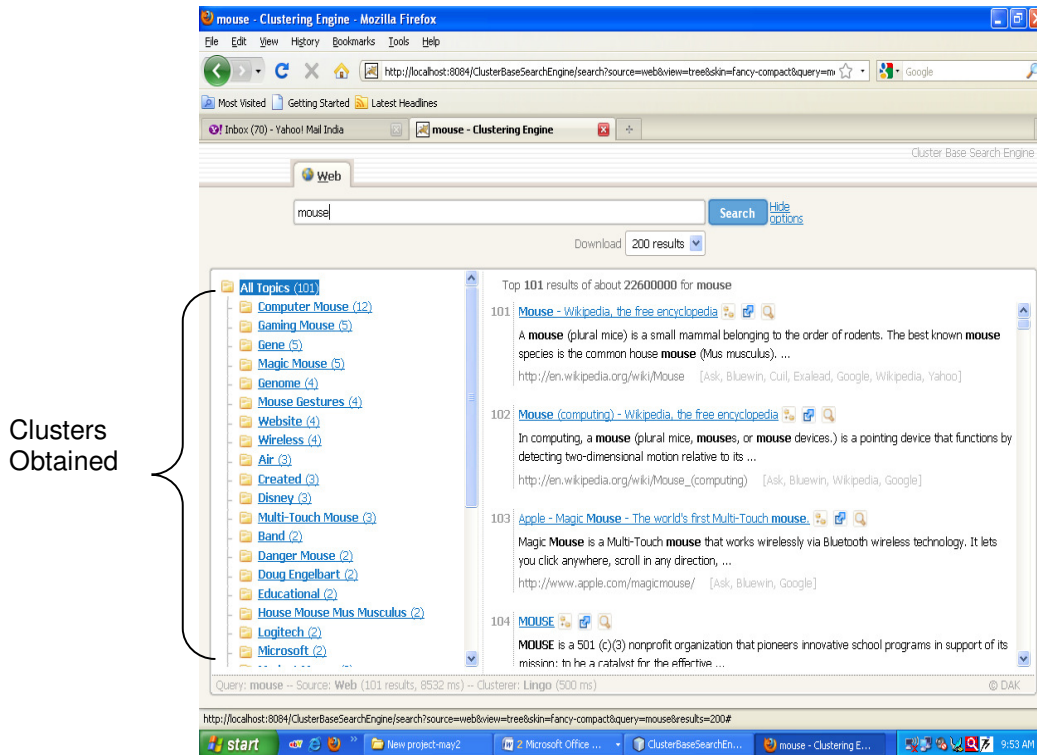


FIGURE 10: Clusters for a ambiguous query “mouse” & k=200 results

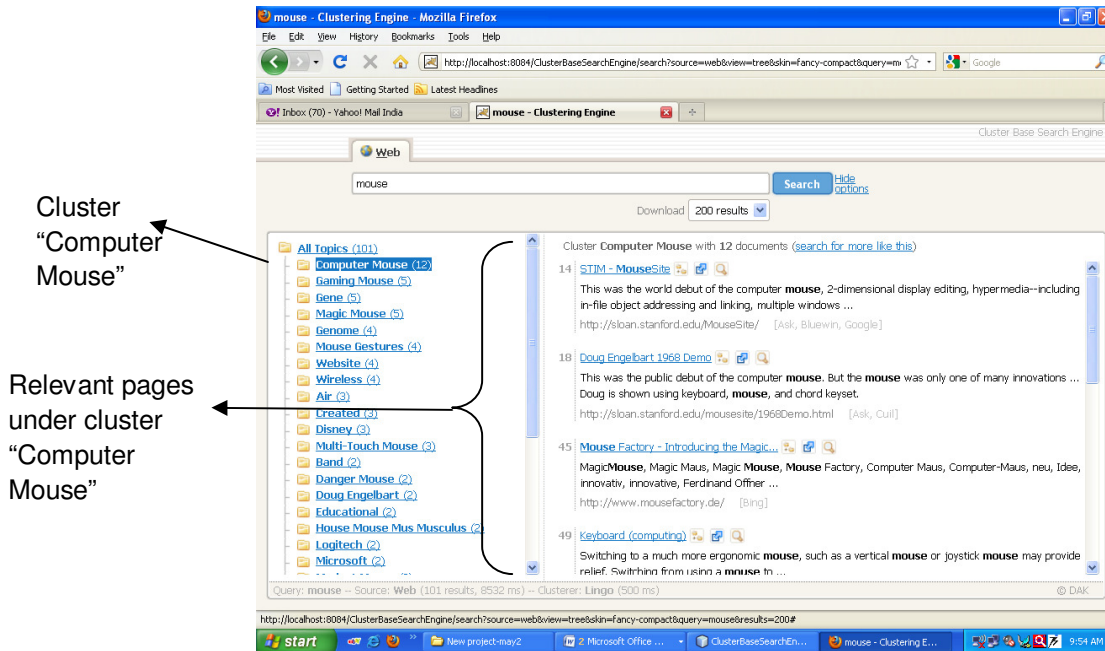


FIGURE 11: Relevant pages under the cluster “Computer Mouse”

From each type of query, some sample queries are taken for the testing of system. The Table 3 shows the name of query under each type, its clusters obtained & the processing time required. In the table the clusters are shown for top 200 results for each query. From the list of clusters obtained, only first 15 clusters are shown in the Table 3.

Query Type:-Ambiguous			
Sr. No	Name of Query	Clusters	Time
1	Mouse	Computer Mouse, Mickey Mouse, Website, Cells from Mouse, Gaming Mouse, Common Mouse, House Mouse, Technology, Gene, Graphics, Series, Apple, Magic Mouse, Support, Windows	844 ms
2	Tiger	Panthera tigris , Year of Tiger, Animal, News, Tiger Woods, Tiger Pictures, Website, Map, Tiger reserve, Art, Mac OS X, Tiger Airways, Wikipedia, Big Cats, China	906 ms
3	Java	Java Developers, Java Language, Java Platform, Download, Sun Microsystem,Java Tutorials, Java Applets, Java Virtual Machine, Java News, Java Resoursec,Community, Java Implementations, Java Runtime Environment, Java EE, Open Source, Learn Java,Class,Coffee	735 ms
4	Apple	Apple Computer, Mac OS X, Apple Products, Music, Developer, New Yark, iPod, Macintosh, Valley, AAPL Stock, Experience, Hardware & Software , Programs, Series, Tree	735 ms
5	Sahara	Western Sahara, Sahara Desert, Sahara Services, Map, Sahara Group, Design, Film Directed,India,Photos,Vegas Hotels, Website, Matthew McConaughey, Sahara Occidental, South Africa	719 ms

6	Apache	Apache Project, Open Source, Apache Software Foundation, Web Server, Apache Related, Apache Tribe, Acute Physiology & Chronic Health Evaluation, Apache License, Download, United States, Apache II Score, New Maxico, Reviews, Apache Maven, Attack Helicopter	891 ms
7	Jobs	Job Opportunities, Positions, Services, Market, Career Advice, Jobsuche, Research ,Switzerland Jobs, Books, Employee, Graduates, Post Your Resume, Career Opportunities, Employment Opportunities, People	735 ms
8	Tree	Tree of Life, Trees Used, Tree Structure, Family Tree, Forest, History, Tree of Life Web Project, Abstract, Data Structure, Green, Service, Art, Defining, Living, Maximum Likelihood, Music	875 ms
9	Ups	Company,Tracking,Shipping,UPS Freight, Uninterruptible Power Supply, Protect, APC, Press, Uninterruptible Power Systems, United Parcel Service, Air Freight, Browse UPS Portfolio UPS Solution Finder Solutions, Fields,Ireland,Package	265 ms
10	Jaguar	New Cars, Jaguar Panthera Onca, Jaguar XF, Jaguar XJ, Performance, Engine, Reviews, Google Buchsuche-Ergebnisseite, Land, Buy, Classic, Jacksonville Jaguars, Luxury, Big Cats, Jaguar E-Type	657 ms
11	Saturn	Planet Saturn, Rings Saturn, Saturn's Moons, Jupiter & Saturn, Solar System, Saturn Cars, News, View Saturn, Google Buchsuche-Ergebnisseite, Saturn Wikipedia, Saturn Corporation, Downloads, Fact, ION, Media Market	844 ms
12	Jordan	Michael Jordan, Air Jordan, Jordan Website, Photos, Jordan News, Jordan Born, December, MySpace, Hashemite Kingdom of Jordan, Woman, Middle East, New York, Research, Review, Wikipedia	640 ms
13	Quotes	Quotes & Quotations, Famous Quotes, Quotes Collection, Market Quotes, Quotes Saying, Love Quotes, Inspirational Quotes, Quotes of the Day, Trades & Quotes, Funny Quotes, Auto Insurance, Quote Topics, Compare Auto, Humor, Research, Life Insurance	672 ms
14	Matrix	Systems, Matrices, Method, Matrix Games, Analysis, Wikipedia, Extracellular Matrix, Human, Matrix Group, Revolutions, Applications, Download, International, Laurence Fishburne, Material, Power, Select	656 ms
15	Light	Light Source, Design, Seeing the light contact, Electric, Electromagnetic Radiation,News,Organic,Search,Website,Blue,Energy,Music,Point,Video	828 ms
Query Type:-General Terms			
16	Yellow pages	Search Yellow pages, Local Business Directory, White Pages, Local Business Listings, Phone numbers, Maps & Directions, Telephone Directory,Companies,Classifieds,International,People,Sourse,City Guides, Complete, Global	806 ms
17	Maps	World Maps, Google Maps, Driving Directions, Download Maps, Digital Maps, Image Map, Bing Maps, Historic, Yahoo, Genetic Linkage Maps,	859 ms

		Germany Map, International, Live, Models, National Geographic, Code	ms
18	Health	Health news, Health medical, National Health, Health Fitness, Health & Medical News, Public Health, Centers, Diet, Children's Health, Diseases & Conditions, Health Articles, Health System, Health Information Resources, Health Magazine, Health Promotion	687 ms
19	Flower	Flowering plants, Send Flowers, Delivery Send Flowers, Flower Garden, Shop, Flower Show, International, Pictures, Wedding, Directed, Flower Power, Mothers Day, Protein, Research, Stem	718 ms
20	Music	MUSIC Videos, New MUSIC, MUSIC Song, World MUSIC, Internet, Country MUSIC, MUSIC Lyrics, Listen to MUSIC, MUSIC Games, Search, Performance, Electronic MUSIC, Album, Internet, Radio, MUSIC Festival	719 ms
21	Chat	Chat Rooms, Live Chat, Chat with people, Chat with friends, Community, Web Chat, Chat System, Games, Help, Blogs, News, Voice Chat, Chatrooms, Login, Windows	688 ms
22	Games	Puzzle Games, Flash Games, Download Games, Play Arcade, Fun Games, Racing Games, Alzheimer's Disease, Internet, Summer Olympics, Kids, Learning, Funny Games, News, Models, Publisher	672 ms
23	Radio	Radio Broadcasting, Music Radio, Internet Radio, News, Digital Radio, Talk Radio, Radio Stations Live, Streaming Radio, Public Radio, Local, Switzerland, BBC Radio, Radio Shows, Analysis, Programming	828 ms
24	Jokes	Blonde Jokes, Collection, Cartoons, Category, English, Games, Funny Pictures, Laugh, People, Clean Funny, Sex, German, Lots, Computer, Human	672 ms
25	Graphic design	Art design, Web design, Website design, Advertising, Graphic design Illustrator, Graphic design Portfolio, Graphic design Studio, Graphic design Schools, Typography, World of Graphic design, Graphic design Blog, Graphic design Program, Marketing, Process, Freelance Designers, Graphic design Agency	703 ms
26	Resume	RESUME Services, Cover letter, Writing Samples, Templates, RESUME Help, Sample Cover, Tips, Search, Graphic Design, Jobs Post, Portfolio, RESUME Builder, Website, Examples & Templates, Publishing	687 ms
27	Travel	Information & Travel, Cheap Hotels, World Travel, Travel Holiday, Travel Tourism, Travel Services, Destination Guide, Car rentals, Time Travel, Airline Tickets, Switzerland Travel, Tours, Travel Blog, Travel Directory, Travel Discounts	671 ms
28	Time zones	Countries & Time Zones, Standard Time, Daylight Saving Time, Time Map, World Clock, Time Difference, Current Local Time, UTC TIME, Time Zones are observed, United states, Date Time, Eastern, Page Time Zones, Time Zones	703 ms
29	World war 2	History of World, Second World, Timeline for World, WW2, World War 2, Germany in World, German World, Army, Day by Day, World War 2 Weapons, Europe after World, Video, Books, World War II Memorial, United States, Adolf Hitler	672 ms

30	Ford	Ford Motor Company, Ford Dealer, Ford Parts, Henry Ford, New Cars, Performance, Ford Fiesta, Reviews, Engine, Going, United States, Breast Cancer, Europe, Explorer, Limited	766 ms
Query Type:-Compound Query			
31	Travel to indonesia	Bali Indonesia, Indonesia Hotels, Indonesia Tours, Indonesia Islands, Travel Information & Travel Guide, Holiday in Indonesia, Indonesia, Jakarta Travel, Visit Indonesia, Travel Tips, Southeast Asia, Travel Warnings, City, Culture, History	797 ms
32	Photos of pets	Animal Photos, Pictures of Dogs, Pictures of Cats, Pet Photo Gallery, Pet News, Pets & People ,Featuring, Puppies, Digital, Kids, Life, Pets Like, Send, Contests, Health	657 ms
33	how to prepare for gate-11	Exam, GATE 2010,Time To Prepare, method, September 11,Attacks,Blog,City,July,Subjects,John,Present,Sample,Steps,Study	891 ms
34	the enemy of the state	Enemy of the state movie, Enemy of the state 1998,Review of Enemy of the state, Trial & Execution of Saddam Hussein, Video, Enemy of the state film, Gene Hackman , Enemy of the People, Lupe Fiasco, Jerry Bruckheimer, Directed by Tony Scott, Office, Public Enemy, Wolverine, Love story Mix tape, Declared, Enemy of the State Award, Making, Crimson Tide, Death	703 ms
35	topics related to thrust areas in computer engineering	Related Research, Computer Science & Engineering,University,Related Course, Education, Electrical & Computer Engineering Department, Mechanical Engineering, Civil Engineering, Management, New Thrust, Systems Engineering, School, Response	704 ms
36	To be or not to be	Google Buchsuche-Ergebnisseite, Games, Tobe T, Face book, Name Tobe, News, Reviews ,Seiten , Service , People, Play Games, Question, Search, Tobe, Hooper, Years	781 ms
37	New York times	City New York, New York times Company, New York Times Newspaper, Breaking News, New York Times Magazine, United States, New York Times Copyright, Readers, Privacy Policy, Report, New York Review of Books, Travel, Car, Daily Newspaper, Media	703 ms
38	making best use of existing resources	Practices, Available Resources, Decision Making, Programs, Software, Sources, Existing Work, Making more efficient use of Existing Resources,Difference,Health,Natural,Training,Land,Report,Schools	812 ms
39	Define skill & confidence	Confidence Definition,Learning,Skill Level,Self,Improve,Communication Skill, Skill Set, Social Skill, Apply Media, Leadership Skill,Game,Test,Coaching,Life,Measure,Facilitator	834 ms

40	giving wings to your future	Giving wings to Dreams, Future Plans, Life,Tip,Children's Future, Future Generation,Help,Save Your Search Strategies for Future Use, Wings to EAA,Spread,Idea,Program,Design,Detroit Red Wings,Mean,Thought	687 ms
Query Type:-People Name			
41	Pratibha Patil	Pratibha Patil News ,Woman Behind Woman, New Delhi, Woman, Governor of Rajasthan, Pratibha Patil Photos, Patil to visit, National, Pratibha Patil Pictures,rashtrapati Bhavan,Video,Female President,Manmohan Singh,Abdual Kalam,Presidential Candidate	969 ms
42	g a Patil	G.A., Pratibha Patil, Department, Georgia GA, Internal Medicine, Journal, Indian National Congress, R.T., S.L., A.Y., Nagana Gowda, Address & Phone Number, Education, PaR, Book	875 ms
43	d a kale	Kale Rang da Yaar,D.Kale,MP3 Download, Kale Rang de Paranda,ND,Dupatta Tera, Brassica Oleracea,Rk,Center,India,S.D.Kale,search Engine,Shazia Manzoor, Authors, High	781 ms
44	Kiran Bedi	India's First Woman, Indian Police Officer, Highest Ranking, Kiran Bedi Film, Kiran Bedi 2009,Woman,Indian Police Service IPS, New Delhi,www.kiranbedi.com-first & Highest Ranking Indian Woman,Foundation,Celebrated,Madam Sir, Reforms, Tihar Prison, Book	734 ms
45	Ujjwal Nikam	Mumbai Terror Attacks, Special Public Prosecutor in the 26/11,Terror Case, Videos, Terrorist, Accused, Latest News, Death Penalty Business, Media, Sabauddin's Acquittal, Search, Conduct Open Trial in 26/11 Case, Conviction, Witnesses	860 ms
46	Dr c d kane	Danity Kane, New CD, Albums,B C D E F G H,M.Kane,D.C,Movie,MySpace,Professor,RedPyramid,Feelgood,M.D,M medicine,Picture, Studio	719 ms
47	Andrew McCallum	Univerity, Author Andrew, People, Profile for Andrew McCallum, Conditional Random Fields, Text Classification,Kamal Nigam, University of Massachusetts Amherst, Labeled Data, Aron Culotta, LinkedIn, Music, Active, Graduate Student, MALLET	750 ms
48	William Stalling	Computer Organization & Architecture, Data Communication, EBook EBook, Network Security, Operating Systems, William Stallings Cryptography, Author William Stalling, Download Torrents,6 th Edition,Bill, Rapidshare Search, Operating Systems Internals & Design Principles, Review, Network Security Essentials, Principles & Practice	766 ms
49	a bachchan a	Aishwarya Rai, Amitabh Bachchan's Movie, Bachchan's Videos,Yeh Kahan Aa Gaye Hum, Film Starring, Bachchan Family,Bollywood Star, Starring Abhishek Bachchan,Blog,Lata Mangeshkar,Role,Latest News, YouTube, Bachchan a Day, Film Directed,Harivansh Rai Bachchan	734 ms

50	Kelly Flanagan	J.Flanagan, Palm Desert Real Estate, Brigham Young University, Blog, VIDEO, Kelly Flanagan's Page, Computer Science Department, Engineering, Jobs, Member, Authors, Ian bannen, John Flanagan, Trace Collection, Elizabeth	750 ms
----	----------------	--	--------

TABLE 3: First 15 Clusters for various queries

6. CONCLUSION & FUTURE WORK

Most of the traditional entity resolution techniques are feature-based similarity (FBS) methods, as they employ similarity functions that compare values of entity features (or attributes) in order to determine if two object descriptions co-refer. The estimation is that context-based and relationship-based algorithms always get better results than FBS because of entity-relationship graph generation, wherein the nodes represent the entities in dataset D and the edges represent the relationships among the entities. For any two entity representations, the co-reference decisions will be made not only based on the entity features, or information derived from the context, but also based on the inter entity relationships, that exist among the two representations. Because of this process, there will be improvement in the performance. The concentration will be made on study of the efficiency of the approach. Also there is probability that it will improve the result of clustering because disambiguation algorithm makes analysis of inter object connection. SVM classifier is used to determine whether the system is stable or not depending on the workload that is assigned for each & every machine treated as client machines also inform about the instability of system when excess load is there. During processing whole data is updated in database stored on server machine. Hence SVM done the work of load balancing over the network & provide a stable network where all requests get distributed equally. Due to this the efficiency of the system will be increased significantly.

7. REFERENCES

- [1].D.V.Kalashnikov, S.Mehrotra, R.N.Turen and Z.Chen, "Web People Search via Connection Analysis" IEEE Transactions on Knowledge and data engg.Vol 20, No11, Novr 2008.
- [2]. D.V. Kalashnikov, S. Mehrotra, Z. Chen, R. Nuray-Turan, and N.Ashish, "Disambiguation Algorithm for People Search on the Web," Proc. IEEE Int'l Conf. Data Eng. (ICDE '07), Apr. 2007.
- [3]. M. F. Porter. *An algorithm for suffix stripping*. Program Vol. 14, no. 3, pp 130-137.
- [4]. S. I. Osinski, J. Stefanowski, and D. Weiss. "Lingo: Search Results Clustering Algorithm Based on Singular Value Decomposition".
- [5]. Z. Dong. "Towards Web Information Clustering". PhD thesis, Southeast University, Nanjing, China, 2002.
- [6] S. I. Osinski. "An Algorithm for Clustering of Web Search Results". Master's thesis, Poznań University of Technology, Poland, 2003.
- [7] G. Salton. "Automatic Text Processing — The Transformation, Analysis, and Retrieval of Information by Computer". Addison-Wesley, 1989.
- [8] O. E. Zamir. "Clustering Web Documents: A Phrase-Based Method for Grouping Search Engine Results". Doctoral Dissertation, University of Washington, 1999.
- [9] J. Stefanowski and D. Weiss. "Web search results clustering in Polish- Advances in Soft Computing, Intelligent Information Processing and Web Mining", Proceedings of the International IIS: IIPWM'03 Conference, Zakopane, Poland, vol. 579 (XIV), 2003, pp. 209-22.

Impact of Ground Effect on Circulation Controlled Cylindrical Surfaces

Byron W. Patterson

*West Virginia University (WVU)
Mechanical and Aerospace Engineering Dept. (MAE)
Center for Industrial Research Applications (CIRA)
PO Box 6106
Morgantown, West Virginia, 26506, USA*

bpatter6@mix.wvu.edu

Gerald M. Angle, II

*West Virginia University (WVU)
Mechanical and Aerospace Engineering Dept. (MAE)
Center for Industrial Research Applications (CIRA)
PO Box 6106
Morgantown, West Virginia, 26506, USA*

Gerald.Angle@mail.wvu.edu

Emily D. Pertl

*West Virginia University (WVU)
Mechanical and Aerospace Engineering Dept. (MAE)
Center for Industrial Research Applications (CIRA)
PO Box 6106
Morgantown, West Virginia, 26506, USA*

Emily.Pertl@mail.wvu.edu

James E. Smith

*West Virginia University (WVU)
Mechanical and Aerospace Engineering Dept. (MAE)
Center for Industrial Research Applications (CIRA)
PO Box 6106
Morgantown, West Virginia, 26506, USA*

James.Smith@mail.wvu.edu

Abstract

Circulation control technology and motion in close proximity to the ground have both shown aerodynamic benefits in the generation of lift. Recent research efforts at West Virginia University have explored the potential of merging the two phenomena, in an attempt to enhance both technologies. This paper initiates this combined effort by experimentally investigating the impact ground effect has on the separation location of a jet blown tangentially over circulation controlled cylindrical surfaces. Previous experimental research on circulation controlled cylinders found an optimal radius of curvature and volumetric flow rate; whose model and optimal findings are built upon by this work through the addition of ground effect analysis by varying the ground height. The experiment investigates some of the variables that individually influence circulation control and ground effect; the variables are the radius of curvature, velocity of the jet, and the height from the ground. Data analysis revealed that for a constant volumetric flow rate and varying the height to radius (h/r) value, there is a large amount of variability in the data, indicating that the proximity of the ground has significant impact on the separation location and consequently influence on the potential lift characteristics. Furthermore, when this flow rate was analyzed, it was found that at an h/r of approximately 4.8, it appears that an optimal h/r occurs, based on the surface pressure and flow separation from the cylinders when not influenced by the ground. The data also found that at both radii, 0.520 and 0.659 inches, showed benefit when tested in close proximity to the ground. The findings demonstrate that there is further enhancement potential of the lift generating capability by uniting the lift enhancement of circulation control methodology with the ground effect flight regime.

This effort is a preliminary study of a larger effort to determine if merging the two phenomena indicates a lift enhancement. This model does not have a free stream velocity, and subsequently does not measure

lift, however, the findings depicted in this effort indicate that there is potential for enhancement, which is currently being researched by the authors.

Keywords: Ground Effect, Cylindrical Jet, Jet Separation

1 INTRODUCTION

This research effort combines the aerodynamic benefits of circulation control technology along with the added benefits of typically associated with ground effect flight. Circulation control is a lift augmentation technology that improves the coefficient of lift of a conventionally shaped lifting surface. A circulation control wing differs from the traditional wing largely in the trailing edge. A circulation control trailing edge is normally blunt and circular, whereas the conventional wing has a sharp edge. While there is an additional amount of lift generated by a circulation control surface, the trailing edge tends to increase the effects of parasitic drag [1]. Along with an altered trailing edge, other geometric differences of the circulation control wing include the presence of air chambers within the structure, and the jet slots used to supply the energized jet to the rounded trailing edge.

Circulation control technology has been applied to a wide range of applications, including Short Take-off and Vertical Landing (STOVL) vehicles. It is a desired method for STOVL applications since these vehicles are designed for remote locations, where a normal length runway is not available. The high lift benefits provided by a circulation control wing allow the vehicle to land in little to no space due to the lower horizontal speed requirements to obtain a specific lift force. Besides STOVL vehicles, circulation control has been adapted for use on helicopter rotor blades, wind turbines, watercraft, and ground effect and ground contact vehicles.

The second phenomena considered in this investigation is the benefit gained through ground effect motion. Similar to circulation control, the presence of a lifting surface induced by ground effect results in larger lift coefficients. This result can simply be explained by realizing that as a lifting surface approaches the ground the air underneath the wing becomes pressurized, similar to a ram pressure. Thusly, as the air pressure increases, an increase in the lift created by the surface is noticed. Traditionally, ram pressure describes a technique that forces air underneath the lifting surface, however, for this effort, the term is used to describe the increased pressure due to flow onset.

Many efforts have been conducted on trying to design the structure of the lifting surface so as to capture more of the ram pressure effect, thereby increasing the overall lift. Mantle presents a multitude of designs for aerodynamic cushion craft forms, which have a downward shaped structure at the furthest outboard location of the wing; some of wings are called ram wings and channel flow wings, illustrating the focus of ram pressure on a wing in ground effect [2]. While the wings presented by Mantle are altered to capture the ram pressure and increase the lift, traditional wings also experience ground effect; however energy is often lost from the pressure gradient at the wing tips [2]. Just as with circulation control, inducing the phenomenon of ground effect has been applied to many applications including STOVL vehicles, hovercraft, and watercraft. While both of the presented phenomena have benefits by themselves, amalgamating the two potentially permits further lift and possibly control benefits, applicable for many industries including wind turbines, motorsports, and automotive.

This research effort explores the merging of the two phenomena, attempting to determine whether the combination further enhances or detracts from each other. To investigate the influences of the two lift enhancements, a model was constructed that identifies the angular separation point of a blown jet on a cylinder, which represented the trailing edge of a circulation control airfoil, with decreasing height above a ground plane. Since the model does not have any free stream velocity, the ram pressure as explained is not considered at this point in the research program, since this effort is a preliminary study in order to determine if further wind tunnel research where flow onset is present is needed. Rather, the surface pressure on the cylinder is measured as a function of the angular location from the slot exit. The data from the angular surface pressure can then be compared to the same quantity but at a different height above the ground. What's more, the performance of a ground effect induced circulation control cylinder is

now believed to be dependent upon a multitude of variables including, but not limited to, the trailing edge radius, the velocity of the jet, and the height from the ground.

2 BACKGROUND

2.1 Circulation Control

Circulation control technology exploits a fluid dynamic phenomenon, known as the Coanda effect. This phenomenon, discovered by Henri Coanda in 1910, is experienced by the common person on a daily basis [3]. A simple example is when a liquid is poured from a glass, the liquid has a tendency to adhere to the edge and curl around, resulting in the annoying dribble of liquid from the glass. Another example is when a finger is placed, or the back of a spoon, under a thin water stream from a faucet, the stream attaches to the finger, flows around the blunt object, and again becomes a uniform flow on the adjacent side. It is necessary to point out, that for the latter example, while the flow is uniform on the adjacent side, the flow is at an angle offset from the original direction; this concept can be applied to circulation control lifting surfaces, where the finger is represented by the circular trailing edge of the modified airfoil, and the flow is shown by the energized air in the model produced by the jet slots. Reba [3] defines the anomaly as the tendency of a fluid, either gaseous or liquid, to cling to a surface, that is near an orifice from which the fluid emerges. Newman [4] offers an alternate definition, describing the Coanda effect as the deflection of plane jets by adjacent boundaries.

Similar to the glass of liquid and stream of water visuals, the Coanda effect can be experienced on a circulation control surface. The air flowing over a lifting surface can be influenced by a jet of air blown out of a small slot over a region of a surface. Some of the research efforts have utilized a circulation control lifting surface with two orifices for the jet of air to expel, which are located at the top and bottom of the circular trailing edge, shown in FIGURE 1. This dual slot configuration enables the ability to increase or decrease the lift force generated, together or alternately if required. Along with the exit slot difference, a circulation control wing or lifting surface differs from the conventional wing by the blunt trailing edge and the internal plenum structure for the energized air supply, shown by the NASA 0417 airfoil and the NASA 0417 CC airfoil. Many efforts, however, including this work, utilize only one exit slot, illustrated in FIGURE 2.

The Coanda effect would not be as advantageous for the standard airfoil design, such as the NASA 0417 airfoil with a sharp trailing edge. If a blown jet were applied to this conventional design, the fluid would adhere to the surface until the sharp point, where the flow would break from the airfoil, consistent with the Kutta condition. This would result in a jet flap, which produces beneficial lift performance, however, this enhancement is met by a higher energy cost in the pumping of the air than a circulation control airfoil like the NASA 0417 CC airfoil with the rounded trailing edge.

As the fluid leaves the slot, b , in FIGURE 2, whether with one or two orifices, the jet, at a given jet velocity, V_{jet} , attaches to the surface due to the imbalance of centrifugal and pressure based suction (vacuum) forces [3]. This effort uses the term 'vacuum' to describe the pressure gradient of the energized jet. As observed by Henri Coanda in his jet exhaust efforts, due to the presence of an increased jet velocity, the pressure on the surface of the cylinder is less than the atmospheric pressure, creating a vacuum that pulls the jet towards the surface [3]. As the air traverses an angular displacement, θ , along the cylinder, the air reaches the separation point, where the free stream pressure, p_∞ , and the pressure at the surface are equalized by the inertia (centrifugal) force of the jet, culminating in a zero net force, and the separation of the flow from the cylindrical edge. Newman found by theoretical calculations that the fluid has the potential of attaching through angular displacement of up to 180 degrees from the jet exit [4].

Previous efforts by the authors have found empirically that with an optimal radius of curvature and jet velocity, the energized air has the potential to attach at angles up to 231 degrees [5]. In addition, this jet has a higher velocity than the surrounding free stream air, resulting in a pressure gradient that pulls more air into the low pressure segment called entrainment. The further entrainment of air into the flow increases the angular displacement of the boundary layer, and increases the amount of the jet attached to the surface. Coanda found that as the jet flowed around the edge, it entrained up to 20 times the amount of air, relative to the original jet [3].

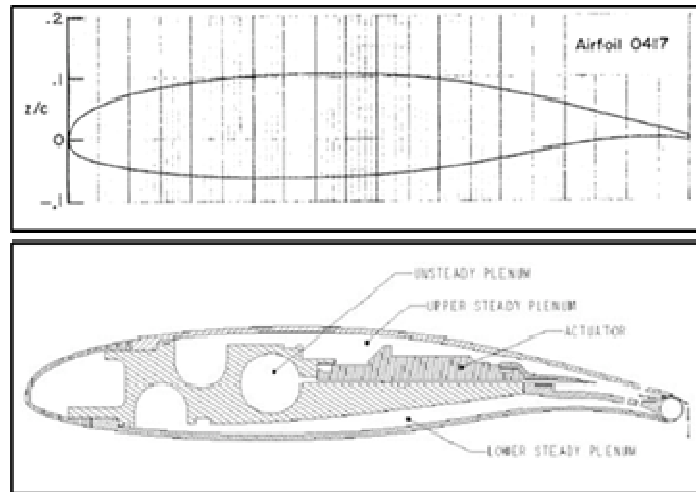


FIGURE 1: NASA 0417 airfoil (above) [6] and NASA 0417 CC airfoil (below) [7]

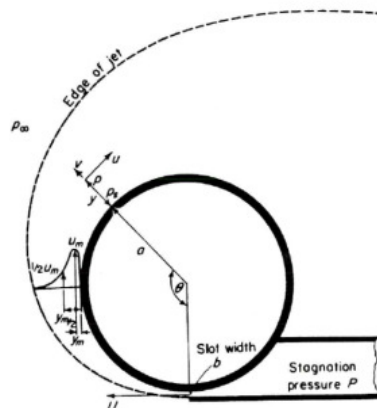


FIGURE 2 : Fluid flow around a cylinder [4]

The main advantage of circulation control technology over traditionally shaped lifting surfaces is the increase in lift due to the attachment of the energized air flow. Fisher [8] found that a circular cylinder consistently produced greater Lift-to-Drag (L/D) values than the 50% ellipse airfoil, whose results were found to be comparable to a conventional airfoil. His findings indicate that the drag on the circular cylinder was minimized as the lift was optimized, showing that when the blown jet is activated, the circulation control model's drag was overcome by a larger increase in lift. Fisher also found that a circulation control airfoil outperformed the 50% ellipse airfoil, in regards to the L/D value. Note that this result is only applicable during periods of jet activation [8]. Along with the findings of Fisher, Cagle and Jones found that as the velocity of the jet of air increases, there is an increase in the coefficient of lift, as shown in

FIGURE 3 [7]. In Cagle and Jones' graph, the velocity of the jet is non-dimensionalized through the blowing coefficient, C_{μ} , which relates the slot height t , the chord length c , the ratio of specific heat γ , the ambient density ρ_{∞} , the free stream velocity V_{∞} , the Mach number of the air jet at the slot M_j , and the plenum pressure P_o , as defined by Ambrosiani in Eq. (1) [9].

Englar [10] offers an alternate definition of the blowing coefficient per unit span in Eq. (2), which is dependent on the mass flow rate \dot{m} , velocity of the jet V_j , the dynamic pressure q and the chord length c [10]. Cagle and Jones' findings show that for $C_{\mu} = 0$ and $C_{\mu} = 0.060$, there is a lift enhancement of around 2.5, corresponding to a maximum coefficient of lift of 1.3 and 3.4, respectively. A traditional NASA 0417 airfoil is proven to generate a maximum lift coefficient of 1.8 [6]. Thus, when a circulation control airfoil is compared to a traditional airfoil, there is a lift generation by a factor of around 2.

$$C_{\mu} = \frac{t}{c} \frac{2\gamma M_j^2}{\rho_{\infty} V_{\infty}^2} P_o \left[1 + \frac{\gamma - 1}{2} M_j^2 \right]^{\frac{-\gamma}{\gamma - 1}} \tag{1}$$

$$C_{\mu} = \frac{\dot{m} V_j}{q c} \tag{2}$$

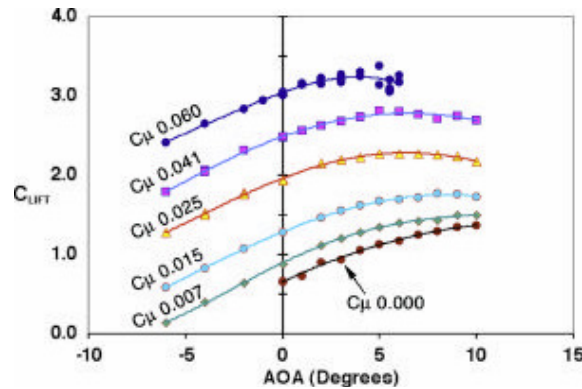


FIGURE 3 : NASA CC 0417 C_L [7]

However, along with large amounts of lift, the geometry of a circulation control airfoil in FIGURE 1 generates a substantial amount of parasitic drag, during periods of deactivation, due to the altered trailing edge shape. When comparing a conventional NACA 0018 airfoil and a NACA 0018 circulation controlled airfoil at a similar Reynolds number of 4.0×10^5 , and coefficient of lift of 0.60, the coefficient of drag was 0.018 and 0.763, respectively [11]. The data for the circulation control NACA 0018 was collected by one of the authors for a CC-NACA0018 wind turbine project [12].

The origin of this effort stems from a previous effort by the authors to explore the relationship between the radius of curvature, jet velocity, and angular separation [5]. The results are shown in FIGURE 4. As the radius of curvature increased, there was a decrease in the angular separation point. Conversely, as the jet velocity increased, there was a delay in the separation of the flow, increasing the angle from the jet exit to the point of separation. This effort culminated in an optimal cylinder radius and jet velocity, as related to the separation point, resulting in a radius of 0.659 inch and a volumetric flow rate of 30 ft³/min. For this current research effort, the optimal radius was used, along with the 0.52 and 0.943 inch radius cylinders, which were the closest to the optimal radius of those previously tested.

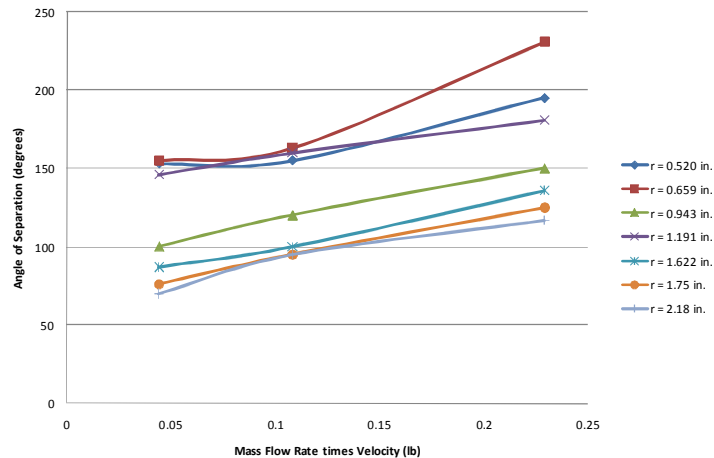


FIGURE 4 : Angle of separation and mass flow rate velocity [5]

2.2 Ground Effect

The second phenomena that this effort considered was the additional lift experienced while a moving surface is in ground effect. Mantle defines an air cushion craft as “any craft designed to operate for a significant periods of time in the proximity of the surface over which it operates and to generate a significant part of its lift through pressurized airflow” [2]. Mantle later states in his introduction that his definition also applies to the ram wing, wing in ground effect, WIG, and channel flow craft. Both the ram wing and the channel flow craft were described in the introduction section of this paper. The previous definition is illustrated in FIGURE 5, showing how the air pressure generates under the craft and influences the surroundings. Mantle documents two performance gains by flying in ground effect. The first performance gain is that the stagnation point, defined by the Kutta condition, at the rear of a wing moves aft on the under surface. This movement increases the curvature of the streamlines, resulting in an increased circulation and lift. The second performance gain results because, as the wing approaches the ground, the span wise flow to the tip is lessened, weakening the tip vortices, and decreasing the lift induced drag [2].

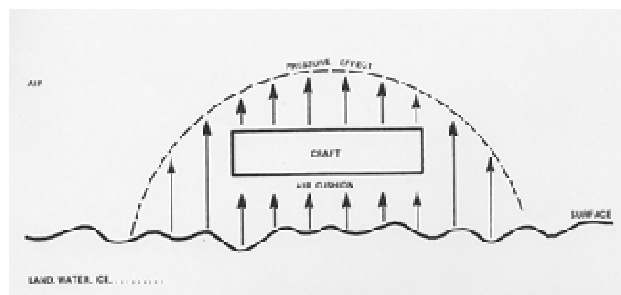


FIGURE 5 : Air cushion craft [2]

The coefficient of pressure is defined in Eq. (3), where ΔP is the pressure difference between the local and ambient pressure, A_{jet} is the area of the jet (1.188 in^2), and the T is the thrust of the jet. Coulliette and Plotkin offer an alternate definition in Eq. (4), for the coefficient of pressure for a zero thickness airfoil, where U_∞ is the free stream velocity, $u(x)$ is the horizontal velocity contribution, the h_{te} is the height of the trailing edge, and $h(x)$ is the height of the lower surface of the airfoil [13]. Traditional textbooks define the coefficient of pressure as depicted in Eq. (5), however, this form is not helpful for the current work since the dynamic pressure is dependent on the free stream velocity, which is absent from the model [14].

$$C_p = \frac{2(\Delta P)(A_{jet})}{T} \tag{3}$$

$$C_p(x) = 1 - \frac{u(x)^2}{U_\infty^2} = 1 - \frac{h_{te}^2}{h(x)^2} \tag{4}$$

$$C_p = \frac{p - p_\infty}{\frac{1}{2}\rho_\infty U_\infty^2} = \frac{p - p_\infty}{q_\infty} \tag{5}$$

The amount of pressure increase due to the presence of the ground, illustrated in FIGURE 5, is substantiated by an effort by a group of researchers at NASA Ames Research Center [15]. The group explored the forces and pressures induced on circular plates both in and out of ground effect. They found that there was an increase in the coefficient of pressure C_p while the plates were in ground effect. The group explored many height-to-plate diameter ratios, h/d_e , including 3.3 and 12.2. These two values represent the coefficient of pressure experienced as the plate is displaced further from the ground. As demonstrated by their effort, the closer the 20 inch plate was to the ground, the larger the coefficient of pressure. This fact is illustrated by simply looking at the scales of the coefficient of pressure in the detailed report. The scale for $h/d_e = 12.2$ is much smaller, indicating that the pressure is equally smaller.

While the NASA research effort illustrates the increase in the coefficient of pressure, the main advantage to ground effect is the increase in the coefficient of lift. Plotkin and Dodbele offer a definition of the alteration to the lift curve slope for a slender wing in ground effect in Eq. (6), where $C_{L\alpha}$ is the lift coefficient in ground effect, $(C_{L\alpha})_\infty$ is the lift coefficient out of ground effect, H is the height at the lowest point of the wing, and b is the wing span [16]. Eq. (6) culminates into FIGURE 6, which shows that at lower trailing edge height, the coefficient of lift in ground effect is substantially larger. The A in the graph is the aspect ratio of the slender wing. FIGURE 6 visually shows that the pressure experienced in ground effect results in a larger coefficient of lift, thereby demonstrating that a wing in ground effect has the potential to be enhanced when combined with the lift benefits of circulation control shown in FIGURE 3.

$$\frac{C_{L\alpha}}{(C_{L\alpha})_\infty} = 1 + \frac{1}{8}\left(\frac{b}{2H}\right)^2 - \frac{1}{32}\left(\frac{b}{2H}\right)^4 \tag{6}$$

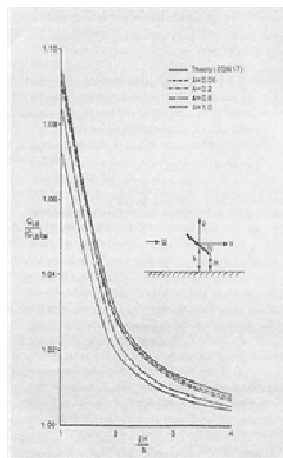


FIGURE 6 : Lift curve slope for slender wing in ground effect [16]

3 EXPERIMENT

3.1 Investigation

The investigation experimentally explores the impact that the radius of curvature, jet velocity and the height from the ground have on the delay in the flow separation of circulation control cylinders. The radius of curvature was changed between three different radii, including 0.520, 0.659, and 0.943 inches. The jet velocity was changed between three velocities relating to the volumetric flow rates of 10, 20 and 30 ft³/min. The height was changed six times. The heights are not constant values across all the radii, because the height in this effort is defined as the distance from the center of the cylinder to the top of the ground. Since the heights differ, when considering the height, the non-dimensional height-to-radius h/r quantity is used. Understanding the relationship between these three variables results in a better understanding of the effect circulation control and ground effect can have on each other.

3.2 MODEL, TEST SET-UP, TESTING METHOD

The setup for the testing of the three defined variables was conducted with the apparatus in FIGURE 7. This model is the same as the one used in the previous effort by the authors that defined the optimal radius of 0.659 inch and volumetric flow rate 30 ft³/min [5]. However, the model was reconfigured to have a variable ground for the current work. Similar to the original construction of the model, a computerized router table was used to cut out the peg holes on the side of the model; using a router table ensured that the holes were at the same locations on both the steel and LexanTM composite sides of the model, thereby ensuring the ground was level and parallel to the axis of the cylinder. The only other alteration to the original model was the plenum chamber. Previously, there was slight height variation in the height; the plenum was corrected so that the height as a function of the axial span was constant.

Along with the model, the components for obtaining the data needed to be assembled as are depicted in FIGURE 8. As visible in FIGURE 9, the instruments for data acquisition include a thermocouple, a pressure regulator, a volumetric flow rate sensor, and two shut-off valves. All of these devices were useful for the calculation of the jet velocity and the mass flow rate. While not visible in FIGURE 9, a pitot-static tube was employed to determine the actual velocity of the air leaving the slot. The principle sensor was the Heise digital pressure gauge. This measurement tool was used to measure the pressure from the surface pressure tap and the total and static pressure from the pitot-static tube.

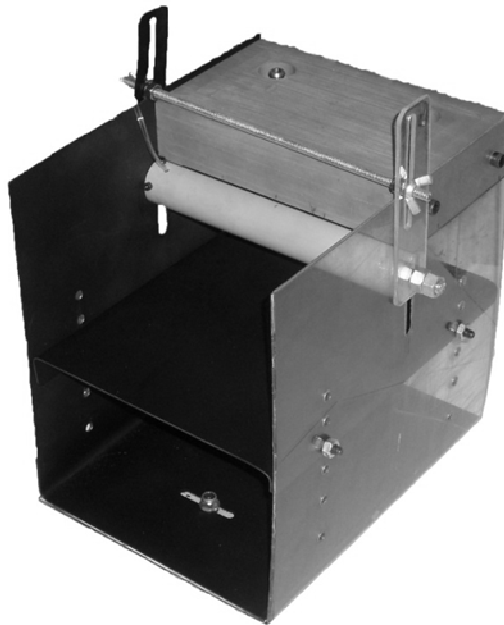


FIGURE 7: Model

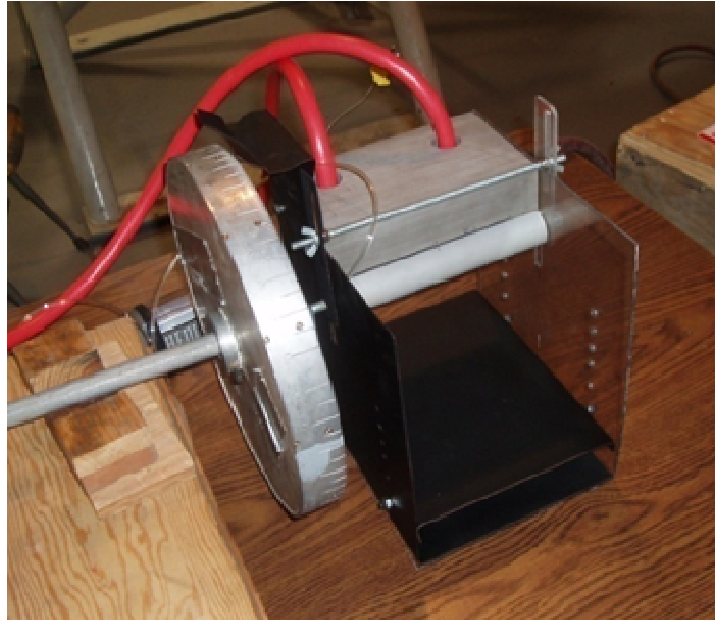


FIGURE 8 : Model with data acquisition equipment connected



FIGURE 9 : Data acquisition equipment

Over the course of completing the experiment, the same task was completed fifty-four times, for the six different heights, three different mass flow rates, and the three different radii. The repetitious task measured each surface pressure at every ten degrees, until the point of separation, where more points were measured to find a more refined separation location.

An important part of the testing method is to determine the location of the separation point. The point is generally located in step five of the test method and more accurately found in step seven. Upon reviewing the data, the separation point is defined as the point just before the ambient pressure is achieved. The separation point was chosen at the point just before the ambient pressure because if the pressure is the same as ambient the flow near the surface is no longer exposed to the vacuum, and thus free to detach

from the cylinder. FIGURE 14 shows the surface pressure of the cylinder with radius of 0.520 inch as a function of the angular displacement from the slot exit for the five different height locations measured. As the angular displacement increases, the surface pressure reached a horizontal, namely ambient pressure. The region of pressure lower than ambient pressure is the region where the jet is influenced by the surface, hence the Coanda effect is present and a vacuum is produced, thus holding the jet and entraining more air into the flow. Another measurement process was to determine the actual velocity of the jet. This value was obtained by measuring the static and total pressure of the airflow at five locations across the axial span of the slot, for the three different mass flow rates. Through Eq. (7) and Eq. (8), a variant of the continuity equation, the velocity of the jet could be determined.

$$P_{total} = \frac{\rho_j V_j^2}{2} + P_{static} \quad (7)$$

$$\rho_j = \frac{P_{static}}{T_j R} \quad (8)$$

4 RESULTS

4.1 Velocity Distribution

Across the span wise direction of the jet, the model exhibited a range of velocities, as shown in FIGURE 10. From this graph, it can be realized that there is a dip in the velocity from the left of the slot, labeled zero, to the center of the slot, indicated as location three. The explanation resulted from the use of structural bolts, which were placed in the plenum chamber to provide support for the plenum chamber and to ensure that the slot height remained constant. Since the bolts inhibited the flow of the air in the plenum, a lower velocity was produced, as measured at locations one through five. At both the zero and six locations, the velocities were expected to be lower than the maximum velocity, due to the interference of the side walls of the chamber on the flow. The maximum velocities of 184, 225, and 340 ft/s were determined, which correlates to the volumetric flow rates of 10, 20, and 30 ft³/min, respectively.

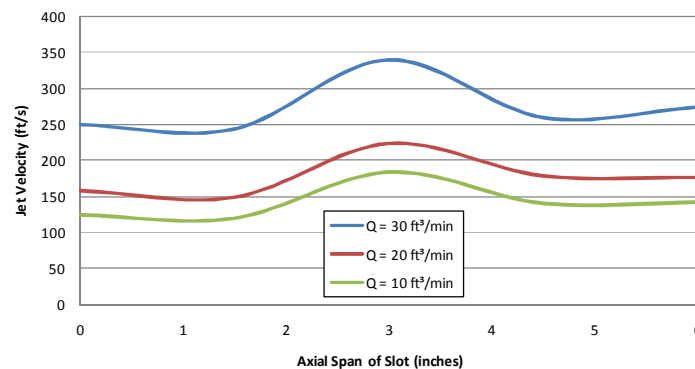


FIGURE 10 : Distribution of Jet Velocity

4.2 ANGLE OF SEPARATION AND GROUND HEIGHT

The first comparison of interest is the relationship of angular separation as a function of the height from the ground. As discussed, the h/r value is the variable of consideration when discussing the height from the ground. For FIGURE 11, FIGURE 12, and FIGURE 13, the same radius is compared for each respective graph which serves as a means to determine the impact that the volumetric flow rate has on the separation point, which is minimal. This indicates that a specific value for the rate is not the principal interest for initial analysis; similarly, if there is variability in a certain volumetric flow rate, such as the 20 ft³/min case in FIGURE 12 than that specific rate should be further investigated.

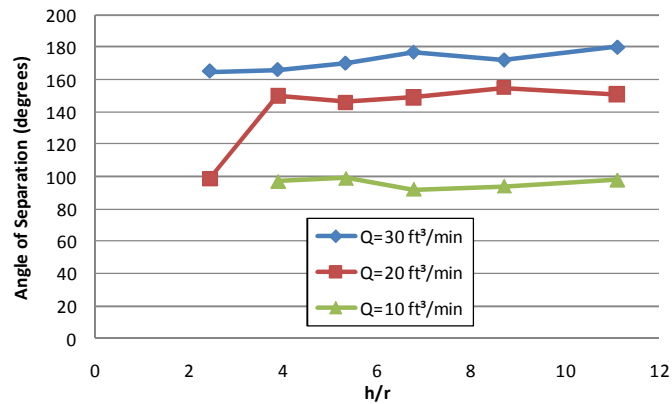


FIGURE 11 : Impact of ground proximity on the angular separation for r = 0.52 inch

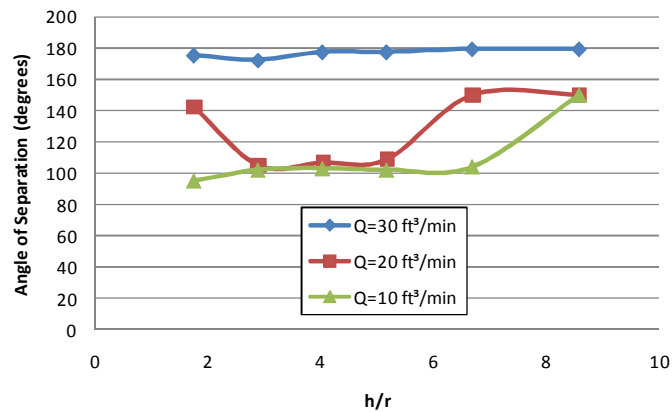


FIGURE 12 : Impact of ground proximity on the angular separation for r = 0.659 inch

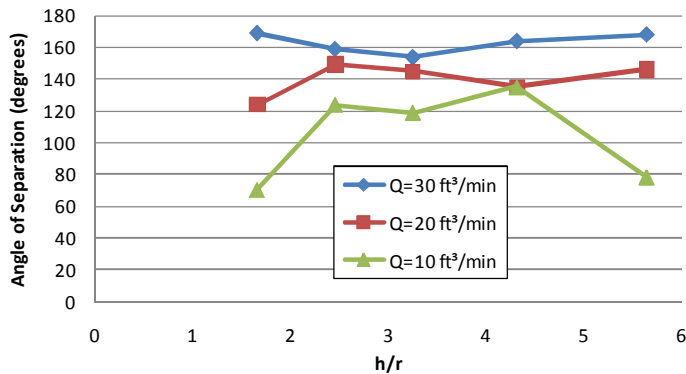


FIGURE 13 : Impact of ground proximity on the angular separation for r = 0.943 inch

When comparing the volumetric flow rate across the three different radii, each rate had a different degree of variability. For the volumetric flow rate of 30 ft³/min, the variability was relatively constant for the three radii. Most of the angles of separation for the subject volumetric flow rate were around 170 degrees. The relative constant angle of separation for 30 ft³/min indicates that this rate is not of further interest for this analysis. Since little change is occurring for the rate, it is safe to say that the angle of separation at 30 ft³/min is minimally affected by the variation in ground height. This conclusion is substantiated by the fact

that the subject rate is the fastest rate tested, suggesting that the faster the rate, the less it is impacted by the radii or height from the ground. Conversely, for the volumetric rate of 10 ft³/min, there were large variations between the three graphs and even within each graph, especially FIGURE 13. Thusly, 10 ft³/min is a rate for further analysis, since changes in the height alters the angle of separation in some manner. The final rate of 20 ft³/min did not exhibit the large disparity as 10 ft³/min, but it differs across each graph more than 30 ft³/min. However, since the lowest rate displays the largest change it will be the only volumetric rate for further analysis at this time. Future research will consider the relatively moderate variation in the 20 ft³/min volumetric flow rate and explore the pressure distribution just as is done for the lowest volumetric flow rate in the following section.

4.3 PRESSURE DISTRIBUTION

The next group of figures analyzes the surface pressure of the cylinder as a function of the angular displacement from the jet exit for the three radii, the different ground heights, and the subject volumetric flow rate. FIGURE 14, FIGURE 15, and FIGURE 16 all have a volumetric flow rate of 10 ft³/min, as discussed in the previous section. The figures culminate into FIGURE 17, which further illustrates the evident relationship of height to the pressure at an angle of 30 degrees in each the previous graphs (FIGURE 14, FIGURE 15, and FIGURE 16). The peak of all of these figures is a normalized pressure approaching unity, indicating that the recorded surface pressure is the same as ambient pressure, further illustrating that the flow separated from the cylindrical surface.

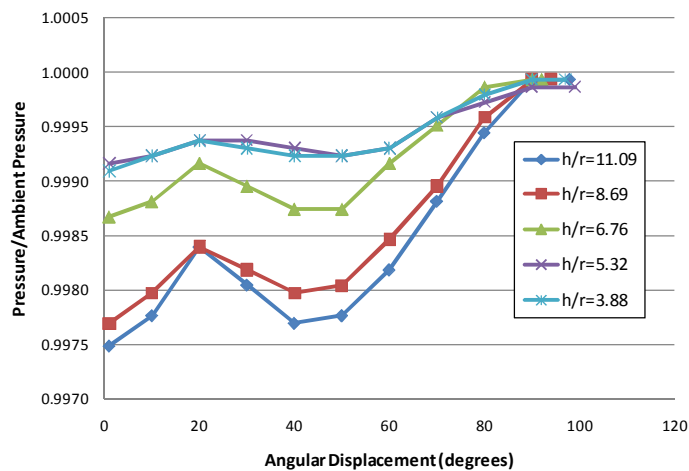


FIGURE 14 : Angular displacement vs. dimensionless pressure r = 0.520 inch

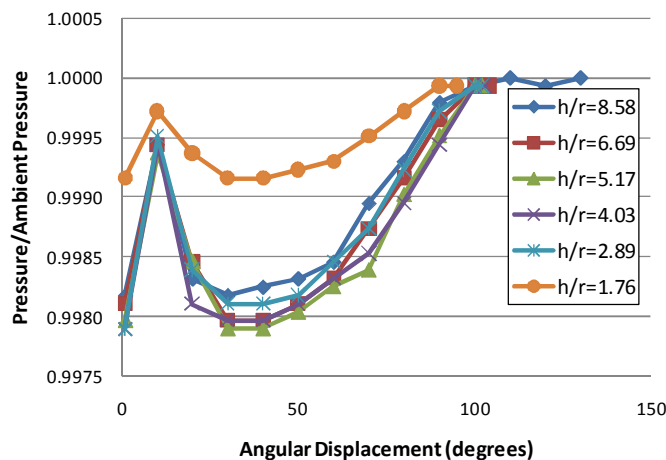


FIGURE 15 : Angular displacement vs. dimensionless pressure r = 0.659 inch

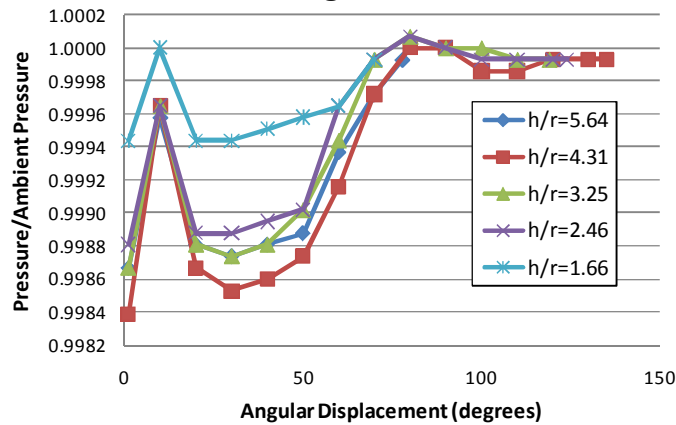


FIGURE 16 : Angular displacement vs. dimensionless pressure $r = 0.943$ inch

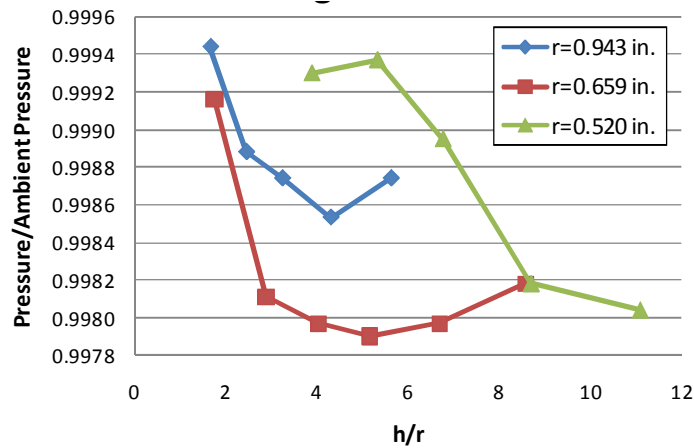


FIGURE 17 : Dimensionless pressure vs. h/r at 30 degrees from blown jet exit

FIGURE 14, FIGURE 15, and FIGURE 16 compare the angular displacement and the dimensionless pressure variable for each of the height from the surface tested. All of the figures have the same general trend, with a high pressure point (relative to ambient pressure) occurring in the 10 to 20 degree region. In one case, in FIGURE 16, for the h/r value of 1.66, the dimensionless pressure reaches one. It is suspected that this high pressure location is attributed to a weakening of the vacuum and a subsequent inflow of the high pressure airflow, characteristic of the entrainment Henri Coanda observed. Thus, in the subject region, more air is permitted to enter the vacuum further extending the angular displacement. Following the entrainment region, there is a significant drop in the pressure to another low pressure location at approximately 30 degrees for all of the radii. For a radius of 0.520 inch, in FIGURE 14, the low pressure region occurs later in the angular displacement than the other radii tested which indicates this value as a likely candidate for further research.

In addition, the results from FIGURE 14, as compared to the other two graphs, are spread out, such that the entrainment location and low pressure region occur at a larger angular displacement, suggesting that the smaller the radii, the larger the angular separation point. This conclusion is substantiated by previous work conducted by the authors, where, as the radii decreased, there was an increase in the angular separation point. However, in this previous study, the smallest radii, also 0.520 inch was not the optimal radii, illustrating that there is a threshold where a further decrease in the radii adversely impacted the separation location. While the initial test points of FIGURE 14 are prolonged, it is evident that the separation point occurs similar to the other radii. The final result of consideration from FIGURE 14 through FIGURE 16 is the separation location. Previous work suggested that the 0.659 inch was the

optimal radii in terms of largest angular separation point displacement. This effort also found that the 0.659 inch radii exhibited the largest average angular displacement when considering all of the height of the ground test locations. While the subject observation is not a new finding, its existence validates the test set-up of the current effort.

FIGURE 17 illustrates the dimensionless pressure vs. h/r at 30 degrees from the exit of the blown jet for each radius in FIGURE 14, FIGURE 15, and FIGURE 16. The location of 30 degrees for the blown slot exit plane was chosen based on the observation that the trough, or low pressure region, of each occurred approximately in this region. From the curve for the radius of 0.943 inch in FIGURE 17, it is evident that the pressure ratio decreases then increases, representing a minimum pressure point; the point of sign change correlates to an h/r value of 4.31. Similarly, for the curve representing 0.659 inch, the trend decreases and increases; the h/r value at the sign change is 5.17. Lastly, the h/r value for the curve illustrating the radius of 0.520 inch is 5.32, but the trend is reversed from the former two radii. The trend for the 0.520 inch radii increases and then decreases, representing a maximum pressure point. Furthermore, the two curves where the minimum is found represent the two highest radii, whereas the curve where the maximum point is found for the smallest radius. This finding indicates that there is a relationship between the radius of the cylinder and the ground height, and it appears that the preferred diameter is at some location between 0.520 and 0.659 inch diameters. Therefore there is an optimal h/r where circulation control and ground effect have the potential to enhance each other. In addition to the sign change finding, it is important to note that the h/r values at the sign change for the three radii, all occur at the relatively same value. This shows that there is a point where the ground maximizes or minimizes the surface pressure of the cylinder at 30 degrees. The unknown point resides between an h/r value of 4.31 and 5.32, which occurs at the largest radius and lowest radius tested, respectively. By identifying an optimal h/r value, it can further be stated that circulation control and ground effect, when combined, has the potential to enhance the lift augmentation of each other, since there is a relation between the pressure and the h/r value.

The results from this current effort primarily serve as a preliminary investigation to determine whether there is enhancement from the amalgamation of ground effect and circulation control prior to the development of a technology demonstration model. As discussed from theoretical and empirical research, each of the two, separately, exploit phenomenon that yield proven benefits in terms of lift augmentation.. The current effort does not demonstrate an increase in the lift augmentation by combining the two technologies, as would be the goal in proving the discussed technology for implementation. Rather, the research enclosed serves as the first step in proving this methodology to increase lift but it does not serve as a reference to improve a known technology, especially since this technology is only recently being explored and as of yet to be installed in a commercial application. Results from this effort demonstrate that as geometric parameters were altered, general trends were formed, such as when the radii is increased there is a decrease in the localized pressure, and a subsequent low pressure region, resulting in further entrainment of air flow. However, in the previous trend conclusion, there is a threshold where a further increase in the radii, increases the localized pressure. The general trends such as the one discussed are the basis for continuing the development of a technology demonstrator, in the form of wind tunnel models. This next phase of experimentation will provide empirical data to delineate whether there is lift augmentation from the combination of the two technologies.

5 CONCLUSION

This effort concludes that there is a potential for the further enhancement of lift by combining the aerodynamics benefits of circulation control and ground effect. As shown from FIGURE 14 through FIGURE 17 there is an optimal h/r value, between 4.31 and 5.32, which is where the maximum and minimum for each radius resides. In addition to an optimal value, these figures demonstrate that at a radius between 0.520 and 0.659 inch, there is an inversion between a positive and negative function, respectively, showing that there is an optimal radius, as well as a height-to-radius relationship in regards to the surface pressure of the cylindrical surface.

For future work in this subject, there are a few areas for further investigation. The focus of the results section for this work was on only one volumetric flow rate of 10 ft³/min, since it demonstrated the largest variability. However, as shown in FIGURE 11 through FIGURE 13, the volumetric flow rate of 20 ft³/min

exhibited some degree of change, suggesting that there is a some sort of relationship between radius and the h/r value, as found in case of $10 \text{ ft}^3/\text{min}$.

Another area of work, which is currently being pursued by the authors, is using the findings from this effort in an environment of flow onset. The effort is amalgamating ground effect and circulation control by conducting wind tunnel experimentation and determining the lift enhancement.

6 ACKNOWLEDGEMENTS

This work was also made possible through the research funding from the West Virginia NASA Space Grant Consortium.

7 NOMENCLATURE

b	slot height
b	wing span, Eq. (6)
C_D	coefficient of drag
C_L	coefficient of lift
C_{La}	lift coefficient in ground effect
$(C_{La})_\infty$	lift coefficient out of ground effect
C_p	coefficient of pressure
C_μ	blowing coefficient
c	chord length
D	drag force
H	height at the wing trailing edge
$h(x)$	height of the lower surface of the airfoil
h_{te}	height of the trailing edge
h/d_e	height to plate diameter
h/r	ground height to radius of curvature
L	lift force
L/D	lift force/drag force
M_j	jet Mach number
\dot{m}	mass flow rate
P_∞	free stream pressure
P_o	plenum pressure
P_{static}	static pressure
P_{total}	total pressure
Q	volumetric flow rate
q_∞	dynamic pressure
R	universal gas constant, $1716 \text{ ft lb/slug } ^\circ\text{R}$
Re	Reynolds number
r	radius of curvature
t	slot height
T	thrust of the jet
T_j	temperature of jet
U_∞	free stream velocity
$u(x)$	horizontal velocity contribution
V_j, V_{jet}	velocity of jet

V_∞	free stream velocity
γ	ratio of specific heat
ΔP	local pressure difference
θ	angular displacement
ρ_j	density of the jet

8 REFERENCES

- [1] Byron W. Patterson et al., "Drag Reduction Methodologies for Circulation Control Applications".
- [2] Peter J. Mantle, *Air Cushion Craft Development*. Bethesda, MD: David W. Taylor Naval Ship Research and Development Center, January 1980.
- [3] Imantus Reba, "Applications of the Coanda Effect," *Scientific American* , pp. 84-92, 1966.
- [4] B.E. Newman, "The Deflexion of Plane Jets by Adjacent Boundaries - Coanda Effect," in *Boundary Layer and Flow Control Vol. 1.*: Pergamon Press, 1961, pp. 232-264.
- [5] Byron W. Patterson, Gerald M. Angle II, Emily D. Pertl, and James E. Smith, "Delay in Flow Separation for Circulation Controlled Cylinders," in *ASME International Mechanical Engineering Congress and Exposition (IMECE)*, Vancouver, British Columbia, Canada, November 12-18, 2010.
- [6] Robert J. McGhee and William D. Beasley, "Effects of Thickness on the Aerodynamic Characteristics of an Initial Low-Speed Family of Aviation for General Aviation Applications," Hampton, Virginia, June 1976.
- [7] Christopher M. Cagle and Gregory S. Jones, "A Wind Tunnel Model to Explore Unsteady Circulation Control for General Aviation Applications," in *22nd AIAA Aerodynamic Measurement Technology and Ground Testing Conference*, St. Louis, Missouri, 2002.
- [8] David T. Fisher, "Wind Tunnel Performance Comparative Test Results of a Circular Cylinder and 50% Ellipse Tailboom for Circulation Control Antitorque Applications," Monterey, California, MS Thesis 1994.
- [9] Jack P. Ambrosiani, "Analysis of a Circulation Controlled Elliptical Airfoil," West Virginia University, PhD Dissertation 1971.
- [10] Robert J. Englar, "Subsonic Two-Dimensional Wind Tunnel Investigation of the High Lift Capability of Circulation Control Wing Sections," Bethesda, Maryland, Report ASED-274 April 1975.
- [11] Harry J. Goett and W. Kenneth Bullivant, "Tests of N.A.C.A. 0009, 0012, and 0018 Airfoils in the Full-Scale Tunnel," Langley, VA, Report No. 647 1939.
- [12] Gerald M. Angle, "Data Tables from the Blue CC-NACA0018 Model Wind Tunnel Testing," Morgantown, West Virginia, 2009.
- [13] C. Coulliette and A. Plotkin, "Aerofoil ground effect revisited," *Aeronautical Journal*, pp. 65-74, February 1996.

- [14] John J. Bertin and Russell M. Cummings, *Aerodynamics for Engineers*, 5th ed. Upper Saddle River, NJ, United States of America: Pearson Prentice-Hall, 2009.
- [15] David C. Bellavia, Douglas A. Wardwell, Victor R. Corsiglia, and Richard E. Kuhn, "Forces and Pressures Induced on Circular Plates by a Single Lifting Jet in Ground Effect," Moffett Field, California, March 1991.
- [16] A. Plotkin and S.S. Dodbele, "Slender Wing in Ground Effect," *AIAA Journal Vol. 26 No.4*, pp. 493-494, April 1988.

INSTRUCTIONS TO CONTRIBUTORS

The *International Journal of Engineering (IJE)* is devoted in assimilating publications that document development and research results within the broad spectrum of subfields in the engineering sciences. The journal intends to disseminate knowledge in the various disciplines of the engineering field from theoretical, practical and analytical research to physical implications and theoretical or quantitative discussion intended for both academic and industrial progress.

Our intended audiences comprises of scientists, researchers, mathematicians, practicing engineers, among others working in Engineering and welcome them to exchange and share their expertise in their particular disciplines. We also encourage articles, interdisciplinary in nature. The realm of International Journal of Engineering (IJE) extends, but not limited, to the following:

To build its International reputation, we are disseminating the publication information through Google Books, Google Scholar, Directory of Open Access Journals (DOAJ), Open J Gate, ScientificCommons, Docstoc and many more. Our International Editors are working on establishing ISI listing and a good impact factor for IJE.

The initial efforts helped to shape the editorial policy and to sharpen the focus of the journal. Starting with volume 5, 2011, IJE appears in more focused issues. Besides normal publications, IJE intend to organized special issues on more focused topics. Each special issue will have a designated editor (editors) – either member of the editorial board or another recognized specialist in the respective field.

We are open to contributions, proposals for any topic as well as for editors and reviewers. We understand that it is through the effort of volunteers that CSC Journals continues to grow and flourish.

IJE LIST OF TOPICS

The realm of International Journal of Engineering (IJE) extends, but not limited, to the following:

- Aerospace Engineering
- Biomedical Engineering
- Civil & Structural Engineering
- Control Systems Engineering
- Electrical Engineering
- Engineering Mathematics
- Environmental Engineering
- Geotechnical Engineering
- Manufacturing Engineering
- Mechanical Engineering
- Nuclear Engineering
- Petroleum Engineering
- Telecommunications Engineering
- Agricultural Engineering
- Chemical Engineering
- Computer Engineering
- Education Engineering
- Electronic Engineering
- Engineering Science
- Fluid Engineering
- Industrial Engineering
- Materials & Technology Engineering
- Mineral & Mining Engineering
- Optical Engineering
- Robotics & Automation Engineering

CALL FOR PAPERS

Volume: 5 - Issue: 3 - May 2011

i. Paper Submission: May 31, 2011

ii. Author Notification: July 01, 2011

iii. Issue Publication: July /August 2011

CONTACT INFORMATION

Computer Science Journals Sdn Bhd

M-3-19, Plaza Damas Sri Hartamas
50480, Kuala Lumpur MALAYSIA

Phone: 006 03 6207 1607
006 03 2782 6991

Fax: 006 03 6207 1697

Email: cscpress@cscjournals.org

CSC PUBLISHERS © 2011
COMPUTER SCIENCE JOURNALS SDN BHD
M-3-19, PLAZA DAMAS
SRI HARTAMAS
50480, KUALA LUMPUR
MALAYSIA

PHONE: 006 03 6207 1607
006 03 2782 6991

FAX: 006 03 6207 1697
EMAIL: cscpress@cscjournals.org